The University Of Sheffield.

Thesis Title

Study of Carbide Composites and Their Interfaces for Generation IV Nuclear Reactor

By:

Tanagorn Kwamman

A thesis submitted in partial fulfilment of the requirements for the degree of Doctor of Philosophy

The University of Sheffield
Faculty of Engineering
Department of Materials Science and Engineering

Submission Date

December 2018

Abstract

Carbide based materials (SiC, TiC and ZrC) have long been suggested for use within core components and structural materials in the next generation of fission reactors. Their characteristics satisfy the reactor material criteria in terms of good mechanical property, corrosion resistance, fission product retention ability, and low neutron cross section absorption. However, a major drawback of such materials is their brittleness. Thus, the aim of this project is to overcome this brittle behaviour by the fabrication of carbide composites. In addition to this, understanding the various composite interfaces (Ex. TiC/TiC, TiC/SiC and SiC/SiC) will give crucial information for materials design and simulation.

TiC-SiC composites were prepared by spark plasma sintering (SPS). The relative density of TiC-30%SiC (70% and 30% mole of TiC and SiC, respectively) and TiC-50%SiC (50% and 50% mole of TiC and SiC, respectively) reached to approximately 99 % without sintering aids at SPS temperature of 2100 °C, 50 MPa. Morphology and mechanical properties correlation were investigated by Scanning Electron Microscopy (SEM) and Transmission Electron Microscopy (TEM). They exhibited excellent thermal and mechanical properties. Thermal conductivities of TiC-30% and 50% SiC are 67 and 50 W/m K^{-1} respectively and stable over 100 – 500 °C. Their Vickers hardness was 26-31 GPa. Remarkably, the fracture toughness of TiC-SiC composites (~ 7.9 MPa √m) was considerably higher than TiC, SiC and previous reports.

Moreover, ZrC-SiC composites were prepared and investigated by similar procedure as TiC-SiC composites. Their mechanical and thermal properties were worse than TiC-SiC composites in that their facture toughness and thermal conductivity was about 3.2 MPa √m and 30-50 W/m K^{-1} at room temperature. However, ZrC-SiC composites are interesting in term of low neutron absorption.

Acknowledgements

I would like to express my sincere gratitude to Professor Mark Rainforth, my research supervisor, for his patient guidance, enthusiastic encouragement and useful critiques of this research work. I would also like to especially thank Dr Kerry Abram for his advice and assistance throughout the entirety of my PhD as my thesis coach. Additionally, I would like to thank ISL group.

I wish to thank the following people for their valuable technical support of this project: Dr Martin Stennet, Ben Palmer, Michael Bell, Dr Nik Reeves, Dr Peng Zeng, Mr Dean Haylock.

I would like to thank Royal Thai Scholarship for their financial support of my PhD. I would also like to extend my thanks to the Development and Promotion of Science and Technology Talents Project, for their financial support from high school until master degree. A special thanks also to the Thailand Institute of Nuclear Technology (Public organization) to give me a position as a researcher.

Although I sometimes struggled with the problems of study and life in general, during my PhD in Sheffield, I have really enjoyed this journey. I have learned a lot from all my new friends here. Thanks to all for being awesome! I would like to thank my best desk buddy, Dr Daniel Cooper for experimental support and for discussions of our work. I have also been privileged to discover, in Sheffield, Bouldering, my favourite activity ever; falling second place only to my PhD. I would therefore like to thank my bouldering buddies Dan, Sean, Joe, Michael, Peng, Liam and James for spending time doing my favourite activity with me. It was fun!

I would like to thank my close friends: Jern, Nueng, Yoo, Por, Tee, and Nipa for your emotional support. I am so lucky to be surrounded by lovely Thai friends here: Tim, Mon, Aung, Duen, Pati and Natcha. I would like to thank my fantastic part-time English tutor, Tom for help with English grammar and punctuation.

Finally, to my mother Pensri Junjumras, I am eternally grateful for your moral and emotional support and encouragement throughout my study. I also thank my little sister, Noppasorn Junjumras for being a reason to bring me back to Thailand.

Declaration

To my mother who made everything possible.

Table of Acronyms

ATF: Accident tolerant fuel
3C-SiC: Cubic silicon carbide
6H-SiC : Hexagonal silicon carbide
BSE: Backscattered electrons
CL: Cathode luminescence
CMC: Ceramic matrix composite
Cp: Specific heat
CVD: Chemical vapor deposited
CVI: Chemical vapour infiltration
dpa: displacement per atom
ED: Electron diffraction
E_0: Elastic modulus (GPa)
EDX: Energy dispersive X-ray analysis
F-M: Ferritic-martensitic stainless steels
GFR: Gas-cooled fast reactor
GIF: Generation IV International Forum
HV: Hardness
IASCC: irradiation assisted stress corrosion cracking
IEA: International Energy Agency
IG: Intergranular
K_{IC}: Fracture toughness
K: Thermal conductivity (W/m K)
LFR: Lead-cooled faast reactor
LOCA: A loss-of coolant accident
MSR: Molten salt reactor
NITE: Nano-infiltration and transient eutectoid
ODS: Oxide-dispersion-stenghened steels
pb: Brige flexure
PIP: Polymer infiltration an pyrolysis
PWR: Pressurized Water Reactors
PyC: Pyrolytic carbon
RD: Relative density
e_f: Flexural strain
σ_{fs} : Flexural strength (GPa)
P: Loading (kg)
d: The length of the resultant indent (mm)
C_p: Specific heat

Table of contents

1. Introduction and research objectives

To meet increased demand for electricity with the provision of clean, reliable energy and a reduction of air pollution, nuclear power has been considered as important electricity production. In 2011, 2236 million tonnes CO_2 emission was produced from generating 2518 TWh of electricity by coal-fired reactors, whereas only 73 million tonnes of CO_2 was produced from nuclear power plants generating the same amount of electricity [1]. According to an International Energy Agency (IEA) report, nuclear energy accounted for approximately 18.7 % of total world electricity in 2016 [2]. More than 430 commercial nuclear power plants in 31 countries are in operation, and a further 72 power plants are under construction [2].

In mid-2001, the Generation IV International Forum (GIF) was chartered, which consists of members from 14 countries: Argentina, Brazil, Canada, France, Japan, South Korea, South Africa, the UK, the USA, Switzerland, the EU (Euratom), China, Russia and Australia with the aim of sharing their R&D knowledge [3]. In late 2002, GIF announced a roadmap of proposed new reactor concepts for Generation IV (Gen IV) nuclear reactors for deployment between 2020 and 2030 [3-6]. The purposes of new designs are to enhance safety, reliability, protect against proliferation and minimise nuclear waste [3-6]. There are six candidates for advanced systems from 130 proposed systems: three thermal neutron reactors (GFR, SFR and LFR) and three fast neutron reactors (VHTR, MSR and SCWR) [3-6]. The new reactors operate at higher temperatures than today's reactors [3-6]. Furthermore, fast neutron reactors offer significantly more efficient use of uranium fuel. Running the reactors at the high temperatures requires a material that retains shape and strength, while also allowing neutron transport [7, 8]. Hence, materials selection and development is an important key to the success of the Gen IV reactors. Material characterisation and in-situ experiments should be integrated to construct an accurate model to predict reactor damage during their lifetime in extreme conditions (high temperature, high pressure and neutron irradiation) inducing material defects from atom scale to macro scale [7, 8].

After the Fukushima accident in 2011, several cladding materials are proposed to use in Gen IV reactors instead of Zr-based materials to improved safety for water-cooled reactors in a loss-of-coolant accident (LOCA) [4, 9]. Refractory carbides such as silicon carbide (SiC), zirconium carbide (ZrC) and titanium carbide (TiC) are promising candidates for LFR, VHTR and GFR reactors according to their superior properties; their high melting point, excellent resistance to fission products attack, high thermal conductivity at very high temperatures, and low neutron absorption cross-sections [4, 9]. Therefore, their properties may allow the SiC-

based claddings to operate at higher temperatures (> 850 °C) [10-14]. However, the drawbacks of SiC include being challenging to sinter without sintering aids and having a low fracture toughness [15, 16]. Incorporation of refractory carbides such as TiC and ZrC in SiC have been reported to enhance their toughness [17-22]. SiC/SiC$_{fibre}$ have been widely studied for cladding [10-14]. By contrast, there are few reports regarding TiC/SiC and ZrC/SiC composites for nuclear applications, even though the thermal conductivity of TiC/SiC composites tend to be better than SiC/SiC$_{fibre}$ due to the benefit of TiC conductivity which increases proportionally to temperatures[15, 16]. In contrast, SiC/SiC$_{fibre}$ thermal conductivity changes inversely to temperature [10-14]. The structural properties of TiC/SiC and ZrC/SiC composites must be understood in the context of the applications in which they will be used. Development of databases that correlate physical, chemical, and nuclear properties would accelerate and facilitate innovations in nuclear designs [7, 8].

Therefore, this research aims to develop the process route to manufacture TiC/SiC and ZrC/SiC composites with high density, strength and toughness and good thermal conductivity, correlate microstructure with mechanical and physical properties, and understand the toughening mechanisms in these composites.

2. Literature review

2.1 Generation IV (Gen IV) nuclear reactors

Table 2.1 shows the six proposed designs of Gen IV reactors by GIF [4, 23-25]. The three fast reactor designs consist of GFR (Gas-cooled Fast Reactor), SFR (Sodium-cooled Fast Reactor) and LFR (Lead-cooled Fast Reactor). The other three thermal reactor designs are VHTR (Very high-temperature reactor), SCWR (Supercritical water-cooled reactor), and MSR (Molten Salt Reactor).

Table 2.1 Summary of Gen IV reactor systems [25]

Reactor system	Coolant	Neutron spectrum	Core outlet temperature (°C)
Gas-cooled fast reactor (GFR)	Helium gas	Fast	~ 850
Lead-cooled fast reactor (LFR)	Liquid metal Pb, Pb-Bi	Fast	550-800
Sodium-cooled fast reactor (SFR)	Liquid sodium	Fast	~550
Very high-temperature reactor (VHTR)	Helium gas	Thermal	> 900
Supercritical water-cooled reactor (SCWR)	Supercritical water	Thermal	350-620
Molten salt reactor (MSR)	Molten salt	Thermal	700-800

All six designs have extremely high operating temperatures and neutron damage up to ~150 dpa (displacement per atom) compared to previous commercial reactors; for example, PWR (Pressurized Water Reactors) operates at 325 °C [4, 23-25]. The thermal neutron reactors use thermal neutrons which are moderated by a neutron moderation, so their energy (0.025 MeV) is significantly lower than fast neutron reactors (1-20 MeV) [26]. Nevertheless, for thermal neutron reactors, the nuclear cross-section of uranium-235 is much higher. Thus thermal neutron reactors tend to cause fission reaction of uranium-235 instead of being captured by uranium-238 resulting in increased fission yield [26]. On the other hand, fast neutron reactors continue the fission reaction by fast neutrons without the neutron moderator. Hence, they have an advantage in terms of the increase in the transmutation of undesirable and fertile isotopes into usable fuel, leading to the reduction of nuclear waste [4, 5, 23-25, 27-30].

Non-water coolants are applied to Gen IV nuclear reactors as shown in Table 2.1. Helium gas as a coolant providing a high energy neutron spectrum due to a low absorption cross-section is proposed to use in VHTR and GFR, which run at an extremely high temperature [4, 5, 23-25, 27-30]. Sodium is a candidate for SFR reactor because of its relatively low melting temperature (98 °C), low neutron capture cross-section, low occurrence of troublesome fission products, excellent flow characteristics and excellent compatibility with fuel and structural

materials [4, 5, 23-25, 27-30]. LFR utilises a lead (Pb) or a lead-bismuth eutectic (Pb-Bi) as the coolant. An obstacle to using Pi-Bi is the generation of ^{210}Po (the highly active isotope) [4, 5, 23-25, 27-30]. One of the most challenging aspects of lead technology is its corrosive nature, which requires careful oxygen control and the use of highly corrosion-resistant materials [4, 25]. However, SCWR is the light water reactor that operates above the thermodynamic critical point of water (374 °C, 22 MPa), which only exists as vapour [3, 4, 23-25, 31].

2.2 Material challenges for Generation IV nuclear reactors

Gen IV reactors share some similar desirable requirements for the structural materials used in the core reactor (which contains the fuel assemblies, the moderators and the control rods) and outside the core reactor. Firstly, excellent dimensional stability against thermal and irradiation creep and void swellings are required [4, 24, 25, 27, 28, 30]. Secondly, favourable mechanical properties such as strength, ductility, creep rupture, fatigue and creep-fatigue interactions are necessary [4, 24, 25, 27, 28, 30]. Moreover, acceptable resistance to radiation damage (irradiation hardening and embrittlement) under high neutron doses (10-150 dpa or 'displacements per atom'), helium embrittlement is essential [4, 24, 25, 27, 28, 30]. In this regard, resistance to stress corrosion cracking (SCC) and irradiation assisted stress corrosion cracking (IASCC) are essential. Finally, workability, weldability, and cost are other crucial aspects that need to be considered with the materials selection process [32].

As shown in Figure 2.1, the Gen IV reactor operates at a higher temperature and neutron damage level (dpa) than Gen II/III reactors. The high operating temperature of the Gen IV reactors would limit the utilisation of zircaloy as the cladding [5, 8, 30]. The beta to alpha phase transformation in the zircaloy takes place at a temperature above 800 °C resulting in the embrittlement of the cladding [5, 10, 33, 34]. In the Fukushima Daiichi accident in 2011, a loss-of-coolant accident (LOCA) occurred in high-temperature steam (> 400 °C) and directly contacted the zircaloy cladding, leading to a reaction between water and Zr to generate hydrogen gases which then ignited/exploded [35, 36]. During LOCA, the mechanisms protecting against corrosion and deformation were slowed down. Thus, an interest in accident-tolerant fuel cladding has led to modification of zircaloy by a coating process and development of novel fuels with an advanced cladding concept (metallic fuel and composite fuel) [13, 28, 37]. Consequently, advanced materials such as F/M stainless steels, austenitic stainless steels, ODS alloys and refractory ceramics are proposed as candidates for fuel claddings in the Generation IV reactors, based on the maximum service temperature and neutron absorption as

shown in Table 2.2 [5, 25, 32, 38] [13]. Hence, the cladding material analysis related to the new fuels needs to be investigated to evaluate the potential fuel performance.

Table 2.2 Calculated effective neutron absorption cross-section (neutron absorption cross section per unit of yield strength compared to Zr alloys) and maximum service temperature for selected materials for Generation IV nuclear reactors [13]

Materials	Maximum service Temperature (°C)	Effective neutron absorption cross-section relative to Zr alloys
Zirconium alloys	400	1
F/M stainless steels	500	15
Inconel	500	15
Austenitic stainless steels	600	15
ODS alloys	700	15
Nb-1Zr alloy	800	20
Zirconium carbide (ZrC)	900	0.20
Silicon carbide (SiC)	900	0.10
Tantalum alloys	1000	50
Molybdenum alloys	1100	10
Tungsten alloys	1200	35

*Based on neutron irradiation between 10 dpa and 50 dpa (the displacement per atom, dpa, is the average times that an atom is displaced for a given fluence)

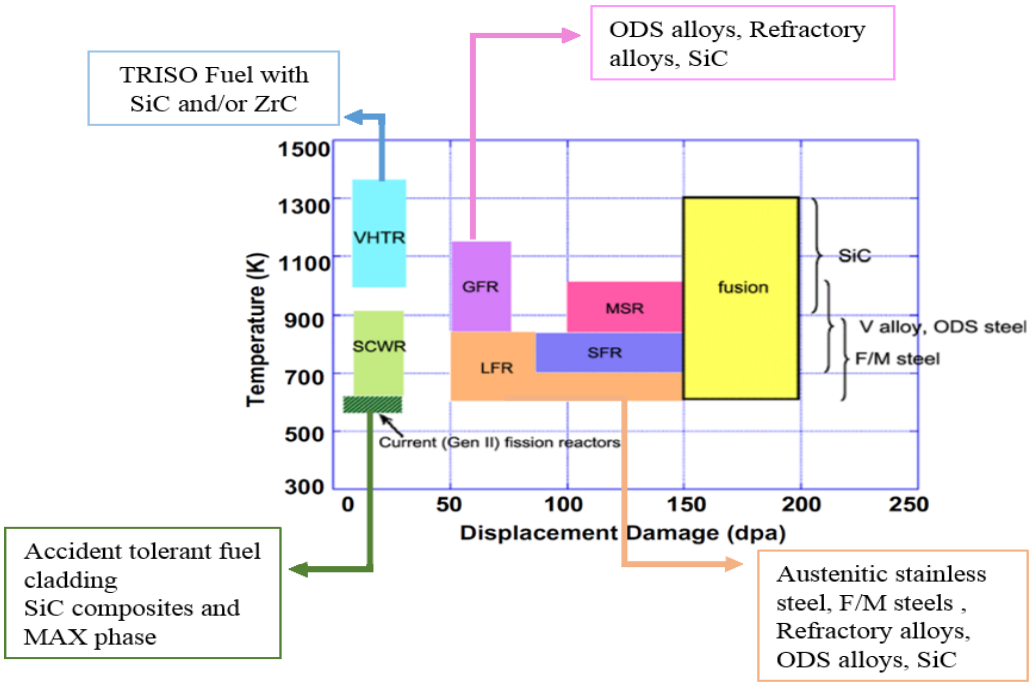

Figure 2.1 Main characteristics of Generation IV nuclear fission reactor systems. Note: Abbreviations: F-M, Ferritic–martensitic stainless steels (typically 9–12 wt.% Cr); ODS, oxide-dispersion-strengthened steels (typically ferritic–martensitic) adapted from [32]

2.3 Application of carbide materials in Generation IV nuclear reactors

Carbide based materials are suitable for high-temperature applications and considered as potential candidates for core components and structural materials in Gen IV reactors [5, 13, 25, 30, 32, 38]. Their characteristics satisfy the main criteria of cladding materials for VHTR, LFR and GFR regarding corrosion resistance, fission product retention ability, excellent mechanical property, and low neutron cross section absorption [27, 38-41].

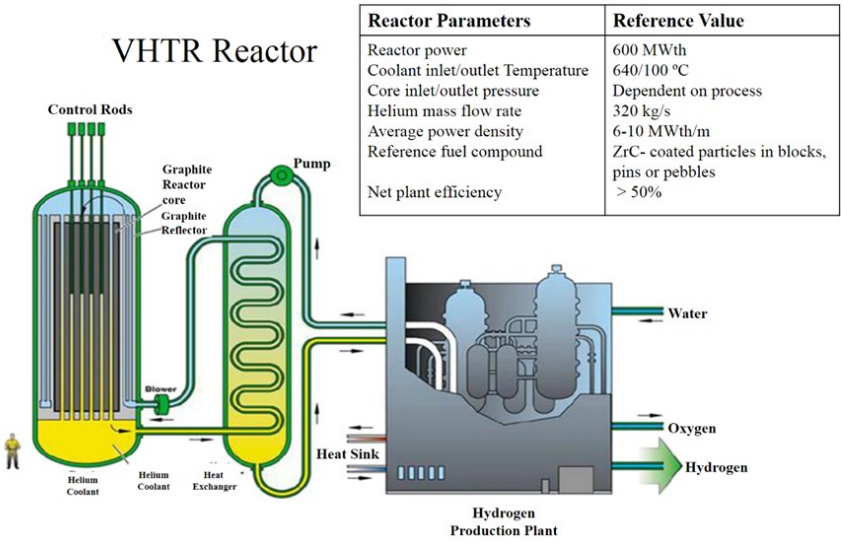

Reactor Parameters	Reference Value
Reactor power	600 MWth
Coolant inlet/outlet Temperature	640/100 °C
Core inlet/outlet pressure	Dependent on process
Helium mass flow rate	320 kg/s
Average power density	6-10 MWth/m
Reference fuel compound	ZrC- coated particles in blocks, pins or pebbles
Net plant efficiency	> 50%

Figure 2.2 Outline of Very High-Temperature Reactor (VHTR) components adapted from [4, 25]

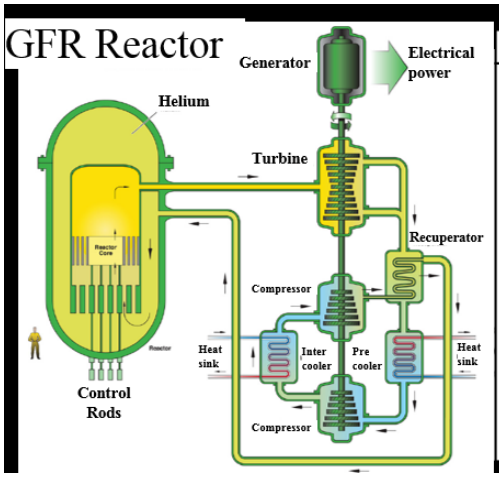

Reactor Parameters	Reactor Value
Reactor power	600 MWth
Net plant efficiency (direct cycle helium)	48%
Coolant inlet/outlet Pressure	490 °C /850 °C At 90 bar
Average power density	100 MWth/m^3
Reference fuel compound	UPuC/SiC (70/30%) with about 20% Pu content
Volume fraction, Fuel/Gas/SiC	50/40/10%
Conversion ratio	Self-sufficient
Burnup, Damage	5% FIMA; 60 dpa

Figure 2.3 Outline of Gas-cooled Fast Reactor (GFR) components adapted from [4, 25]

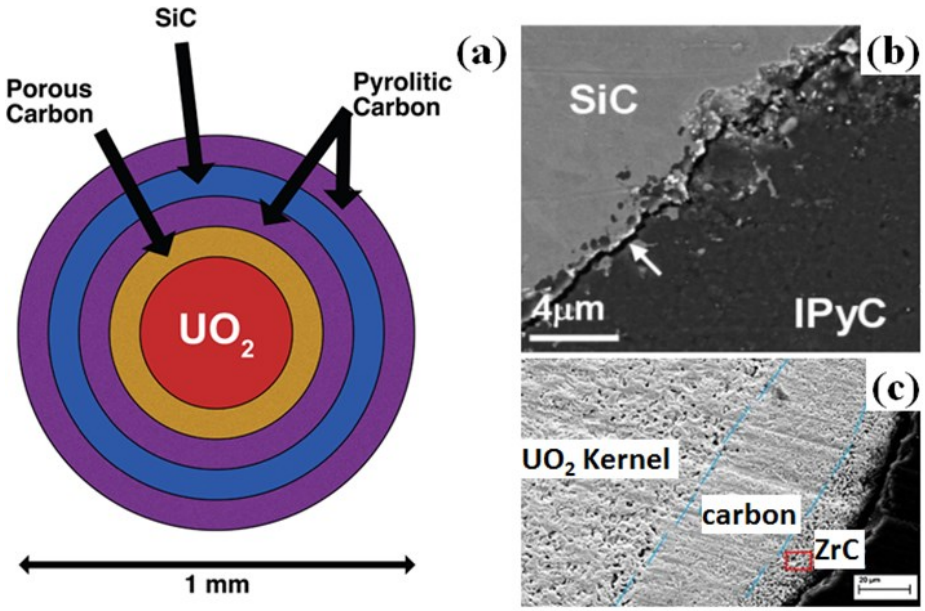

Figure 2.4 The triple-isotropic coated fuel particle (TRISO) [42-45]

Triple-isotropic coated fuel particle (TRISO) is the candidate fuel and cladding methodology of VHTR (Figure 2.2) and GFR (Figure 2.3) [8, 45]. The TRISO (~ 1 mm diameter) consists of a UO_2 kernel at the centre, surrounded by an inner porous pyrolytic carbon layer (PyC), a silicon carbide layer (SiC), and an outer dense pyrolytic carbon layer [42-45]. The porous carbon absorbs the gaseous fission products, the SiC layer acts as a hard barrier to fission products, and the outer PyC layer provides strength as shown in Figure 2.4 [42-45]. TRISO has several advantages in terms of ability to retain fission products and burn-up efficiency. However, various phenomena can lead to TRISO failure: a radial shrinkage of PyC layers (Figure 2.4b) from neutron irradiation and irradiation creep of PyC layers from outward and inward stress differences generated by containing fission gases [45]. Furthermore, tangential stresses in the SiC layers cause the de-bonding between PyC and SiC layers resulting in cracking along fuel particles as shown in Figure 2.4b [42-45]. Therefore, the failure mechanisms need to be understood to generate accurate models to assess how the fuel behaves relative to the criteria [42-45]. Additionally, alternate layers are introduced to improve the efficiency of containing fission products, for example, a ZrC layer as shown in Figure 2.4c [42-45].

Table 2.3 GFR fuel matrix and structural material reference requirements [29].

Requirement	Reference Value
Melting and decomposition temperature	> 2000 °C
Radiation-induced swelling	< 2% over service life
Fracture toughness	> 12 MPa $m^{1/2}$
Thermal conductivity	> 10 W/mK
Neutronic properties	- Have low neutron absorption - Maintain proper safety parameters during service time

Furthermore, silicon carbide (SiC), zirconium carbide (ZrC) and titanium carbide (TiC) are candidates for fuel cladding GFR. Their properties meet the requirement of GFR materials apart from the fracture toughness (K_{IC}) as summarised in Table 2.3 [29]. Their properties and applications will be explained further.

2.3.1 Silicon carbide (SiC)

Silicon carbide is a refractory ceramic, and its bonding is strong covalent (300 kJ/mol bond energy) leading to a high melting point, thermal and chemical stability, extremely hard and robust materials [15, 46]. There are more than 250 polytypes of silicon carbide, for example, 6H-SiC, 4H-SiC and 3C-SiC as shown in Figure 2.5. Hexagonal 6H-SiC and 4H-SiC (α-SiC) are the most common structures, although they differ in their stacking layers: ABCACBABCACBA, ABACABAC and ABC respectively [15, 46]. Their structures have a close-packed layer (0001) of the hexagonal system, and the (111) plane of the cubic system is identical, while their stacking layers differ. The cubic 3C-SiC (β-SiC, zinc-blende) is the preferred polytypes for TRISO fuel coating. Regarding previous reports, β-SiC possibly has a higher radiation resistance against neutron bombardment than α-SiC [15, 46, 47].

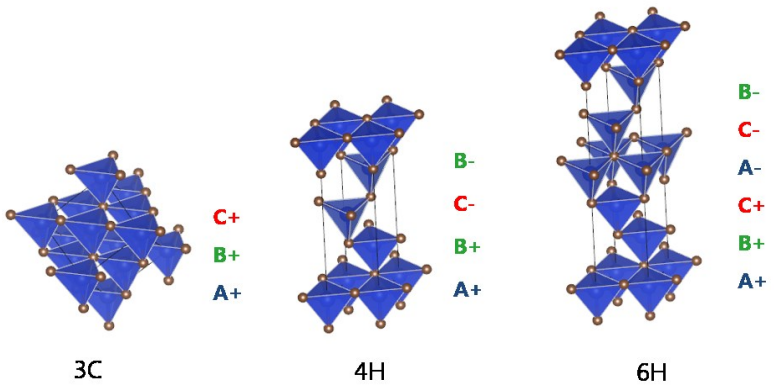

Figure 2.5 Crystal structure of 3C-SiC (β-SiC), 4H-SiC (α-SiC) and 6H-SiC (α-SiC)

2.3.1.1 Physical and mechanical properties of SiC

The thermal conductivity (*K*) of β-SiC is shown in Figure 2.6. The *K* of high purity single crystal SiC is significant higher compared to polycrystalline SiC. Below -73°C the *K* of SiC dramatically increases with increasing temperature [46]. However, above -73°C, it decreases with increasing temperatures [46]. Thermal conductivity also depends on microstructures. *K* lessens with decreasing grain size because of grain boundary scattering. However, the differences in grain sizes become less significant with increasing temperature because the phonon-phonon scattering dominates other grain boundary scattering [15, 46, 48]. Impurities such as residual sintering additives also lower the *K* [46].

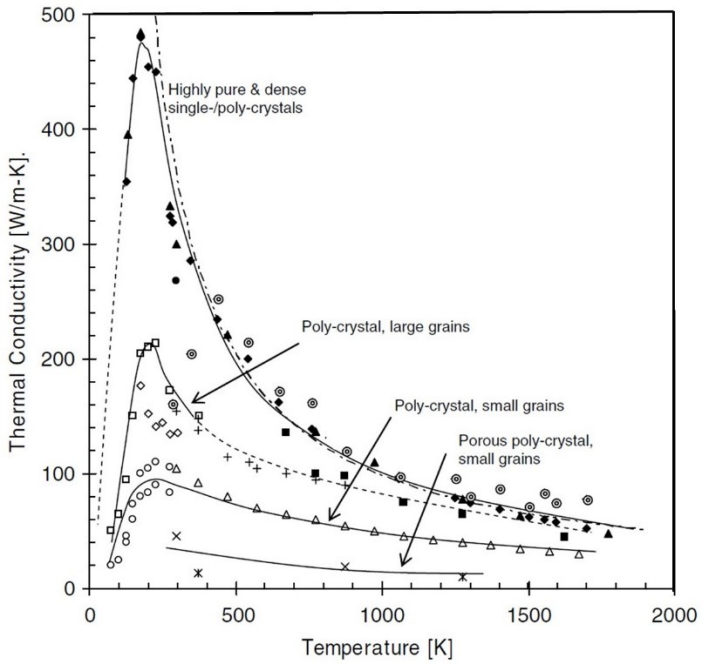

Figure 2.6 Thermal conductivity of SiC at elevated temperatures [46].

Additionally, Figure 2.7 illustrates the coefficient of thermal expansion (α) of β-SiC. As a result of the firm covalent bonding of SiC, thermal expansion is small (4 - 5 x 10^{-6} K^{-1}) [46]. Apparently, β-SiC exhibits a linear thermal expansion from room temperature up to approximately 700 K, then roughly stabilises as a function of temperatures.

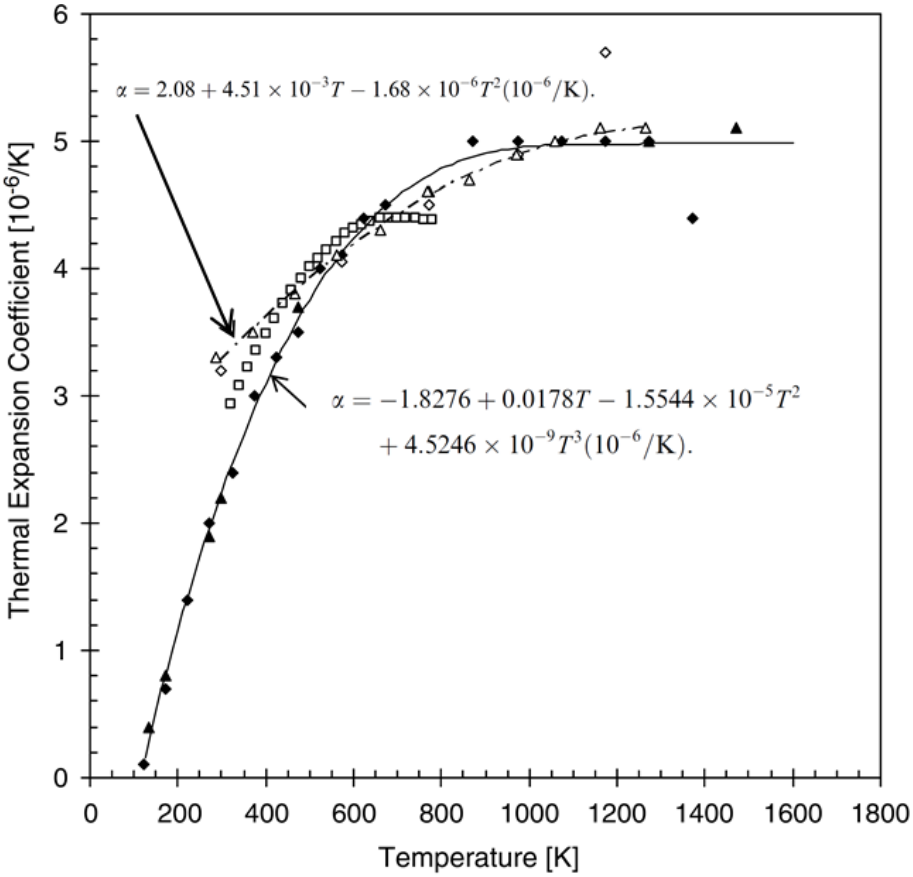

Figure 2.7 Thermal expansivity of β-SiC (cubic structure) at elevated temperatures [46]. Note that ▲ is prepared by CVD from Pickeringe *et al*.[49], ♦ is prepared CVD from Rohm and Haas Co.[50], ◊ is prepared reaction bonded from Suzuki *et al*.[51], Δ is from Li & Bradit [52] and □ is prepared by fluidized bed from Pojour *et al.* [53]

The elastic modulus (E_0) of pore-free SiC is about 470 GPa at room temperature [15, 46]. At elevated temperatures, SiO_2 films protect bulk SiC resulting in a slight decrease in the elastic modulus [15, 46]. The fracture toughness (K_{IC}) of α-SiC and β-SiC with various sintering additives measured from several methods is approximately 2-5 MPa √m as summarised in Table 2.4.

Table 2.4 Fracture toughness data of SiC at room temperature

Materials	Sintering Additives	Fracture Toughness (MPa √m)	Method	Ref.
Sinter α-SiC[a]	B,C	2.6–3.4	Vickers	[54, 55]
		2.0–3.4	SCF[d]	[54, 56, 57]
		3.01	DT[e]	[56]
		3.9–5.4	SENB[f]	[58]
		2.91	CNB[g]	[58]
		4.7	Fractography	[59]
Hot-pressed α-SiC[b]	Al_2O_3, WC, Co	3.8–4.7	Vickers	[60]
		3.9–4.4	SCF[d]	[57]
		3.8–5.2	DT[e]	[56]
Hot isostatic pressed α-SiC	AlN	4.5–5.1	SCF[d]	[61]
CVD β-SiC		2.4–5.1	Vickers	[50, 62-65]
		2.7	SCF[d]	[50]
		3.8–4.1	DCB[h]	[65]
		3.7	DT[e]	[65]
		3.4–4.4	SENB[f]	[65]
		3.46 (0.16)[c]	Vickers	[46]
		3.20 (0.12)[c]	CNB[g]	[46]
Sintered β-SiC	B, C	2.6–3.0	Vickers	[66]
		3.1	DT[e]	[67]
		2.3	SENB[f]	[68]
Hot-pressed β-SiC	Al	2.5–4.5	SCF[d]	[69]
Hot isostatic pressed β-SiC	AlN	3.5	SCF[d]	[69]
Reaction-bonded β-SiC	Al	3.7	SENB[f]	[69]

[a] Carborundum Co., Hexoloy-SA.
[b] Norton Co., NC-203.
[c] Numbers in parenthesis are one standard deviation.
[d] SCF: Surface crack in flexure.
[e] DT: Double torsion.
[f] SENB: Single-edge notched beam flexure.
[g] CNB: Chevron notched beam.
[h] DCB: Double cantilever beam.

2.3.1.2 Effect of irradiation and elevated temperature on SiC

Silicon carbide has been widely studied for nuclear applications, such as advanced nuclear fuel forms, structural components for fission reactors systems, blanket structures for fusion energy systems and the immobilisation of nuclear waste [11, 15, 46, 47, 70, 71]. It has a low neutron absorption cross-section (0.10 relative to zircaloy), which is an essential characteristic of cladding materials. The SiC-based cladding (the Westinghouse concept [28]) has claimed more benefits than zircaloy claddings regarding lower absorption of thermal neutrons, no hydrogen pick up, low corrosion rate, slower degradation in a severe accident and no hydrogen generation at elevated temperatures [28]. Furthermore, the ultimate tensile strength of SiC-based materials changes slightly from 0 - 1500 °C, whereas that of zircaloy claddings drop significantly [7]. In addition, zircaloy is oxidised in steam at 1200 °C, while the mass of the SiC rarely changes [28].

Neutron irradiation and fission products cause failure in SiC through swelling, irradiation-induced creep and thermal conductivity degradation. The microstructure evolution of polycrystalline β-SiC with grain sizes around 5-10 μm (fabricated by chemical vapour deposition, CVD) was investigated under fast neutron irradiation (1130 °C, 1.5 x 10^{25} n/m^2) [72, 73]. The formation of voids is likely to start from silicon vacancies and carbon vacancies (black spot defect), then further accumulate to form dislocation loops, which seem to be more substantial at 1460 °C. The results indicated that with increasing irradiation temperature, the size of dislocation loops increased and the density decreased. At temperatures below 800 °C, defects and small dislocation loops were predominate before developing to form more extensive dislocation networks [72, 73].

The behaviour of α-SiC (a mixture of 4H and 6H form) under irradiation has been investigated [74-77]. Several modes of damage can occur during irradiation: void formations from incoming ion and helium clusters, a displacement of a single atom, and amorphisation [74]. α-SiC has been implanted using He (with 0 – 24.7 MeV He ions up to 2500 appm), giving rise to a distortion of the corresponding carbon atom network [74]. At present, the mechanism of electron amorphisation remains unclear and with many attempts to explain the details by using electron-beam irradiation within a transmission electron microscope (TEM). Amorphisation occurs with acceleration voltages of 300 kV at room temperature (Figure 2.8), and the size of the damage zone is increased with increasing irradiation time [78].

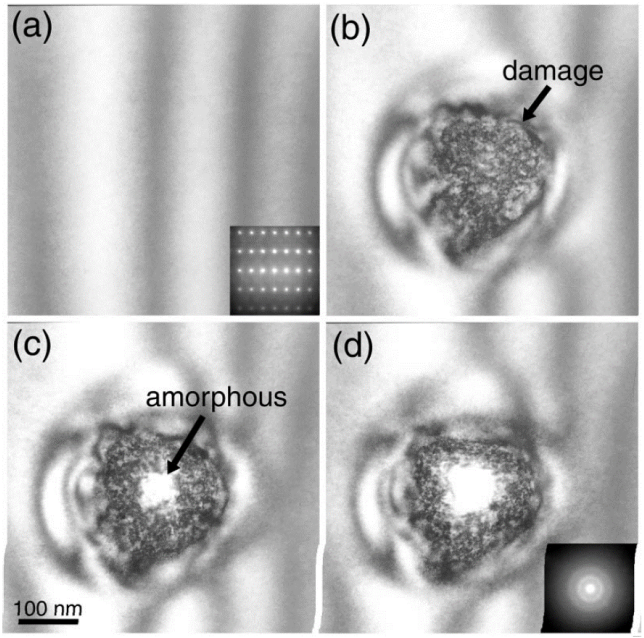

Figure 2.8 Time evolution of microstructures during irradiated with a 300 keV electron beam at a flux of (a) 0, (b) 4.1x10^{24}, (c) 8.3x10^{24}, and (d) 12.4 x10^{24} *e* cm^{-2} [78].

During service, cladding materials have to withstand high radiation levels and high temperatures. Defect formation from neutron irradiation influences their mechanical integrity. Moreover, corrosion/oxidation resistance to fuels, modulators and coolants are the significant development issue of SiC for the fuel cladding.

2.3.2 Zirconium carbide (ZrC)

In principle, ZrC has similar properties and characteristics to titanium carbide (TiC), which is a Group IV carbide. The unique properties come from a weak metallic bond of Zr-Zr and a strong covalent bond of Zr-C (5.812 eV), which is slightly higher than that of Si-C bond (4.677 eV) [79]. The physical properties of ZrC crucially depend on the stoichiometry. The only stable structure of ZrC is that a carbon atom is in an octahedral site (at stoichiometry), forming a face-centred cubic close-packed structure (Fm3m space group, Figure 2.9).

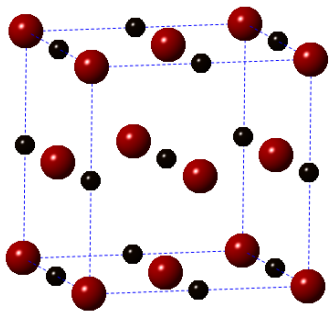

Figure 2.9 The crystal structure of ZrC (red balls and black balls represent Zr atoms and C atoms, respectively)

2.3.2.1 Physical and mechanical properties of ZrC

It has been reported that as temperatures increase, the thermal conductivity (K) of ZrC increases markedly (Figure 2.10), which is an opposite trend to the SiC response. This increase is attributed to the contributions of phonon and electronic conduction, and the changes of specific heat [15, 79]. The thermal expansion of ZrC follows the same trend as other carbides. Therefore, it is easy to avoid mismatch expansion in the carbide composites. The thermal expansion coefficient (α), measured by X-Ray diffraction, reportedly increases with increasing temperature [15, 79].

The Young modulus of single crystal ZrC (C/Zr = 0.89-0.94) is about 406 GPa and decreases with porosity, as shown in Table 2.5. The fracture toughness of high-purity $ZrC_{0.93}$ measured by Vickers indentation is approximately 1.4 MPa √m [68]. However, from the

Chevron-notched beam flexure method (ASTM C1421) is 2.7 MPa √m, twice as large as that measured by indentation techniques [68]. ZrC readily oxidises at ~ 600 °C, which is a lower temperature than that of SiC. Shimada *et al*. proposed the oxidation mechanism of ZrC which starts with the formation of oxycarbide at low temperatures [80]. With a temperature increase to ~1300 °C, zirconia starts creating passive oxide layers which are a barrier to oxygen diffusion and protects ZrC from further oxidation [79].

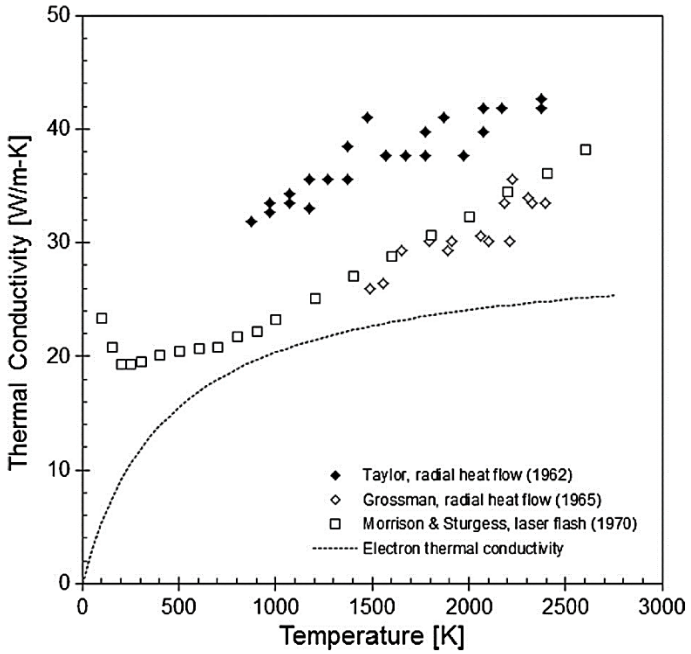

Figure 2.10 Variation of thermal conductivity with temperature for near stoichiometric and hyper-stoichiometric ZrC [79]

2.3.2.2 Effect of irradiation and elevated temperature on ZrC

Irradiation has a strong effect on the physical and mechanical properties of zirconium carbide. Irradiation induces the formation of dislocation loops as well as other microstructural changes. Neutron irradiation of less than one dpa at 130 - 350 °C induced 2 - 3.5% swelling in ZrC, resulting in lattice expansions and grain boundary cracks [79]. Recently, $ZrC_{0.98}$ was tested under fast neutron irradiation (~1.5×10^{24} n/m^2 at 150 - 1500 °C) [79]. The density decreased with increasing irradiation temperatures with a slight change in lattice parameters [79].

Figure 2.11 illustrates how the microstructure changed from neutron irradiation as a function of temperatures [81]. At moderate temperatures (660 – 1000 °C), the dominant defects were unidentified loops (Figure 2.11a) [81]. At 1260 °C, there was a mixed population of

distinct Frank loops (Figure 2.11b), while at 1496 °C, the microstructures further evolved into prismatic loops and small voids (~ 5 nm) as shown in Figure 2.11c [81]. Moreover, it was reported that proton irradiation caused swelling which lattice parameters changed 0.09 % and 0.11% at 0.7 and 1.5 dpa respectively (2.6 MeV at 827 °C) [75].

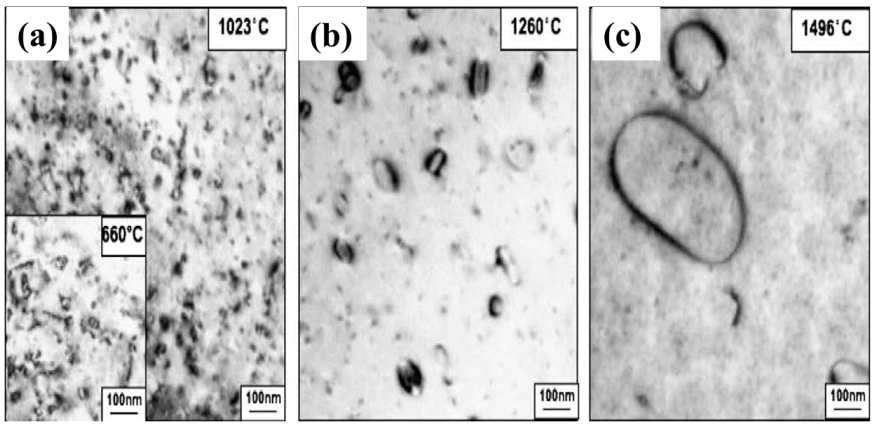

Figure 2.11 Left-unidentified small loops at dose level of 3.7 x10^{25} n/m^2, 660 °C and (a) 2.0 x10^{25} n/m^2, 1023 °C. Middle-mixed Frank and (most likely) prismatic loops for (b) 9.4 x10^{25} n/m^2, 1260 °C and (c) Right-large prismatic loop at 5.8 x10^{25} n/m^2, 1496 °C [81]

The thermal properties of ceramics depend upon composition porosities, chemical composition and lattice defects. Figure 2.12 illustrates the variation of thermal diffusivity of $ZrC_{0.87}$ with irradiation temperature in a fluence range 1.8–9.0 x10^{25} n/m^2 (E > 0.1 MeV) [79]. The thermal diffusion of $ZrC_{0.87}$ was projected to fall by about 15 % at < 1200 °C, attributed to increased phonon scattering [75, 79, 81]. This relative insensitivity of thermal conductivity/diffusivity of ZrC to neutron irradiation at higher temperatures may be attributed to the increased contribution from electronic heat conduction and the reduced number of matrix defects [75, 79, 81].

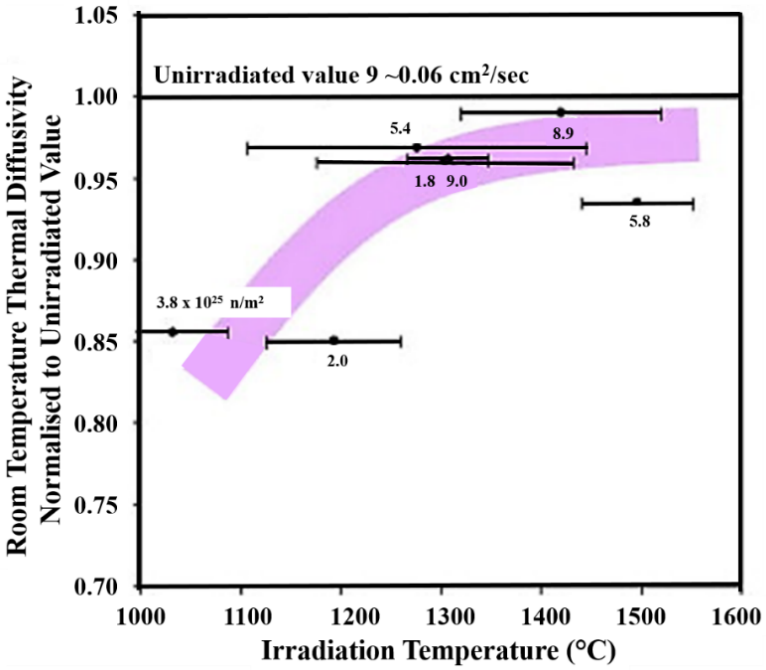

Figure 2.12 Variation of thermal diffusivity of $ZrC_{0.87}$ with irradiation temperature (Numbers next to data points indicate fast neutron fluence in x 10^{25} n/m^2) [79]

The mechanical properties of ZrC strongly depend on the Zr/C composition, leading to a challenging investigation. Irradiation induces hardening of zirconium carbide. The elastic modulus of $ZrC_{0.98}$ irradiated to a fluence of 1.5 x 10^{24} n/m^2 increases ~1.2 % at room temperature. However, at 1100 °C, there is no change in the elastic modulus. The hardness of the same samples increases ~12% and ~7% at room temperature and 1100 °C respectively [82]. Furthermore, irradiation causes a reduction in fracture strength due to solute segregation at the grain boundary.

2.3.3 Titanium carbide (TiC)

Titanium carbide (TiC) is an interstitial carbide form of the Group IV metal and carbon. The properties and characteristics are quite similar to zirconium carbide and hafnium carbide in that the metal-to-carbon bonds are relatively stronger than the metal-to-metal bonds [15]. TiC has unique properties such as high strength, high wear resistance and high melting point (3067 °C) [15]. Therefore, TiC has been utilised in several applications such as coating, cutting, grinding materials, and nuclear materials for the Gen IV nuclear reactor. TiC crystal structure is NaCl structure (space group Fm3m) as shown in Figure 2.13

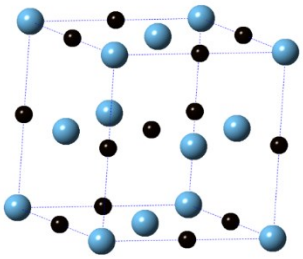

Figure 2.13 Titanium carbide (TiC) crystal structure

2.3.3.1 Physical and mechanical properties of TiC

TiC properties are summarised in Table 2.5. Compared to ZrC, the Young modulus of TiC is slightly lower [15]. Also, TiC has better chemical stability in that it is resistant to most acids and slow oxidation processes at 800 °C [15, 48, 83].

Table 2.5 A summary of the key properties of carbide materials [15]

Carbide	Mp (°C)	Crystal structure	Young modulus (GPa)	Thermal conductivity (W m^{-1} K)	Thermal expansion (x10^{-6}/°C)	Vickers hardness (GPa)
TiC	3067	Rock salt	410-510	21	7.4	28-35
ZrC	3420	Rock salt	350-440	20.5	6.7	25.9
α-SiC	2545	Hexagonal	470	43	5.1	24.5-28.2
β-SiC	2545	Zinc blende	290-410	25.5	3.8	24.5-28.2
Ti_3SiC_2	> 3000	Hexagonal	343	34	9.1	4-6

2.3.3.2 Effect of irradiation and elevated temperature on TiC

The thermal expansion coefficient (α) of TiC increases as a function of temperature as shown in Figure 2.14. TiC exhibits significantly higher thermal expansion compared to SiC. However, the benefit of TiC is that the α is closed to nuclear fuels such as UC (uranium carbide), and UN (uranium nitride), which prevent thermal mismatch [84].

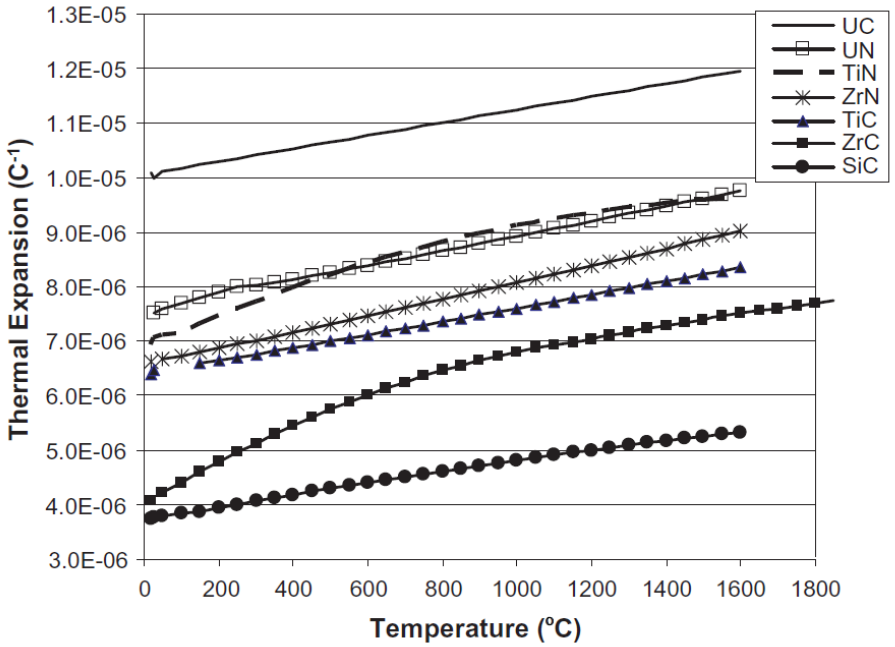

Figure 2.14 Average thermal expansion coefficients (α) of fuel, carbide and nitride materials [84]

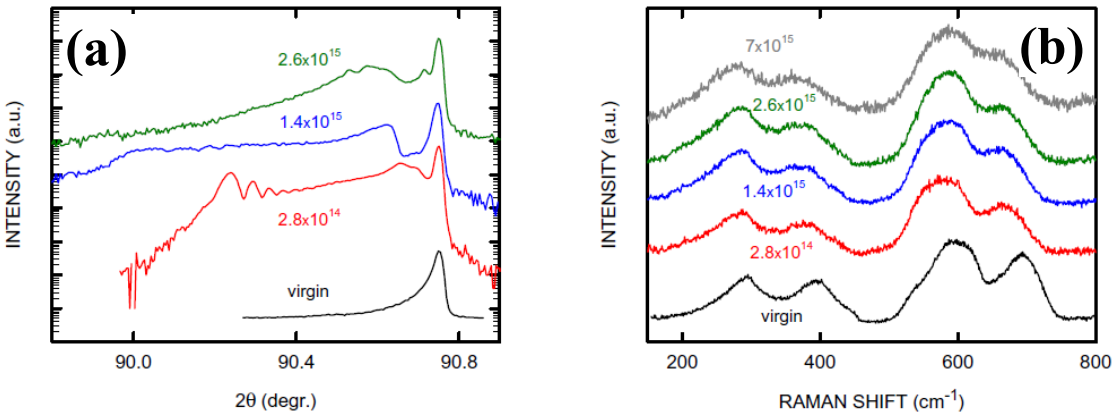

Figure 2.15 XRD diffraction pattern (a) and Raman spectra (b) of TiC crystals irradiated at room temperature with 1.2 MeV Au ions at several fluences [77]. Note: the fluence is the number of particles or photons, or the quantity of energy, passing through the medium

Pellegrino *et al*. reported the irradiation effects on TiC by 1.2 MeV Au ions [77]. Even at the highest fluence used (7 x 10^{15} cm^{-2}), TiC is not amorphized upon ion irradiation as confirmed by XRD results in Figure 2.15a. At a fluence of 2.8 x 10^{14} cm^{-1} (Figure 2.15c), the shape of XRD has been ascribed to a significant increase of disorder level without amorphisation found at the fluence of 2.8 x 10^{14} cm^{-1} [77]. The formed carbon vacancies destroy the symmetry of stoichiometric TiC (NaCl structure) at the site of nearby atoms,

therefore allowing the Raman-active modes obtained by TiC_x with $x < 1$ after Au irradiation as shown in Figure 2.15b [77].

Overall, the different response to irradiation of TiC and ZrC as compared with SiC could be because TiC and ZrC present a mixture of covalent, metallic and ionic bonds, whereas SiC is predominantly covalent [15]. Thus, the more ionic character of TiC and ZrC play an essential role in the dynamics (mobility and recombination) of defects created during irradiation to prevent amorphisation [15, 70, 75-77].

2.3.4 Carbide based composites

So far, the general properties of SiC, TiC and ZrC have been discussed as well as the effects of irradiation on structural and mechanical properties. We found that the primary drawback of SiC, TiC, and ZrC is their brittleness. Their fracture toughness is approximately 3-5 MPa √m. Ceramic composites have been investigated to overcome this behaviour, which improves not only mechanical properties but also chemical and physical properties [34, 41, 85, 86]. SiC/SiC_{fibre} composites have reported toughness of up to 20-30 MPa √m [87]. Hence, another ceramic matrix composite (CMC) materials such as TiC/SiC and ZrC/SiC composites are attractive in terms of high fracture toughness, yet still have low neutron absorption [9, 70, 75, 77, 81]. Furthermore, in terms of heat transfer, their thermal conductivities increase proportionally to temperature, but SiC and SiC/SiC composites decrease slightly as temperatures increase [17, 19, 88]. In this session, we will summarise the literature reviews based on SiC/SiC, TiC/SiC and ZrC/SiC composites.

2.3.4.1 SiC/SiC composites

SiC/SiC composites are promising materials for Gen IV reactors: VHTR, SFR, GFR. They are also proposed to use as accidental tolerant fuel (ATF) cladding in Light Water Reactors (LWR) due to their slower reaction with steam and better retention of mechanical properties during high temperatures, or a loss-of-coolant accident (LOCA) [10, 89]. The SiC/SiC_{fibre} composites consist of three major components: fibre (SiC fibre), interphase (PyC or BN) and matrix (SiC) as shown in Figure 2.16. According to a U.S. Department of Energy report, the third generation of SiC fibre or Hi-Nicalon Type S can withstand 1800 °C with high tensile strength (even at 1800 °C), a high Young modulus, and high thermal conductivity [90]. SiC matrix preparations include chemical vapour infiltration (CVI), nano-infiltration and transient eutectoid (NITE), polymer infiltration and pyrolysis (PIP), and reaction sintering (RS)

[90]. Katoh *et al.* reported the characteristics of SiC matrix as shown in Table 2.6 [71]. NITE-SiC shows excellent mechanical properties among other methods.

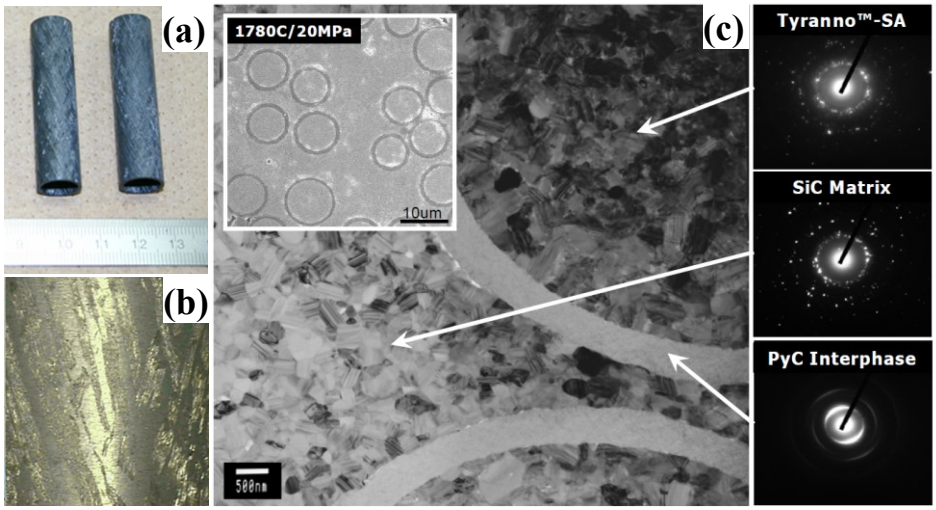

Figure 2.16 Microstructure (a-b) and TEM micrograph (c) of SiC/SiC made by NITE process (the nano-infiltration and transient eutectic-phase) [89, 91]

Table 2.6 Key properties for SiC/SiC assumed in blanket designs and typical values for CVI and NITE composites [71]

Key properties (unit)	**2D CVI**	**3D CVI**	**NITE**
Thermal conductivity, thru-thickness (W/m K)			
Non-irradiated, 500 °C	~ 15	25-40	15-40
Non-irradiated, 1000 °C	~10	20-30	30-30
Irradiated, 500 °C	2-3	5-8	-
Irradiated, 1000 °C	4-6	12-18	-
Electrical conductivity, thru-thickness (S/m)			
Non-irradiated, 500–1000 °C	0.1-1000	-	-
Irradiated, 500–1000 °C	-	-	-
Tensile properties, in-plane			
Ultimate tensile stress, 500–1000 °C (MPa	250-350	100-200	300-400
Matrix cracking stress, 500–1000 °C (MPa)	~150	-	200-250
Modulus, 500–1000 °C (GPa)	~250	~200	300-400

Interphase instability from materials mismatch in PyC/SiC and BN/SiC is a drawback of this composite [71]. MAX phase (Ti_3AlC_2 and Ti_3SiC_2) is proposed to use as the interphase. MAX phases are a carbide/nitride layered ternary compound with the general formula $M_{n+1}AX_n$ (M: early transition metal; A group A element; X: carbon/nitrogen; n = 1-3). Interestingly, this phase combines unique properties from metals (high electrical conductivity, high thermal conductivity, and machinability) and ceramics (high elastic modulus, high-temperature strength, and oxidation and corrosion resistance [92].

2.3.4.2 TiC/SiC Composites

Although SiC has excellent mechanical properties, oxidation resistance, and nuclear application, the low fracture toughness of SiC (3 - 4 MPa √m) makes it less reliable in applications. The introduction of transition metal carbide in SiC is well known that can improve the fracture toughness of SiC ceramics. Several investigations have shown that the dispersion of TiC particles results in the improved fracture toughness of SiC ceramics by deflecting the cracks around the TiC particles [36, 93].

Chen *et al*. reported an effect of SiC on TiC/SiC composite properties prepared by spark plasma sintering (SPS) [17]. The electrical conductivities increased significantly as introduced SiC, 2-5 x 10^5 S m^{-1} at room temperature, which is higher than TiC and SiC [17]. The thermal conductivity of TiC–SiC composite was between that of TiC and SiC which increase proportionally to SiC content, but slightly decreases with temperature (18-48 W K^{-1} m^{-1} at the room temperature) [17]. Cabrero *et al*. also studied the characteristics of TiC-SiC with various SiC contents [19]. With the increasing of SiC volume contents to 50 % vol, fracture toughness (K_{IC}) reached to 5.6 MPa.√m attributed to the crack deflection [19].

SiC particle size also affects the composite properties and microstructures [94, 95]. Kim *et al*. showed that the smaller starting powder sizes of α-SiC led to the finer microstructures [95]. Furthermore, An *et al.* reported that the higher the α-SiC content, the more elongated grain shapes, according to β-α phase transformation, which influences the mechanical properties as shown in Figure 2.17 [94]. Also, the strength increased proportionally to α-SiC contents (> 10 % vol), whereas the fracture toughness decreases with increasing α-SiC contents as shown in Figure 2.17 [94].

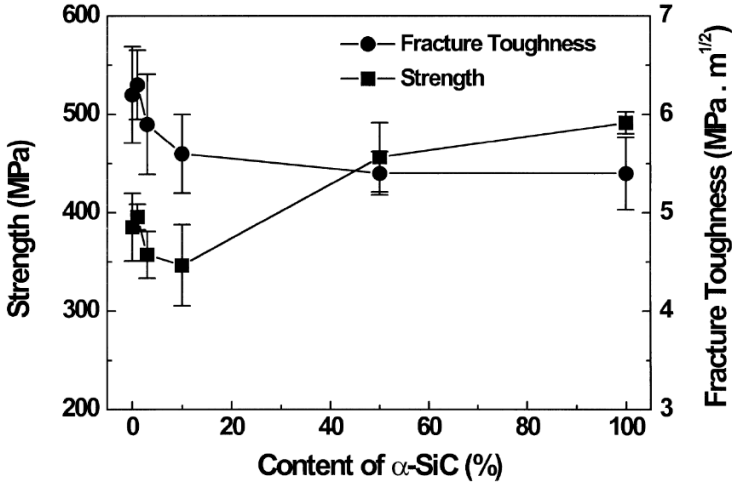

Figure 2.17 Flexural strength and fracture toughness of SiC/TiC composites as a function of α-SiC contents [94]

2.3.4.3 ZrC/SiC Composites

There are two major limitations of ZrC; poor sintering due to an extremely high melting point, and low oxidation resistance due to the formation of the active porous oxide layer. It was proposed that SiC is the most successful additive to improve these drawbacks [22]. Table 2.7 summarises the mechanical properties of ZrC/SiC composites at room temperature, compared to ZrC. The composite Vickers hardness and fracture strength are significantly greater than ZrC [22, 96].

Table 2.7 Mechanical properties of ZrC/SiC composites and ZrC-based ceramics in the previous literature [22, 96]

Materials	Sintering method	Vickers's hardness (GPa)	Fracture Strength (MPa)	Fracture Toughness (MPa √m)	Young's modulus (GPa)
ZrC-30 vol% SiC	SPS	18.8 ± 1.2	523.4 ± 19.6	4.0 ± 0.3	390 ± 6.9
ZrC	SPS	17.9 ± 0.6	407 ± 38	-	464 ± 22
ZrC-9 vol% $MoSi_2$	SPS	20.0 ± 0.5	591 ± 48	3.3 ±0.4	467 ± 22
ZrC-20 vol% SiC	HP	9.6	450	3.9	-

ZrC readily oxidises at 800 °C to form zirconium oxide (ZrO_2) and residual carbon. However, silicon oxide (SiO_2) duplex layers enhance the oxidation behaviour of ZrC-SiC composites. The oxidation properties of ZrC/30 vol % SiC composite were investigated in air using the furnace and oxyacetylene torch in the range of 800-1500 °C [97]. Figure 2.18(a) represents the specific mass-change as a function of exposure time at 800 and 1100 °C, which indicates that the oxidation process mainly occurred via limited interface reaction due to the

oxide layer of ZrO_2. At 1300 °C and 1500 °C, the ZrC/30 %vol SiC has higher oxidation resistance in air than ZrC as shown in Figure 2.18(a) [97]. The oxidation rate of SiC is negligible at a temperature below 1100 °C in the air. Thus, the active SiO_2 layer can seal pores and cracks resulting in an increased density and reduced oxygen diffusion [97].

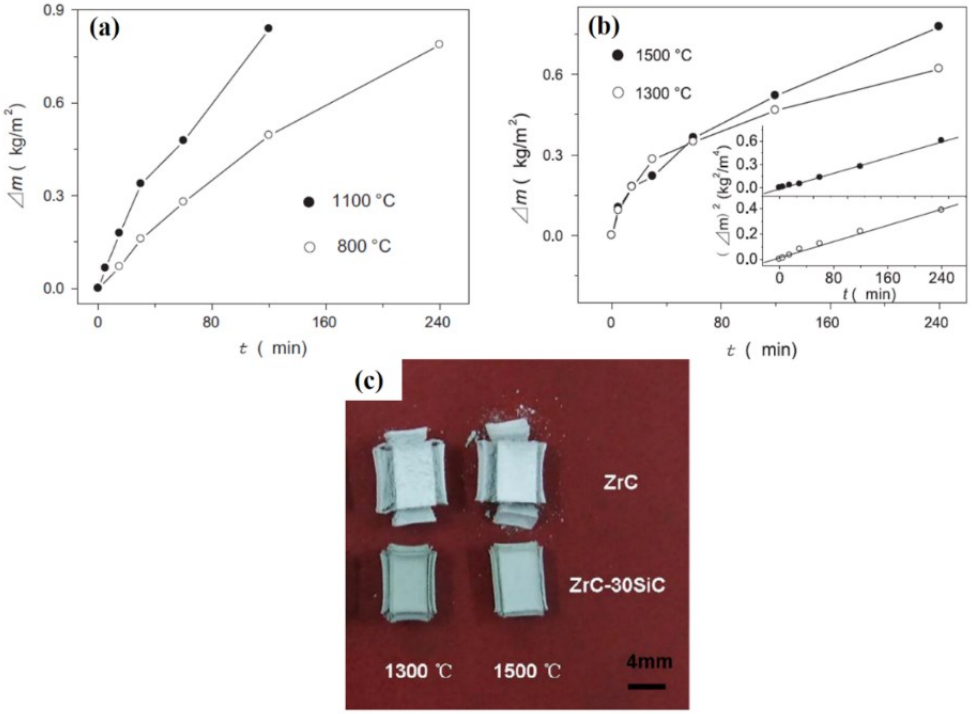

Figure 2.18 Specific mass-change (Δm) as a function of exposure time (t) for (a) ZrC–30%SiC during oxidation at 800 and 1100 °C, (b) at 1300 and 1800 °C and (c) optical micrograph of ZrC and ZrC/30% vol SiC oxidized at 1300 and 1500 °C for 15 min [97]

Furthermore, the oxidation of ZrC/β-SiC composites with various β-SiC contents in ambient air has been reported [98]. The oxidation behaviours of the composite were influenced by the formation of ZrO_2 and SiO_2 and temperature ranges. ZrC/ 30 wt% SiC and 10% wt SiC showed good oxidation resistance up to 1700 °C, which is much more stable than ZrC [98].

2.4 Sintering of ceramics

Sintering is a process of joining particles together with heat. The processes can occur with or without a liquid phase. The presence of liquid phase is called the liquid phase sintering, and solid state sintering for an absence of liquid phase [99, 100]. The densification can be achieved by the application of external pressure during heating, giving the method of pressure sintering in which hot pressing, hot isotactic pressing, and spark plasma sintering are typical examples [99, 100].

2.4.1 Solid-state sintering

The reduction in the surface free energy of the sintering compact is the driving force for sintering. This can happen by (1) an increase in the average size of particle leading to coarsening, and/or (2) the elimination of solid/vapour interfaces by the creation of grain boundary area, followed by grain growth, which leads to densification. These two mechanisms are usually in competition [99, 100].

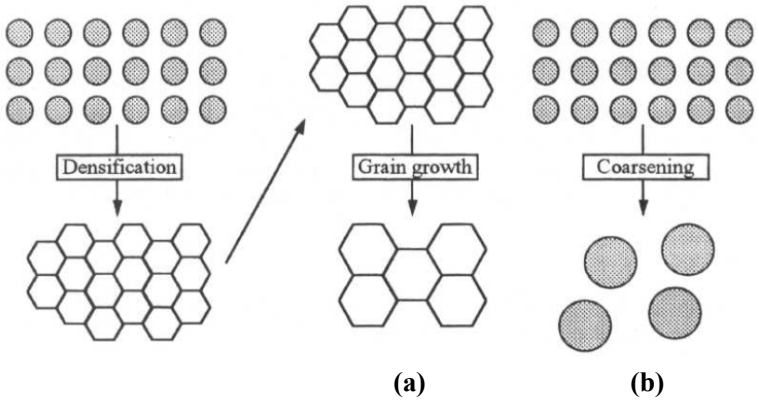

Figure 2.19 Schematic of two possible paths by which a collection of the particle can lower its energy. (a) Densification followed by grain growth. In this case, shrinkage of the compact has to occur. (b) Coarsening where the large grains grow at the expense of the smaller ones [99].

Grain growth (Figure 2.19a) is the process where the increase in the average grain size of polycrystalline material and coarsening (Figure 2.19b) is the process where the increase in the average grain size is accompanied by an increase in the average pore size [99, 100]. Coarsening also increases the diffusion distance for matter transport, thereby reducing the rate of sintering. The coarsening mechanisms therefor need to be suppressed to achieve a high density. Additionally, the microstructure is stabilized such that the pores and the grain boundaries remain attached, which depends primarily on the ability to reduce the intrinsic (pore-free) mobility of the grain boundaries [48, 83, 99, 101].

The grain boundaries play an important role in the sintering process. The grain boundary is a region with a complex structure, about 1-2 unit cells wide, between two crystalline domains. In the sintering of polycrystalline materials, part of the energy decrease due to the elimination of internal surface area associated with the pore goes into creating new grain boundary area. The grain boundary moves by diffusion of atoms (ions) from one side of the boundary to the other so that atoms previously aligned with one grain becomes aligned with the others, causing it to grow at the expense of its neighbour [48, 83, 99, 101]. Growth occurs

in such a way that the convex grain loses atoms while the concave grains gains atoms with the result that the boundary moves toward its centre of curvature.

The presence of the grain boundaries also dictates the equilibrium shape of the pores at the intersection with the boundaries. At equilibrium, the chemical potential of the atoms in the pore surface must be the same everywhere, which is equivalent to saying that the curvature of the pore surface is the same everywhere [48, 83, 99, 101]. There must also be a balance of forces at the junction between the grain boundary and the pore surface to ignoring possible torque as shown in Equation 2.1. For exist densification, the grain boundary energy (γ_{gb}) need to be less than twice the solid/vapour energy (γ_{sv}). This implies that the equilibrium dihedral angle (Ψ) define as has to be less than 180°.

$$\cos\left(\frac{\psi}{2}\right) = \frac{\gamma_{gb}}{2\gamma_{sv}} \qquad \text{Equation 2.1[99]}$$

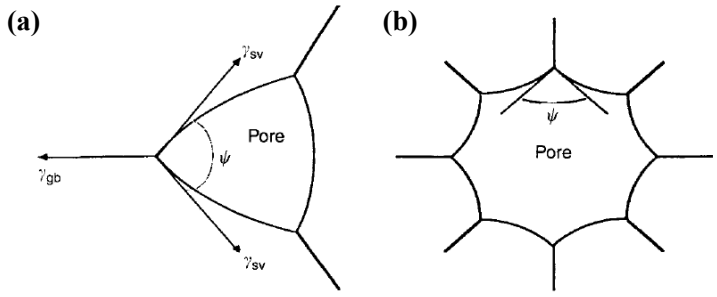

Figure 2.20 Pore shape and pore stability are determined by the dihedral angle and the pore coordination number: (a) The pore with the concave surfaces will shrink while (b) the pore with the convex surfaces will grow (or become metastable) [99]

The local driving force during the sintering process itself is curvature differences. Matter transport during sintering is driven by potential chemical gradients arising from differences in the curvature of the free surfaces in the compact of particles [48, 83, 99, 101]. When compared to atoms under a flat surface at the same temperature and composition, the atoms under a convex surface have a higher chemical potential while the atoms under a concave surface have a lower chemical potential. This gradient in the chemical potential produces a driving force for matter transport from the convex particle surfaces and from the grain boundaries between the particles to the concave necks between the particles [48, 83, 99, 101].

Atomic transport from the grain boundaries to fill up the pores and is dependent on the effective stress on the grain boundaries. The relationship between the externally applied stress

(σ_a) and the effective stress on the grain boundary (σ_e) has been commonly achieved by using the stress intensification factor (ϕ) that depends on the geometry of the porous compact:

$$\sigma_e = \sigma_a \phi \qquad \text{Equation 2.2 [83]}$$

The stress intensification factor is also equal to the ratio of the total cross-sectional area (of the solid phase plus the pores), A_t, to the effective cross-sectional area (of the solid-phase only), A_e. For polycrystalline materials, ϕ is equal to the cross-sectional area of the grain, A_g, divided by the grain boundary area, A_{gb}:

$$\phi = \frac{A_t}{A_e} = \frac{A_g}{A_{gb}} = \frac{1}{\rho} \qquad \text{Equation 2.3 [83]}$$

In sum, the curvature causes local variations in partial pressures and vacancy concentrations. The difference of partial pressure (P) between a convex surface and concave surface ($P_{convex} > P_{concave} > P_{flat}$), therefore the atoms migrate from the convex to the concave.

2.4.1.1 Factor affecting solid state sintering

The critical factors that control sintering are summarised below [48, 83, 99, 101];

- Temperature: it is clear that increasing temperature will significantly enhance the sintering kinetics because of diffusivity is activated.
- Green body density: the higher the green density, less pore volume has to be eliminated.
- Atmosphere: it can enhance the diffusivity of a rate-controlling species, e.g., by influencing defect structure. The sintering atmosphere gas is vital to consider. Also, the solubility of the gas in the solid effect on the gas pressure in the pores.
- Impurities or sintering aids: their effects can be summarized as follows:
    - Form a liquid phase as introduction of small amount sintering aids which can from low-temperature eutectics and therefore enhanced sintering kinetics.
    - Suppress coarsening by reducing the evaporation rate and lowering surface diffusion, e.g. boron in SiC
    - Suppress grain growth and lower grain boundary mobility
    - Enhance the diffusion rate. Once the rate-limiting ion during sintering is identified, the addition of the proper dopant that will go into solution and create vacancies on that sub-lattice, in principle, enhance the densification kinetics.
    - Narrow grain size distributions and decrease the abnormal grain growth

- Particle size: since the driving force for densification is the reduction in surface area, the larger the initial surface area, the higher the driving force. however powder agglomeration according to dominant electrostatic on particle need to be concerned

2.4.2 The liquid-phase sintering

Liquid-phase sintering offers significant advantages over solid-state sintering. It is much more rapid and results in uniform densification. In many cases, the presence of liquid phase at grain boundaries probably plays a significant role for examples of these are silicon ceramics, such as SiC and Si_3N_4, where the native silicon oxide film the starting powders is only known approximately, while the silica participates in forming the liquid phase together with the intentionally introduced additives. It can enhance grain boundary transport rates significantly, accelerating densification even below any eutectic temperatures in the additive/host system [48, 83, 99, 101].

During liquid-phase sintering, the compositions of the starting solids are formed a liquid phase upon heating. A wetting liquid will penetrate between grains and exert an attractive force, pulling them together [48, 83, 99, 101]. A sequence of dominant stages is shown below Figure 2.21 ;

- Melting: melting of the liquid-forming additive and redistribution of the liquid
- Particle rearrangement: particle rearrangement of the solid majority phases driven by capillary stress gradients.
- Solution precipitation: densification and shape accommodation of the solid phase involving solution-precipitation. The chemical potential gradient induces the dissolution of atoms at the contact points and their precipitation away from the area between the two particles, which naturally leads to shrinkage and densification. Furthermore, the kinetics of densification will be much faster than in the case of solid-state sintering, because diffusion is now occurring in the liquid where the diffusivities are orders of magnitude higher than those in the solid state.
- Skeleton sintering: final densification driven by residual porosity in the liquid phase: once a rigid skeleton is formed, liquid-phase sintering stops and solid-state sintering takes over, and the overall shrinkage or densification rates are significantly reduced

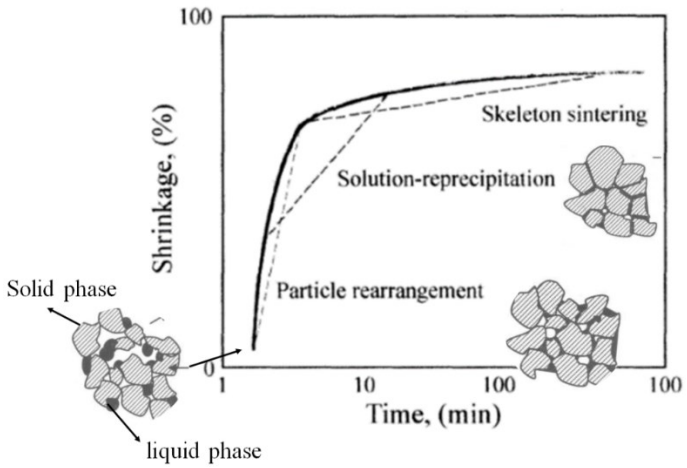

Figure 2.21 Time dependence of shrinkage evolution of liquid phase sintering [83]

The rapid densification can only happen when the liquid phase sintering meet the condition: (1) appreciable solid/liquid solubility in order for material transfer away from the contact areas to occur, (2) the finer the solid phase, the higher the capillary pressures that can develop and the faster the densification rate, (3) wetting of the solid phase by liquid is needed, and (4) sufficient amount of liquid to wet the solid phase must be present [83].

If sufficient liquid is present, initial rearrangement leads to fully dense materials. The relative amount of liquid and solid at this condition depends on the rearranged density of the solids. In the event that the solids could rearrange to approach a dense random packing, then approach a dense random packing, then approximately 35 vol% of liquid would fill all the voids space without further solid skeleton densification [48, 83, 99, 101]. Such large volume fractions of liquid are often used in porcelains and in cemented carbides. In the case of clay ware and porcelains, the liquid phase is molten silicates that remain as glass after cooling. This gives the ceramic ware glassy appearance, and such ceramics are referred to as vitrified. Investigations remains a subject of study. One reason is that equilibrium is difficult to determine.

2.4.3 Pressure-Assisted Sintering technique

2.4.3.1 Hot pressing

Hot pressing is a convenient laboratory method for preparing dense samples. Due to the driving force for densification is the chemical potential gradient between the atoms in the neck region and that at the pore. Chemical potential and vacancy concentration effect from applied pressure. The concentration of vacancies in an area subjected to a stress C_{stress} is shown in

$$C_{stress} = \left(1 + \frac{V_m \sigma_b}{RT}\right) C_0 \qquad \text{Equation 2.4}$$

$$C_{stress} = \left(1 + \frac{V_m \sigma_b}{RT}\right) C_0 \qquad \text{Equation 2.4 [99]}$$

where σ_b is the effective stress at the boundary due to the applied stress, C_0 is the equilibrium concentration of vacancies, and V_m is the molar volume [99]. For compressive applied stress, σ_b is negative, and the concentration of vacancies at the boundary (i.e., between the particles) is less than that at the edges, which results in a net flux of vacancy from the neck into the boundary area and leads to densification [99].

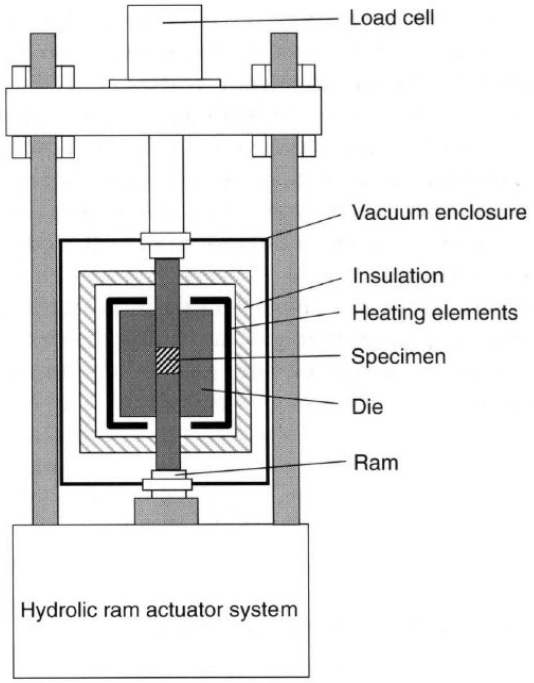

Figure 2.22 Schematic of the hot pressing process [99]

The schematic of the hot pressing process is shown in Figure 2.22 Schematic of the hot pressing process Sample is generally contained in a graphite die at applied pressures. In some cases, boron nitride coating say can be used to reduce reaction of the graphite with the sample at the process temperature below 1350 °C. An example of temperature/pressure profile is shown in Figure 2.23 which an applied pressure is usually maintained during the cool-down period as well. The covalently bonded materials such as B_4C, SiC, and Si_3N_4 can be densified by the hot pressing [102]. For example, at 1650 °C under 50 MPa with metal additives (Al, B and C), SiC obtained approximately 95% relative density [102].

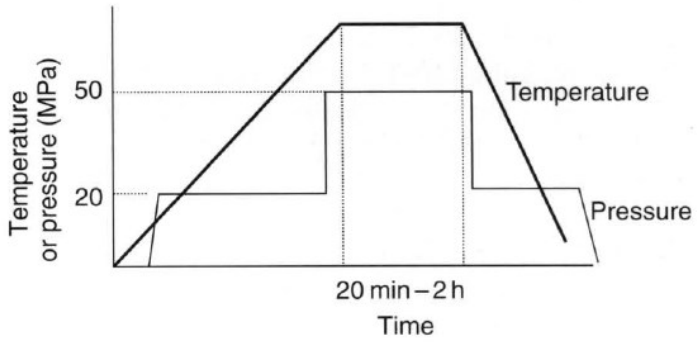

Figure 2.23 Schematic temperature/pressure schedule for hot pressing with high strength

2.4.3.2 Hot Isotactic Pressing (HIP)

Hot-isostatic pressing (HIP) uses isostatic pressuring and heat to solidify the sample. There are two alternative methods for HIPing; encapsulated and not encapsulated. For the encapsulated method, the power sample is sealed in deformable metal containers under vacuum prior to HIP [48, 83, 99, 101]. For the not encapsulated method, another shaping method (dry pressing or injection moulding) is used to compact the powder sample before HIPing.

Schematic of the HIP is shown in Figure 2.24. A compressor introduces inert gas pressure, and the sample is heated to the sintering temperature, which may be up to 2000 °C and as much as 200 MPa. During HIPing, the isostatic pressure from the collapsed container transmits to the sample. Heating elements are typically graphite, molybdenum, tungsten, or tantalum. HIPing is also used to recondition parts in which internal damage, such as resulting from fatigue or creep, may have accumulated during service. Also, commercial hot isostatic presses may have internal chamber diameters approaching 1 metre. Moreover, nano-structured monolithic SiC ceramics with a grain size of approximately 100 nm could be prepared by HIP at 1850 °C, using B_4C,AlN and Al_2O_3 as sintering aids [102].

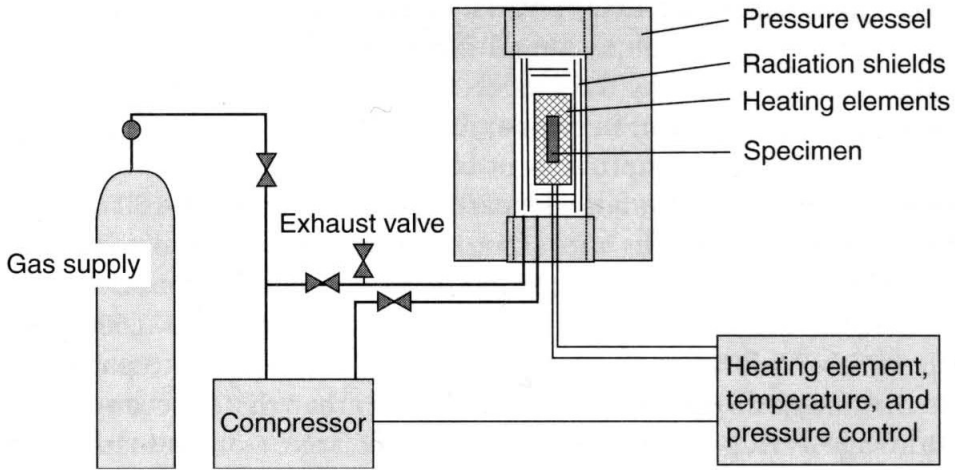

Figure 2.24 Schematic of hot isostatic pressing equipment [101]

2.4.3.3 Spark plasma sintering (SPS)

SPS is similar to a conventional hot pressing apparatus with different heating source as shown in Figure 2.25. Heating rate can reach to 600 °C/min by passing an ON-OFF DC current pulse through a powder compact contained in a graphite die, under an applied pressure of 30-50 MPa. The temperature is usually measured by optical pyrometer on the graphite die wall because specimen temperatures are difficult to evaluate. A design of sintering die and punch assembly made of graphite is extremely important subject to joule heating according to the sintering progress, interaction of powder material, system resistivity, and the function as direct heating elements in order to assume the role of maintaining the homogeneity of sintering temperature [99, 101-103].

Extraordinary high densification rates achieve faster and easier than in conventional sintering processes [99, 101-103]. Material transfers are promoted by spark discharges generated in the voids between the particles as shown in Figure 2.27. When a spark discharge appears in a gap or at the contact point between the particles of materials at an early stage of sintering, a local high-temperature state (discharge column) of several to ten thousands of degree centigrade is generated momentarily [99, 101-103]. This causes evaporation and melting on the surface of powder particles in the SPS process, and “neck” are formed around the area of the contact point between particles, Figure 2.27. The main factors promoting sintering in these processes are the Joule heat generated by the power supply or high-frequency induction heating elements and the plastic flow of materials caused by the hydraulically or mechanically driving pressure [99, 101-103]. The various phenomena according to ON-OFF DC pulse is summarised in Figure 2.27.

The SPS gains a few advantages over conventional sintering methods such as example minimizing grain growth, enhancement of electro-migration and strong preferential orientation effect. However, the limitation of specimen shape is a drawback of SPS in that only simple slabs can be contained in the compression die [99, 101-103].

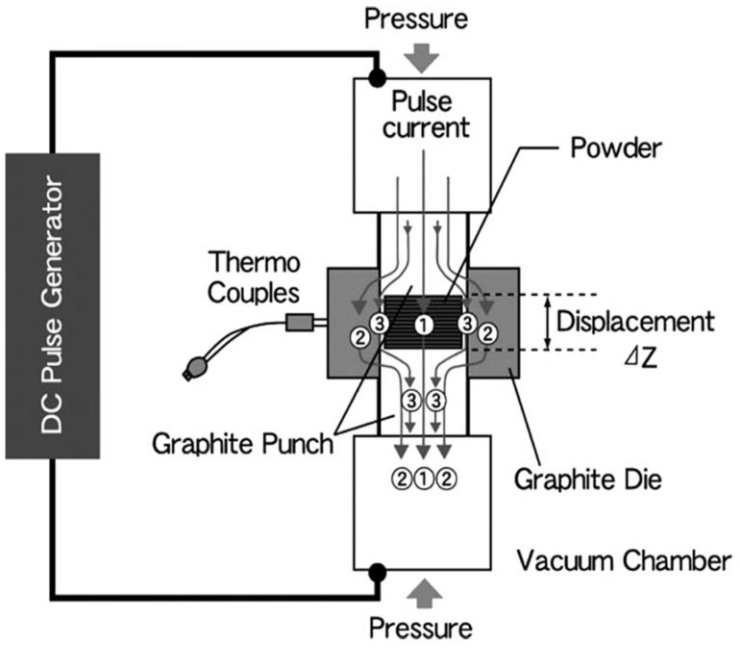

Figure 2.25 (a) Schematic of plasma sintering and (b) a spark plasma sintering apparatus [103]

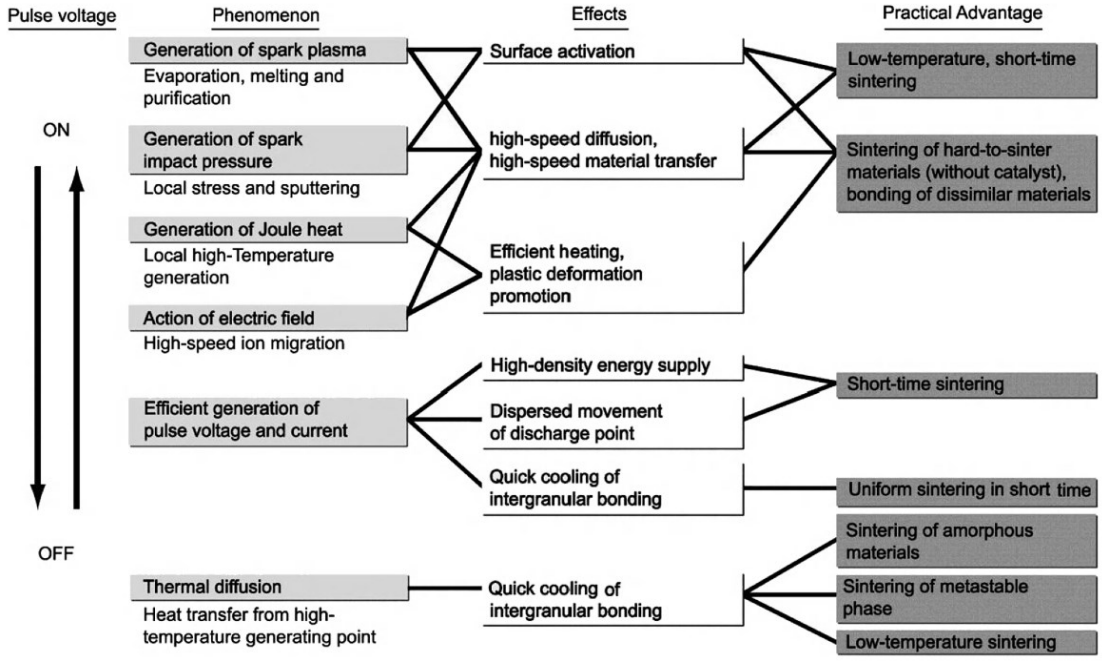

Figure 2.26 Effect of ON-OFF DC pulse energizing [103]

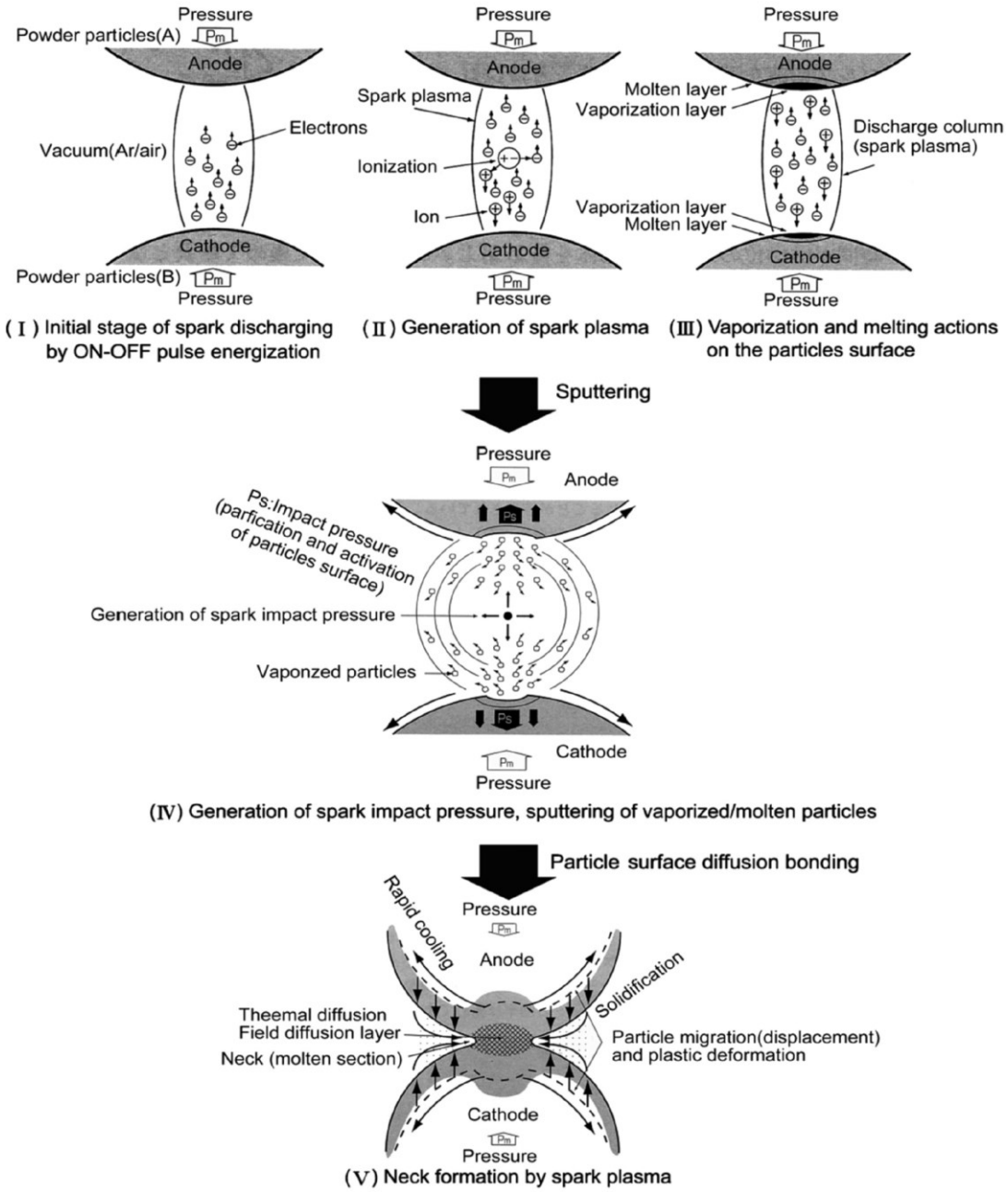

Figure 2.27 Basic mechanism of neck formation by spark plasma sintering [103]

2.5 Fracture toughness

Fracture toughness (K_{IC}) is a mechanical property term that indicates material resistance to fracture as the presence of cracks or other stress-concentrating defects. For crack-free samples, the loading (F/n) will share in each chain of atoms (where F is loading, and n is a number of chain) [104-106], Figure 2.28a. For cracked samples, loading is now carried by a few bonds at the crack tip which leads to a stress redistribution Figure 2.28b. As the presence of flaw will locally amplify the applied stress at crack tip (σ_{tip}) [104-106]. Catastrophic failure

occur when $\sigma_{tip} \approx \sigma_{max}$ (Figure 2.28c) which is the reason why brittle fracture occurs rapidly and without warning, with cracks propagation at velocities approaching at velocities approaching the speed of sound [104-106].

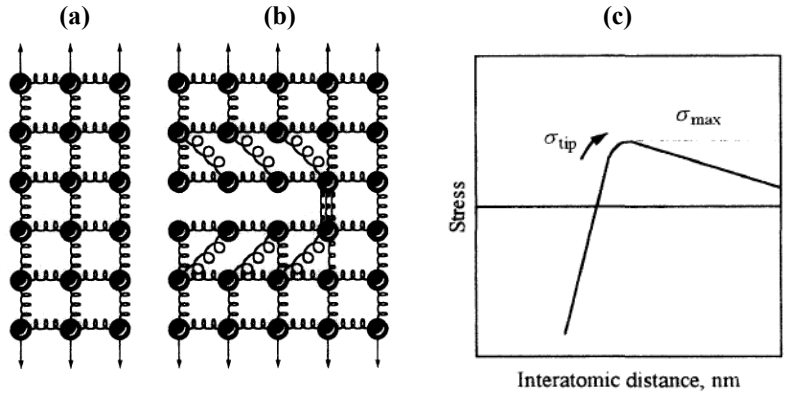

Figure 2.28 (a) Depiction of a uniform. (b) Stress redistribution as a result of the presence of a crack. (c) The relationship between given applied loads versus interatomic distance [99].

As applied stress, for uniform solid, the work done is converted to elastic energy that is stored in the stretched bonds. It can be defined by the area under the stress-strain curve. The total energy change of the system upon introduction of the crack is simply shown in Equation 2.5, where γ is the intrinsic surface energy of the material, t is the thickness of the plate.

$$U_{tot} = U_0 + \frac{V_0 \sigma_{app}^2}{2E} - \frac{\sigma_{app}^2}{2E}\left[\frac{\pi c^2 t}{2}\right] + 2\gamma t$$

Strain energy; Elastic energy; surface energy; Free energy in the absence of stress; Strain energy released

Equation 2.5 [99]

Failure is caused by the spontaneous extension of cracks, which can be described by the Griffith/Irwin criterion (Equation 2.6). The general idea of fracture is to balance the energy consumed in forming new surface as a crack propagates against the elastic energy released. Fracture of material in tension occurs when stress intensity factor (K_I) more than critical stress intensity factor (K_{IC}),

$$K_{IC} = Y\sigma\sqrt{\pi a}$$ Equation 2.6 [48]

Where σ is the stress in the uncracked body, α is a crack length, and Y is a geometric factor, which describes the geometry of crack as shown in

Figure 2.29. The critical condition for fracture, then, occurs when the rate at which energy is released is higher than the rate at which it is consumed.

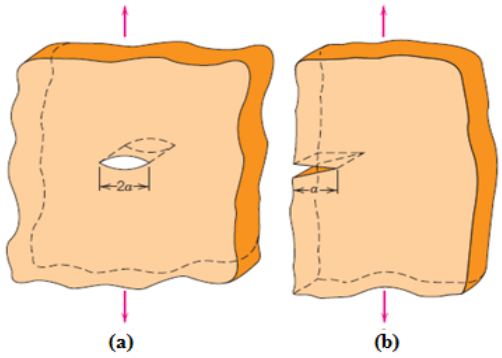

Figure 2.29 Schematic representation of (a) an interior crack and (b) and edge crack [48]

2.5.1 Toughening

The ideas behind the toughening process is to enhance the energy needed to extend crack propagation. The toughening mechanisms for ceramics are summarised below [104-106];

- **Crack deflection:** The process of crack deflection is that cracks tilt or twist away from planar geometry shown in Figure 2.30. In polycrystalline materials, cracks tend to be deflected along weak rain boundary. For homogeneous materials, cracks tend to crack in planar: however; the non-uniform materials, the crack tends to propagate along weak interfaces as a deflection. For composite materials, according to the residual stress from thermal expansion mismatch between matrix and reinforcement, the crack is deflected, and the strain energy release rate is greater in the direction of deflection.
- **Crack bridging:** The crack surface behind the crack tip is shielded by ligaments such as whiskers, continuous fibre or elongated grains as shown in Figure 2.30b. The bridging reduces the crack-tip stress intensity by support partially the applied load. The increased fracture toughness is influence by increasing in fibre reinforcing phase, the difference between Young's modulus of matrix and reinforcement, and the ratio of the fracture energy of matrix and reinforcement
- **Transformation toughening:** Transformation-toughened materials owe their considerable toughness to the stress-induced transformation of a metastable phase in the vicinity of propagating crack. Since the original discovery that the tetragonal-to-monoclinic transformation of zirconia

- **R Curve behaviour:** R curve behaviour refers to a fracture toughness which increase as the crack grows as shown in Figure x. The primary mechanisms responsible for this type of behaviour are the same as that operative during crack bridging or transformation toughening.

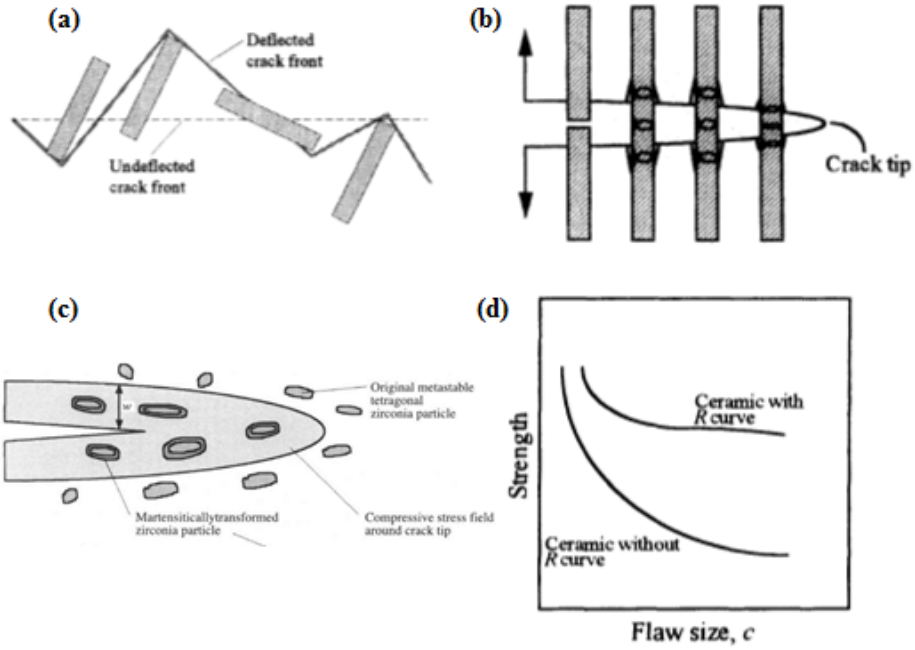

Figure 2.30 Schematic of (a) crack deflection [99]

According to literature reviews, SiC, TiC and ZrC are promising candidates for nuclear generation IV both in-core and out-core structure material according to their mechanical and neutronic properties. In order to improve the fracture toughness of these carbides, an introduction of other carbides to form carbide composites could increase the energy required for crack propagation. Additionally, spark plasma sintering (SPS) is reported that is the excellent pressure-assisted sintering technique for dense ceramic composites. Therefore, in this project, TiC/SiC and ZrC/SiC will be prepared by SPS.

3. Experimental procedure and background

3.1 Characterisation techniques and their background

3.1.1 X-ray diffraction (XRD) technique and phase refinement

This technique is used to determine crystal structures, orientations and crystallinities of powdered or polycrystalline specimens. The diffraction patterns are also a 'fingerprint' of materials and therefore can be used for phase identification by comparison with standard XRD diffraction patterns [107, 108].

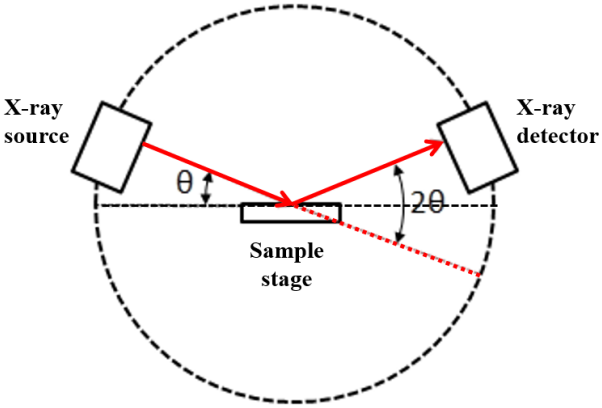

Figure 3.1 X-ray diffractometry working scheme [107, 108]

Figure 3.1 illustrates the simple schematic of X-ray diffractometry, consisting of X-Ray sources, detectors and specimens. When the X-ray beam hits the specimen, the detectors move and record the diffracted beam intensities as a function of 2Θ. The sharp intensities appear when Bragg's law condition is satisfied as shown in Equation 3.1, where *n* stands for an integer, λ stands for wavelength and *d* is inter-planar spacing [107, 108]. Each peak corresponds to a plane of atoms in a crystal structure. Peak intensities relate to phase concentrations, and peak widths are influenced by crystallite size/strain effects [107, 108].

$$2dSin\theta = n\lambda \qquad \text{Equation 3.1}$$

The Rietveld method is a full profile fitting used to refine phase contents [109]. Varying parameters such as crystal parameter, thermal parameters, scale factors, phase fraction and specimen displacement backgrounds in control manner have been used to minimise the differences between the calculated diffraction and experimental data [109]; GSAS and Topas software were used in this project.

3.1.2 Scanning electron microscope (SEM) and chemical analysis

SEM is used to investigate the surface morphology, topology and chemical composition of materials. In principle, an electron beam from an electron gun is bombarded onto a specimen. The signals that return from the specimen are collected, which contain the different types of electron interaction: secondary electrons (SE), backscattered electrons (BSE), characteristic X-rays, Auger electrons and cathode luminescence (CL) as shown in Figure 3.2.

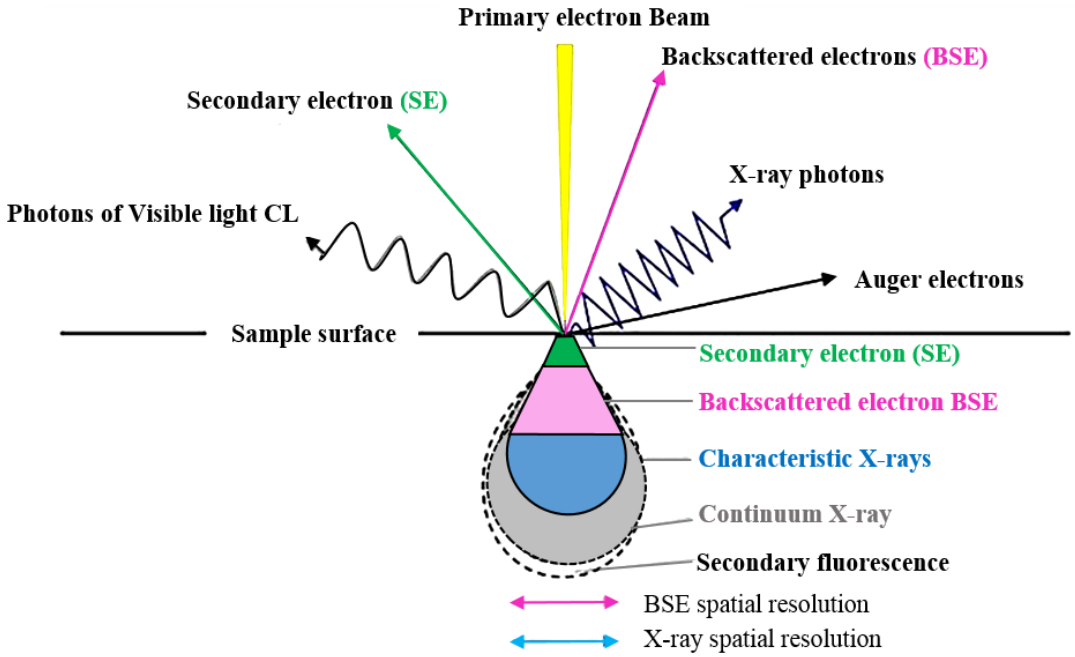

Figure 3.2 The different types of signals produced when high-energy electrons impinge on a specimen [110]

In this project, SE, BSE and characteristic X-ray were the main techniques to characterise the samples. SE are specimen electrons ejected by the primary electron. The contrast in SE is primarily due to topography. In order to reveal more detailed structure information, SE-SEM images were taken at low incident electron voltage. BSE are primary electrons scattered by the atoms in the specimen which escape from the specimen surface, whose intensity is proportional to the atomic number of the target elements [110]. In fact, the interaction volume of BSE is much larger than of SE, so the BSE signal can be ~ 10 μm, but SE is about 10 nm depending on the incident beam energy. Energy Dispersive X-Ray Analysis (EDX) is a technique used for elemental analysis depending explicitly on the energy differences of two involved electron shells.

3.1.3 Transmission electron microscopy (TEM)

TEM is well known as a powerful tool providing a broad range of characterisation techniques with high spatial and analytical resolution [111-113]. TEM images are generated from electrons which have been transmitted through the specimen. Hence, TEM specimens need to be thin enough to let electrons pass through [111-114]. Electrons coming through a thin specimen are separated into undeviated 'direct beam' electrons or scattered by a variety of processes within the specimen resulting in non-uniform intensity as shown in Figure 3.3. Therefore, information we get from TEM can be attributed to some form of electron scattering [113].

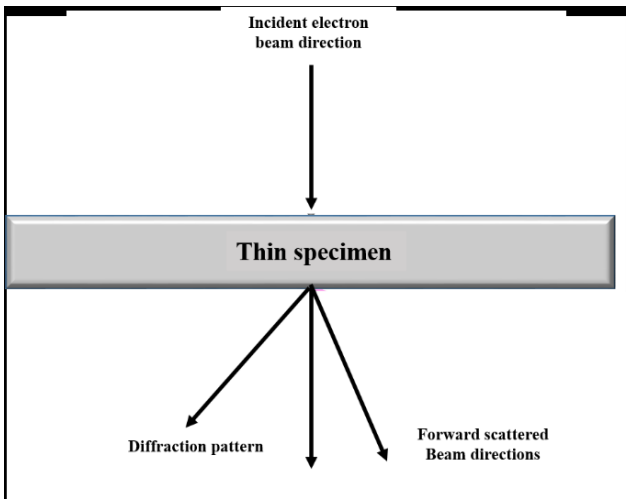

Figure 3.3 Signals produced by electron bombardment of a thin specimen.[113]

The contrasts or 'grey scale differences' in TEM micrographs are utilised to characterise the materials morphologies. Also, TEM image contrast arises because of the scattering of the incident beam by the specimen. There are three main contrast mechanisms [113]. Firstly, a mass-thickness contrast: thick areas scatter electrons more than thin areas, so they appear as darker contrasts. Secondly, a diffraction contrast explained by Kinematical theory can be used to review crystal defects such as dislocations, stacking faults and precipitates [111-113]; in addition, while taking images the objective aperture is then used to stop diffracted beams, and only undiffracted electrons attribute to the images [111-113]. Finally, the phase contrast results whenever electrons of different phases are allowed to pass through the objective aperture [111-113]. Also, for crystalline specimens, diffraction patterns (DPs) give direct crystallographic information about small areas of the specimen which relate to the TEM images [111-113].

In this project, a combination of TEM image and DFs were used to characterise TiC/SiC composites: grain morphologies, β-α phase transformations, and crystallographic information.

3.1.4 Flash method

The thermal diffusivity (α) was measured by the flash method. After the sample has been stabilised at the desired temperature T_0, a nearly instantaneous pulse of energy (usually a laser or another discharge source) is deposited on its front face, and the temperature increases on the rear face of the sample are recorded as a function of time as shown in Figure 3.4. The thermal diffusivity is then determined from this thermogram related to the thermal conductivity (λ), specific heat (Cp) and density (ρ) as follows [115]:

$$\alpha = \frac{\lambda}{\rho C_p} \qquad \text{Equation 3.2}$$

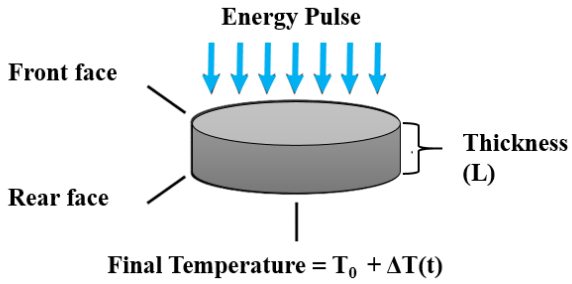

Figure 3.4 Schematic of the flash method [115]

3.1.5 Hardness measurement

Hardness is a measure of resistance to localised plastic deformation. Difference geometries of indenters are utilised to form a permanent surface impression, each of which gives a different number [48, 100, 108]. Thus, care should be exercised when comparing values determined by different techniques. Vickers indentation was used in this research because it well suits the hardness of small selected areas on the specimen. The Vickers indenter has a diamond square pyramid shape as shown in Figure 3.5.

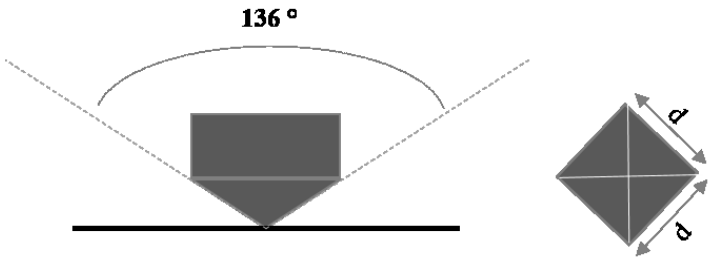

Figure 3.5 Geometry of Vickers indentation

$$HV = \frac{1.4\ 85\ P}{d^2}$$ Equation 3.3

The depth of the resulting indentation is measured and related to a hardness number. The broader and deeper resultant indents represent softer and lower materials. Hardness can be calculated by Equation 3.3 where P is loading (kg), and d is the length of the resultant indent (mm) [48, 100, 108].

3.1.6 Three-point bending test

It is difficult to perform a tensile test on brittle ceramics due to obstacles in specimen preparation and setup [48, 104, 116, 117]. Moreover, the failure of ceramics after only 0.1% strain necessitates that tensile specimens be perfectly aligned to avoid the presence of bending stresses, which are not easily calculated. Thus, the bending test is more appropriate for brittle materials whose stress-strain curves exhibit linear elastic behaviour before failure. In addition, either simple rectangular or cylindrical geometry is suitable. Figure 3.6 illustrates the geometry for three-point bending [118, 119].

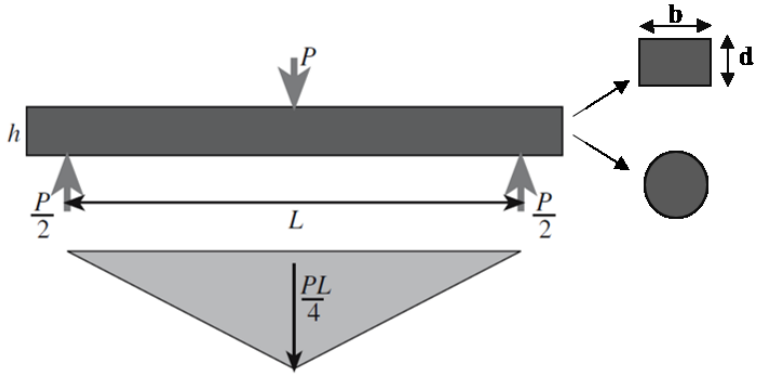

Figure 3.6 A three-point loading scheme for measuring the stress-strain behaviour and flexural strength of brittle ceramics

Flexural strength, modulus of rupture, fracture strength or bend strength is the stress at fracture. For a rectangular specimen, the flexural strength (σ_{fs}) and the flexural strain (e_f) are given by Equation 3.4 and 3.5 respectively, where F_f is the load at fracture, L is the distance between support points, d is beam thickness, b is beam width, and D is the maximum deflection of the centre beam [118, 119].

$$\sigma_{fs} = \frac{3F_f L}{2bd^2}$$ Equation 3.4

$$e_f = \frac{3Dd}{L^2}$$ Equation 3.5

However, the drawback of the bend test is the variation in size differences and stress distribution. Therefore, the strength of the ceramic will be overestimated if massive flaws are located in the interior of the specimen.

3.1.7 Fracture toughness measurement

Toughness is a measure of energy absorption for plastic deformation [48]. Fracture toughness in tension is the K_{IC} (critical stress intensity factor) [48, 118, 119]. Material failure happens when K_I (stress intensity factor) $\geq K_{IC}$. Mainly, an indentation and a bend test are used to measure K_{IC} for ceramics.

3.1.7.1 Fracture toughness from the indentation

Fracture toughness (K_{IC}) can be obtained from the Vickers indentation fracture (VIF). Cracks are created on four corners after Vickers indent on a flat ceramic surface. The crack lengths (l) are inversely proportional to the toughness of materials [120, 121]. Several equations were proposed to calculate the fracture toughness which depends on the types of cracks formed underneath indent surfaces [122, 123]. Median cracks (Figure 3.7a) are formed at high loading, and palmqvist cracks are predominantly formed at low loading (< 10 kg) (Figure 3.7b). Their K_{IC} can be calculated by Equation 3.6 [124] and Equation 3.7 [125], respectively.

The high-quality surfaces need to be prepared and finished by 1 μm diamond suspension. The grinding and polishing methods are shown in Table 3.1.

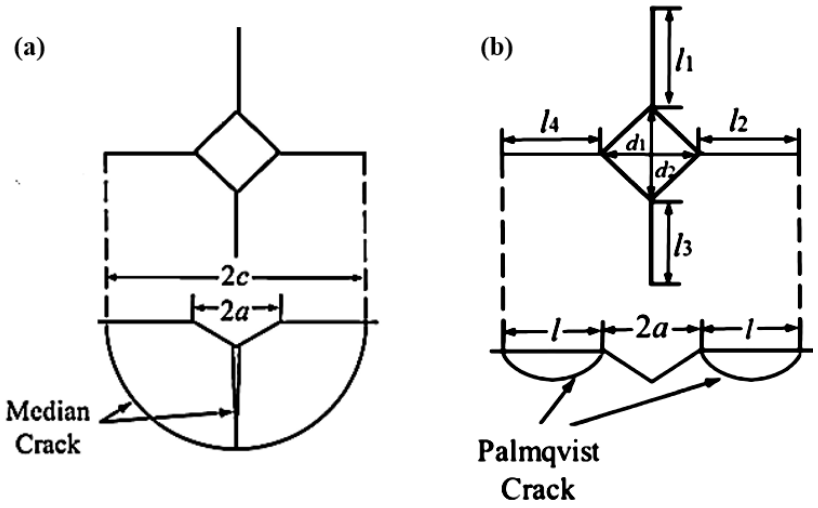

Figure 3.7 (a) median and (b) Palmquist crack system developed from the Vickers indents [122]

$$K_{IC} = 0.016\,(\frac{E}{HV})^{\frac{1}{2}}.\frac{F}{c^{3/2}} \qquad \text{(Astis } et\ al.\text{)} \qquad \text{Equation 3.6 [124]}$$

$$K_{IC} = 0.0089\,(\frac{E}{HV})^{\frac{2}{5}}.\frac{F}{a.l^{1/2}} \qquad \text{(Niihara } et\ al.\text{)} \qquad \text{Equation 3.7 [125]}$$

3.1.7.2 Fracture toughness from a bend test

The fracture toughness of a specimen can also be determined using a three-point flexural test with a pre-cracked specimen. The pre-cracks can be a straight-through crack formed via bridge flexure (pb), a semi-elliptical surface crack formed via Knoop indentation (sc), or a chevron notch (vb) as shown in Figure 3.8[118, 119].

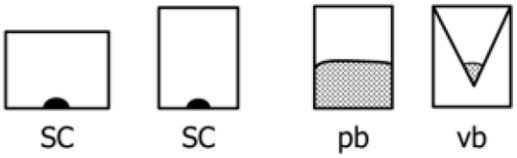

Figure 3.8 Scheme illustrating pre-crack types [119]

In this research, the pre-cracked beam method (pb) was used because the setup is not too difficult and the cracks are large enough to measure [118, 119]. However, the test specimens need to be handled with extensive care prior to a bend test. The indentation method led to consistently higher fracture toughness values compared to the results obtained by the bend test, due probably to underestimation of the real crack length in the indentation method [122].

Several pre-cracks were introduced on a bar-shaped specimen (similar size to the samples for three-point bending test) by 10 kg Vickers indentation as shown in Figure 3.9. Each bar with pre-cracks was then placed in the three-point bend fixture and loaded up to fracture initiation. A constant crosshead speed of 0.24 mm/min was employed for loading. The tests were carried out at room temperature in the standard atmosphere. Graphs of load vs displacement were recorded, and the maximum force was determined from each trace. The fracture toughness value, K_{IC}, was calculated from Equation 3.8, where K_{Ipb} is fracture toughness ($MPa\sqrt{m}$), g is function of the ratio $\frac{a}{W}$ for there-pointing, P_{max} is maximum force a (N), S_0 is outer span (m), a is a pre-crack size (mm), W is the thickness of bar sample, B is the width of bar sample [118].

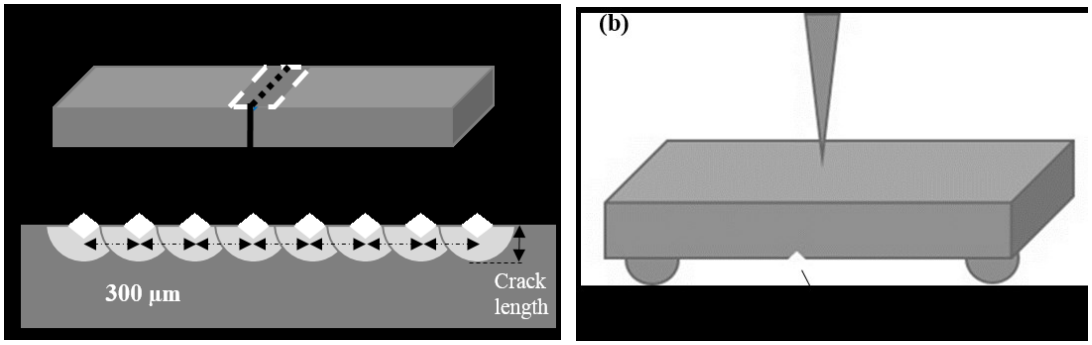

Figure 3.9 Scheme of (a) pre-cracks on a bar sample and (b) three-point bending set up

$$K_{Ipb} = g\left[\frac{P_{max}S_0 10^{-6}}{BW^{3/2}}\right]\left[\frac{3[a/W]^{1/2}}{2[1-a/W]^{3/2}}\right] \qquad \text{Equation 3.8 [119]}$$

$$g = g\left(\frac{a}{W}\right) = \frac{1.99 - [a/W][1 - a/W][2.15 - 3.93[a/W] + 2.7[a/W]^2]}{1 + 2[a/W]}$$

$$\frac{S_0}{W} = 4$$

$$0.35 \leq \frac{a}{W} \leq 0.60$$

3.1.8 Gain size analysis

The mean grain sizes can be defined in several ways as shown in Figure 3.10. Since the cross-section cuts through grains randomly, some observed grains are smaller than actual grains [126]. Few hundred grains need to be measured to create a grain size distribution histogram. In this project, SE and BSE SEM images were analysed by the combination of manually and

automatic modes to obtain ferret diameters (>100 grains) by ImageJ programme. The images were adjusted binarization by chosen suitable thresholds [126]. Consequently, the grayscales were significantly different between pores and matrix or between grains and boundaries. However, noise in the image will effect on the grain size measurement in that they shift a grain size distribution histogram to the low mean the median than an actual value. The ferret diameter measured by ImageJ will be used to plot a grain size distribution curve.

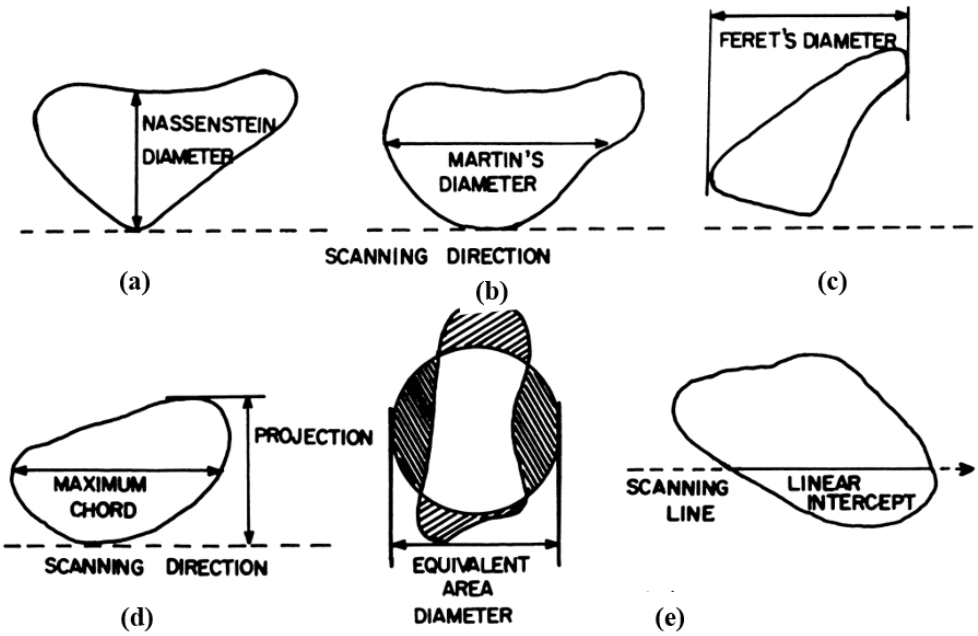

Figure 3.10 Some stereological definitions of grain diameter [126]

3.2 Preparation of titanium carbide/ silicon carbide composites (TiC-SiC)

Commercial silicon carbide, SiC, (cubic structure, 99.8 % purity, 1 μm Alfa Aesar) and titanium carbide, TiC, (99.5 % purity, 2 μm Alfa Aesar) powders were mixed into different mole ratios of TiC (100%, 70 %, 50 % and 0 % respectively). The mixed powder was then milled by a roller mill machine (Excal variable speed motor drive at a speed of 6) in isopropanol using 1.0 mm diameter zirconia balls at room temperature for 24 hours. The powder was then collected and dried at 90 °C. After that, the 7.5g of received powder was sieved through a 200 mesh sieve. Next, it was poured into cylindrical graphite die (diameter 20 mm) and cold-pressed at 1.5 psi for 15 minutes. To avoid welding and in order to obtain a more uniform current flow, thin graphite foils were placed between the powders and the graphite dies. The pressed powder was then sintered by spark plasma sintering (SPS, FCT Systeme GmBH spark

plasma sintering system, type HP D 1050, Germany) under argon gas. The maximal uniaxial load is 50 MPa at 2100 °C for 15 minutes.

3.3 Preparation of zirconium carbide/ silicon carbide composites (ZrC-SiC)

Coarse zirconium carbide, ZrC (99.5 % purity, 44 μm Alfa Aesar) was used as a starting material. It was milled by the same roller mill machine (Excal variable speed motor drive at a speed of 6) using zirconia media (1.0 mm in diameter) in isopropanol for 24 hours before mixing with fine β-SiC (99.8 % purity, 1 μm Alfa Aesar). It was then dried at 90 °C and sieved through a 200 mesh sieve. Next, the milled ZrC powders were mixed with β-SiC powders. The mixed powders were milled, dried and seived as previously. The 7.5g of received powder was poured into cylindrical graphite die with a diameter of 20 mm and again cold-pressed at 1.5 psi for 15 minutes. Thin graphite foils were, as before, placed between the powders and the graphite dies. Again, the pre-pressed powder was sintered by spark plasma sintering (SPS, FCT Systeme GmBH spark plasma sintering system, type HP D 1050, Germany) under argon gas. The maximal uniaxial load is 50 MPa at 2100 °C for 15 minutes.

3.3.1 ZrC particle size

The particle size of the milled ZrC powder was measured by Laser diffraction technique (wet method, Mastersizer 3000 laser particle size analyser, Malvern Instruments). 90 % of the ZrC powder was milled down to about 5 μm as shown in Figure 3.11.

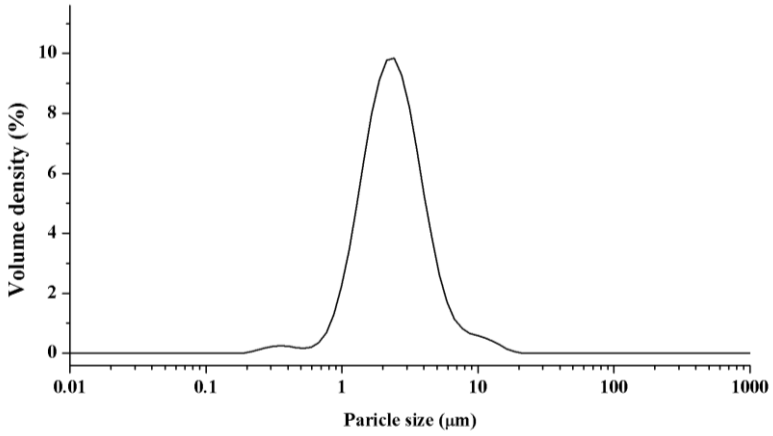

Figure 3.11 Particle size distribution of ZrC powder

3.4 Sample characterisation

X-ray diffraction (Bruker D2 phaser) was utilised to observe the phase structures of the samples, using weighted Cu Kα radiation (λ = 1.5416 A°), scanning from 10 – 80° operation at 30 kV, 20 mA. The samples were ground and polished before investigating their surface morphologies by an optical microscope and scanning electron microscopy (SEM, Hitachi TM300 and Inspect F FEG-SEM). In addition, chemical analysis was evaluated using SEM-EDX. Transmission electron microscopy (TEM, Philips EM 400 and FEI Tecnai Spirit) was used to study their grains and interfaces. The TEM samples were thinned by diamond laps and finished by ion milling. The bulk density of the sintered samples was determined by the Archimedes method in distilled water using a balance with an accuracy of ±0.0001g (MS104S, Mettler, Toleda and Switzerland). Thermal conductivity was identified by a flash method (Flashline 3000, TA instruments) with the square shape specimens (1 x 1 x 0.2 cm).

Hardness tests were conducted using a Vickers indenter with a 1 to 10 kg load for 10 seconds (Durascan 70). Three-point bending tests were measured at room temperature with the head loading rate of 0.24 mm/min (Hounsfield test equipment LTD). The samples were cut into a bar shape (5 x 2 x 20 mm), and both surfaces were ground until flat.

The fracture toughness (K_{IC}) was measured by two methods: an indentation method, and by bend testing. For the indentation method, Vickers indenter was loaded at 5kg on a polished sample. The K_{IC} was calculated from the resultant cracks by Equation 3.6. For the bend test, a bar-shaped sample was put under a series of pre-cracks by 10 kg of Vickers indenters before being processed by the three-point bend testing. Then the K_{IC} was calculated by Equation 3.8.

3.5 SEM specimen preparation

The SPSed samples had their residual graphite papers ground out from their surfaces by diamond grinding pads, using an automatic machine (AutoMet™ 250). Then, their surfaces were polished as per the sequence as shown in Table 3.1 to review the actual microstructure. This surface preparation method was also applied to the samples for the Vickers hardness test, the indentation test and the three-point bending test.

3.6 TEM specimen preparation

TEM sample preparation was adapted from the tripod polishing method [113]. The SPSed samples were cut into 250 μm thin slices by a slow speed diamond saw (Buehler Isomet low speed saw). They were then attached to glass slides using G2 epoxy glue (Agar Scientific). The TEM specimens were mechanically thinned using diamond lapping films (UltraPrep

lapping film) in a sequence of 15, 9, 5, 3 and 1 μm until a thin foil with a thickness of approximately 40-80 μm was obtained. The specimen was further polished with Ar ion milling (PIPS II, GATAN) at 6 keV at an incident angle of 5° until getting a hole. Finally, the surfaces were finished with 0.5 keV.

Table 3.1 Grinding and polishing sequences for SEM specimens

Surface	**Abrasive size**	**Load on specimen (N)**	**Base speed (rpm)/ direction**	**Time (mins)**
Diamond grinding disk	P600	20	241 rpm/ comp.	Until flat surface
Diamond grinding disk	P1200	20	241 rpm/ comp.	Until flat surface
Diamond grinding disk	3 μm	10	241 rpm/ comp	20 mins
TexMet	3 μm MetaDi Supreme diamond suspension	10	141 rpm/ contra	20 mins
MicroCloth	1 μm MetaDi Supreme diamond suspension	10	141 rpm/ contra	20 mins

Comp. = Complementary (platen and specimen holder both rotate in the same direction)
Contra = Platen and specimen holder rotate in opposite directions

4. Results

Porosity in ceramics plays an important role in controlling their properties. Pores are a source of stress concentration which cause subsequent crack growth resulting in a decrease in strength. Furthermore, pores reduce thermal conductivity. Hence, in order to maximise the mechanical and thermal properties of ceramics, the density needs to be considered. Without sintering aids, it is well known that SiC, TiC and ZrC are difficult to densify. According to the literature reviews in Chapter 2, spark plasma sintering (SPS) is a rapid densification process of ceramic powders [16, 102, 127-129]. As with all sintering techniques, the performance of SPS depends on temperature. Therefore, SPS was used to prepare TiC and SiC at various temperatures to optimise the highest density for TiC-SiC and ZrC-SiC composite preparation. In addition, the results of SPS temperature optimisation and characterisation of SPSed TiC, SiC, TiC-SiC and ZrC-SiC composite will be explained in this Chapter.

4.1 Spark plasma sintering (SPS) temperature optimisation

The optimisation of ceramic processing started by finding the optimum SPS temperatures for SiC powders and TiC powders. Figure 4.1 shows the density of SPSed TiC and SPSed SiC as a function of temperature. The word “SPSed TiC” is defined as TiC which was sintered by SPS. It is clear that the densities of SiC and TiC were strongly dependent on the SPS temperature.

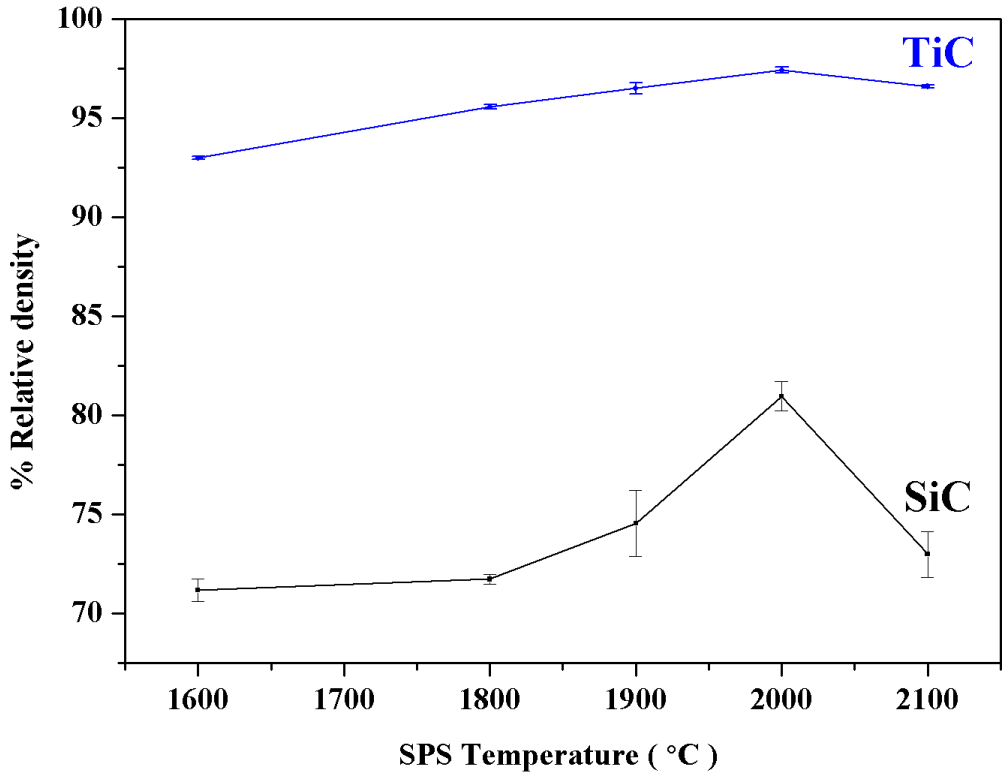

Figure 4.1 A plot showing the relative density against SPS temperature of the relationship between TiC and SiC

Notably, a considerable difference in the relative density between TiC and SiC was found. TiC density increased gradually as a function of SPS temperature. The maximum relative density was ~97.5 % at 2000 °C and then slightly dropped to ~ 96.5 % at 2100 °C (the solid blue line, Figure 4.1). On the other hand, the relative density of SiC was approximately 77 % at 2000 °C and dropped slightly to ~ 73 % at 2100 °C (the solid black line, Figure 4.1).

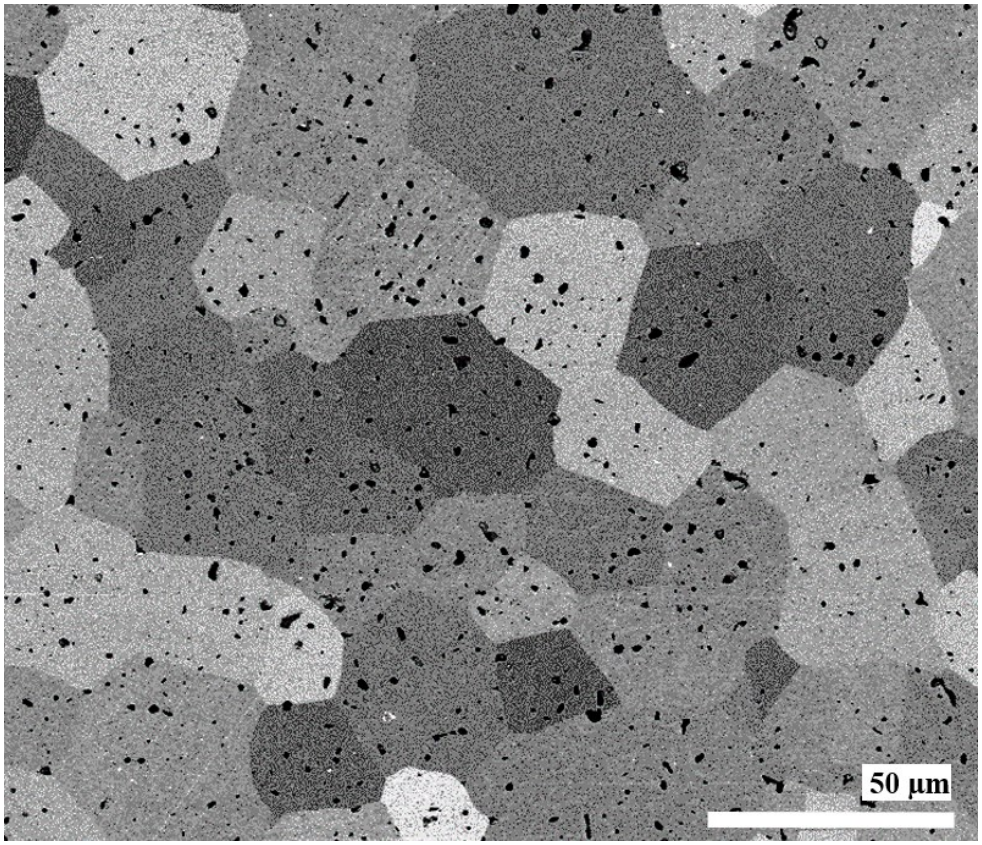

Figure 4.2 Secondary electron SEM micrographs of SPSed TiC at 2000 °C

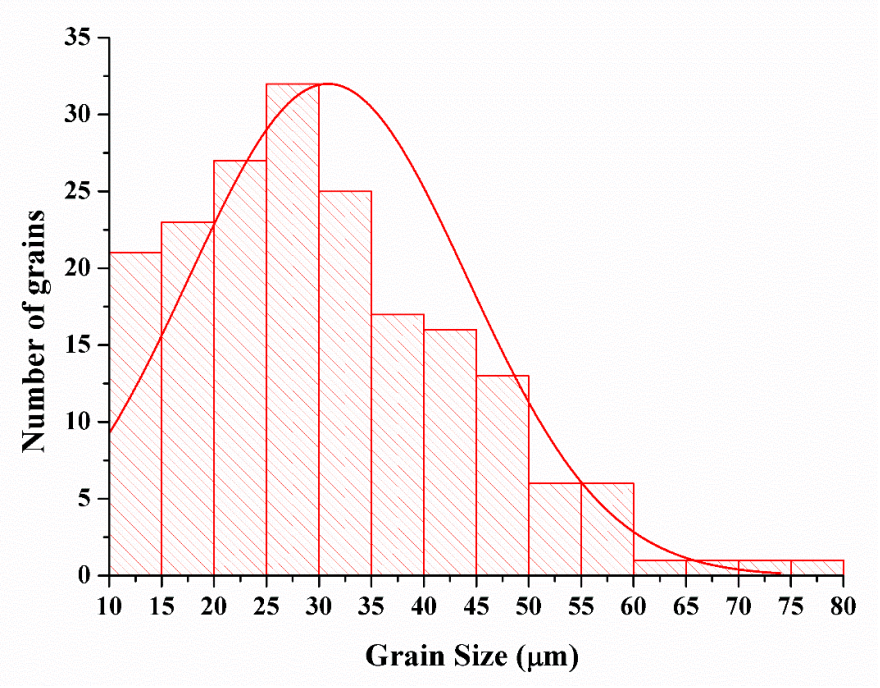

Figure 4.3 Grain size distribution curve of SPSed TiC at 2000 °C (calculated from 190 grains)

Figure 4.2 shows a secondary electron SEM image of the SPSed TiC at 2000 °C. The grains had a polygonal shape. Notably, different grey levels, 'contrast', in the SEM image were observed relating to the surface texture and roughness of SPSed TiC grains. Furthermore, the different orientations of TiC grains have different hardness, thus during grinding and polishing process, the surface finish in each grain was different giving additional contrast in the SEM images. The image analysis software "ImageJ" was used to analyse grain sizes and shapes from SEM images. The grain size distribution of SPSed TiC (Figure 4.3) shows that the mean grain size was approximately 31 μm. For the SiC SPSed at 2000 °C, a continuous network of SiC (grey contrast) and micro-pore (black contrast) was present as shown in Figure 4.4, and the grain size could not be measured.

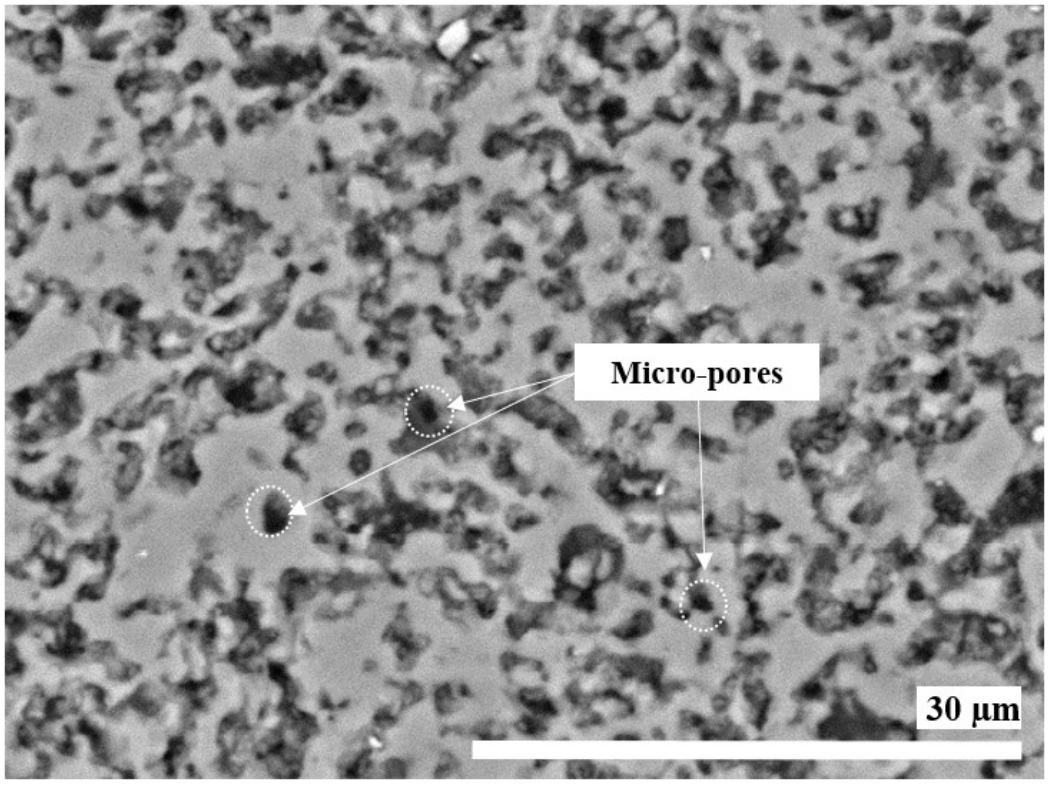

Figure 4.4 Backscattered electron SEM micrographs (BSE SEM) of SPSed SiC at 2000 °C

Although at 2000 °C TiC and SiC reach the highest density, SPSed TiC is considerably denser than the SiC. Although for both materials the optimum density was at 2000°C, this did not necessarily mean that the same would be true for the composite material. Therefore, further SPS temperature optimisation was undertaken using a mixture of 50%mole TiC and SiC (TiC-50%SiC) with the aim to get TiC/SiC composites containing dense TiC and SiC parts.

The TiC-50%SiC composites were significantly denser than SPSed SiC and TiC. The relative density of the composites increased as a function of SPS temperatures and reached a maximum at 2100 °C as shown in Figure 4.5.

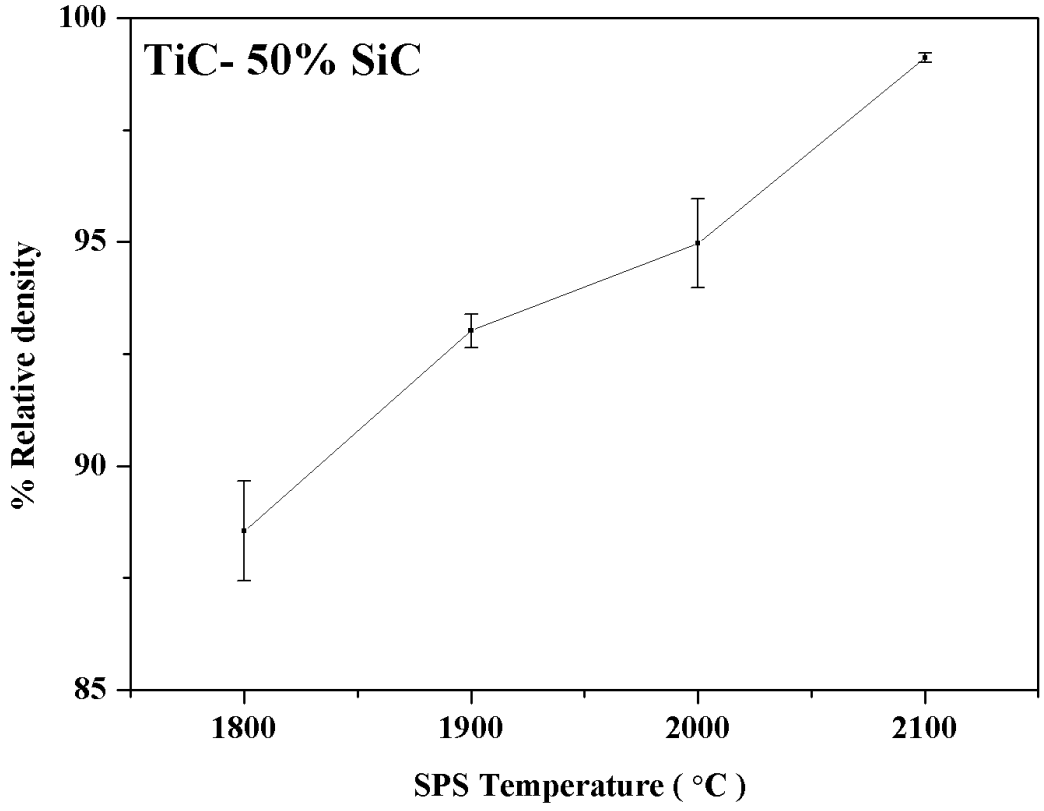

Figure 4.5 Relative density of TiC-50%SiC versus SPS temperatures

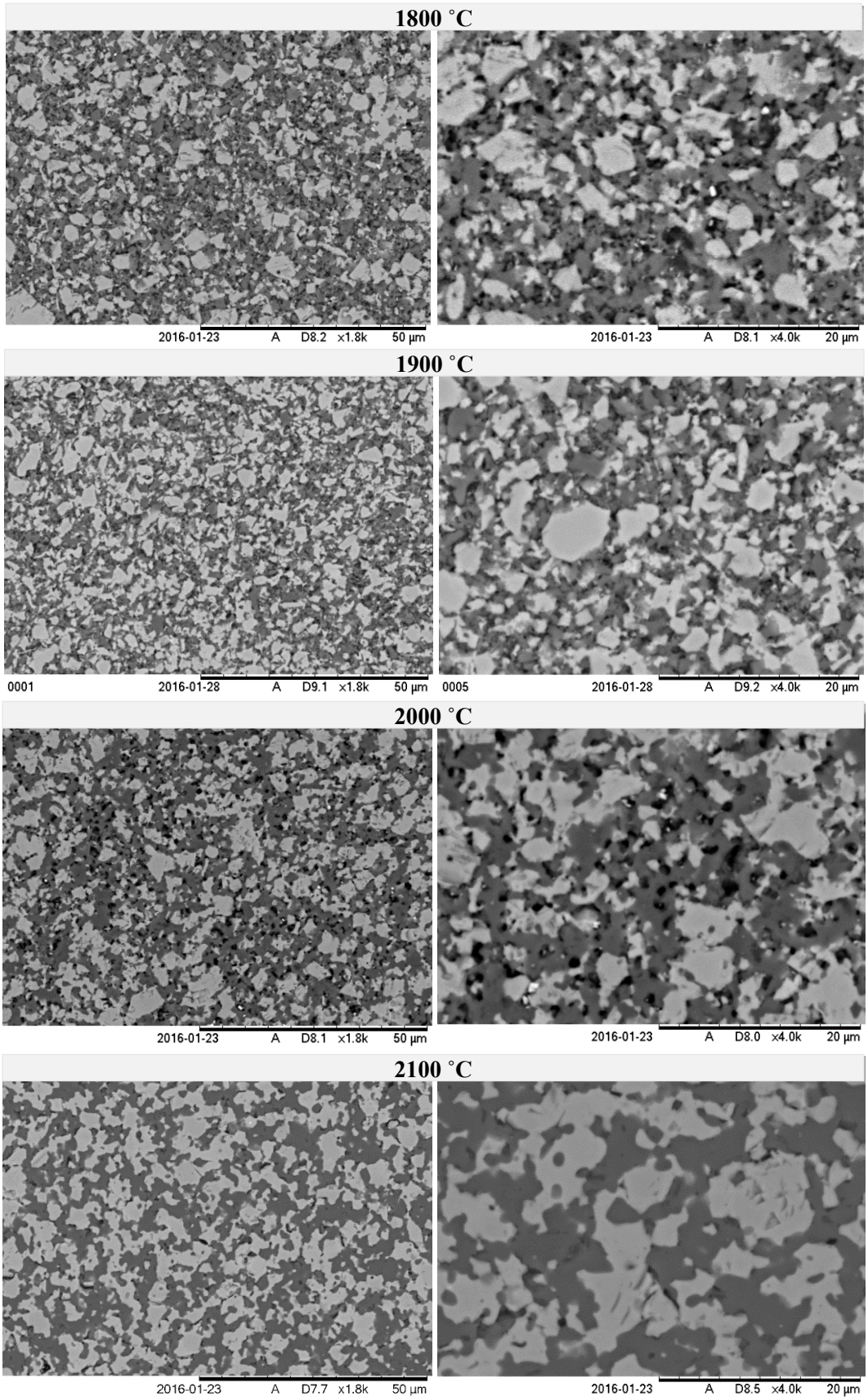

Figure 4.6 SEM micrographs of TiC-50% SiC at SPS temperatures of 1800, 1900, 2000 and 2100 °C. Note that the bright grey contrast represents a TiC grain, and the dark grey is a SiC grain according to chemical analysis by EDX-SEM

Figure 4.6 shows the BSE SEM images of TiC-50%SiC sintered at various temperatures. It can be seen that their microstructures are in good agreement with the measured relative densities. At 1800 °C, incomplete densification was observed in that pore and network of pores covered the entire of the sample surface.

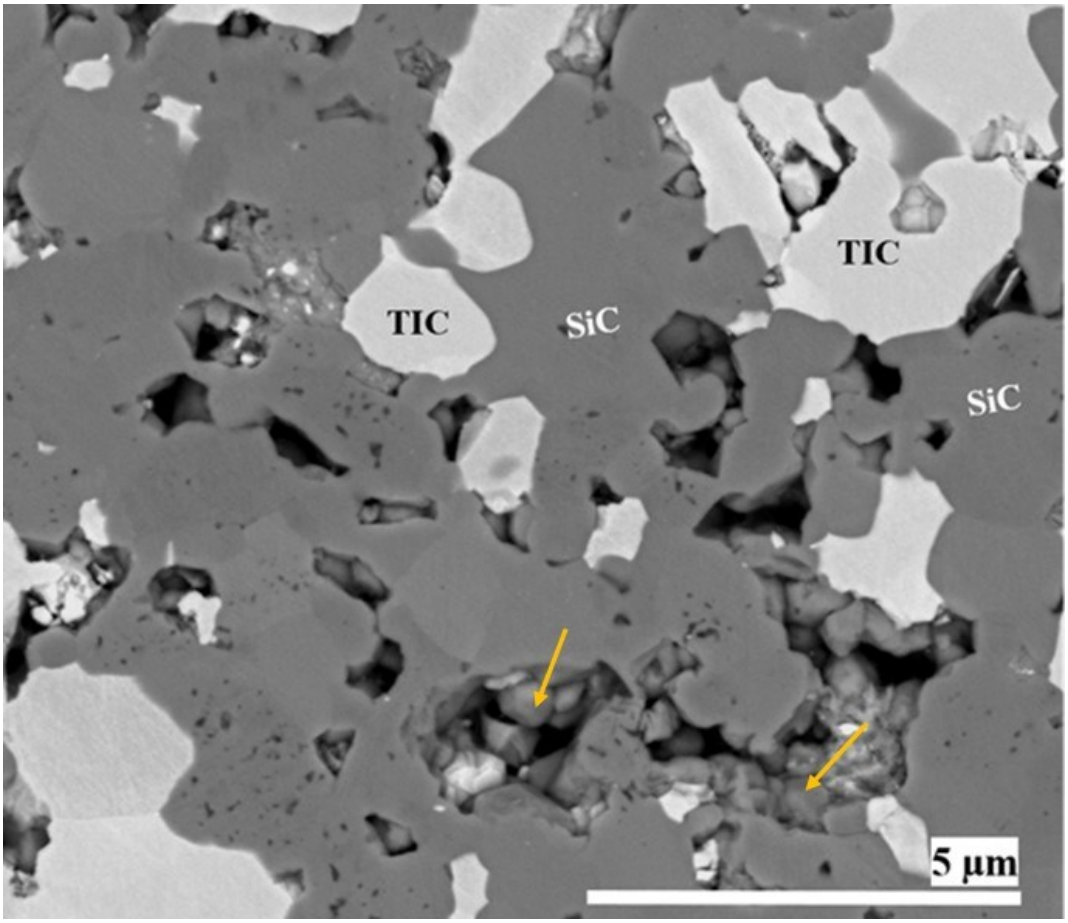

Figure 4.7 BSE SEM micrograph of TiC-50%SiC (SPSed at 2000 °C)

At 2000 °C, Figure 4.7, although TiC-50%SiC was significantly denser than SPSed SiC and TiC network of pores was found primarily located in the SiC regions (as indicated by the yellow arrows in Figure 4.7). Thus, the densification process was not complete At 2100 °C, both TiC and SiC parts of TiC-50% were denser than at lower temperatures. However, the micro-pores still appeared at the triple points and grain boundaries, as shown in

Figure 4.8, indicated by the green dashed circles. Some pores were a consequence of grinding and polishing processes [126]

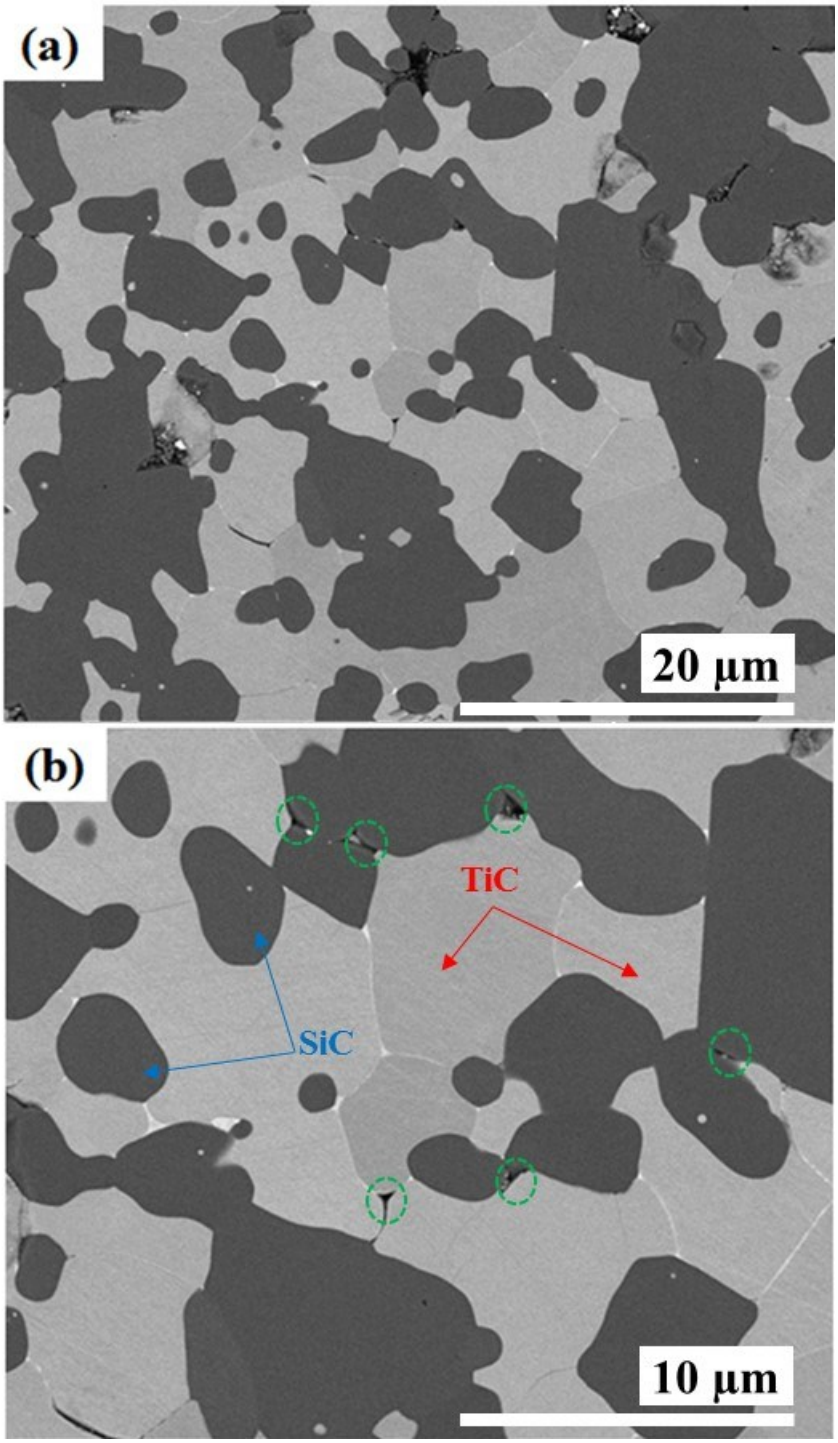

Figure 4.8 (a) BSE SEM micrographs of TiC-50%SiC (SPSed at 2100 °C) and (b) its magnification. Note: the green circles represent micro-pores.

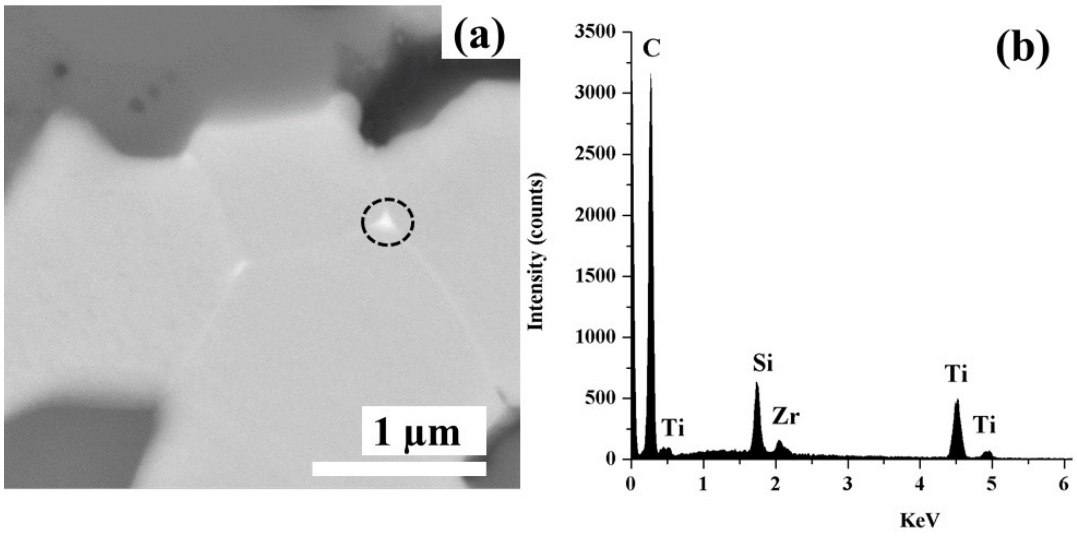

Figure 4.9 Energy-dispersive X-ray analysis (EDX) of TiC-50%SiC (SPSed at 2100 °C)

A layer of bright contrast was observed along the grain boundaries, as shown in Figure 4.8. The SEM EDX (Figure 4.9b) confirmed that it was a zirconium compound which was likely contamination from the zirconia milling media (ZrO_2). However, no peak corresponding to this compound was observed in the XRD patterns.

Figure 4.10 shows the XRD patterns of TiC-50% SiC SPSed at different temperatures using Cu K_α radiation (1.5416 Å) operating at 30 kV, 20mA and scanned from 10-80˚. There were no peaks at ~12˚ characteristic of 312 MAX phase and no evidence of by-products from TiC/SiC reaction [130]. The diffraction peaks corresponding to TiC (space group: Fm-3m [15]) were observed at 2Θ of 35.8˚, 41.8˚, 60.6˚, 72.5˚ and 76.3˚. Notably, cubic SiC peaks (3C-SiC, F-43m [15]) overlapped with the cubic TiC peaks. The peaks at 33.7˚, 34.2˚, 34.8˚, 38.0˚ and 65.7˚ represented α-SiC (hexagonal structure [15]) and confirmed that there was the β-α phase transformation.

Furthermore, the XRD patterns were refined by the Rietveld method. Table 4.1 shows the weight percentage of β-SiC, α-SiC and TiC in TiC-50%SiC SPSed at the various temperatures (the phase contents were normalised by TiC content). The β-SiC phase content was inversely proportional to the SPS temperature; 11 % of the β-SiC transformed to α-SiC at 1800 °C and approximately half at 2100 °C.

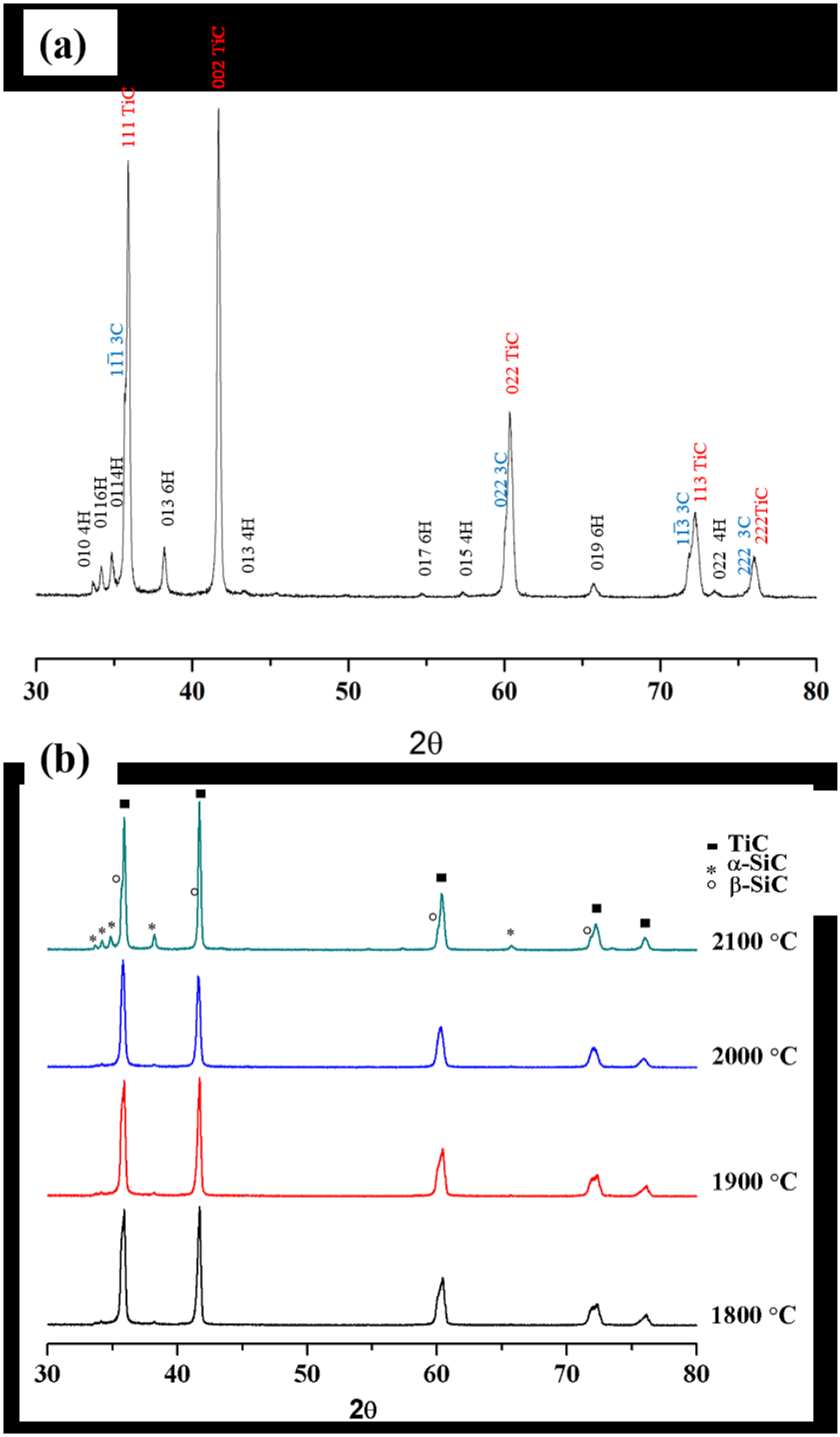

Figure 4.10 The XRD patterns of TiC-50% SiC SPSed at (a) 2100 °C and (b) various temperatures as labelled.

Table 4.1 The phase contents of TiC-50%SiC (refined by Rietveld method)

Phase contents (% wt.)						
SPS temp.	**α-SiC**		**β-SiC**	**TiC**	**Chi²**	**R_p**
	6H-SiC	**4H-SiC**	**3C-SiC**			
1800	10.1	1.0	36.1	59.0	3.49	13.09
1900	6.8	13.7	21.9	59.0	1.80	10.59
2000	11.8	1.2	24.7	59.0	2.84	13.62
2100	13.3	14.4	18.5	59.0	2.54	10.61

Note: 1. Acceptable refinement parameters are; Chi^2 less than 5 and R_p less than 15 %
2. The phase contents of TiC-50%mole of SiC were normalised by TiC content.
3. 50 TiC: 50 SiC (%mole) equals to 59/41 % wt.
4. 70 TiC: 30 SiC (%mole) equals to 77/23 % wt.

In summary, this investigation found that the optimal temperature to enhance the relative density was 2100 °C. Therefore, the SPS at 2100 °C was utilised to fabricate TiC/SiC composites.

4.2 TiC-SiC composite characterisation

4.2.1 Density results

Table 4.2 shows the effect of TiC content on composite relative density. When TiC contents increased (0 % to 100 % mol), the relative densities increased from ~ 73% to 99 % respectively. Only dense samples (> 95% of the relative density) were further characterised. Therefore, the morphology of TiC-50%SiC and TiC-30%SiC were investigated along with their mechanical and thermal properties.

Table 4.2 The relative density of SPSed TiC-SiC composite (at 2100 °C) with different mole ratio of TiC starting powder

Sample code	SiC (% mole)	TiC (% mole)	% Relative Density
SiC	100 (SiC)	0	73.0 ± 1.2
TiC-90%SiC	90	10	84.6 ± 1.9
TiC-50%SiC	50	50	99.0 ± 0.1
TiC-30%SiC	30	70	98.0 ± 0.1
TiC	0 (TiC)	100	98.0 ± 0.1

Note: % mole is based on the starting powder before SPSing.

4.2.2 SEM results

The composites were investigated by secondary electron (SE) SEM and backscattering electron (BSE) SEM along with EDX analysis. The bright grey contrast represented TiC, and the dark grey contrast was SiC according to chemical analysis SEM EDX. Figure 4.11 shows the BSE SEM micrograph of TiC-50%SiC at low magnification. An alternating layer microstructure was observed in TiC-50%SiC composed of large grain zones consisting of large SiC and TiC grains (indicated by red arrows) dispersed in the matrix of small grain zones consisting of small SiC and TiC grains. Figure 4.12a shows the BSE SEM of interfaces between the large grain zone and small grain zone in TiC-50%SiC divided by a dashed line. Moreover, the SEM micrographs were analysed for grain size and shapes by the ImageJ programme. Average TiC grain sizes in the small grain zone and the large grain zone were ~ 2.5 and ~ 4.5 µm as shown in Figure 4.12b and Figure 4.12c, respectively.

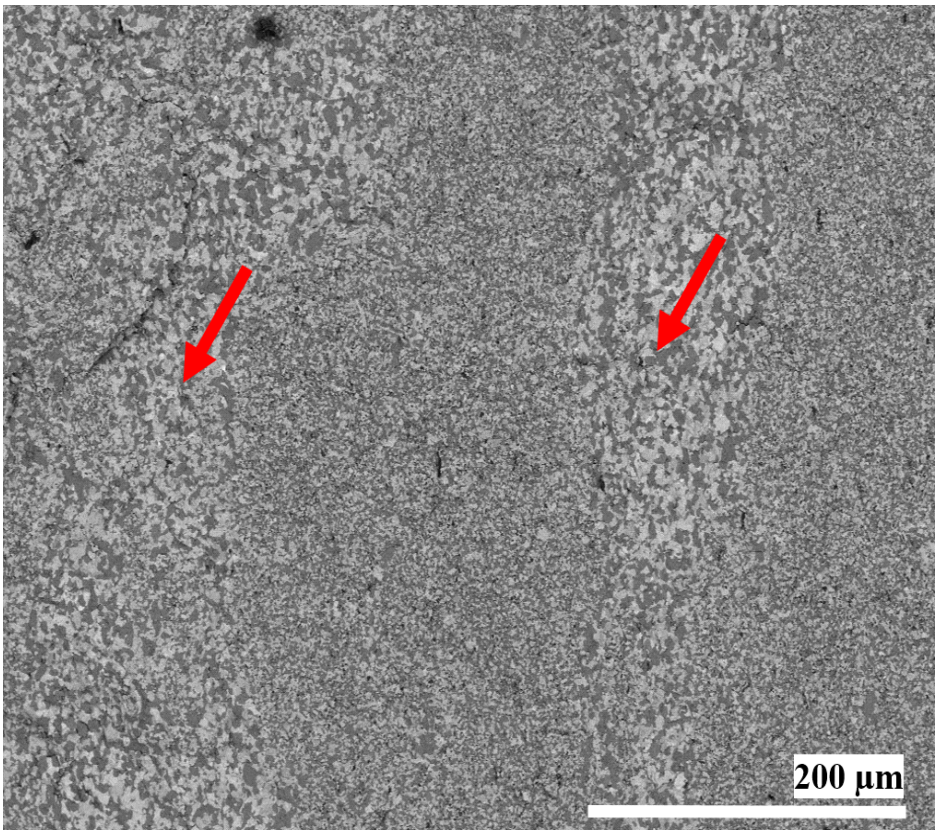

Figure 4.11 Low magnification BSE SEM micrograph of TiC-50% SiC (the arrows indicates the large grain zones dispersed over the specimen)

On the other hand, no evidence of the alternating layer structure was observed in TiC-30% SiC. The average TiC grain size was about 3.5 μm as shown in Figure 4.13(b). Notably, SiC grains were located in three significant positions in TiC-SiC composites: a large agglomerate of SiC grains, along the TiC grain boundaries (intergranular) and inside TiC grains (intragranular). The SiC grain arrangement and composite morphologies will be explained in more detail by TEM and fracture surface SEM images in Section 4.2.4 and Section 4.2.9 respectively.

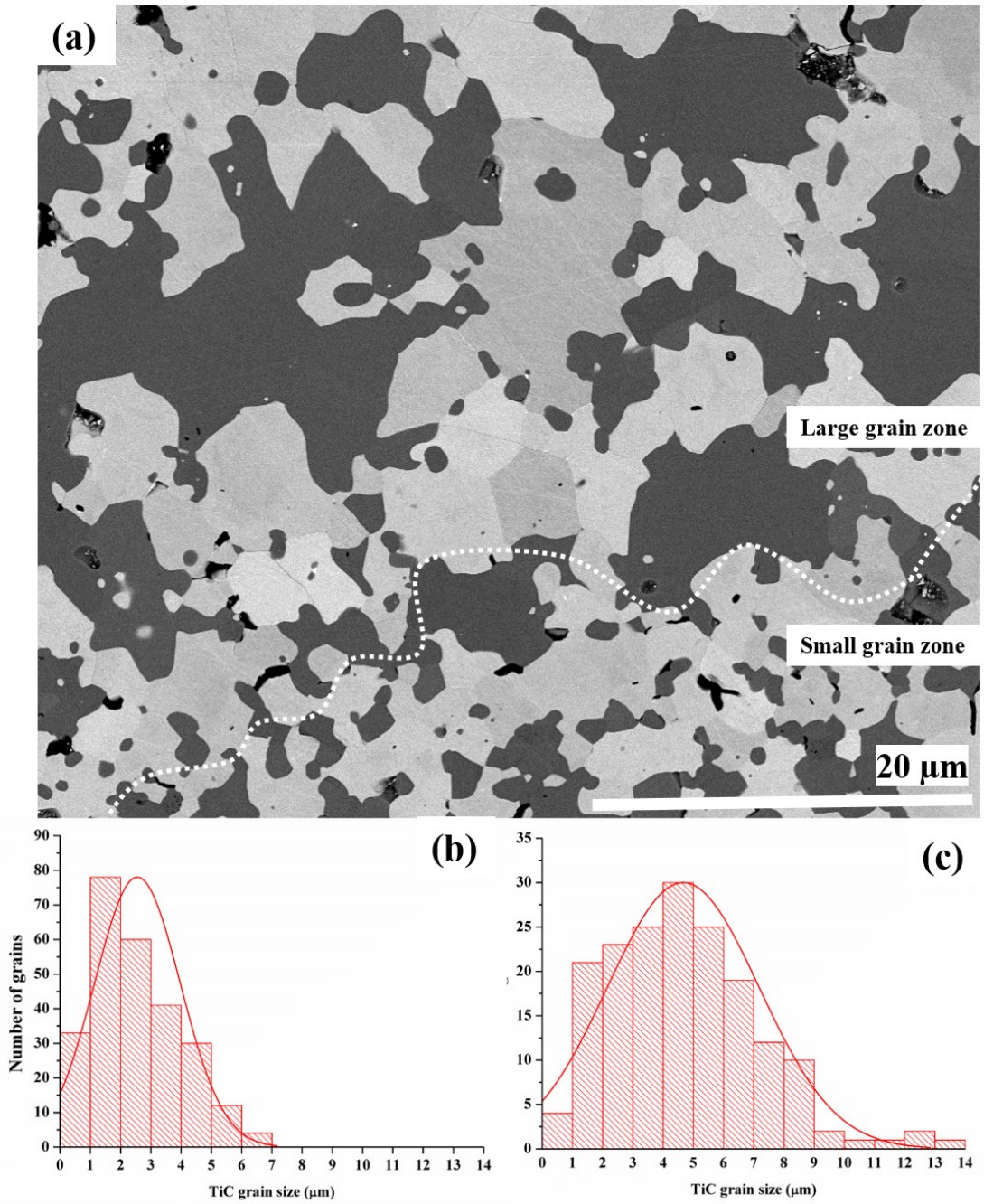

Figure 4.12 (a) BSE SEM micrograph of TiC-50%SiC and TiC grain size distribution curve of (b) the small grain zone and (c) the large grain zone. Note: approximately 200 grains of TiC was used to plot a grain size distribution

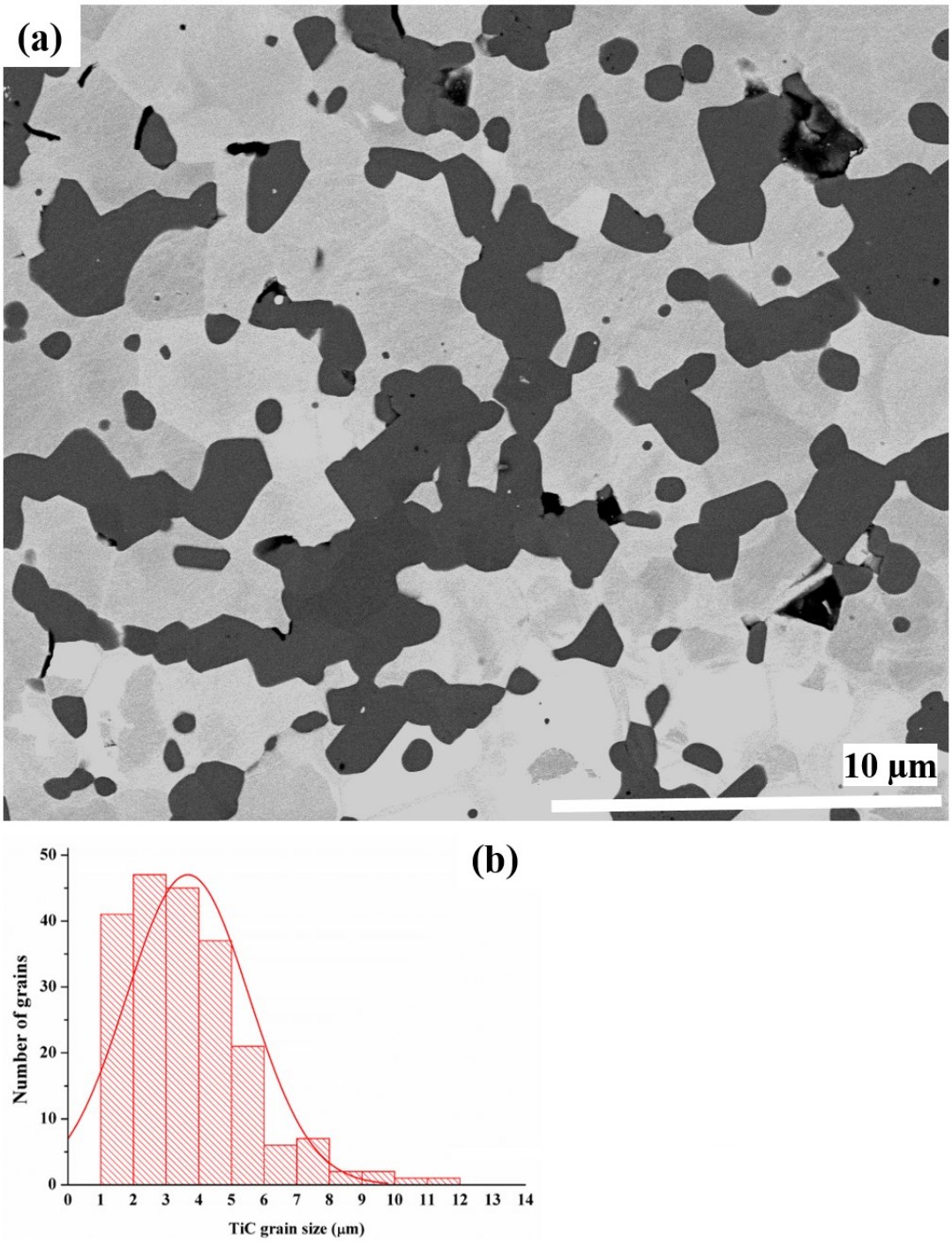

Figure 4.13 (a) BSE SEM micrograph of TiC-30%SiC, and (b) TiC grain size distribution curve

4.2.3 XRD results

Figure 4.14 displays the XRD patterns of TiC-50 % SiC and TiC-30% SiC. The diffraction peaks corresponding to TiC (space group: Fm-3m) can be observed at 2Θ of 35.8˚, 41.8˚, 60.6˚, 72.5˚ and 76.3˚ (ICSD 44494). Notably, several diffraction peaks of cubic SiC (β-SiC, ICSD 24217) overlapped the peaks of TiC. In addition, peaks at 33.7˚, 34.2˚, 34.8˚, 38.0˚ and 65.7˚ were from hexagonal SiC (α-SiC), which consists of 6H-SiC and 4H-SiC (ICSD 24169 and ICSD 24170, respectively), which confirmed the existance of the β/α phase transformation.

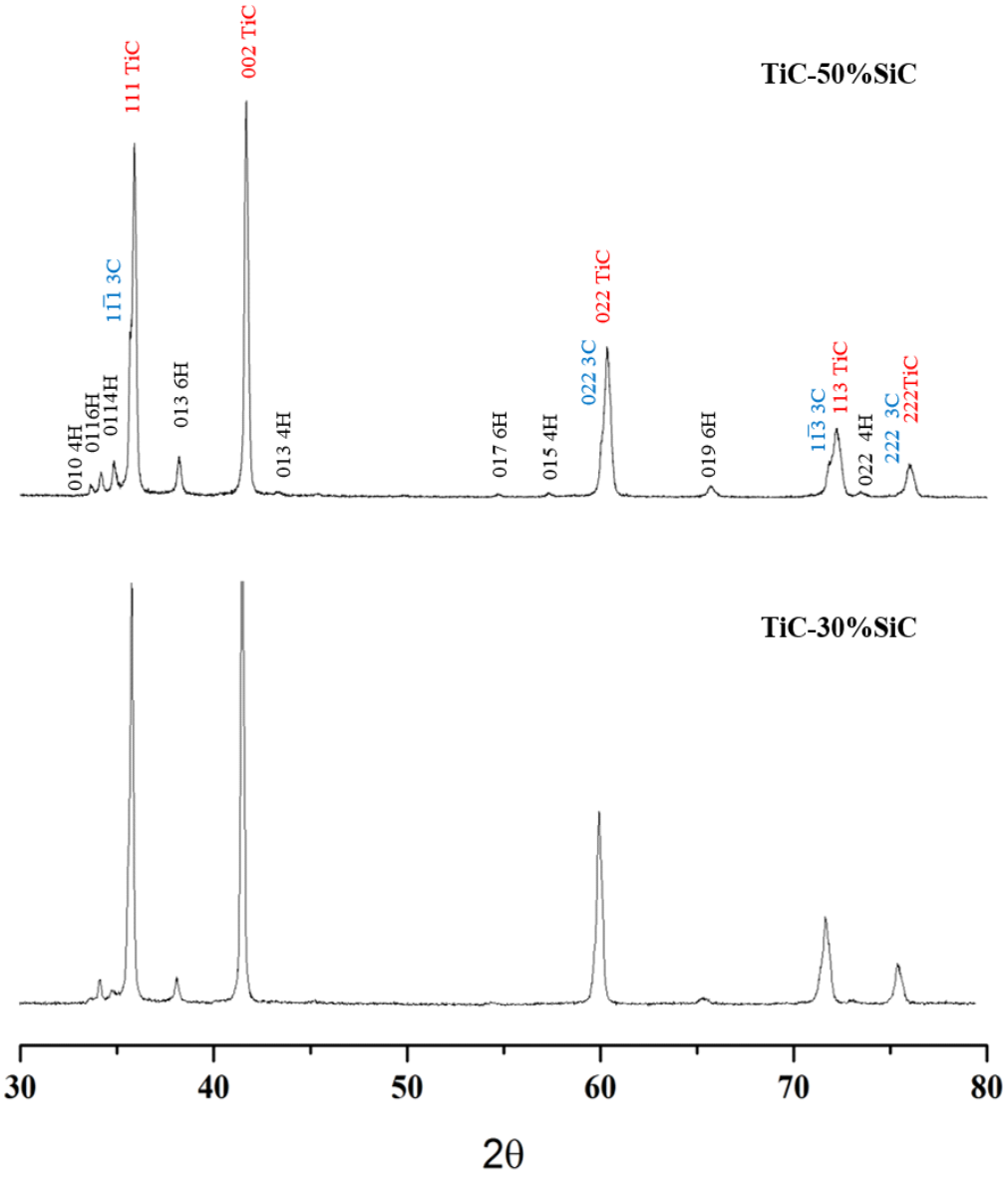

Figure 4.14 X-ray diffraction pattern of TiC-50%SiC and TiC-30%SiC

Table 4.3 illustrates the phase refinements of TiC-SiC composites SPSed SiC at 2100 °C. Approximately 40% of SPSed β-SiC (3C-SiC) transformed to α-SiC (6H-SiC and 4H-SiC), and about half of β-SiC in TiC-50%, SiC changed. However, more than half of β-SiC phase in TiC-30%SiC changed to α-SiC phase.

Table 4.3 Phase refinement of TiC-SiC composites and SPSed β-SiC (2100 °C)

Sample	**Phase contents (% wt.)**			
	α-SiC		**β-SiC**	
	6H-SiC	**4H-SiC**	**3C-SiC**	**TiC**
TiC-30%SiC	8.0	13.6	6.9	71.0
TiC-50%SiC	11.8	12.8	16.4	59.0
SiC	39.9	3.4	56.7	0.0

4.2.4 TEM results

Figure 4.15a and Figure 4.15b show the TEM micrographs of SiC grain arrangement in TiC-50%SiC and TiC-30%SiC, respectively, which confirmed the SiC grains by EDX-TEM. Their SiC grain shapes were a combination of equiaxed SiC grains and elongated SiC grains which could result from the β/α phase transformation.

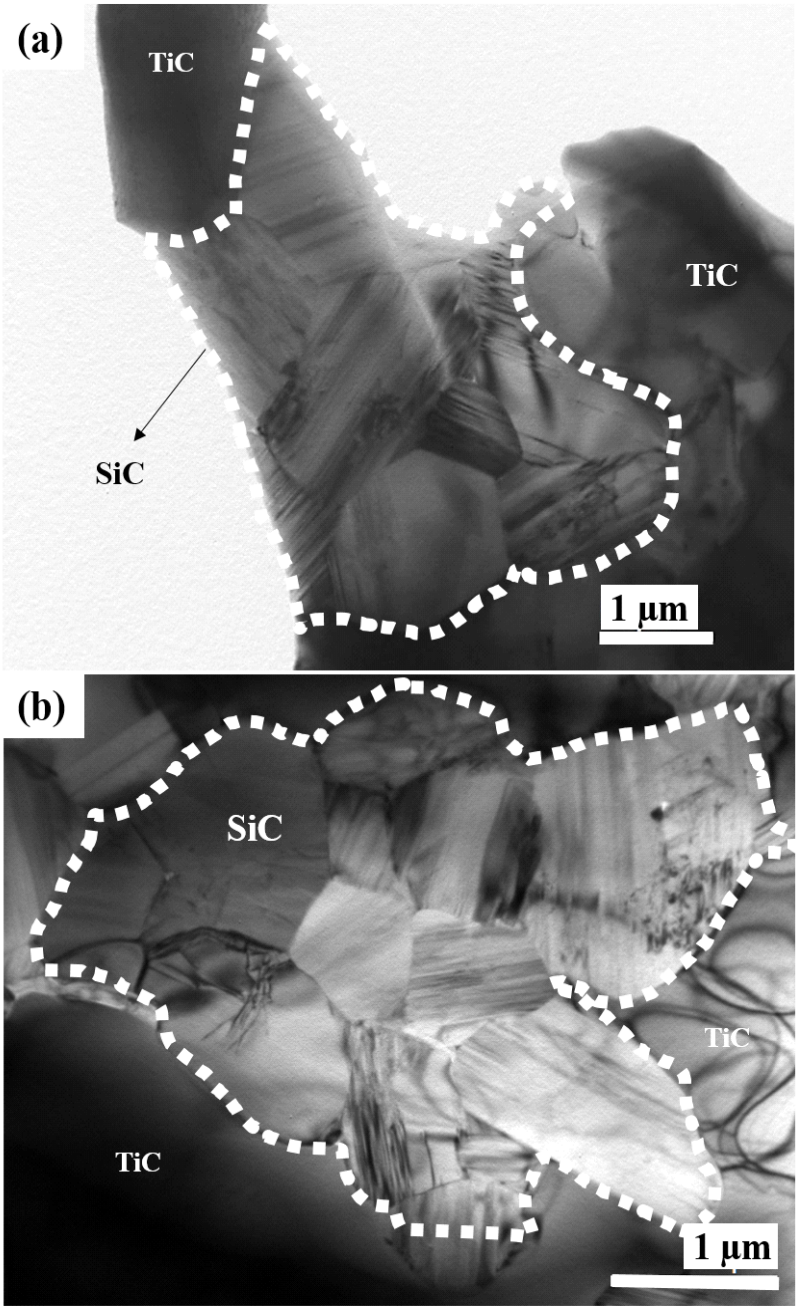

Figure 4.15 TEM micrographs of (a) TiC-50% SiC and (b) TiC-30%SiC

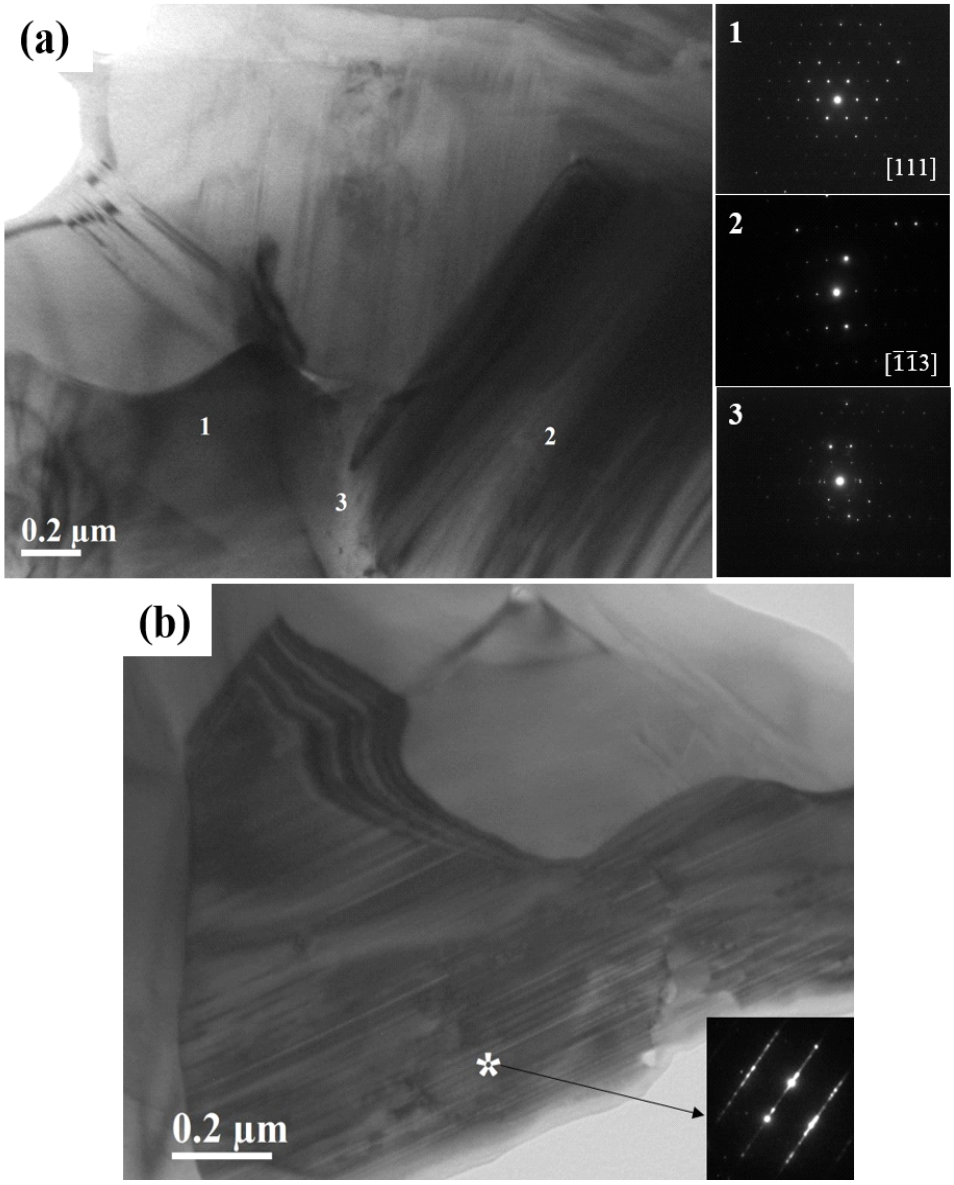

Figure 4.16 TEM micrographs of (a) TiC-50%SiC and (b) its α/β grain composites

Figure 4.16a shows the TEM micrograph of TiC-50%SiC illustrating the β-SiC grains. The insets show the electron diffraction patterns (ED) of adjacent grains (indicated as the "1" and "2" grains) and their interfaces (labelled as the "3" grain). From the ED, it was identified that the "1" grain was at the [111] β-SiC zone axis. On the other hand, the "2" grain was close to the [$\bar{1}\bar{1}$3] zone axis. Figure 4.16b shows a α/β composite grain which the inset ED shows a superposition of $[111]_\beta$ and $[110]_\alpha$ exhibited the streak ED from the random disposition of discrete lamellae of different SiC polytypes.

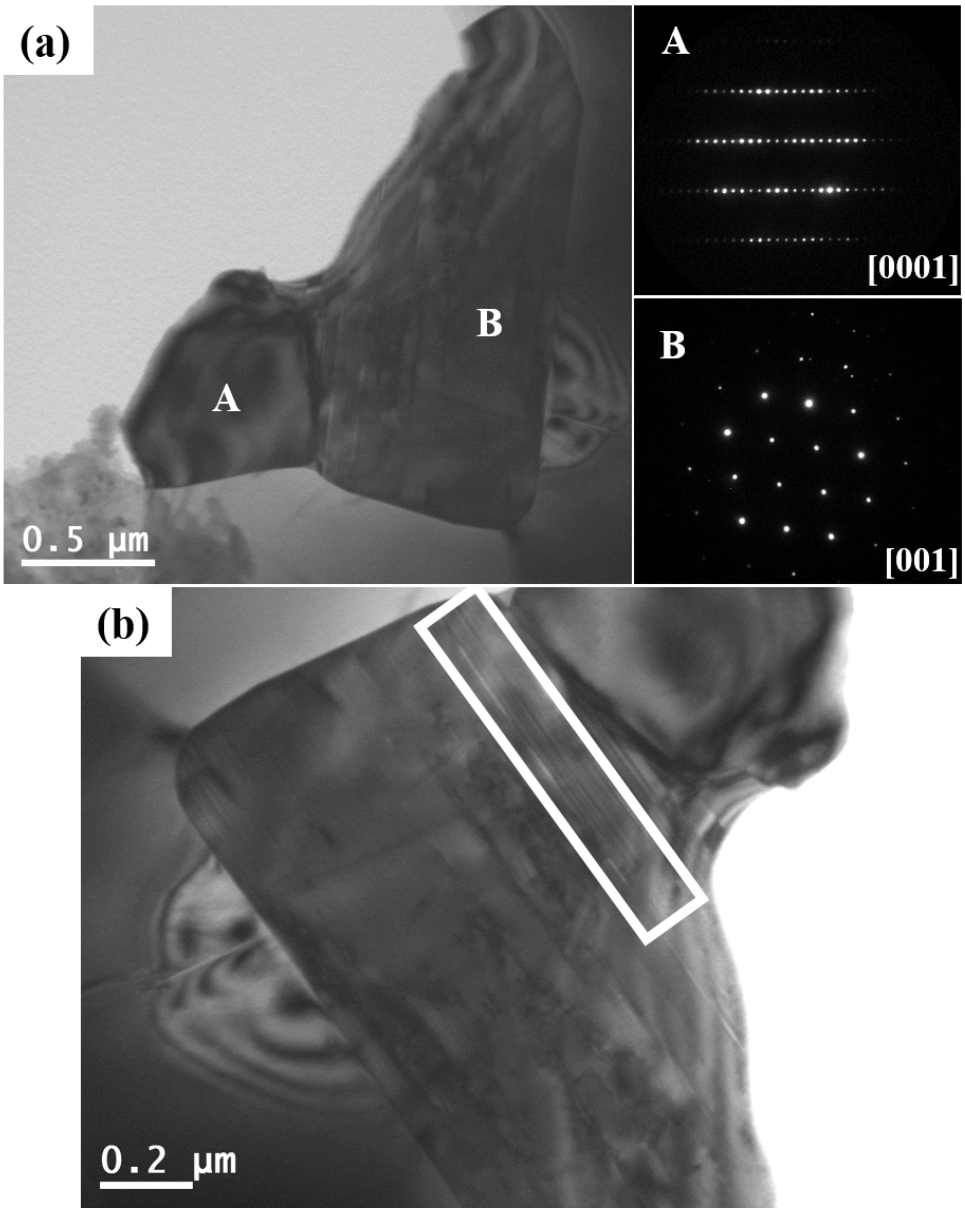

Figure 4.17 TEM micrographs of (a) TiC-30%SiC and (b) the α/β grain composite grain

Similarly, Figure 4.17a shows the TEM micrograph of TiC-30%SiC. The ED confirmed that grain A had transformed entirely to a α-SiC grain ([0001]α zone axis), and the grain B could be a α/β composite grain because the area of the α-SiC phase was found as indicated by the white box in Figure 4.17b which is in good agreement with Heuer's report in that the β/α composite grains (consisted of α core and surrounding by β) from β →α phase transformation [131-134]. Additionally, the β and α patterns are easily identified (extra spots are introduced into the β diffraction pattern by an α polytypes) at/or near the $[110]_{\beta}$ zone axis, and also at this orientation the (111) and (0001) planes are seen edge-on and can easily be directly imaged, even though at moderate magnifications [131-134].

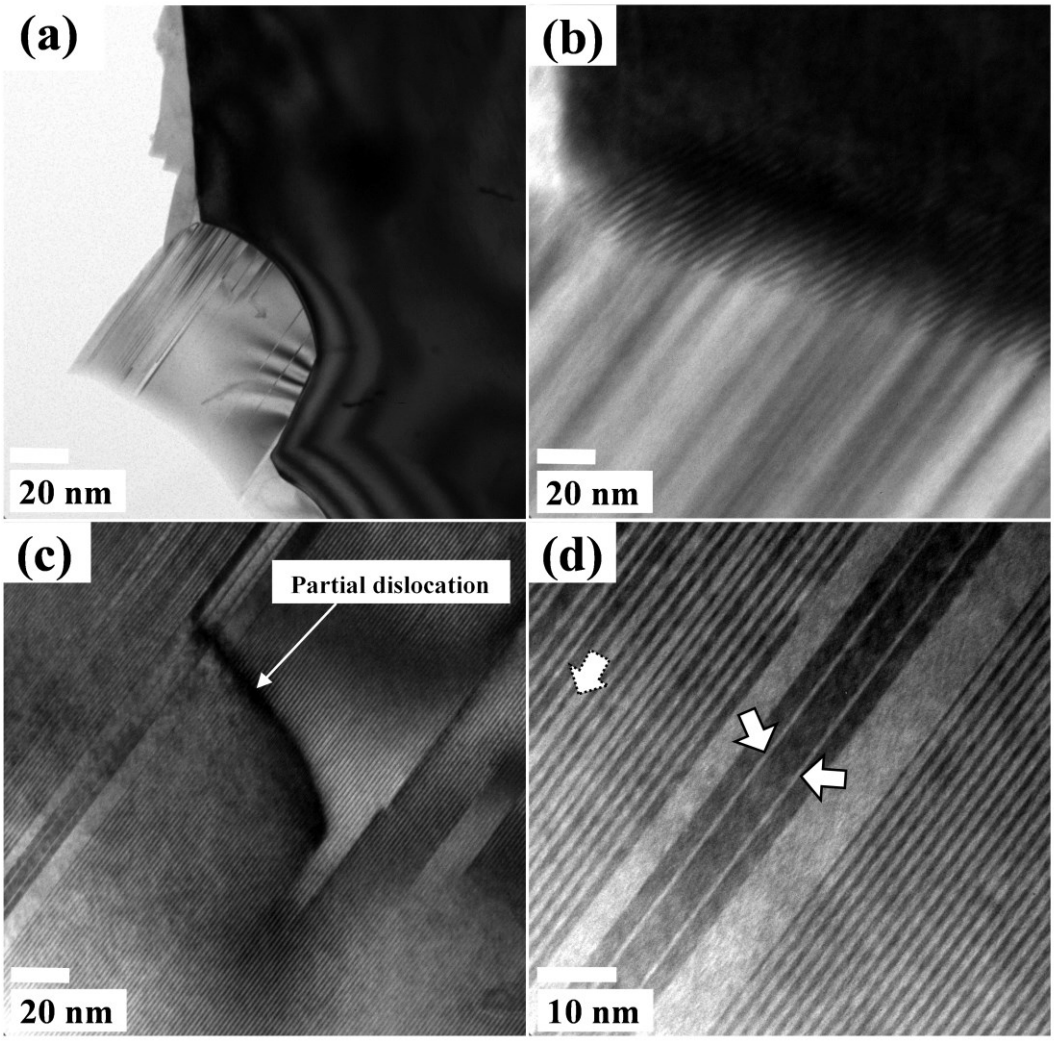

Figure 4.18 TEM micrographs of TiC-30% SiC: (a) the α/β composite grain, (b) SiC-SiC grain boundary, (c and d) lattice fringe of the α/β composite grain

To further understand the β/α composite grains, the TiC-30%SiC specimen was tilted to the [011] zone axis (using 200 kV FEI Tecnai). The lattice fringe of β and α polytypes were seen as shown in Figure 4.18d. The differences in an interplanar structure were used as a phase identification. The 1.5 nm lattice fridges were identified as 6H-SiC and the 2.5 nm in the β phase [131]. In Figure 4.18c, similar features were found to those reported by Ogbuji *et al*., identified as partial dislocations [131-134]. Additionally, the β twin boundaries indicated by the solid arrow in Figure 4.18d, and the faulted layers denoted by the dashed arrow.

4.2.5 Thermal conductivity results

Thermal conductivity (K) of TiC-SiC composites was measured using a thermal properties analyser (Anter Flashline TM 3000) with a high-speed Xenon discharge (HSXS pulse source) from 50 °C to 500 °C. The thermal conductivity results were compared with a reference dense SiC (Chen *et al.* [17]) to avoid a porosity factor. The K of SiC is significantly higher than that of TiC [15]. The K of our SPSed TiC is in good agreement with TiC synthesised by Xue *et al.*[135] in that the K was directly proportional to temperature as shown in Figure 4.19. The K of TiC-30% SiC and TiC-50% SiC were approximately 70 and 50 W/m.°C at 50 °C. However, their K slightly dropped to about 50 and 40 W/m °C at 500 °C, respectively. An effect of SiC contents on the K of TiC-SiC composites will be discussed in Chapter 5.

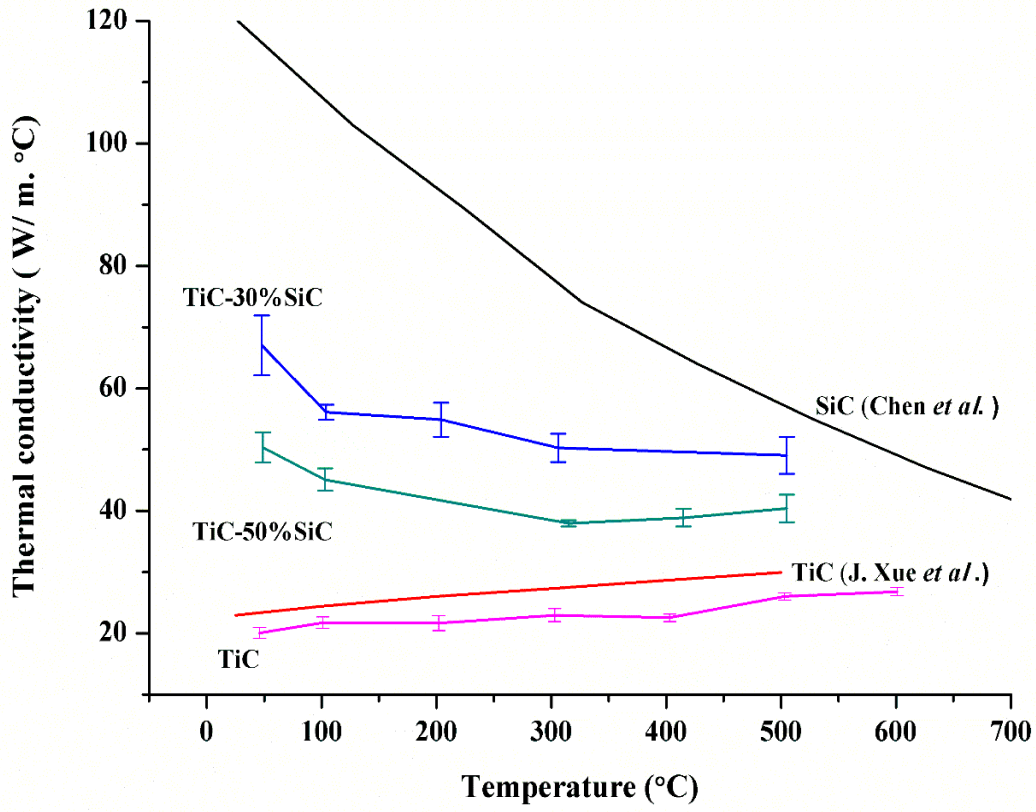

Figure 4.19 Temperature dependence of TiC-30%SiC and TiC-50% SiC thermal conductivity compared with SiC (Chen *et al.* [17]) and TiC (Xue *et al.* [135])

4.2.6 Thermal analysis results

Thermogravimetric analysis (TGA) and differential thermal analysis (DTA) were undertaken with the dried thin foil specimens of TiC-SiC composites in flowing argon at heating rates of 20 °C min^{-1} over the temperature range of 40-1450 °C. Figure 4.20 shows the TGA-DTA thermogram of TiC-50%SiC. The mass loss (~ 2.6 %) from the range of 40 - 153 °C corresponded to a dehydration process (the endothermic reaction). The mass then increased due to an oxidation process at about 153-200 °C, which was in good agreement with the DTA with an exothermal peak at the same temperature range. From 180 to 1450 °C, the sample mass changed slightly. However, a temperature difference existed in the DTA thermogram resulting from the TiO_2 phase transformation. An amorphous TiO_2 completely formed at a temperature of approximately 180 °C, so the mass barely changed.

The oxidation of TiC to TiO_2 is a multi-step exothermic process consisting of four consecutive reaction steps: TiC→ oxycarbide (TiC_xO_{1-x}) → anatase TiO_2 → rutile TiO_2 [136]. Thus, broad exothermal peaks associated with the phase transformation after 180 °C appeared (Figure 4.20). Notably, a huge broad exothermic peak around 1200 °C came from the oxidation of SiC resulting in a slight mass increase (less than 0.5 %) as shown in Figure 4.20. In the case of TiC-30%SiC, similar TGA-DTA thermogram features were observed, whereas the oxidation of SiC started at a higher temperature, 1200 °C as shown in Figure 4.21.

Furthermore, TiO_2 and SiO_2 formation were confirmed by the BSE SEM EDX as shown in Figure 4.22. It can be seen that oxide layers formed on the surface of TiC-30% SiC with a slightly higher density on TiC areas as indicated by the blue area in the EDX mapping. Figure 4.23 shows the SE SEM micrograph of TiC grains of post treatment TiC-50%SiC. We found the feature which looked like crystals cover TiC grains surface which could be the TiO_2 and contaminations as reported by Ning *et al*. [137].

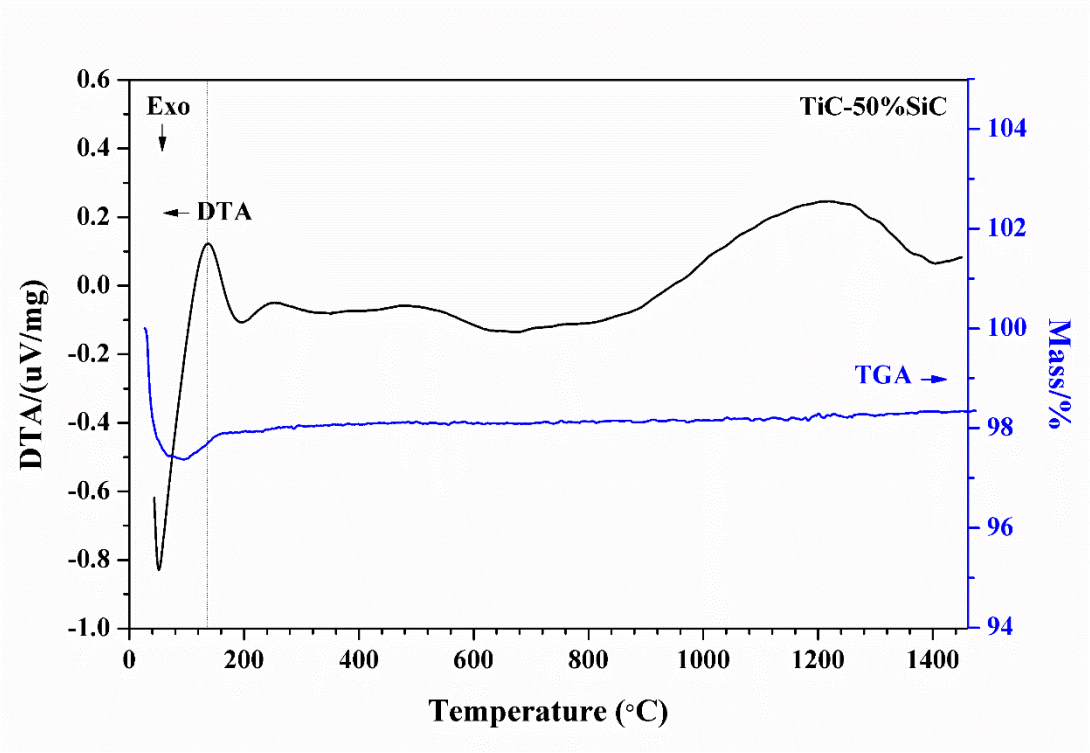

Figure 4.20 TGA-DTA thermogram of TiC-50%SiC operated in argon gas with a 20 ˚C/min heating rate

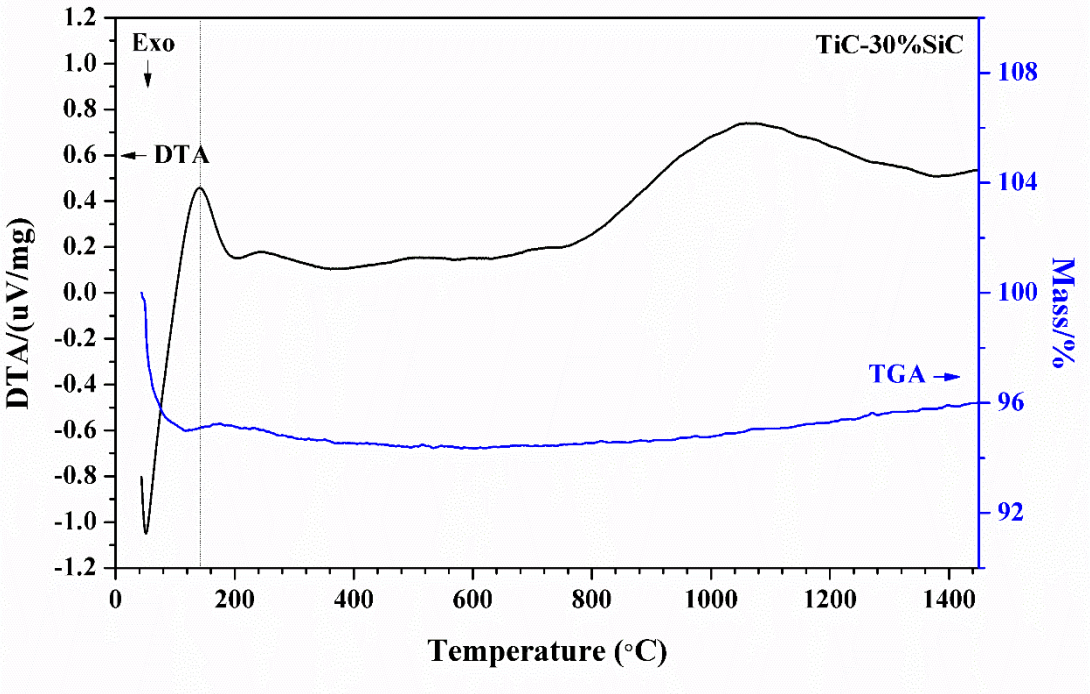

Figure 4.21 TGA-DTA thermogram of TiC-30%SiC operated in argon gas with a heating rate of 20 ˚C/min

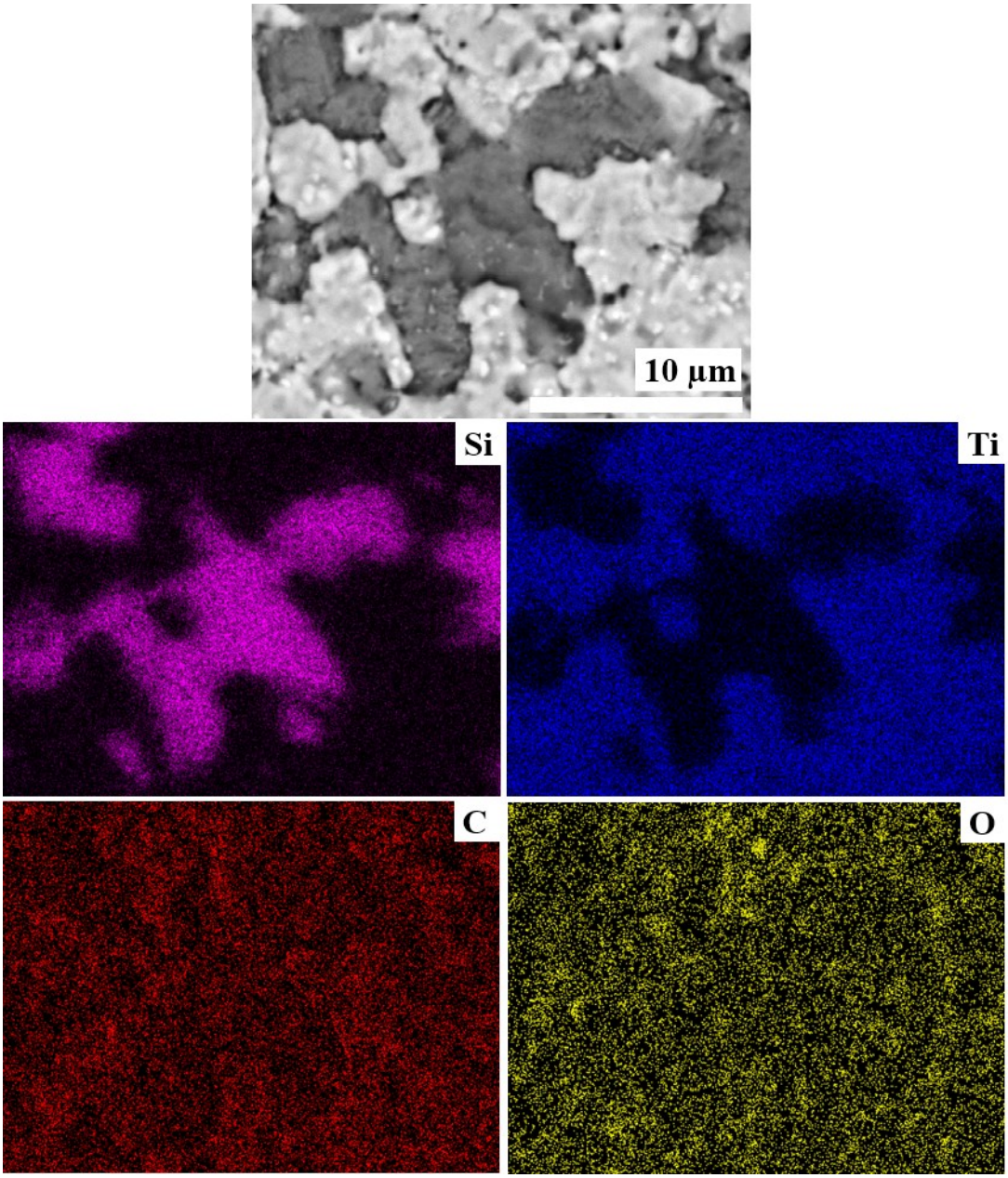

Figure 4.22 BSE SEM and EDX mapping of the post treatment surface of TiC-30%SiC after the TGA-DTA measurement (40 to 1450 ˚C)

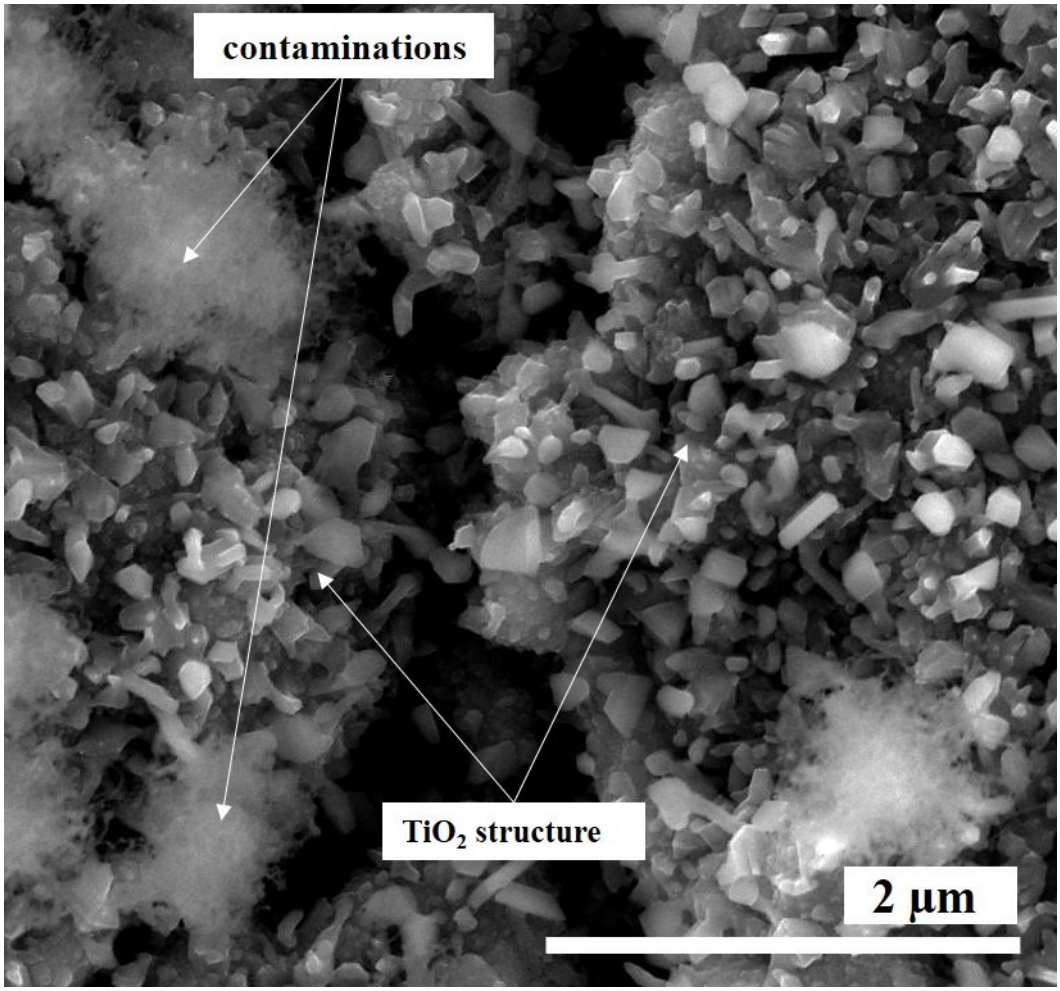

Figure 4.23 SE SEM micrograph of post surface TiC grains of TiC-50% SiC after the TGA-DTA measurement (40 to 1450 ˚C)

4.2.7 Mechanical property results

Table 4.4 summarises the mechanical properties of TiC-SiC composites. The Vickers hardness of the composites (1 kg loading) increased proportionally to SiC content (Table 4.4) following the mixture rule [108]. Fracture toughness (K_{IC}) of the composites was measured by an indentation method with 5 kg Vickers loading [21]. The K_{IC} of TiC-30% SiC and TiC-50% SiC were approximately 7.9 MPa.√m, which were much higher than SiC and TiC (3.7 MPa.√m) [19].

Table 4.4 Main mechanical properties of TiC-SiC composites

SiC (% mole)	Vickers hardness (GPa)	K_{IC} (MPa. √m)
50	31 ± 3	7.9 ± 0.4
30	25 ± 3	7.9 ± 0.2

Crack paths from the Vickers indentation (5 kg loading) were investigated by SEM. Figure 4.24 shows the cracks on TiC-50%SiC surface, which propagated predominately along the grain boundaries: TiC/TiC, TiC/SiC and SiC/SiC (intergranular fracture mode). It was observed that the interaction between the cracks and the submicron SiC, which acted as deflectors, caused tortuous crack paths. Similarly, the surface fracture of TiC-30%SiC was shown in Figure 4.25.

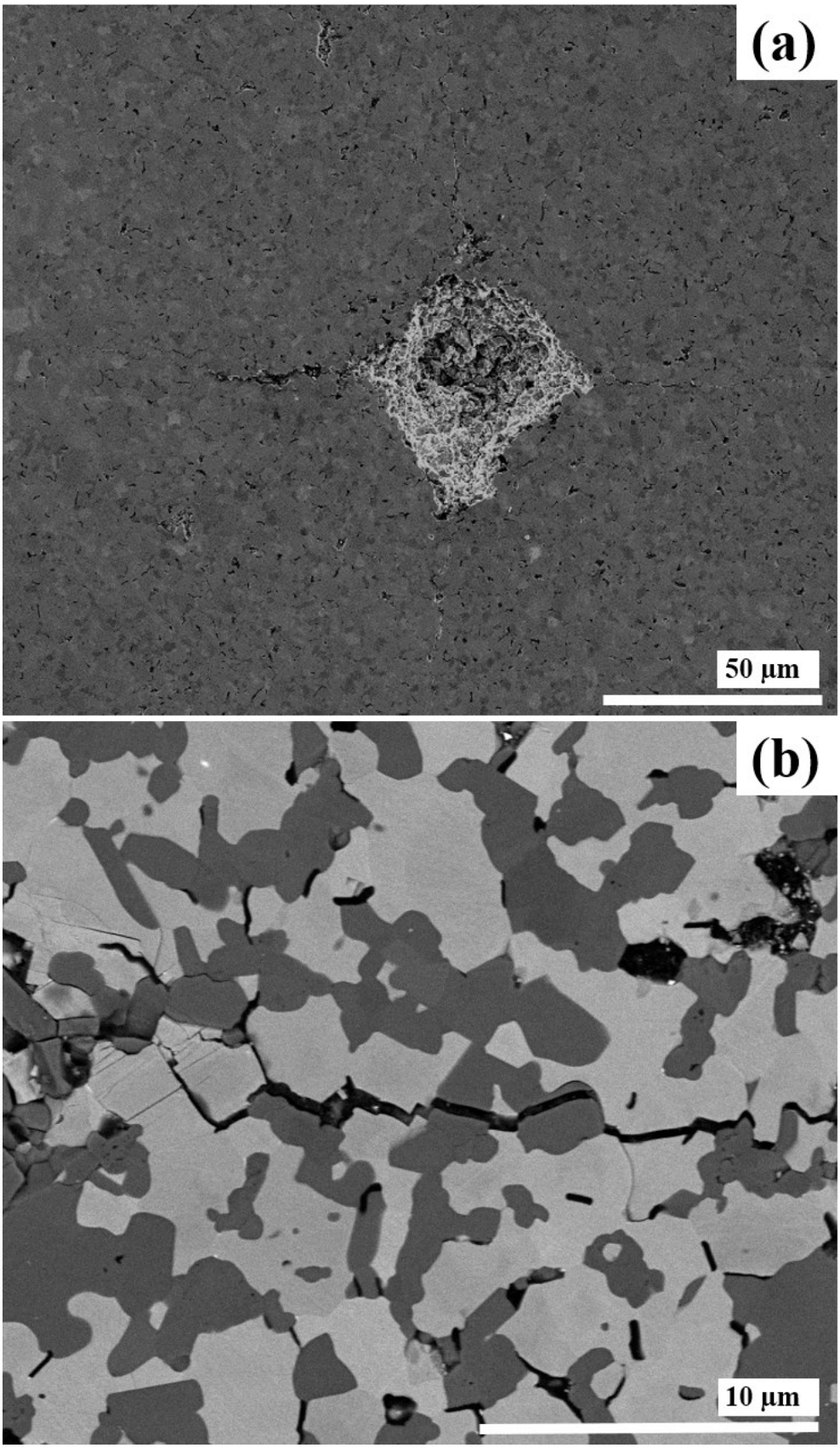

Figure 4.24 (a) SE SEM micrograph of the surface fracture from 5 kg Vickers indention and (b) BSE SEM micrograph of the cracking path of TiC-50%SiC

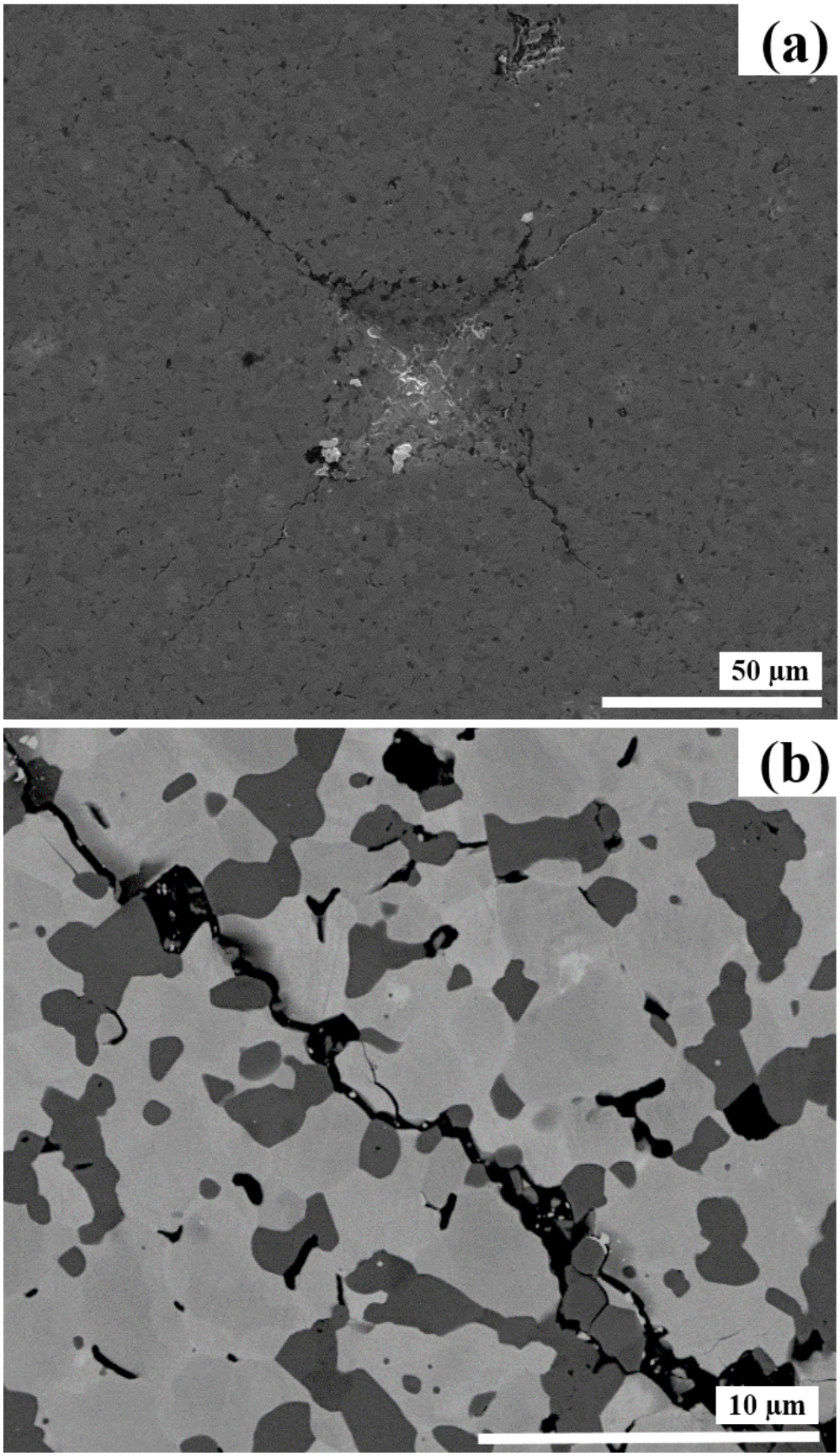

Figure 4.25 (a) SE SEM micrograph of the surface fracture from 5 kg Vickers indention and (b) BSE SEM micrograph of the cracking path of TiC-30%SiC

4.2.8 Three-point bend test results

TiC-50%SiC and TiC-30%SiC were cut into a bar shape and their surfaces were finished by polishing with 1 µm diamond suspension before bend testing. Figure 4.26 shows the flexural stress-stain curve of TiC-50% SiC and TiC-30%SiC. The dashed lines represent TiC-30%SiC curves of three repeating samples, while the solid lines show that of TiC-50%SiC.

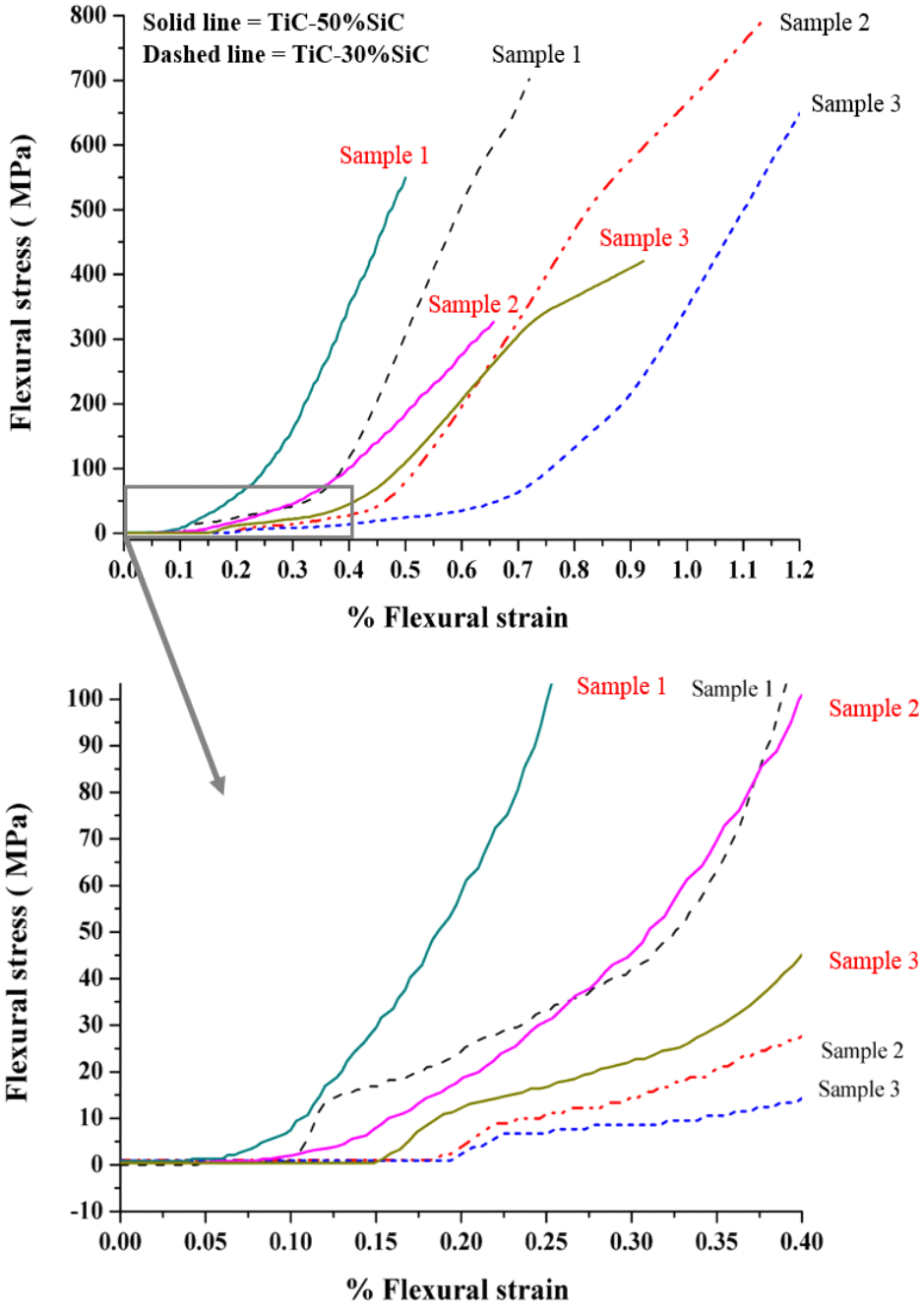

Figure 4.26 Flexural stress-strain curves of TiC-50%SiC and TiC-30%SiC

As can be seen from Figure 4.26, the flexural stress of TiC-30%SiC (350 - 650 MPa) was significantly higher than that of TiC-50%SiC (600-800 MPa). The variability was more extensive in the flexural strain than the flexural stress. Although most refractory carbides have high failure stress, they exhibit low ductility and toughness and usually fracture at ≤ 0.1% strain. However, all specimens of TiC-50% SiC and TiC-30% SiC failed at flexural strain > 0.1%. There was an abrupt change in the slope of the stress-strain curves, which was believed to be a result from crack retarding processes. It can be implied that there were crack barriers or crack deflectors which slowed the crack propagation. The toughening associated with these TiC-SiC composites was in good agreement with the K_{IC} results from the indentation method in that as the SiC was introduced into TiC-SiC composites, the K_{IC} increased.

4.2.9 Fracture surface results

To better understand the fracture mechanisms, the fracture surface of the TiC-50%SiC and TiC-30%SiC specimens from the three-point bend test were investigated by SE and BSE SEM. Figure 4.27a shows a TiC-30%SiC fractography image illustrating a macroscopic crack branching, which left rough and coarse fracture surfaces. Figure 4.27b shows that the SiC grain boundaries could be seen clearly, and their grain sizes were significantly smaller than that of TiC grains.

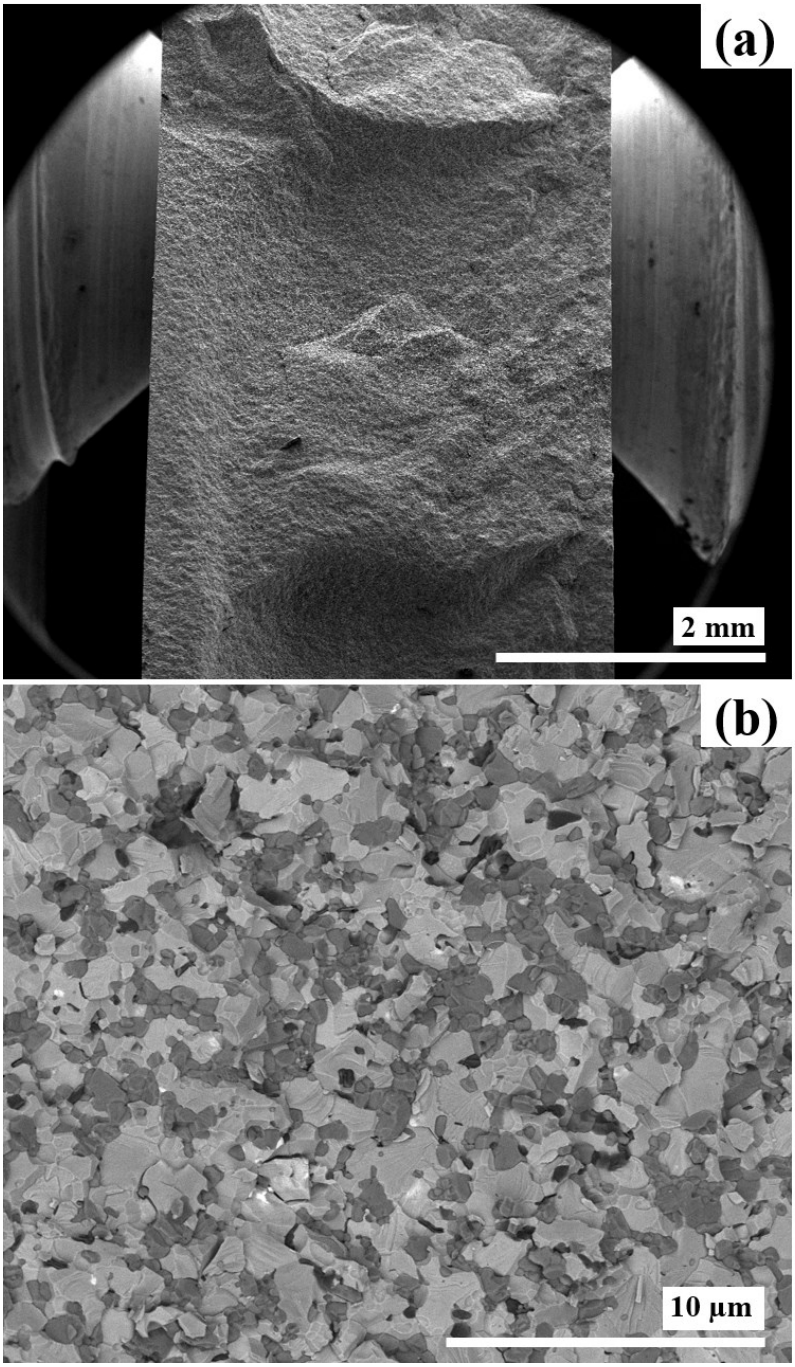

Figure 4.27 Fracture surface BSE SEM micrographs of TiC-30%SiC; (a) macroscopic cracked surface and (b) a higher magnification image

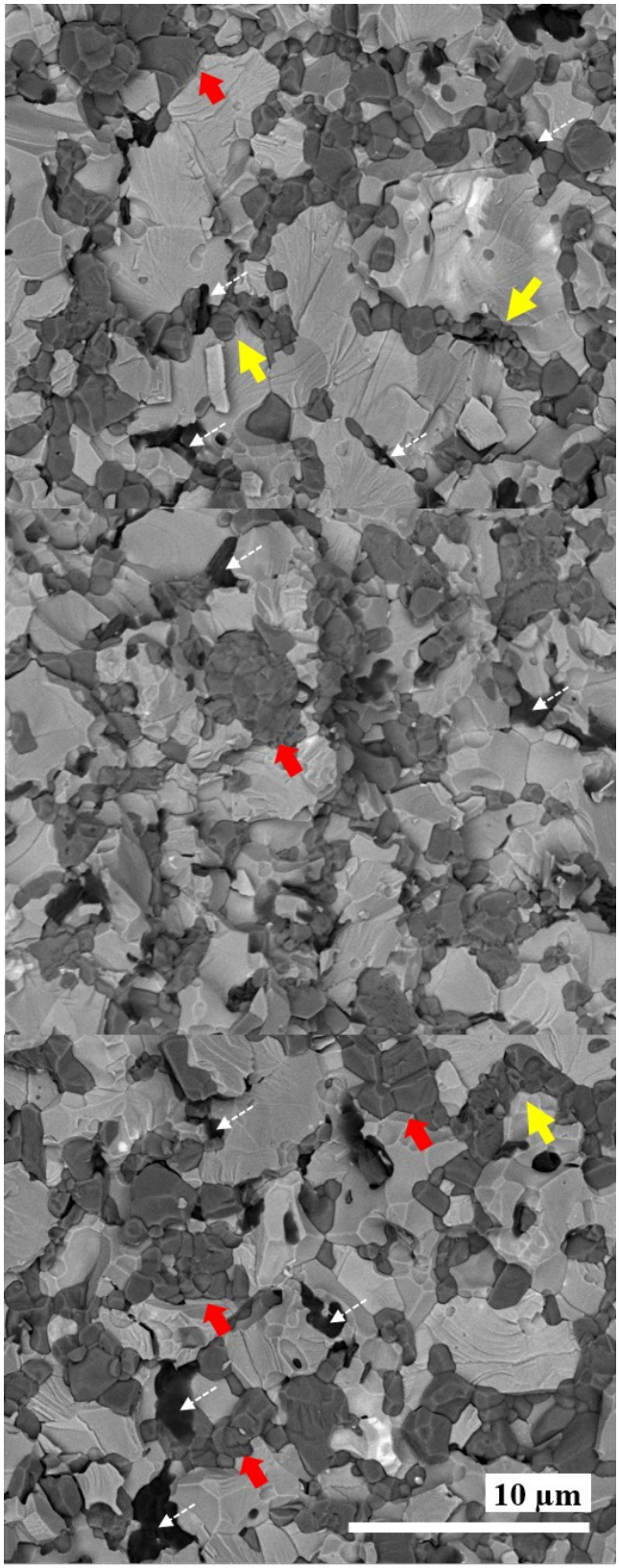

Figure 4.28 Fracture surface BSE SE of TiC-30%SiC showing the SiC grain distribution. Note: the yellow arrows indicate SiC grains at TiC grain boundaries, the red arrows indicate a group of SiC grains, and the white arrows indicate micro-pores

Additionally, micron SiC grains dispersed in the TiC grain matrix were observed. SEM images of TiC-30%SiC fracture surfaces were randomly taken in several areas and merged into one image as shown in Figure 4.28 to maximise the amount of information. Most of the micron size SiC grains were located in clusters. These were either in between the larger sized TiC grains, as indicated by the yellow arrows, or as a general agglomerate, as indicated by the red arrows. Internal micro-pores, as indicated by the white arrows, were distributed across the entire the specimen. A number of secondary cracks could be seen branching off from the primary crack.

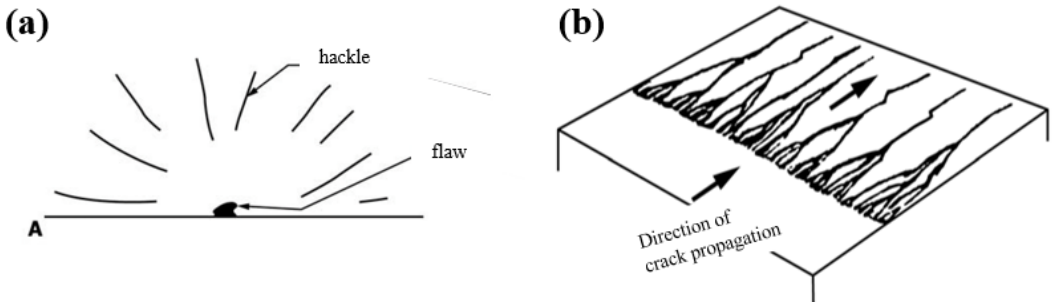

Figure 4.29 Schematic diagrams illustrating transgranular cracking patterns: (a) hackle and (b) twist hackle or 'river' pattern [118, 138]

Two fracture modes were observed, namely, intergranular fracture (IG, along the grain boundaries), and transgranular fracture (TG, through the grains) for both the TiC-50%SiC and TiC-30SiC composites. The fracture surfaces of the IG were smooth and allowed the grain shape to be seen. Intergranular fracture also allowed the second phase at grain boundaries to be seen. In contrast, the TG fracture or 'cleavage fracture' forms when the crack front moves for one plane to another, so it leaves feature markings such as step cleavage, hackle and twist hackle [118, 138]. The hackle is lined on the crack surface running in the local direction of cracking being non-coplanar portions of the crack surface as shown in Figure 4.29a [118, 138]. Twist hackle known as "river" markings results from the propagation crack deflecting onto parallel planes in local, adjacent regions along the crack front as shown in Figure 4.29b [118, 138].

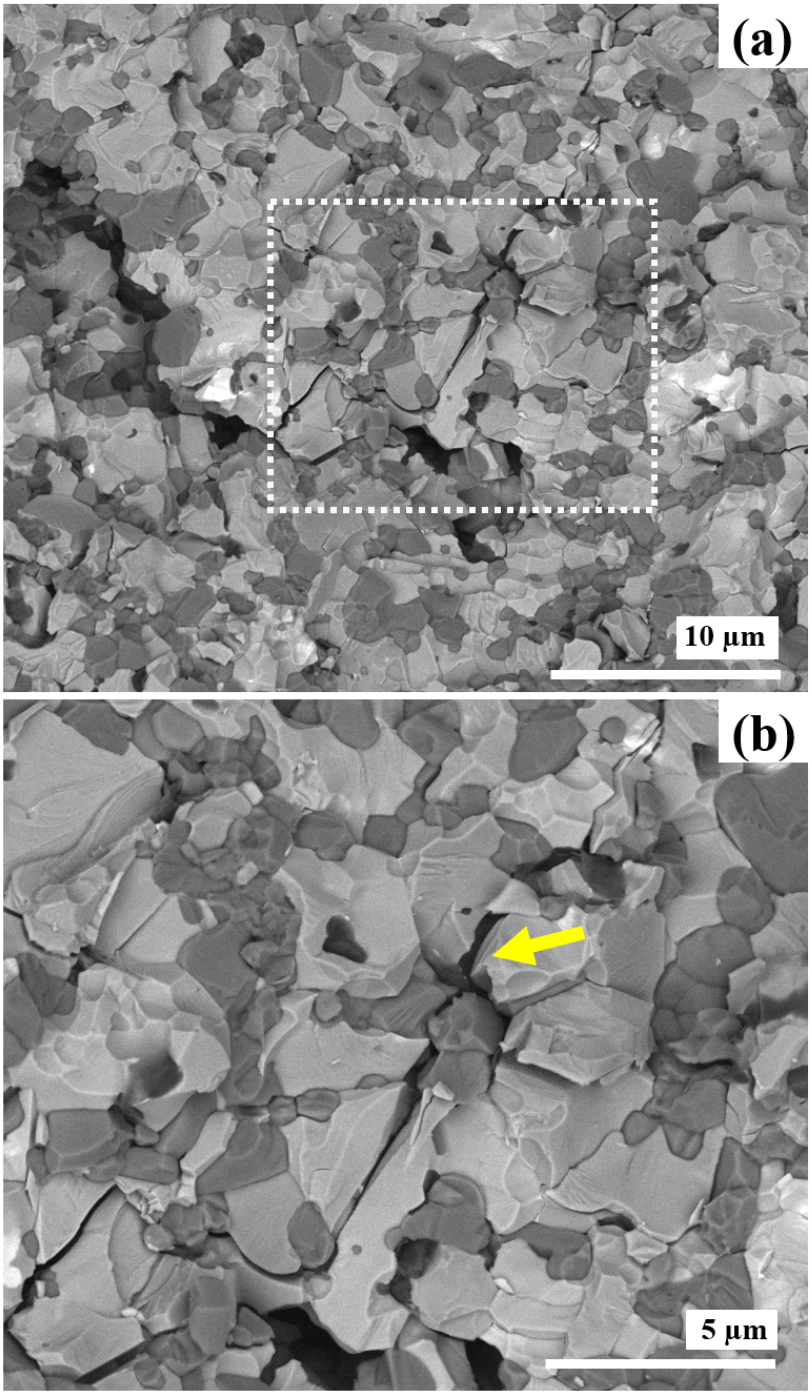

Figure 4.30 Fracture surface BSE SEM of TiC-30%SiC illustrating a cracking line from the three-point bend test

Figure 4.30a shows the crack of the TiC-30%SiC composite. As shown in Figure 4.30b most of the large TiC grains failed via transgranular fracture and exhibited rough fracture facets. However, there was also some IG fracture associated with the TiC grains, typically with the smaller grains. High magnification SEM images were taken to get more information about

the fracture paths and the microscale mechanism of cracking. Extensive IG cracking predominantly associated with the SiC grains can be seen in Figure 4.31a, indicated by the red arrows. This allowed the SiC grain morphology to be seen clearly, with both equiaxed and elongated grain shapes observed. Extensive TG fracture can also be seen in Figure 4.31b, primarily associated with the TiC. The cleavage facets were associated with river lines or 'twist hackle' of crack propagation (the white arrows). This allowed the crack propagation direction to be identified and the point at which the crack propagated from one grain to another to be seen. One such example is shown in Figure 4.31b where the start of the cleavage facet can be seen to be associated with a micro-void, indicated by the yellow circle. Significant cleavage steps were observed, identified by the black arrows.

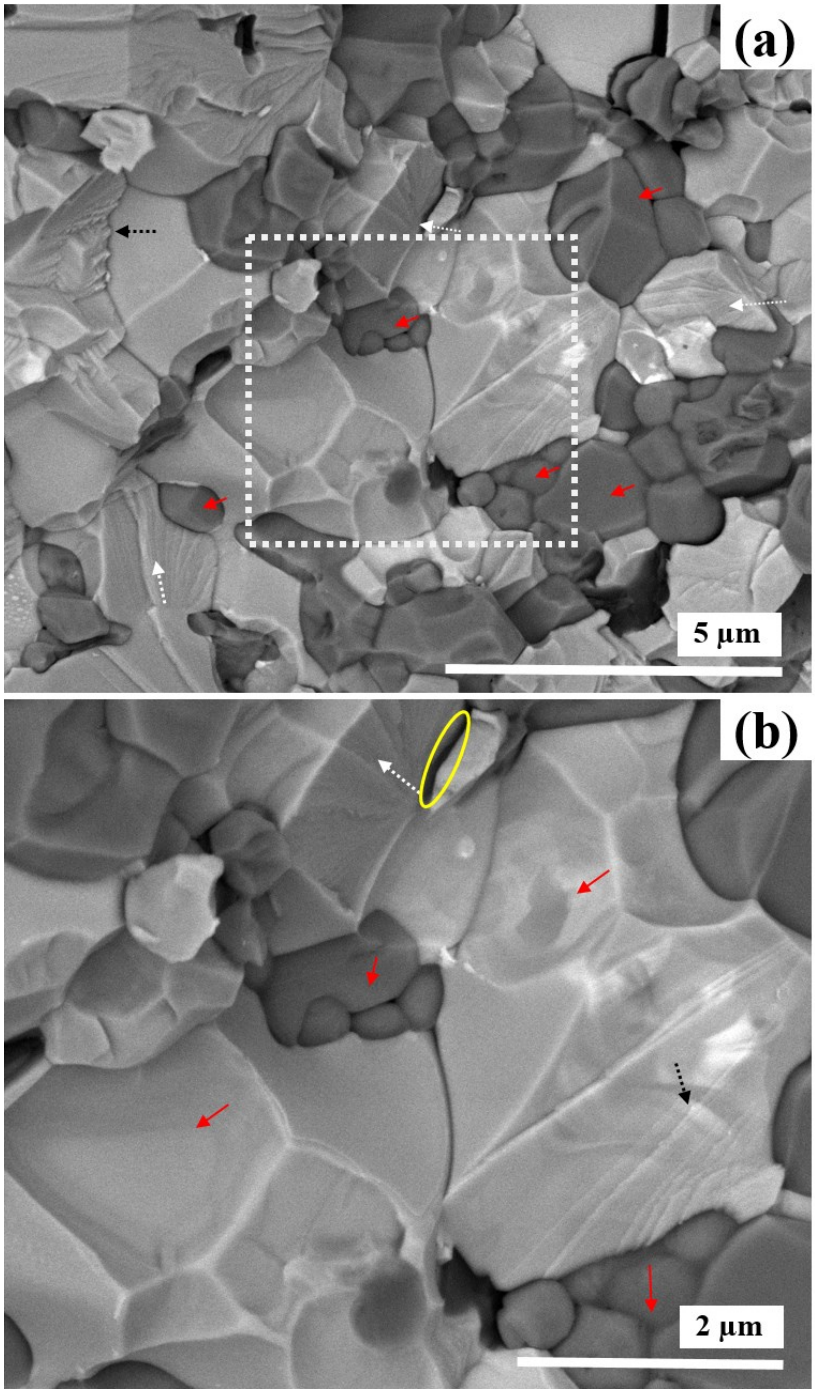

Figure 4.31 Fracture surface BSE SEM of TiC-30%SiC illustrating the IG fracture (indicated by the red arrow) and the TG fracture

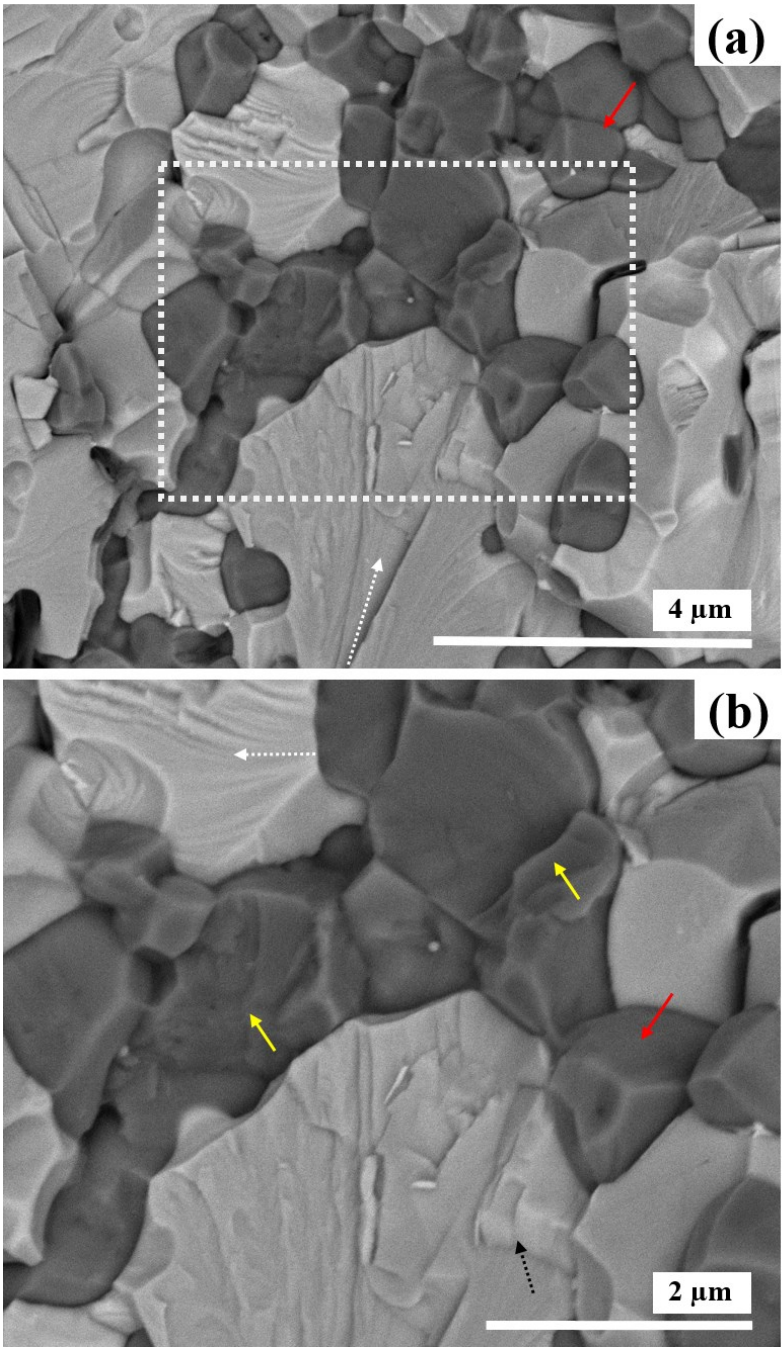

Figure 4.32 Fracture surface BSE SEM of TiC-30%SiC illustrating the TG cracks in TiC and SiC grains as indicated by the yellow arrows

Figure 4.32a also shows the river pattern in a large TiC grain as indicated by the white arrow. Similarly, there was the TG fracture in SiC grains as well indicated by the yellow arrows in Figure 4.32b.

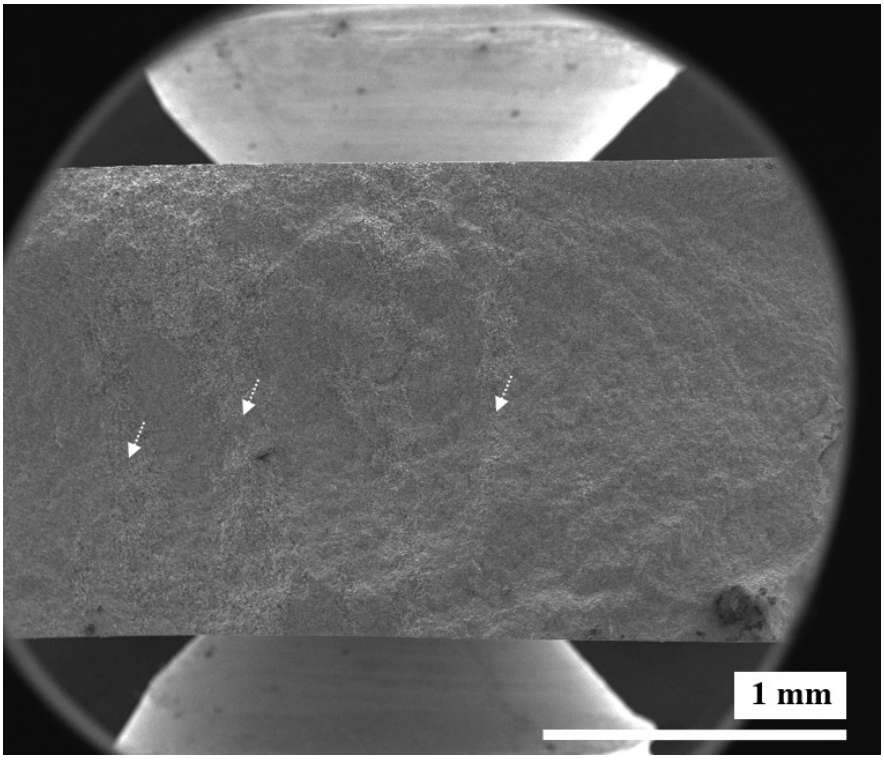

Figure 4.33 Fracture surface BSE SEM micrographs illustrating the macroscopic cracked surface of TiC-50%SiC

As mentioned in Section 4.2.2, TiC-50%SiC morphology consisted of the large grain zones of TiC/SiC dispersed in the small grain zones of TiC/SiC. Figure 4.33 shows a macroscopic and microscopic SEM image of TiC-50%SiC. The macroscopic fracture surface of TiC-50%SiC was smoother compared to the TiC-30%SiC in that the crack surface was in alignment with the loading direction in the three-point bend test. As can be seen in Figure 4.33, the ridges of the large TiC/SiC grain zones, as indicated by the white arrows, were observed where crack branching tended to propagate along the interfaces of the large and small TiC/SiC grain zone, which may have acted as local stress fields.

Figure 4.34a shows the interfaces between the large and small grain zones (the dashed line). Figure 4.34b shows the fracture surface of small grain zone where the IG fracture dominated in SiC grains. Figure 4.34c shows the fracture surface of the large grain zone where most of the SiC and TiC grains failed by TG fracture as can be seen from the cleavage facets. Extensive secondary micro-cracking was observed at the grain zone interfaces which possibly were introduced by differences of thermal mismatch strains between TiC and SiC grains.

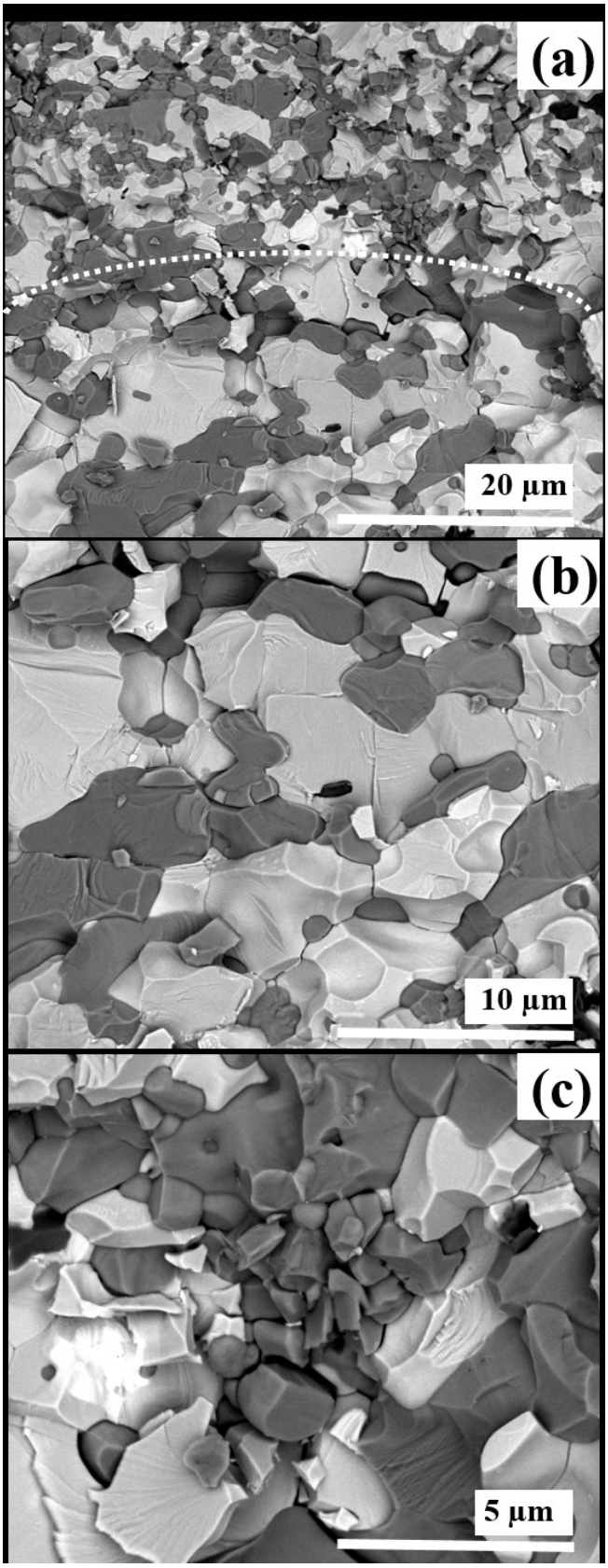

Figure 4.34 Fracture surface BSE SEM of TiC-50%SiC illustrating SiC grain distribution; (a) at the interfaces between a large grain zone an small grain zone, (b) in the large grain zone, and (c) in the small grain zone

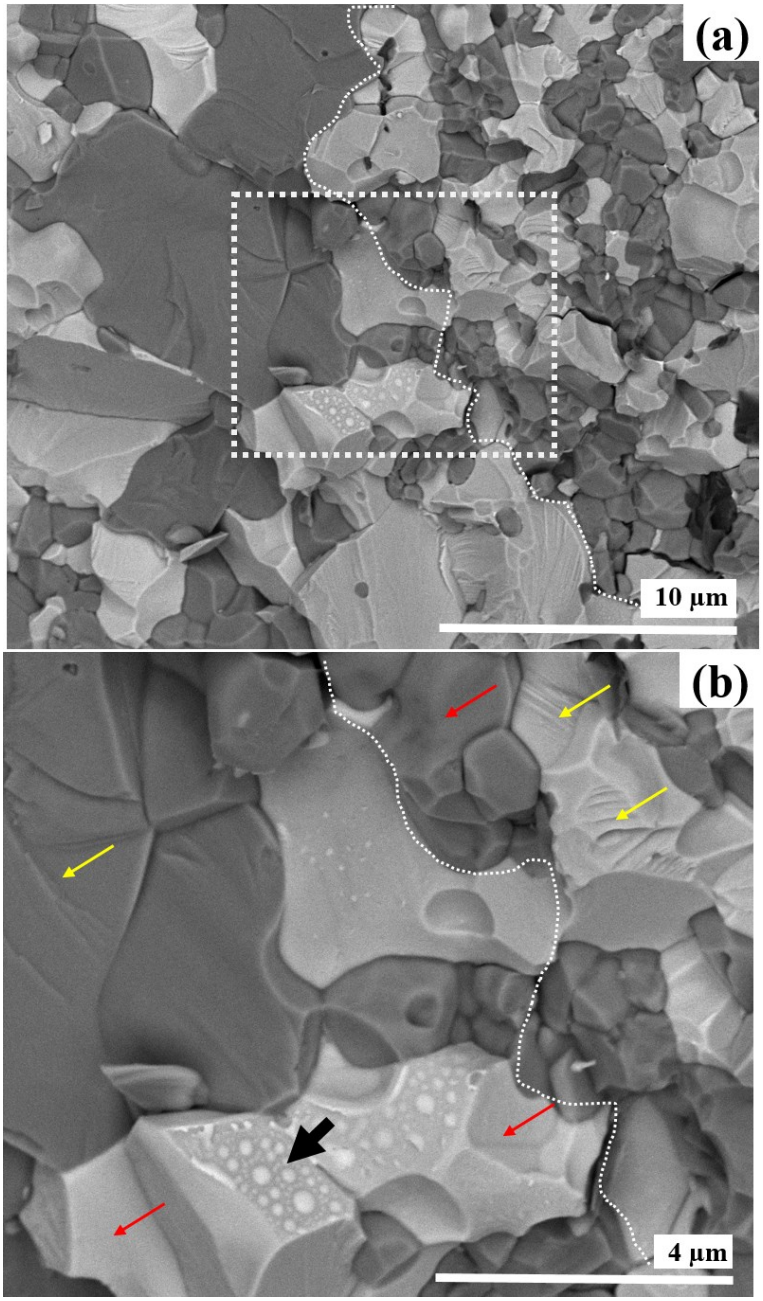

Figure 4.35 Fracture surface BSE SEM of TiC-50%SiC illustrating; the intergranular (indicated by the red arrow), the transgranular (indicated by the yellow arrow) TiC and SiC grains, and glassy phases (indicated by the black arrow) in the large grain zone

Figure 4.35 shows multi-fracture modes in both the coarse grained and fine grained zones of TiC-50%SiC. The yellow arrows point to the TG fracture, and the red arrows indicated the IG fracture. Evidence of glassy phases along the grain boundaries was observed on TiC/SiC and TiC/TiC interfaces which tended to encourage the cracks propagating along grain boundaries indicated by the black arrows.

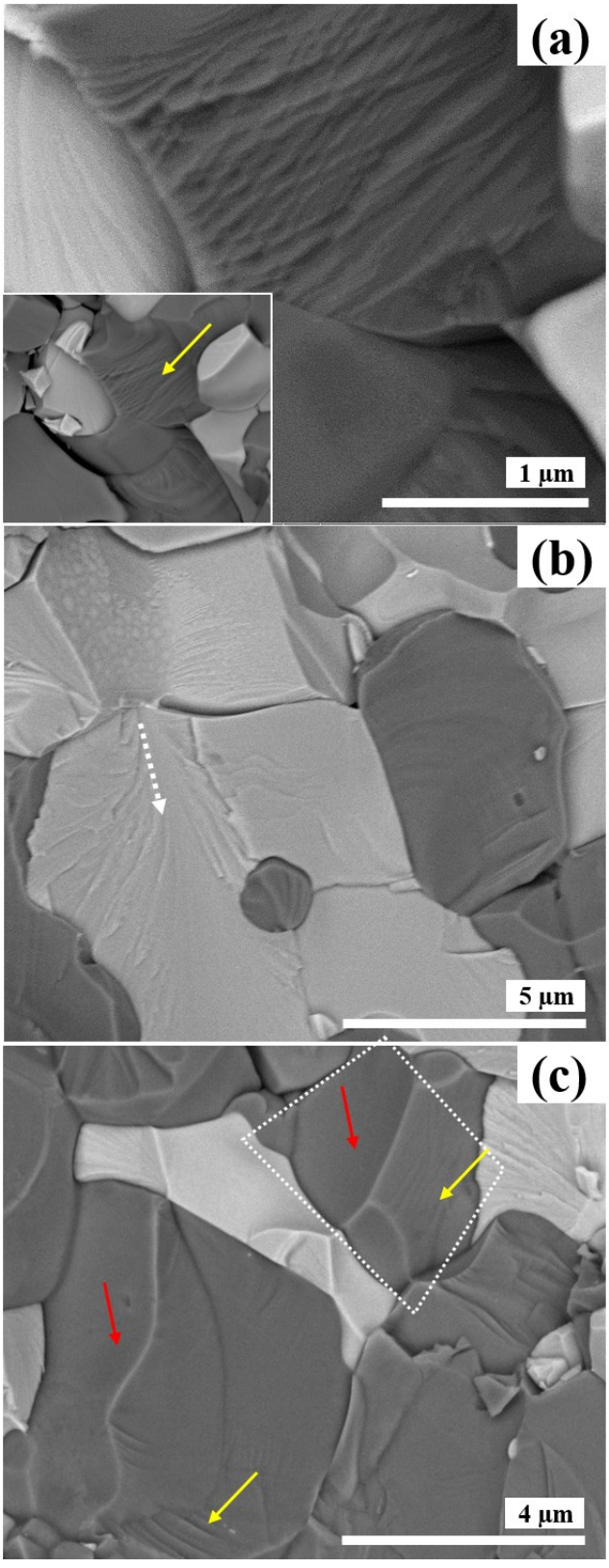

Figure 4.36 Fracture surface BSE SEM of TiC-50%SiC showing the transgranular and intergranular fractures indicated by the yellow arrows and the red arrows, respectively. The white arrow in (b) shows the direction of crack propagation.

Figure 4.36 shows other crack patterns in the SiC grains of TiC-50%SiC. Figure 4.36a shows the twist hackle lines in SiC grains that form a river pattern, with multiple steps in the crack propagation path. Figure 4.36b shows a secondary crack in a large TiC grain which contains an intragranular SiC particle. The crack appears to have originated from the top of this grain and followed hackle lines, and resulted in transgranular propagation through the SiC grain, but also resulting in a secondary crack at the interface between the SiC and the TiC. Figure 4.36c shows large SiC grains (the dashed rectangles) which exhibit both IG and TG in the same grain.

Overall, based on the observed fractographic features, TiC-30%SiC and TiC-30%SiC showed brittle fracture with several crack propagation mechanisms. For the IG fracture, some fracture facets were featureless, whereas some contained glassy phased as the grain boundaries. For the TG fracture, the cleavage surface was dominated by changes in the precise cleavage plane giving characteristic river pattern appearance, presumably as a result of the local microstructure.

4.2.10 Fracture toughness results by precracked bend testing

There are two primary methods used to determine the toughness (K_{IC}) of ceramics; the indentation and a precracked bend test. A series of pre-cracks were introduced into the TiC-30%SiC and TiC-50%SiC specimens using a 10 kg Vickers indentation before the three-point bend testing. The approach to calculating the K_{IC} was explained in Chapter 3. The K_{IC} and specimens details of TiC-30%SiC from the bend tests is shown in Table 4.5.

Table 4.5 Summary of the calculated K_{IC} of precracked TiC-30%SiC beams from the three-point bend test and the specimen sizes

TiC-30%SiC samples	**K_{IC} (MPa. √m)**	**Precrack length (µm)**	**Thickness (mm)**	**Width (mm)**
1	6.9	348 ± 47	1.6	5.0
2	7.3	354 ± 125	1.6	4.2
3	6.9	292 ± 44	1.6	3.0
4	7.4	374 ± 36	1.6	3.0
5	5.9	327 ± 69	1.6	4.0
Avg. K_{IC}	6.9 ± 0.6			

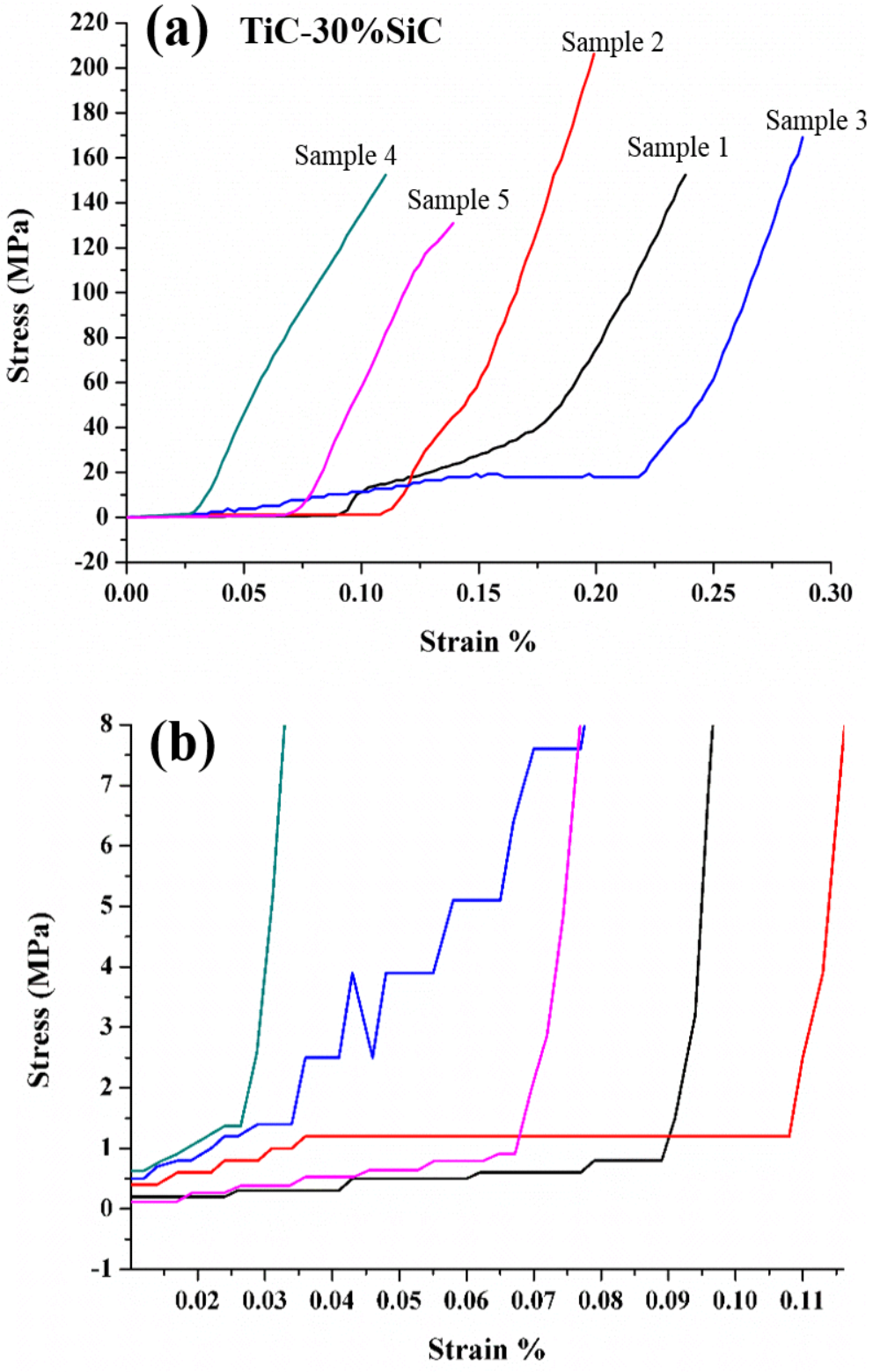

Figure 4.37 (a) Stress-strain curve of precracked TiC-30%SiC and (b) a plot at low strains

An average precrack size was measured in order to calculate the K_{IC} from Equation 3.8, as shown in Table 4.5. The K_{IC} of TiC-30%SiC and TiC-50%SiC were 6.9 ± 0.6 and 6.4 ± 0.9 MPa.√m, respectively, from the bend tests shown in Table 4.5 and Table 4.6. Although the K_{IC} from the indentation method was consistently higher than the bend test, the trend in toughness measurements was in good agreement. Both bend test results and indentation found no statistically significant differences in the K_{IC} of TiC-30%SiC and TiC-50%SiC composites.

The stress-strain curves from the precracked TiC-30%SiC specimens are shown in Figure 4.37. Notably, TiC-30%SiC flexural strain (Figure 4.37) was more than that of TiC-50%SiC (Figure 4.39). The precracks were characterised by SEM after the bend test. Figure 4.38a and b show SEM images of the multiple Vickers indentation on TiC-30%SiC specimens. The precrack surfaces exhibited a corrugated structure. Figure 4.38c shows that radial cracks with ~ 500 μm in diameter formed underneath the indents. Coarse hackles were clearly observed, which associated with a change in a crack direction and was utilised to identify precrack boundaries.

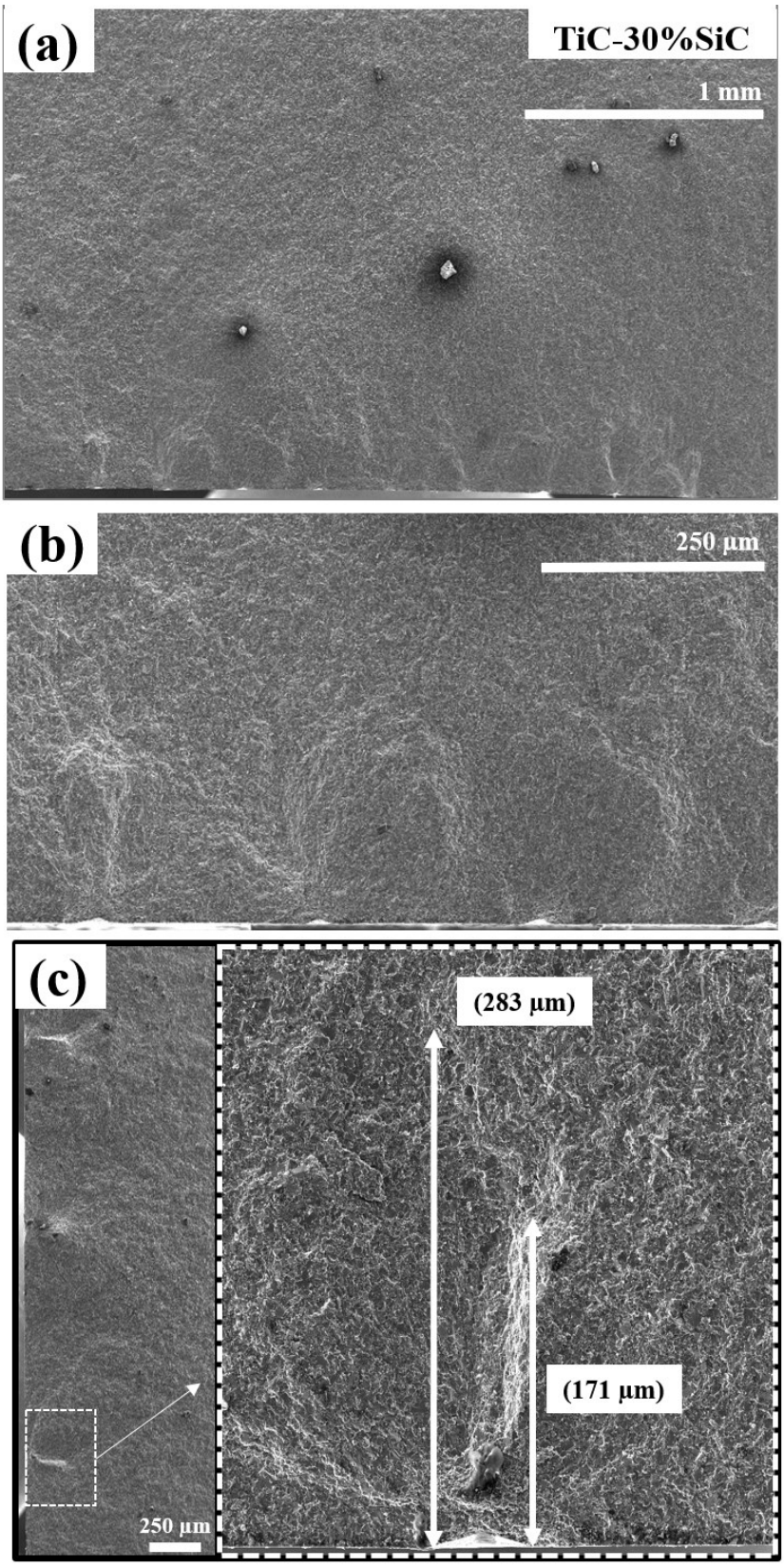

Figure 4.38 Vickers indented precracks in TiC-30%SiC at (a-c) increasing magnifications

Table 4.6 Summary of the calculated K_{IC} of precracked TiC-50%SiC beams from the three-point bend test and the specimen size

TiC-50%SiC samples	K_{IC} (MPa. √m)	Precrack length (µm)	Thickness (mm)	Width (mm)
1	6.9	276 ± 30	2.0	5.0
2	7.3	253 ± 46	2.7	3.6
3	6.7	249 ± 64	2.5	4.0
4	5.7	224 ± 33	1.7	3.9
5	5.2	216 ± 31	2.0	4.0
Avg. K_{IC}	6.4 ± 0.9			

Figure 4.40a and b show the precrack series in the TiC-50%SiC with a ridged texture. Additionally, Figure 4.40c shows an indented crack. The ridge formed during the crack realignment to the plane of maximum stress showing slightly different contrast to the rest of the fracture surface can be seen clearly in TiC-50%SiC compared to TiC-30%SiC. The diameter of median crack was about 500 µm, similar to TiC-30%SiC.

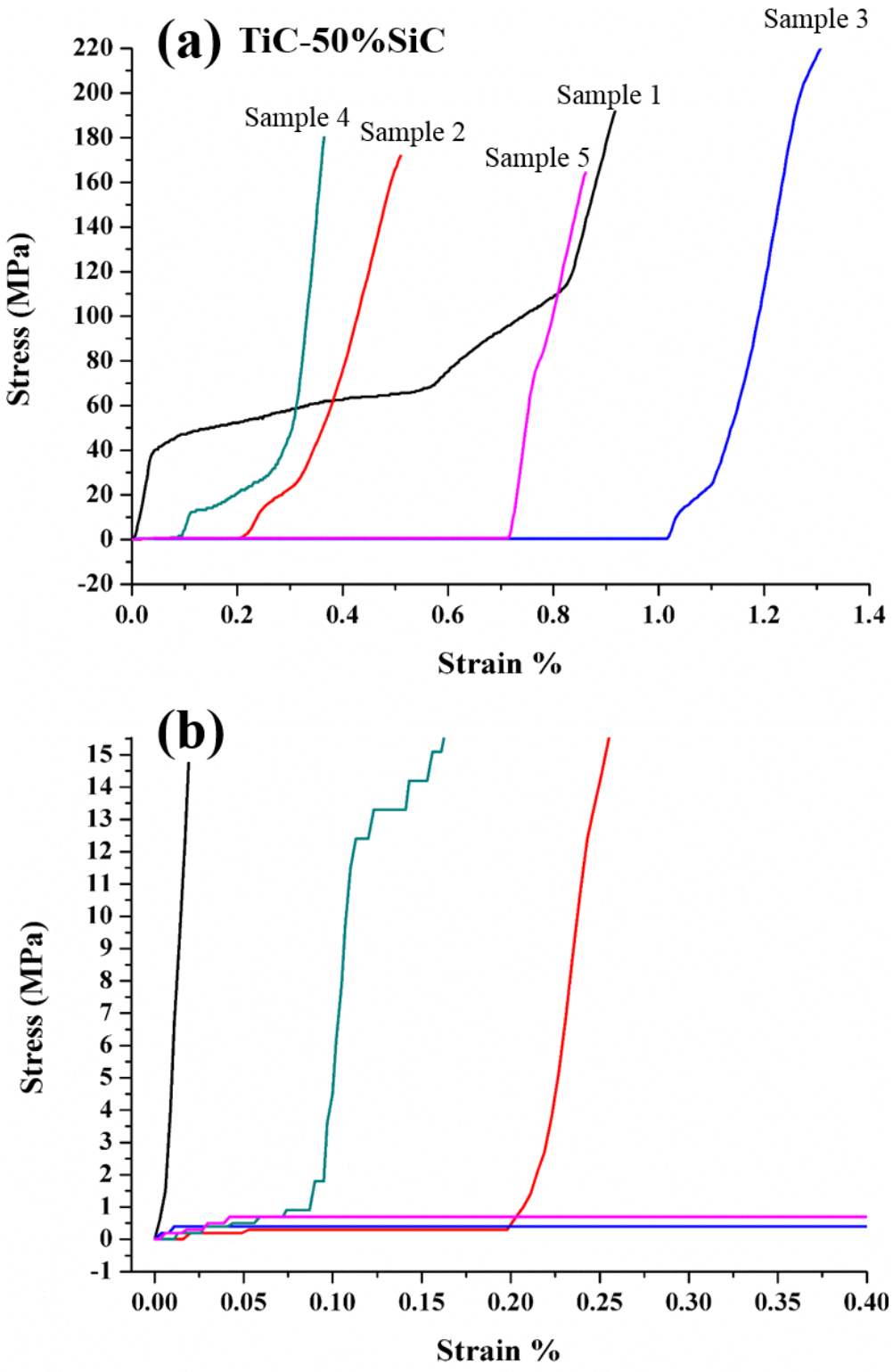

Figure 4.39 (a) Stress-strain curve of precracked TiC-50%SiC and (b) a plot at low strain

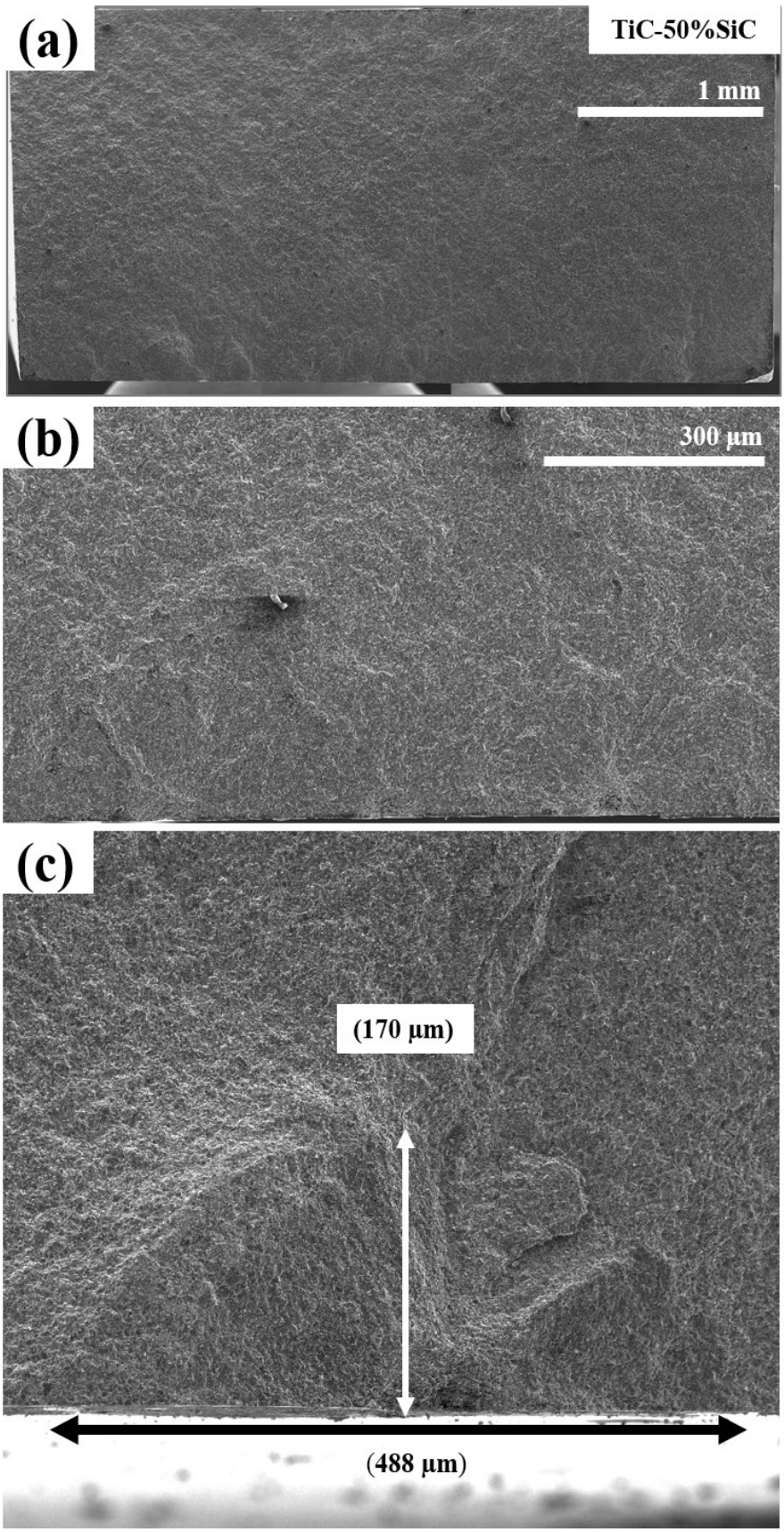

Figure 4.40 Vickers indented precracks in TiC-50%SiC at (a-c) increasing magnification

4.3 Results of ZrC-SiC composite characterisation

ZrC-SiC composites were prepared by SPS at 2100 °C based on the SPS temperature optimisation in Section 4.1. The characterisation results will be explained in this section.

4.3.1 Density results

Table 4.7 shows the relative density of ZrC-SiC composites with a variable mole ratio of β-SiC. The relative density of the ZrC-50% SiC, ZrC-30% SiC relative and ZrC were similar.

Table 4.7 The relative density of SPSed ZrC-SiC composites (at 2100 °C) with various mole ratio of β-SiC starting powder

Sample codes	SiC (% mole)	% Relative Density
ZrC-50% SiC	50	98 ± 0.2
ZrC-30% SiC	30	97 ± 0.2
ZrC	0 (ZrC)	98 ± 0.4

4.3.2 XRD results

Figure 4.41 gives the X-Ray diffraction patterns of ZrC/SiC composites. They mainly consisted of ZrC (ICSD 43370) and β-SiC (3C-SiC, ICSD 24217). However, the peaks of α-SiC (6H-SiC, ICSD 24169, and 4H-SiC, ICSD 24170) confirmed the presence of β/α phase transition. Furthermore, the peaks at 27.25˚ to 32.25˚ were zirconium dioxide (ZrO_2) [22].

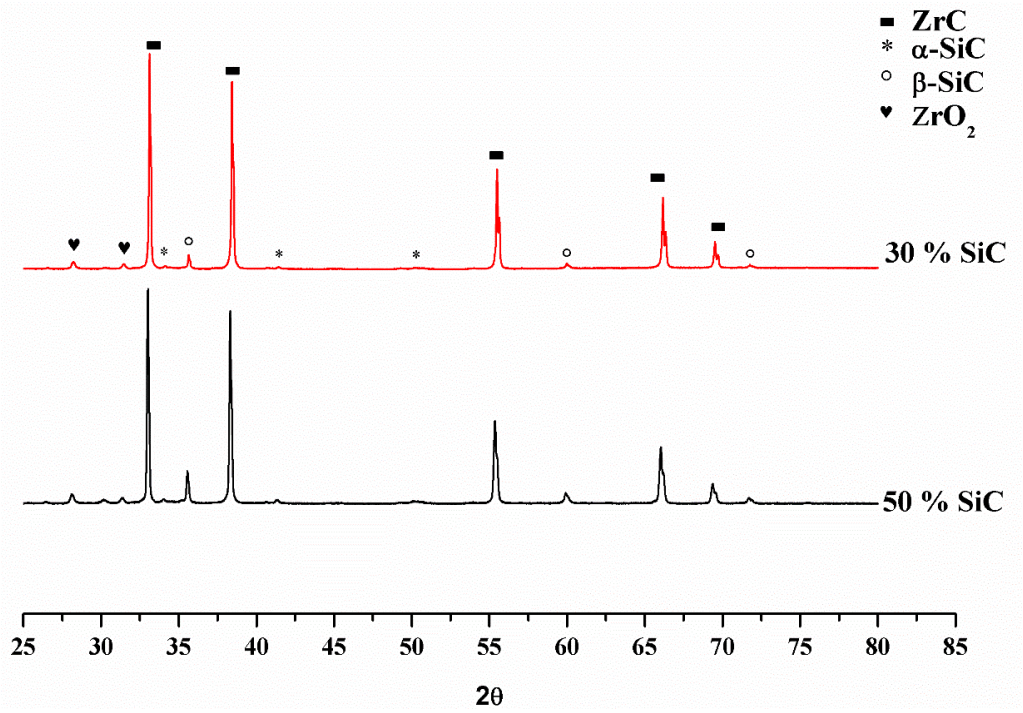

Figure 4.41 X-ray diffraction patterns of ZrC-30% SiC and ZrC-50% SiC

4.3.3 SEM results

Figure 4.42 compares the BSE SEM images of ZrC-50% SiC and ZrC 30% SiC compared to SPSed ZrC. The SiC grains were considerably smaller than the ZrC grains in ZrC-50% SiC and ZrC-30% SiC. The ZrC grain size reduced significantly with the addition of SiC, and further reduced in going from 30% to 50% SiC. Figure 4.44 gives that the average ZrC grain sizes of ZrC-50% SiC and ZrC-30% SiC composites, which were 2.5 and 3.5 μm respectively. Figure 4.43 shows the SEM-EDX mapping of ZrC-30% SiC which the bright contrast represents ZrC grains, and the black contrast was SiC grains.

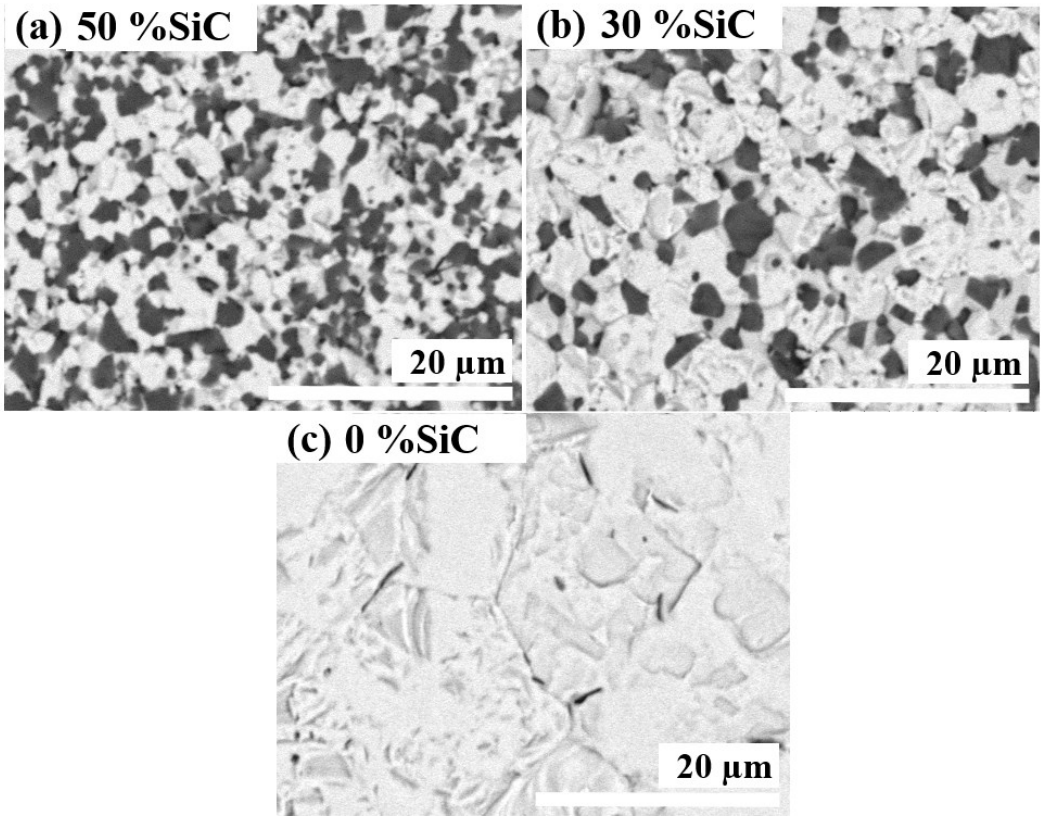

Figure 4.42 BSE SEM images of (a) ZrC-50% SiC, (b) ZrC-30% SiC, and (c) ZrC

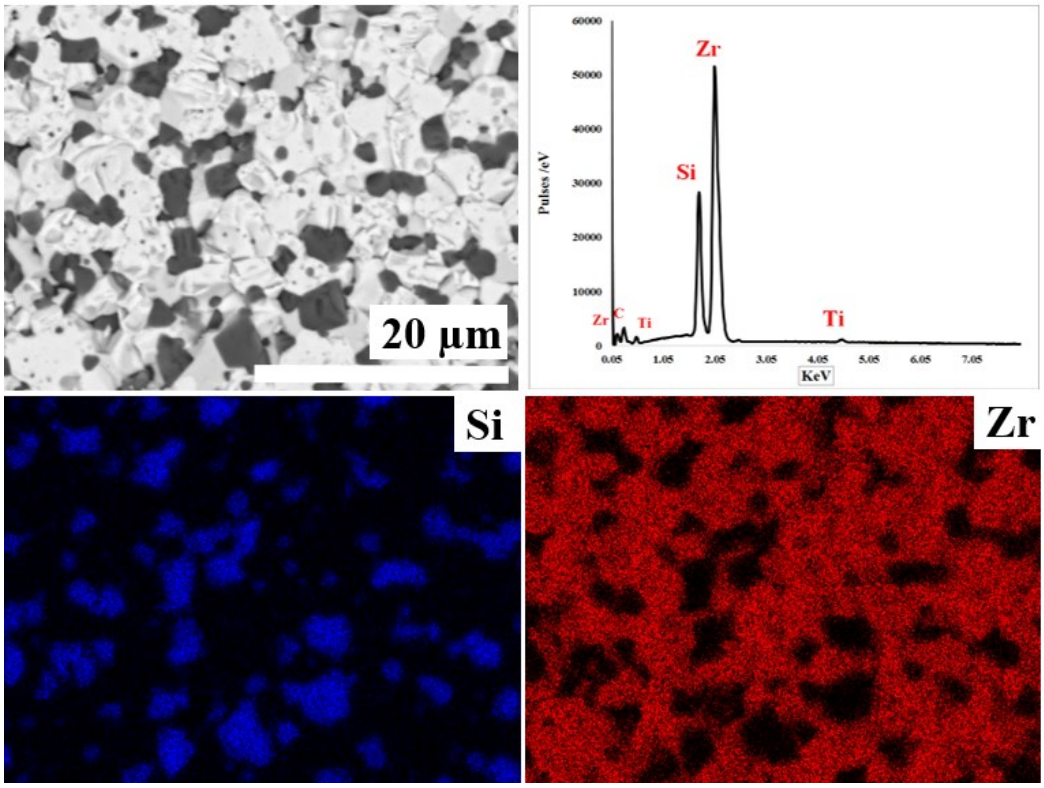

Figure 4.43 SEM-EDX mapping of ZrC-30% SiC

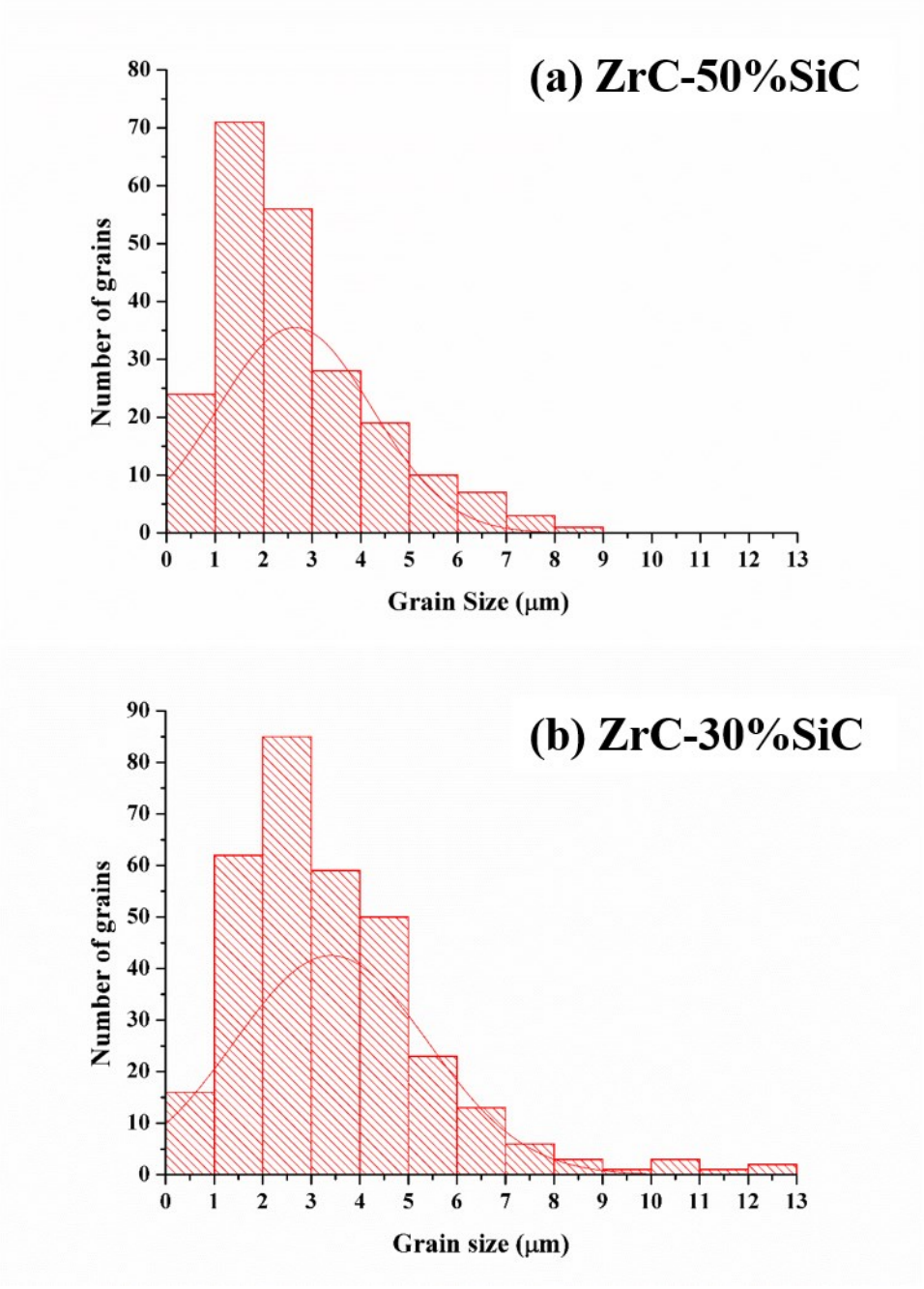

Figure 4.44 the ZrC grain size distribution of (a) ZrC-50% SiC and (b) ZrC-30% SiC

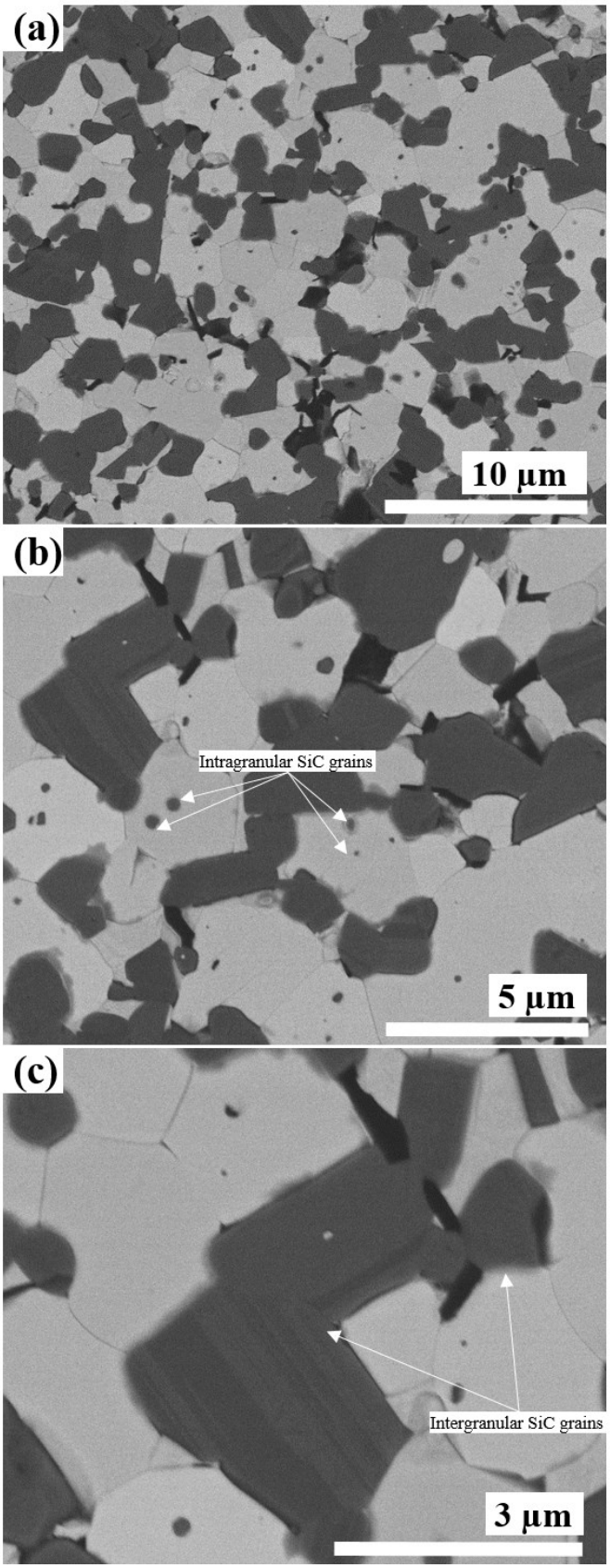

Figure 4.45 the BSE SEM of ZrC-50% SiC at (a) low magnification (b) medium magnification and (c) high magnification

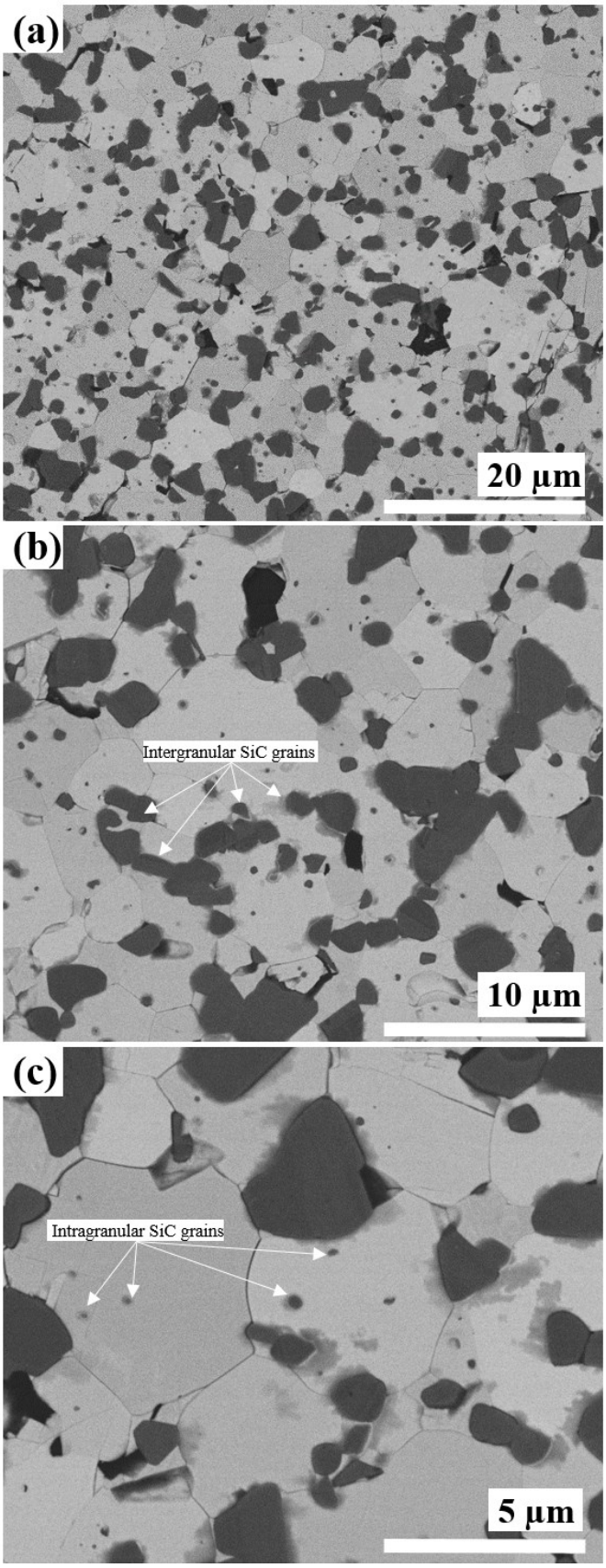

Figure 4.46 the BSE SEM of ZrC-30% SiC at (a) low magnification (b) medium magnification, and (c) high magnification

Figure 4.45a shows the BSE SEM images of ZrC-50% SiC. SiC grains located in two dominant positions: intergranular (Figure 4.45b) and intragranular (Figure 4.45c). The SiC grains were well distributed in the ZrC matrix which exhibited polygonal grain shapes.

Figure 4.46 gives SEM images of ZrC-30% SiC. In contrast to ZrC-50%, SiC volume contents were much less. Similar to ZrC-50% SiC, SiC grains in ZrC-30% SiC were uniformly distributed in the ZrC matrix.

4.3.4 Mechanical property results

Table 4.8 summarises the mechanical properties of ZrC-SiC composites. The Vickers hardness of the ZrC-50% SiC and ZrC-30% SiC were 18 ± 3 GPa and 23 ± 3 GPa, respectively. At 30 mole % SiC showed the highest Vickers hardness among 50% SiC and ZrC. In addition, the fracture toughness (K_{IC}) measured by the indentation method showed that the presence of SiC enhanced the K_{IC} of ZrC-SiC composites. The K_{IC} were 3.6 ± 0.2 and 3.2 ± 0.3 MPa √m for ZrC-50% SiC and ZrC-30% SiC, respectively, whereas ZrC and SiC was 1.1 MPa √m [79] and 2.6-3.4 MPa √m [46], respectively.

Table 4.8 Summary of the Vickers hardness and the fracture toughness (K_{IC}) of ZrC-SiC composites with the various SiC contents

Sample code	SiC (% mole)	Vickers hardness (GPa)	K_{IC} (MPa. √m)
ZrC-50% SiC	50	18 ± 3	3.6 ± 0.2
ZrC-30% SiC	30	23 ± 3	3.2 ± 0.3
ZrC	0 (ZrC)	19 ± 2	1.1 [79]

In addition, the surfaces containing Vickers indentation at 5 kg were investigated by SEM. Figure 4.47 shows the cracking paths of ZrC-50% SiC. Cracks travelled along grain boundaries and then deflected when interacting with SiC grains. The crack lines were tortuous (indicated by the dashed yellow lines). Therefore, the crack propagation required more energy to pass through. Consequently, ZrC-50% SiC was tougher than the monolithic material. Figure 4.48 represented the cracking paths of ZrC-50% SiC which exhibited similar intergranular cracking to ZrC-50% SiC. Furthermore, crack branching was observed when the crack interacted with a group of SiC grains as shown in Figure 4.48b.

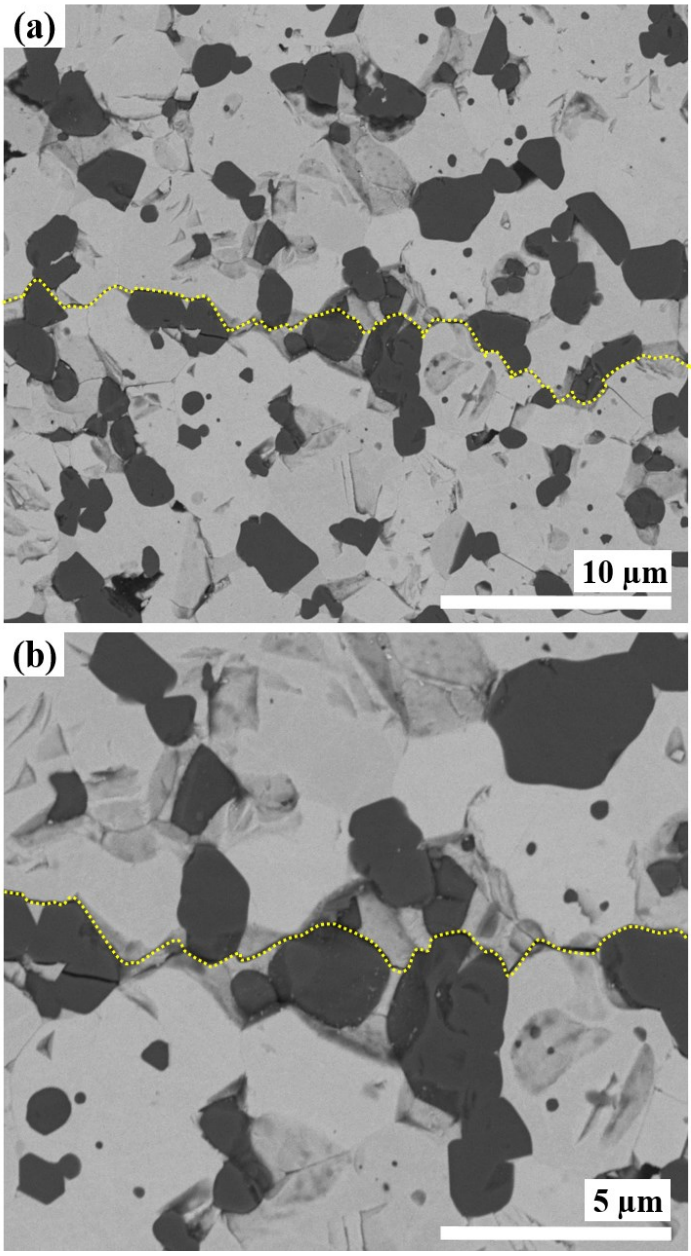

Figure 4.47 BSE SEM images illustrating the cracking paths of ZrC-50% SiC at (a) low magnification and (a) high magnification

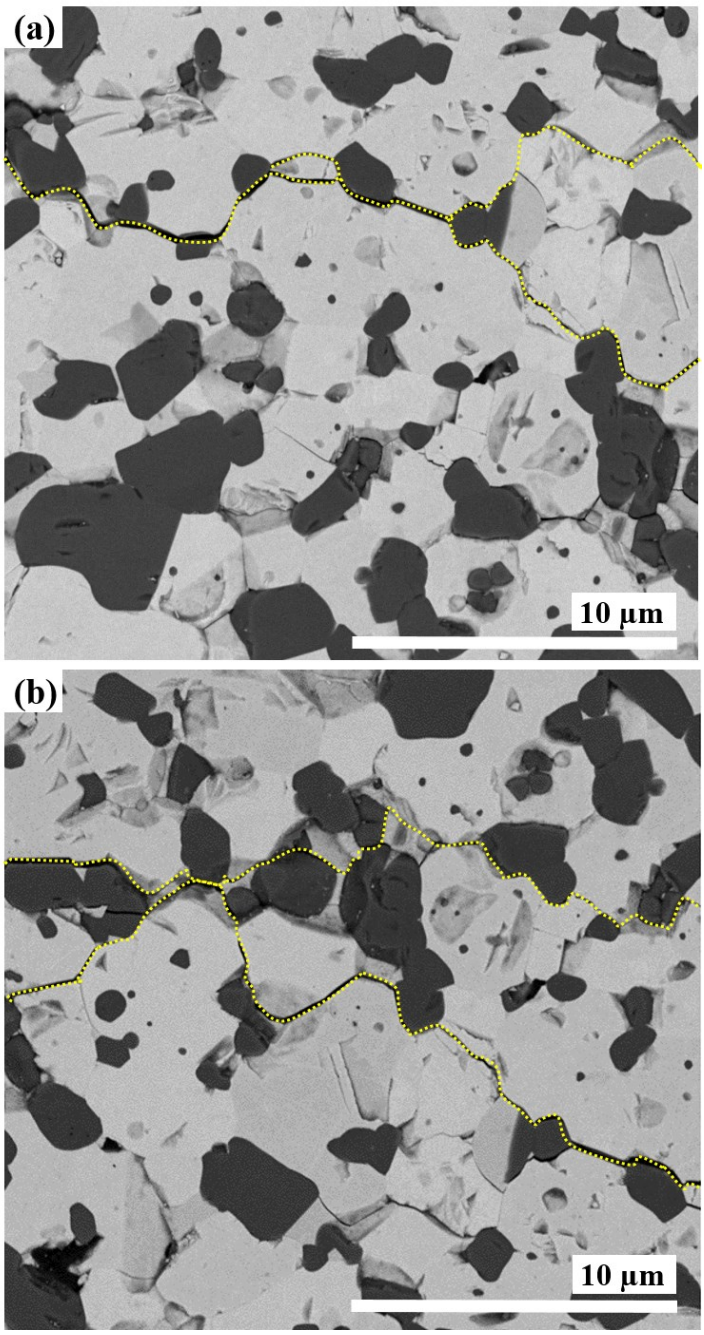

Figure 4.48 BSE SEM images illustrating the cracking paths of ZrC-30% SiC at (a) low magnification and (a) high magnification which represents the crack branching

4.3.5 Fracture surface SEM results

Figure 4.49 shows the stress-strain curves of ZrC-50% SiC and ZrC-30% SiC obtained from the three-point bend test. The ZrC-50% SiC exhibited significantly higher flexural stress than that of the ZrC-30% SiC. This may have been a result of many different microstructural features such as the SiC distribution, porosity, grain size, residual flaws and residual stresses. However, the Young's modulus of the two materials was not significantly different which was considered by the slope of these plots.

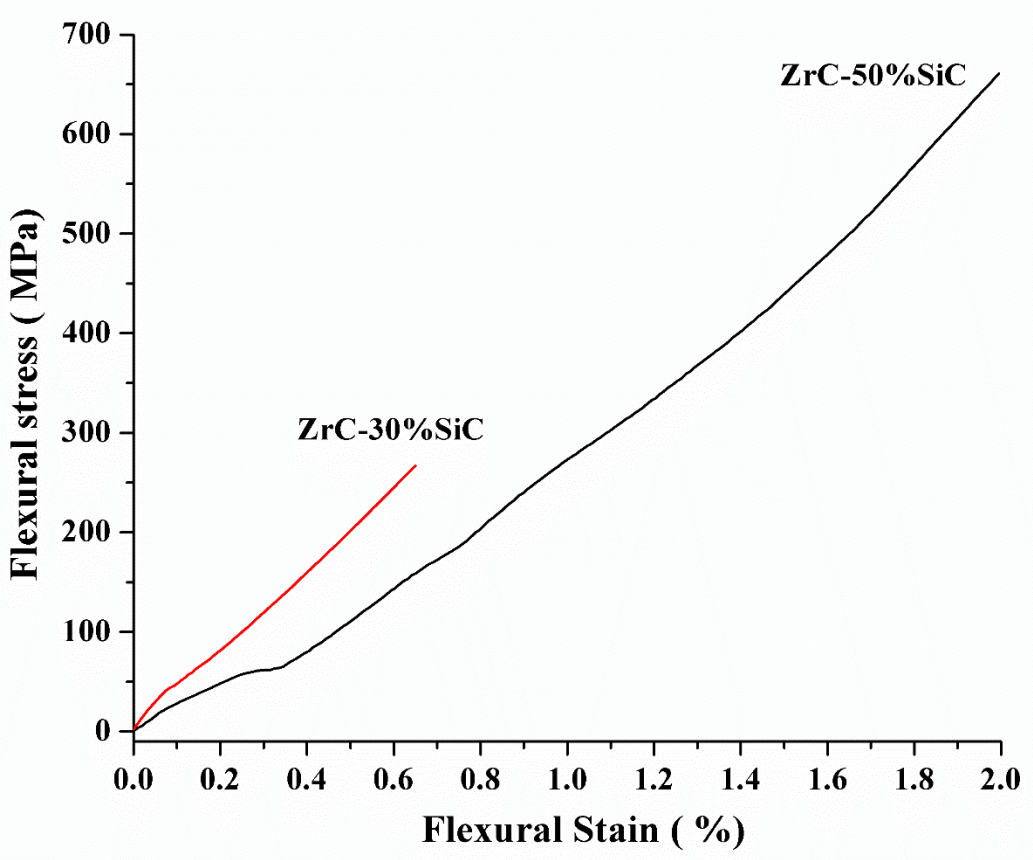

Figure 4.49 Stress-strain curve of ZrC-50% SiC and ZrC-30% SiC conducted by the three-point bend test with 0.24 mm/min loading at room temperature

Figure 4.50 shows a macroscopic SEM image of TiC-50%SiC fracture surface. The cracked surfaces was smooth (a characteristic of brittle fracture). It is in good agreement with the stress-strain curve in that there was no plastic deformation before failure (Figure 4.49).

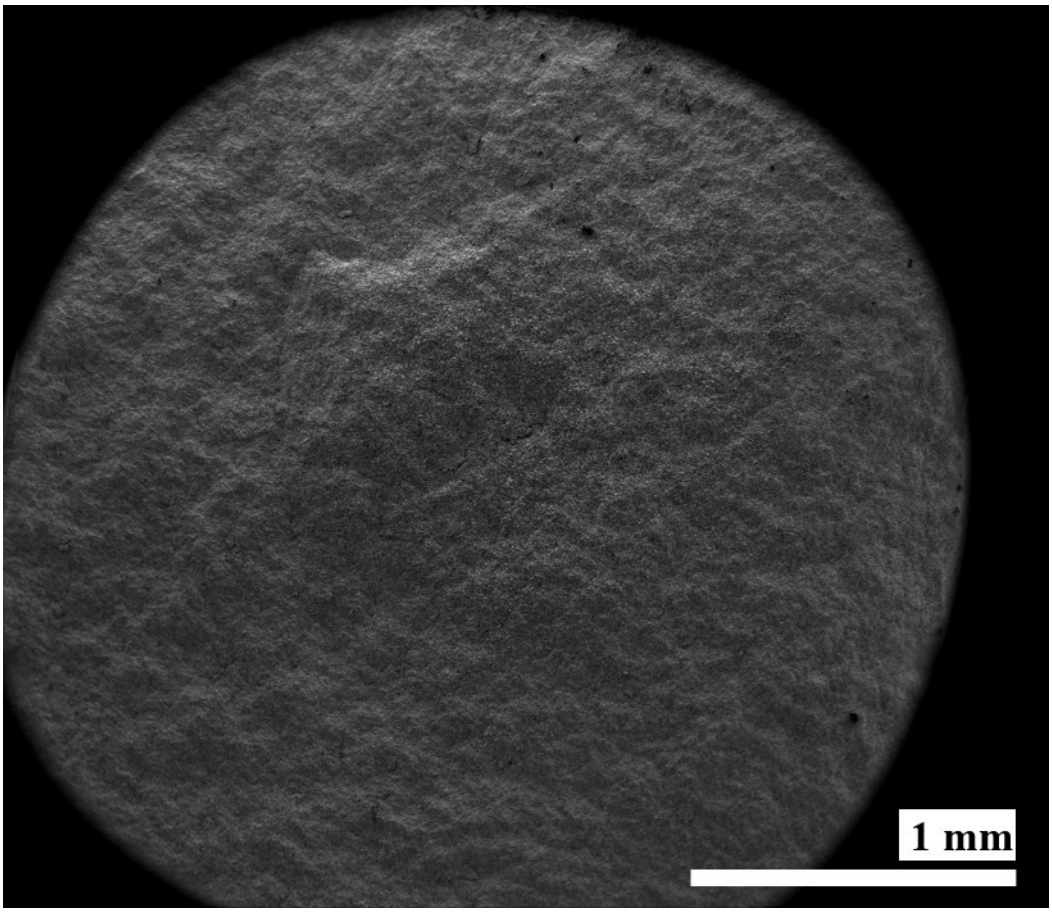

Figure 4.50 Macroscopic fracture surface SEM of ZrC-50% SiC

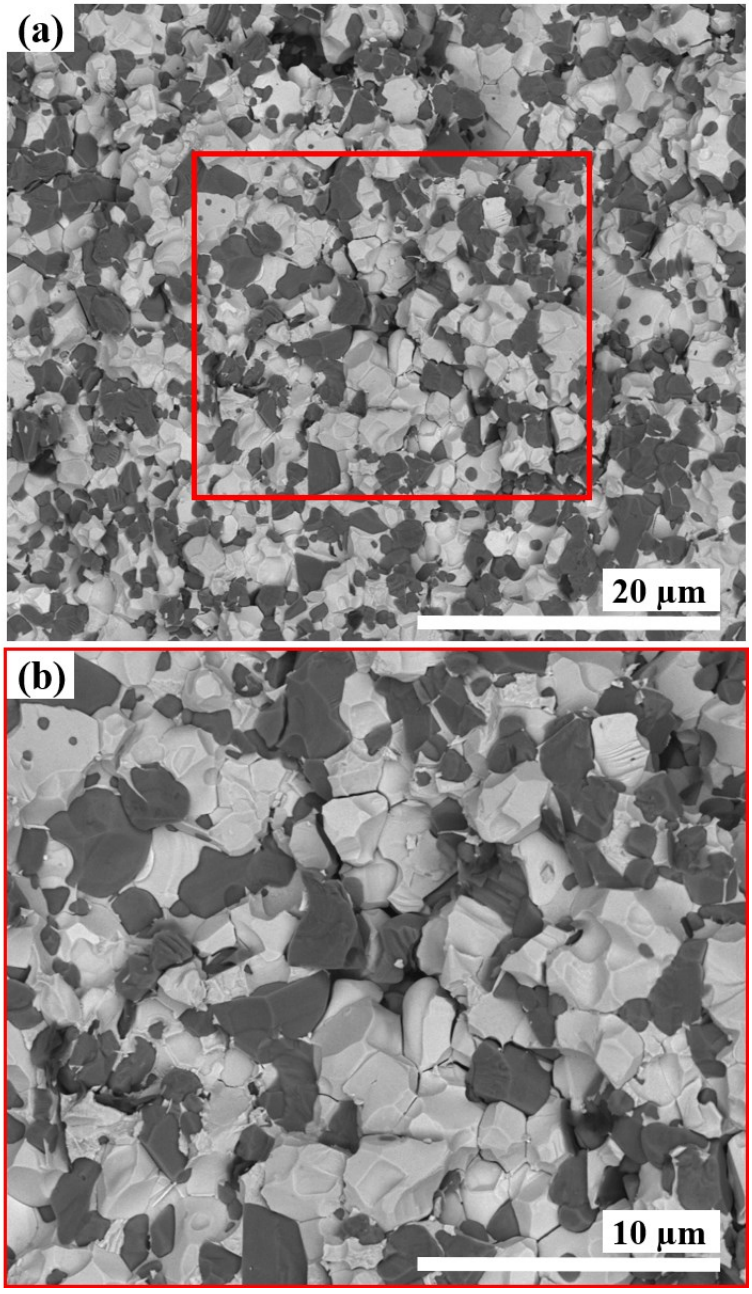

Figure 4.51 Fracture surface BSE SEM of ZrC-50% SiC

Figure 4.51 presents the BSE SEM images of ZrC-50% SiC illustrating the ZrC and SiC grain arrangement. |The SiC and ZrC grains had a uniform distribution. Their grain sizes were not significantly different in this composite. Submicron SiC gains were located within ZrC grains, whereas large SiC grains were located along grain boundaries. There was a mixture of fracture modes in the ZrC-50% SiC. Figure 4.52a shows the TG cracking in SiC and ZrC grains as indicated by the yellow arrows. Notably, cracking was predominantly transgranular for the ZrC and SiC grains larger than approximately 2 µm. However, for small SiC grains (yellow

area in Figure 4.52), IG cracking was observed which left smooth fracture surfaces. Figure 4.52b shows that ZrC filled micro-gaps between SiC grains (the blue arrows). Greater detail of the fracture modes in the ZrC and SiC grains is shown in Figure 4.53. The TG fracture as indicated by the yellow arrows show the river patterns and exhibited terrace-like steps when crossed grain boundaries, which may occur due to the different orientations of neighbouring grains.

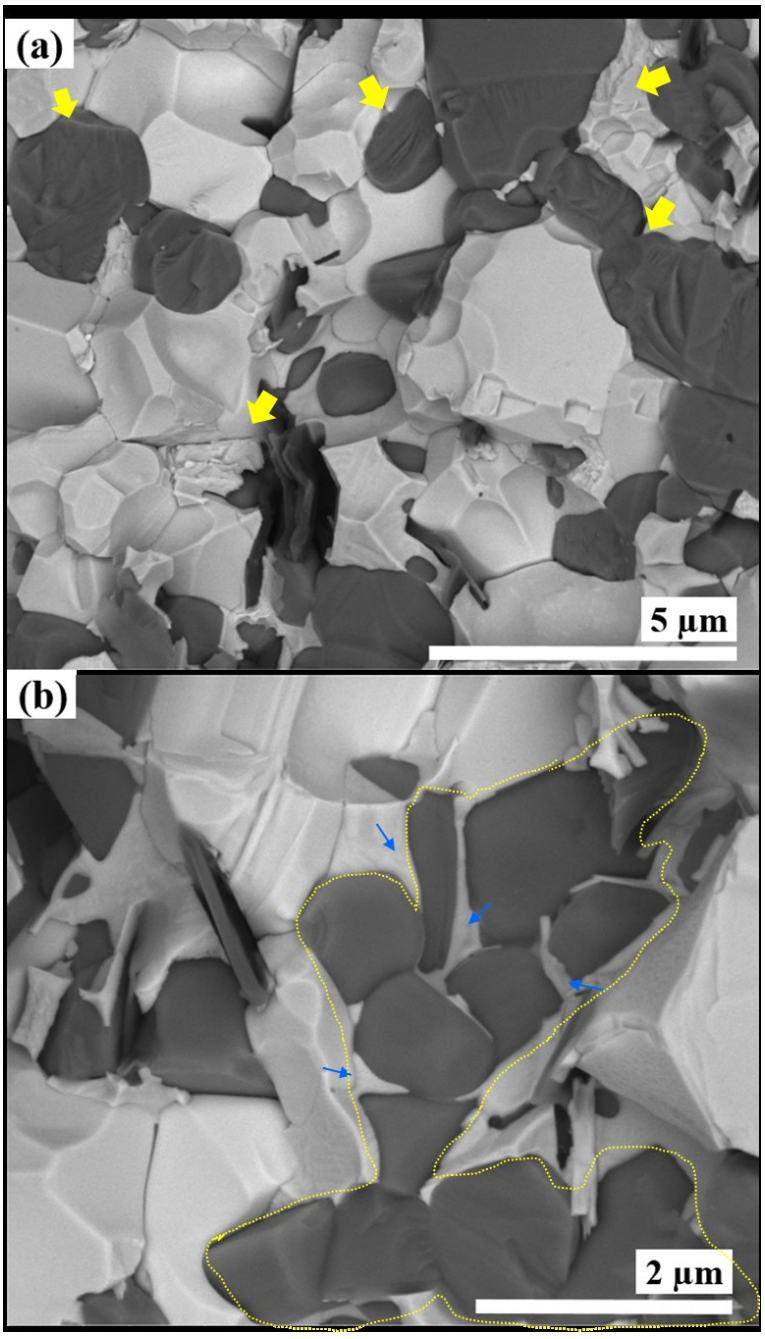

Figure 4.52 High magnification BSE SEM fracture surface of ZrC-50% SiC illustrating (a) TG, and (b) IG cracking in SiC grains

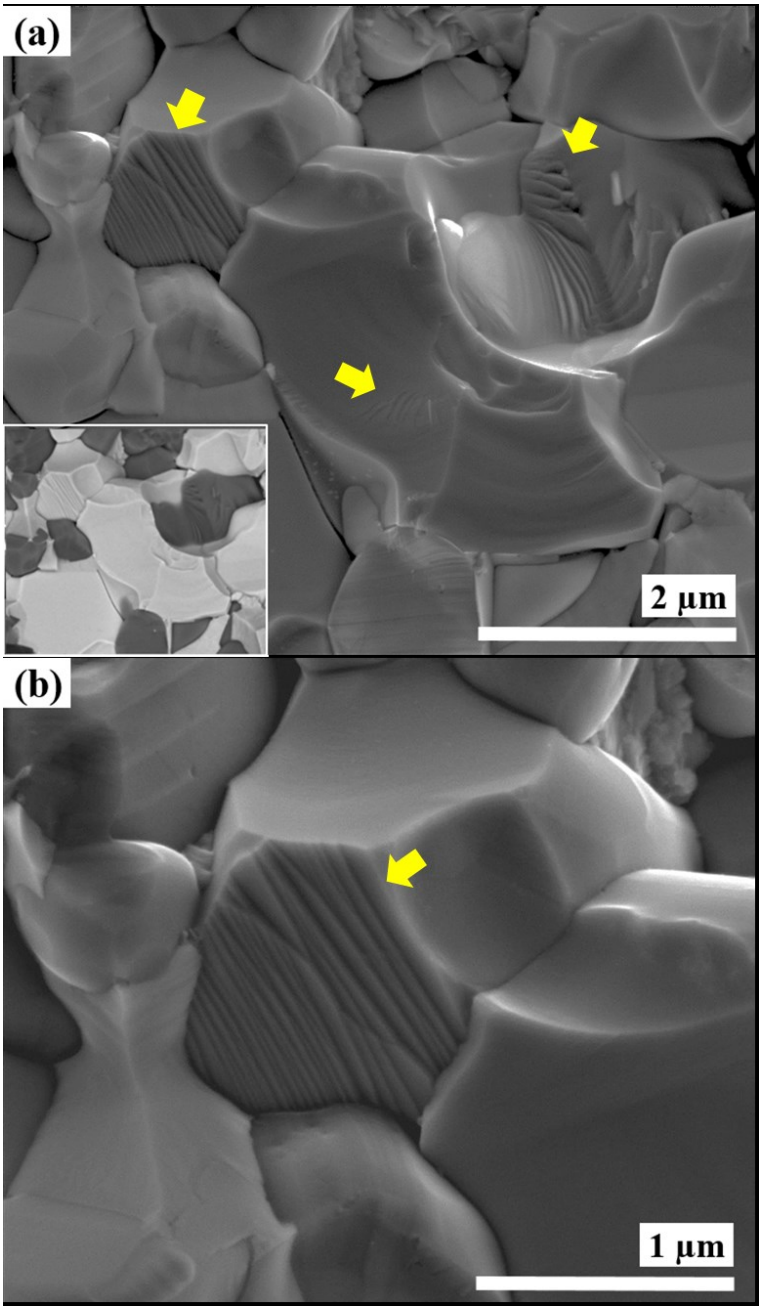

Figure 4.53 High magnification BSE SEM fractural surface of ZrC-50% SiC representing (a) the TG cracking and (b) zoomed in area

Furthermore, Figure 4.54 shows a macroscopic fracture surface SEM image of the ZrC-30% SiC. Similar to ZrC-50% SiC, the fracture surface was a smooth brittle surface.

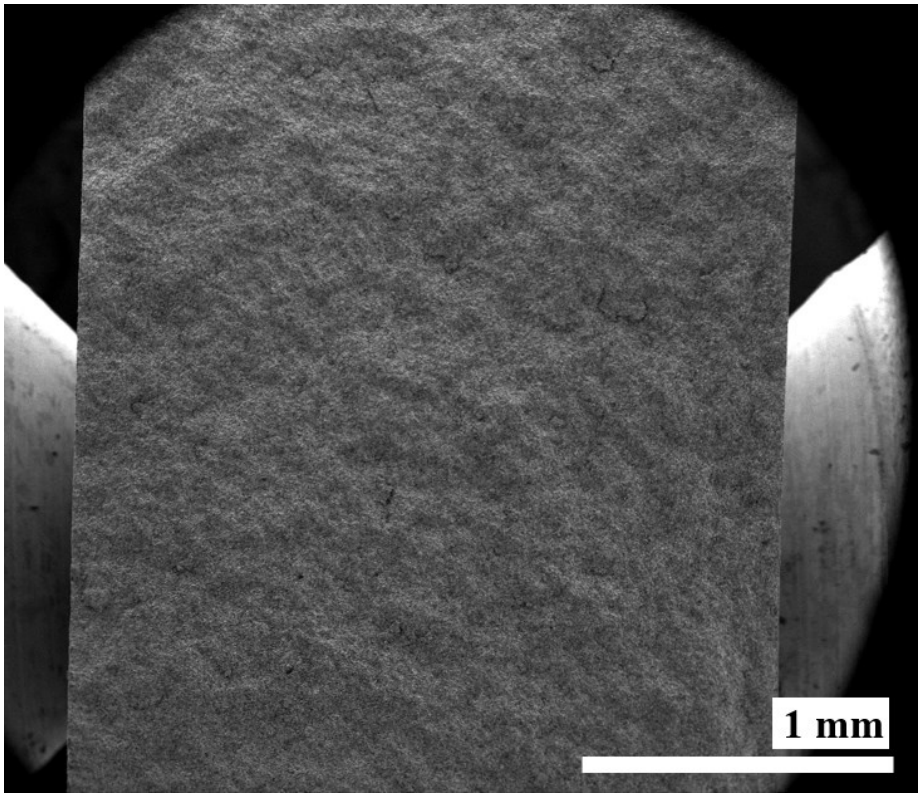

Figure 4.54 Macroscopic fracture surface of ZrC-30% SiC

The SiC grain sizes of ZrC-30% SiC was slightly smaller than that of ZrC-50% SiC as shown in Figure 4.55. There were no significant differences in ZrC grain structures between ZrC-50% SiC and ZrC-30% SiC

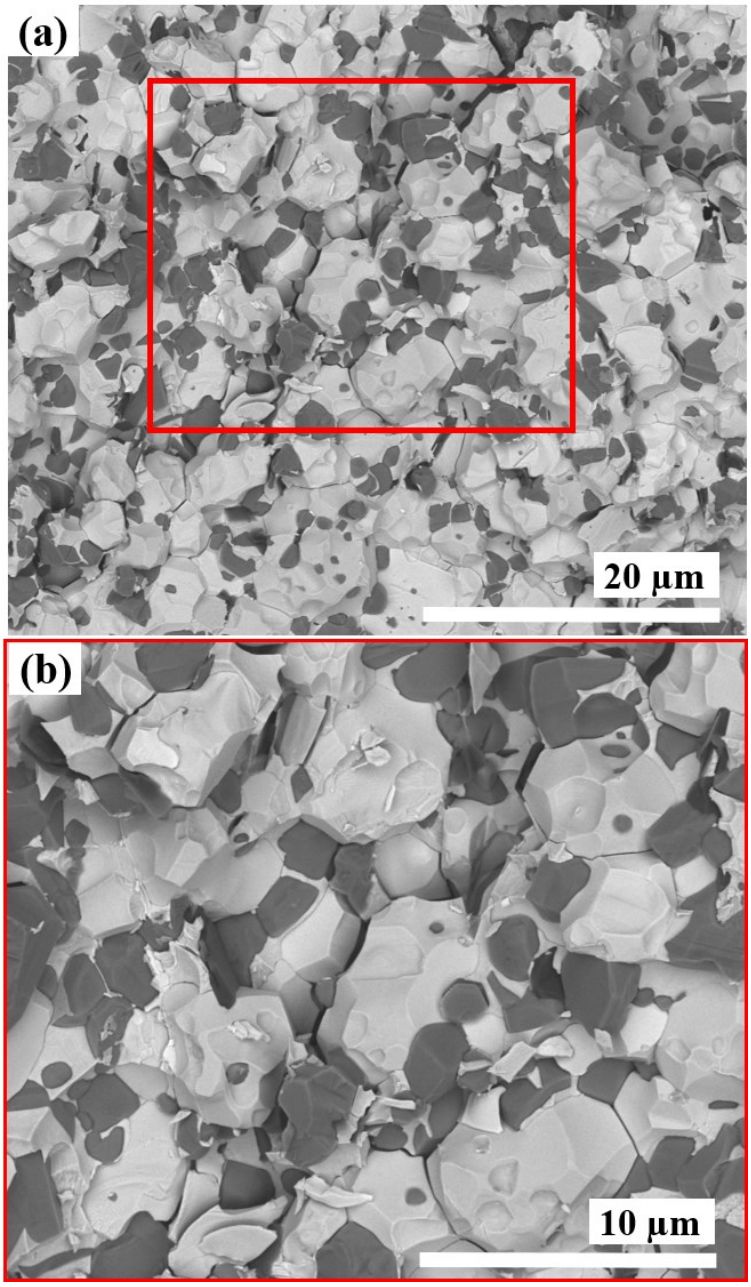

Figure 4.55 Fracture surface BSE SEM of ZrC-30% SiC

Additionally, the TG and IG fracture surfaces were found in ZrC-30% SiC. As can be seen in Figure 4.56a and b, the red arrows indicated the IG cracking; the yellow arrows represented the TG cracking. At the agglomerated SiC grains (the area of dashed yellow line in Figure 4.56a), the cracks travelled along the grain boundaries (TG). The black arrows in Figure 4.56a indicated the crack paths that changed direction when associated with submicron SiC located inside ZrC grains. Additionally, the glassy phase was observed on the fracture facets as shown in Figure 4.56b.

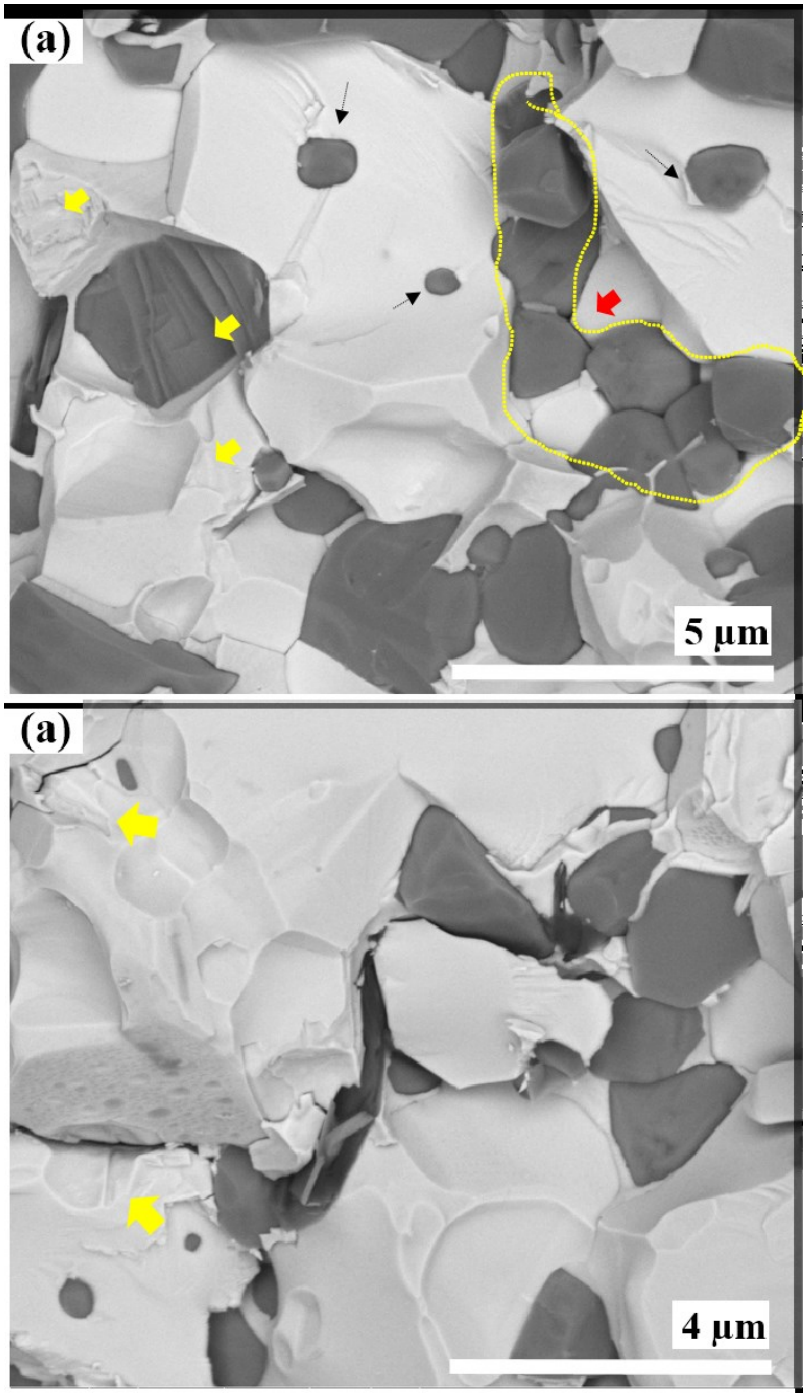

Figure 4.56 High magnification BSE SEM fracture surface of ZrC-30% SiC

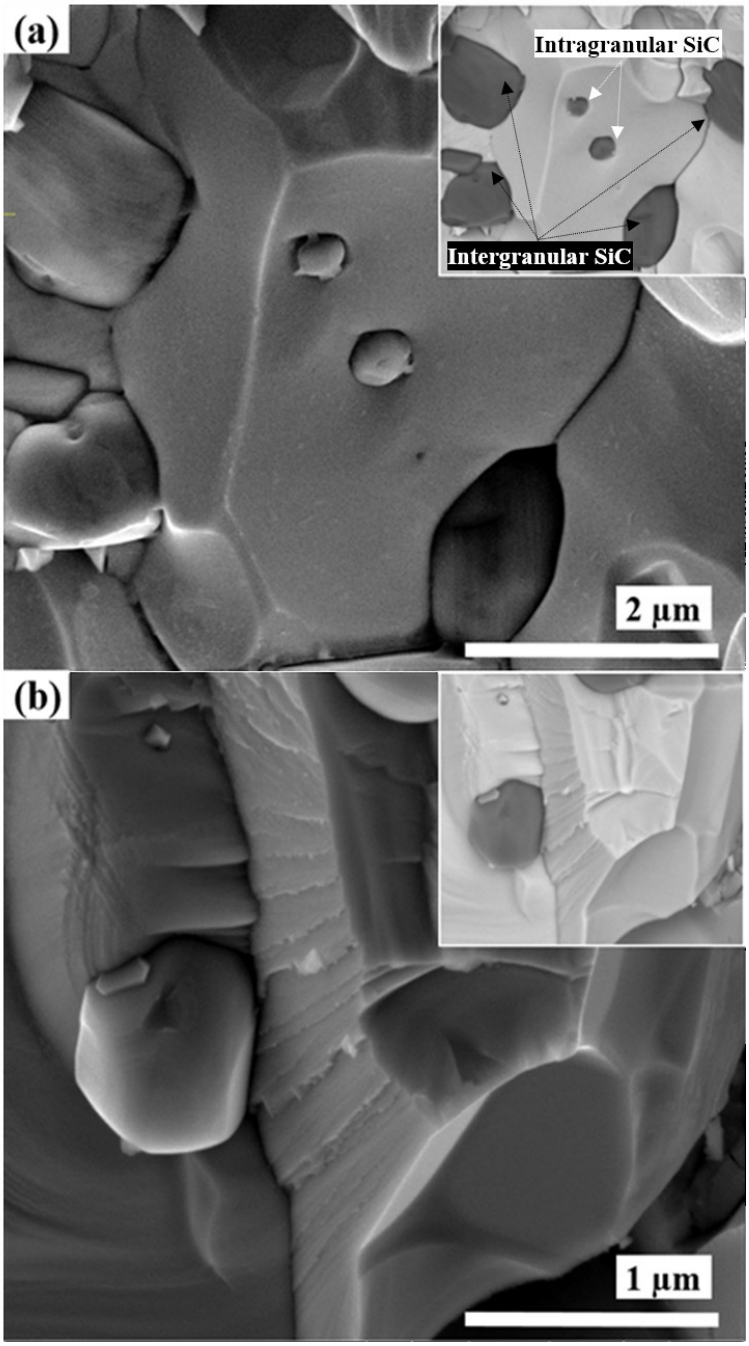

Figure 4.57 High magnification SEM images of ZrC-30% SiC fracture surfaces illustrating ZrC grains which failed via (a) IG fracture and (b) TG fracture

Furthermore, the submicron SiC grains embedded in the ZrC grains (the intragranular SiC grains) can be seen in Figure 4.57a. The SiC grains had a round shape with the glassy phase on their surface. The various cleavage surfaces from the TG fracture were observed in ZrC grains as shown in Figure 4.57b which could be attributed to the crystal planes and their orientations.

4.3.6 The thermal conductivity results

The thermal conductivity (*K*) of ZrC-30% and ZrC-50%SiC were approximately 30 and 50 W/m °C at 50 °C, respectively. These followed the rule of mixtures in which thermal conductivity increased proportionally to SiC contents and slightly dropped as temperature increases. Notably, the *K* remained roughly stable over the temperature of 100-500 °C.

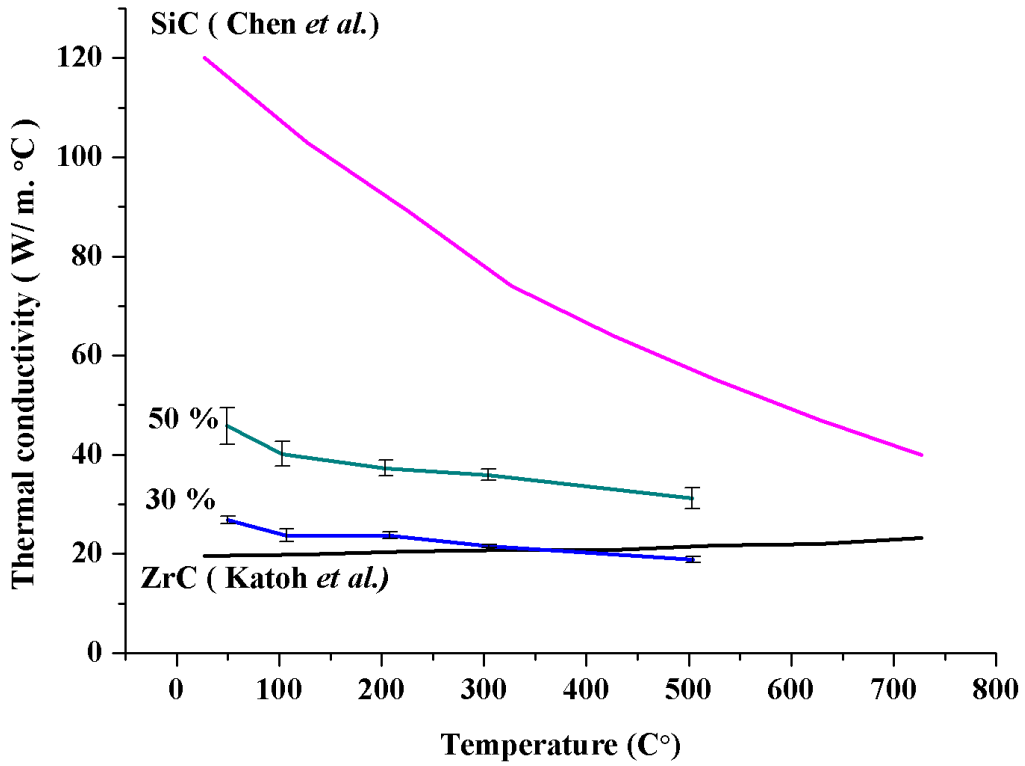

Figure 4.58 Temperature dependence of thermal conductivity of ZrC-30% SiC and 50% SiC compared with SiC (Chen *et al.*) [17] and ZrC (Katoh *et al.*) [34]

4.3.7 Thermal analysis results

Thermogravimetric analysis (TGA) and differential thermal analysis (DTA) were undertaken on dried thin foil samples in flowing argon at heating rates of 20 °C min^{-1} over the temperature range of 40-1450 °C. Figure 4.59 shows the TGA-DTA thermogram of ZrC-50% SiC. The mass loss (~ 5 %) from the 40 -157 °C corresponded to a dehydration process (the endothermic reaction). The mass then increased about 3 % due to an oxidation process (the exothermic reaction) from the range of 157 – 400 °C. After that, the mass barely changed until 1450 °C. Apparently, there was an endothermic peak (the dehydration) at 57 °C and an exothermic peak (the oxidation of ZrC) at 150 °C which is in good agreement with the TGA results. Similarly, Figure 4.62 represents the TGA-DTA thermogram of ZrC-30% SiC which exhibited slightly different behaviour to the ZrC-50% SiC in that there was 2% mass loss from dehydration process, and 0.75 % mass gain from oxidation process.

The resultant surfaces of ZrC-50% SiC and ZrC-30% SiC were investigated by SEM as shown in Figure 4.61 and Figure 4.62, respectively. It can be seen in Figure 4.61 that the rough oxide layers of ZrO_2 covered over ZrC grains (represented by the bright contrast). On the other hand, the texture of SiC was significantly harsher than that before the testing (the black contrast).

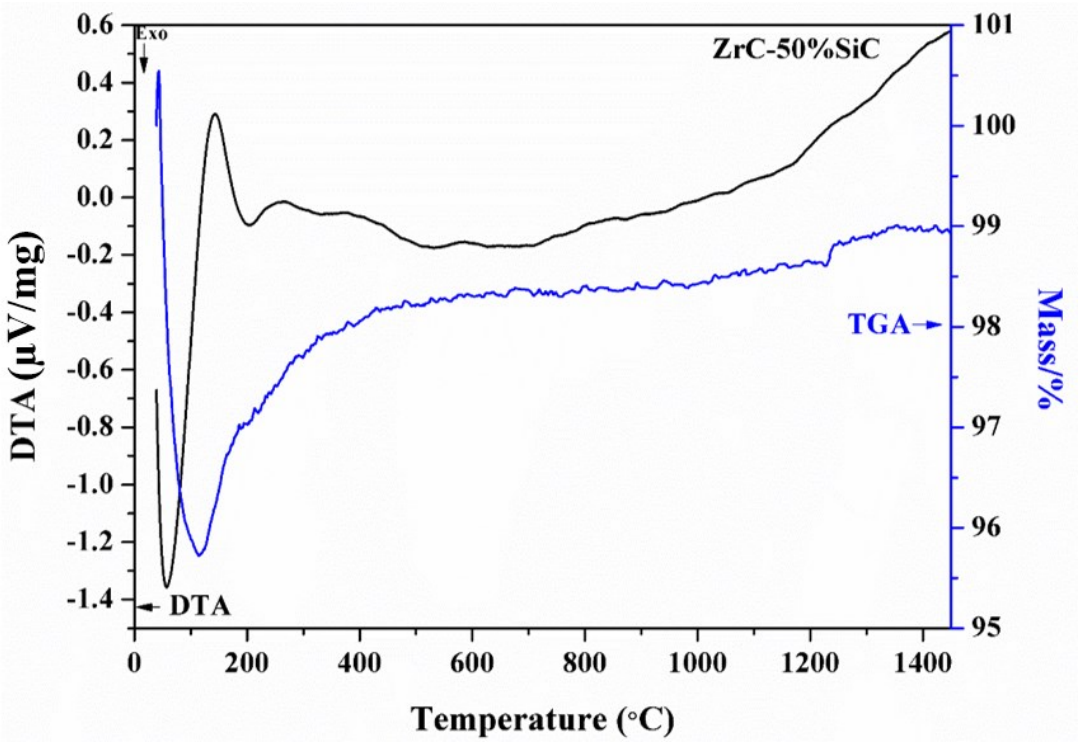

Figure 4.59 TGA- DTA thermogram of ZrC-50% SiC operated in argon gas with the 20 °C/min heating rate

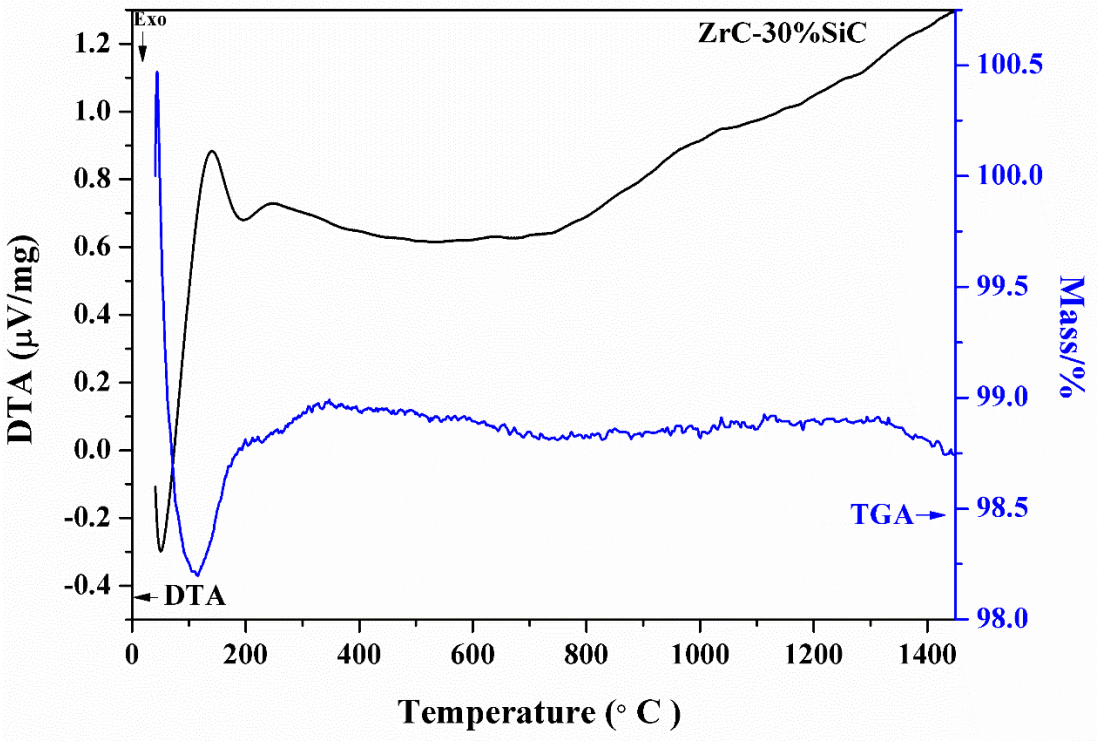

Figure 4.60 TGA- DTA thermogram of ZrC-30% SiC operated in argon gas with the 20 °C/min heating rate

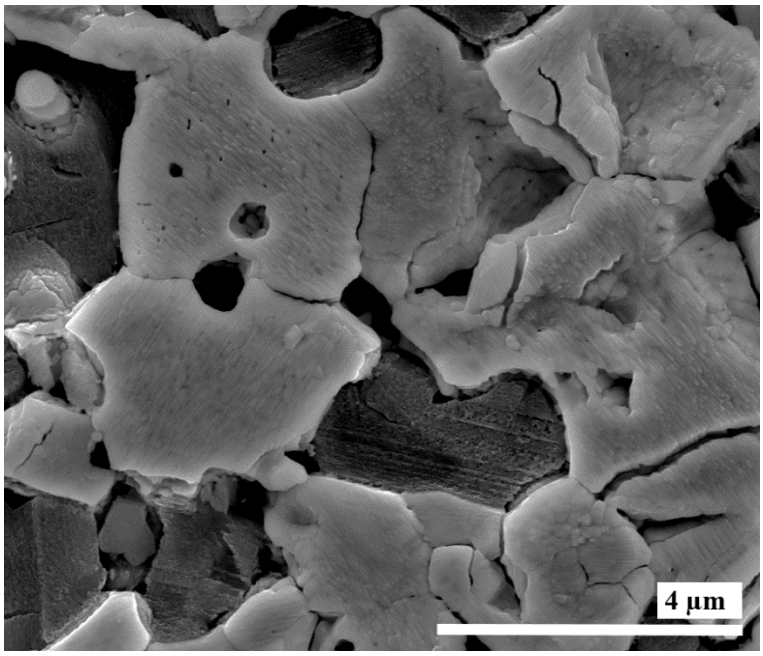

Figure 4.61 SE SEM of ZrC-50% SiC after the TGA-DTA measurement

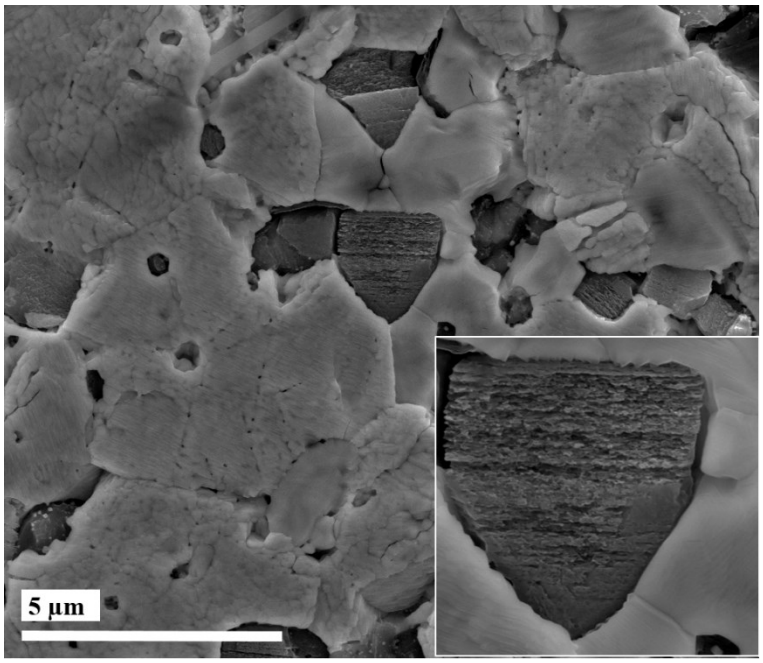

Figure 4.62 SE SEM of ZrC-30% SiC after the TGA-DTA measurement

5. Discussion

5.1. Spark plasma sintering of SiC powders

The SPS results of SiC will be discussed based on the fundamental concept of sintering. The sintering of ceramic powders consists of non-densifying mechanisms (surface diffusion, lattice diffusion, and vapour transport) and densifying mechanisms (grain boundary diffusion, lattice diffusion, and plastic flow) [83]. As shown in Figure 5.1, the non-densifying mechanisms ('1', '2' and '3') lead to the neck growth between particles without causing pore shrinkage, whereas the grain boundary diffusion and the lattice diffusion ('4' and '5') from the grain boundaries to fill the pores leading to densification [83]. Some fundamental factors have a significant effect on sintering such as the sintering temperatures, applied pressure average particle size, gaseous atmosphere, powder characteristics and particle packing. In this work, the effects of SPS temperature was investigated on the resultant SiC and TiC densities.

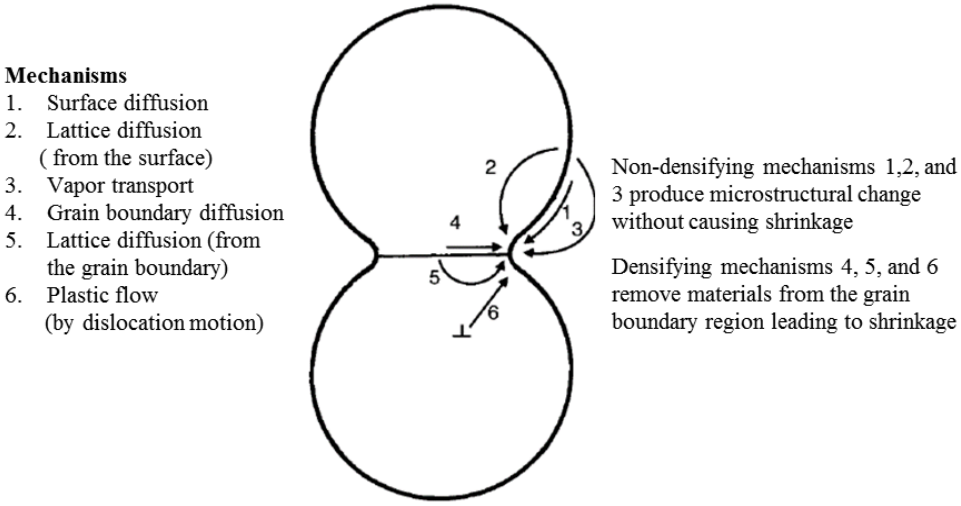

Figure 5.1 Schematic illustrating the sintering mechanisms for a system of two particles [83]

As mentioned in Chapter 2, the solidification of SiC without sintering aid is difficult because of the strong covalent bond of Si-C. [139, 140]. Due to the absence of sintering aid in this work, the sintering process of SiC was solid state sintering. According to SEM images of SPSed SiC (Section 4.1), their microstructures are the evidence that the sintering of SiC at the SPS temperature range of 1600-2100 °C was not complete. There are three stages of sintering process: the initial stage, the intermediate stage, and the final stage which is defined by the microstructure and the relative density [34, 90, 102, 141]. At the SPS temperature of 2000 °C,

the microstructure of SPSed SiC (Figure 4.4 in Chapter 4) suggested an intermediate sintering stage because of the observed solid particle networks and sharp concave necks between individual particles.

Unexpectedly, the relative density of SPSed SiC at 2000 °C was higher than at 2100 °C (Figure 4.1 in Chapter 4). The possible explanation for this may be a combination of the diffusion mechanism and the β-α phase transformation (started at 2000 °C) [15, 46]. In crystalline and polycrystalline materials, the matter transportation relates to the diffusion of atoms, ions or molecules depending on the type and concentration of defects. The rate of diffusion increases rapidly with increasing temperature, which can be explained by Fick's law [83]. Furthermore, the β-α phase transformation is not only generating imperfection or ' defects' such as free surfaces, grain boundaries, stacking faults and crystallographic shear in the SiC structure as mentioned in Section 4.2.4, but also decreasing the Gibbs energy by the growth of the α-SiC plate reported by Mitchell *et al.*[132]. Overall, they could encourage the better matter diffusion rate at 2000 °C. Thus the density of SiC reached the maximum obtainable.

5.2. The effect of incorporation of TiC into TiC-SiC Composites

From Section 4.2.1, the relative density of TiC-50%SiC was considerably higher than SPSed TiC and SPSed SiC monolithic materials. This result may be explained by the fact that the diffusion on the surface and through the lattice is quicker in TiC than in SiC due to lower TiC bond energy compared to SiC [15, 17, 19, 21, 129, 135]. Therefore, the dissolved TiC can diffuse and fill voids in the SiC components leading to the higher relative densities of TiC-50%SiC as confirmed by SEM images (Figure 4.7 and Figure 4.12).

The grain size control is another benefit from the introduction of 50%TiC into SiC. Figure 4.3 and Figure 4.12, show that the TiC grains in TiC-50%SiC were considerably smaller than that of SPSed TiC. These results suggest that the presence of SiC grains cause retardation of the TiC grain growth. During the grain growth process, grain boundaries require sufficient energy to move as shown in Figure 5.3 [48, 83]. However, as the presence of inclusion, pores or other phases along grain boundaries, cause an increase in this energy. Therefore, the grains have high potential to stop growing, if they do not have enough energy to move on [48, 83]. Similar to this finding, as confirmed by the TiC-50%SiC morphology investigation in Section 0, the TiC grain boundaries were pinned when they interacted with the SiC grains located along TiC grain boundaries.

According to the SEM image of TiC-50%SiC (Figure 4.8), both intragranular and intergranular SiC were observed in the TiC-50%SiC microstructure. Intergranular SiC tends to be a result of particle packing. Figure 5.2 illustrates the packing model of various particle size powder which supports this work in that small SiC grains located along the TiC grain boundaries, which have considerably larger grain sizes (Figure 4.8). On the other hand, the formation of intragranular SiC in TiC-50%SiC can be explained by an energy balance. Figure 5.3 is a schematic illustrating the intragranular SiC formation which is adapted from reference [83]. When a submicron SiC is attached to the grain boundary ("attached" in Figure 5.3), during grain growth, the grain boundaries tend to drag the SiC grain ("dragging" in Figure 5.3) resulting in an increase in the area and surface energy. In order to balance the overall energy, the grains are likely to separate to decrease the surface energy, therefore allowing them to contract, and leave the SiC grain in isolation ("separated" in Figure 5.3). Additionally, it has been reported that this kind of structure leads to an increase in the fracture toughness of composites [142-145]. The mechanical tests of TiC-50%SiC will be explained in the following the section.

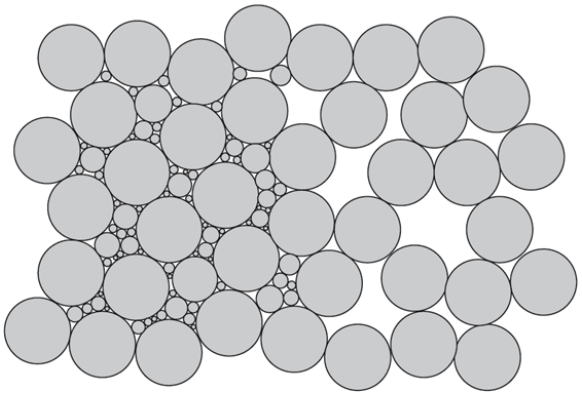

Figure 5.2 Model of particle distribution in 2D packing

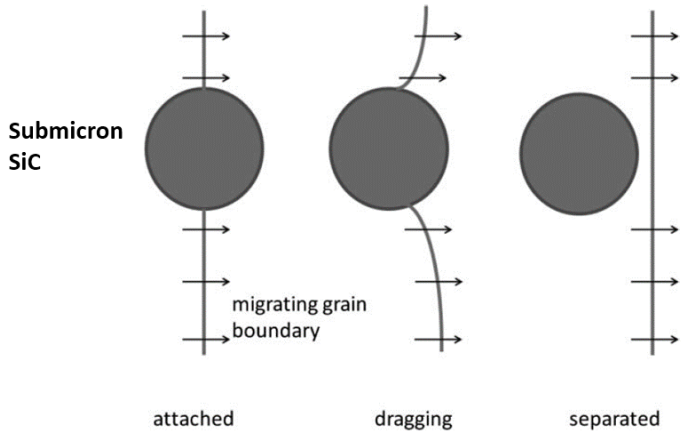

Figure 5.3 Schematic of SiC grains interaction with a migrating grain boundary, where initially SiC grain is attached to the grain boundary and the occupied area which is adapted by [83]

5.3. Discussion of TiC-SiC composites characterisations

In this section, the structure-property correlation will be discussed based on the evidence found and shown in Chapter 4.

5.1.1 Morphology of TiC-SiC composites

The incorporation of SiC leads to the high relative density of TiC-SiC composites and also affected the morphology of each phase, as confirmed by the SEM and TEM results. An alternating layer structure was found in TiC-50%SiC, whilst TiC-30%SiC exhibited the uniform distribution of SiC grains. Hence, it is clear that the SiC content has an influence on TiC-SiC microstructures. There are two possible reasons for the formation of a TiC/SiC large grain zone dispersed in a TiC-SiC small grain zone matrix (Figure 4.12). Firstly, the adhesive force on fine SiC particles (1 μm) could lead to an agglomeration of SiC particles and TiC/SiC as well. Secondly, the mixing process of TiC and SiC powder is complicated and depends on the charge on the surface of the particles. This will be different for SiC and TiC and will depend on the amounts present. This makes it difficult to obtain the optimum mixing conditions

This study has confirmed that TiC-SiC composites gain an advantage in grain shape control by the presence of SiC. According to the XRD results (Section 4.2.3), although approximately half of the starting β-SiC phase in TiC-50%SiC and TiC-30%SiC transformed to α-SiC phase, no elongated grains (aspect ratio ≥ 3), which is a particular characteristic of α-SiC grains, were observed. According to the TEM results (Section 4.2.4), the SiC grains in TiC-50%SiC, and TiC-30% SiC included a mixture of equiaxed and elongated grains with an

aspect ratio ≤ 3. The presence of TiC matrix is likely to make it difficult for the grain growth of α-SiC. In contrast to the present results, Zhan *et al.* reported an effect of β-SiC contents on the α/β-SiC composite microstructure. Less than 30 % wt. of β-SiC exhibited a fine equiaxed grains morphology (Figure 5.4a), whereas for SiC contents higher than 30 % wt., the grains are elongated significantly (Figure 5.4b) [146].

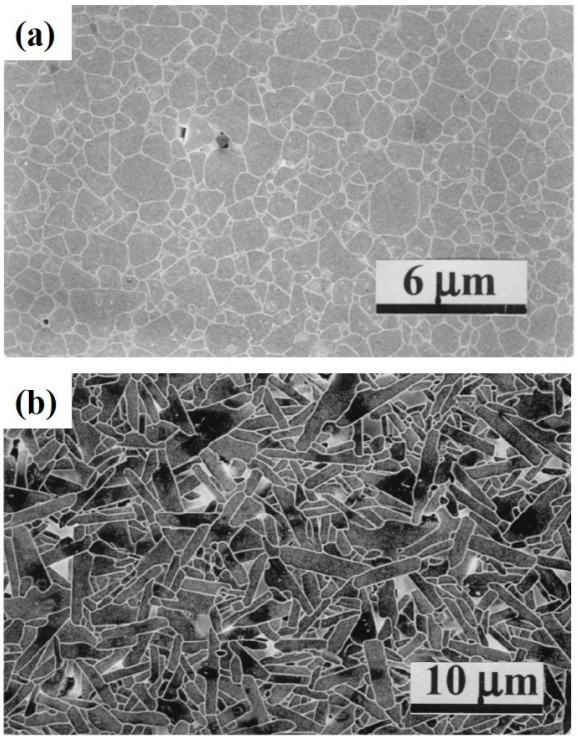

Figure 5.4 The SEM images illustrating grain morphology of SiC grain with less than 30 % wt of α-SiC and (b) more than 30% wt of α-SiC reported by Zhan *et al.* [146]

Even though TiC-50%SiC and TiC-30%SiC reached 99% and 98% relative densities, respectively, micro-pores still appeared which could have been a result of transient stresses due to the differential shrinkage of TiC and SiC grains. The thermal expansion coefficients of TiC, β-SiC and α-SiC are 7.4, 3.8 and 5.1 10^{-6} $C^{\circ-1}$,respectively [15]. Hexagonal α-SiC has an anisotropic expansion, whereas cubic TiC and β-SiC are isotropic. Figure 5.5 shows the schematic explaining a formation of micro-pore at the TiC/SiC interfaces. TiC grains expand greater during a sintering process and shrink more during a cooling process. Hence, it leaves the micro-crack: radial cracks and/or circumferential cracks at their interfaces depending on the shrinkage direction and the interaction between surrounding grains [48]. Consequently, the TiC/SiC interfaces have lower density compared to the bulk density because of these micro-pores.

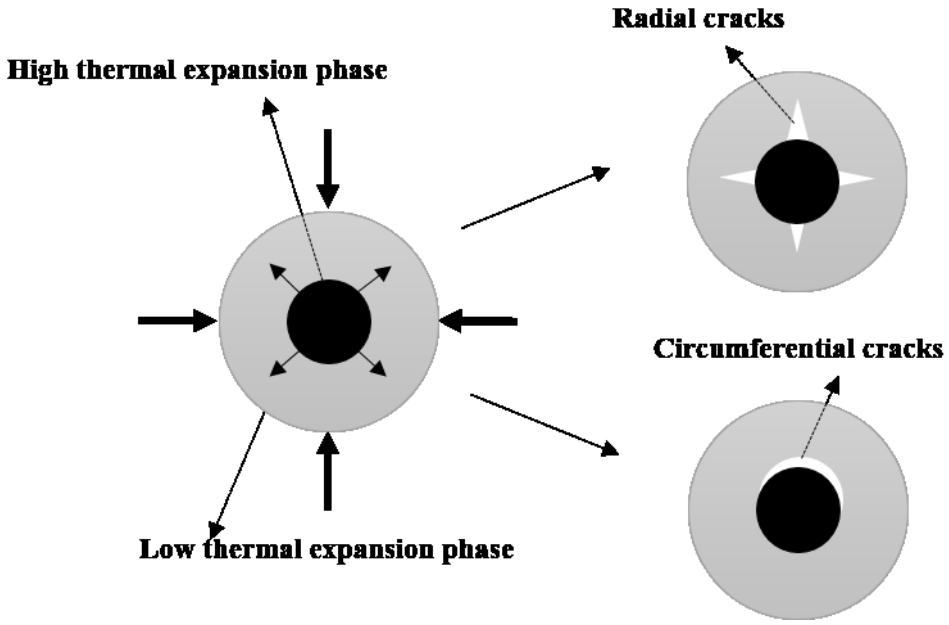

Figure 5.5 Schematic diagram illustrating the effect of the differential thermal expansion of two phases in the flaw formation at their interfaces [83, 147]

The glassy phases of Zr compounds from milling media were found in TiC-30%SiC and TiC-50% as shown in Figure 5.6. Moreover, it be clearly seen that the glassy phase was distributed along the grain boundaries. Although the glassy phases could make the TiC/SiC interfaces weaker, they encourage the crack propagation along grain boundaries (IG fracture), Figure 5.6b. In addition, the glassy phase filled in the micro-voids at the grain boundaries and triple boundaries, therefore TiC-SiC composite densities increased [83].

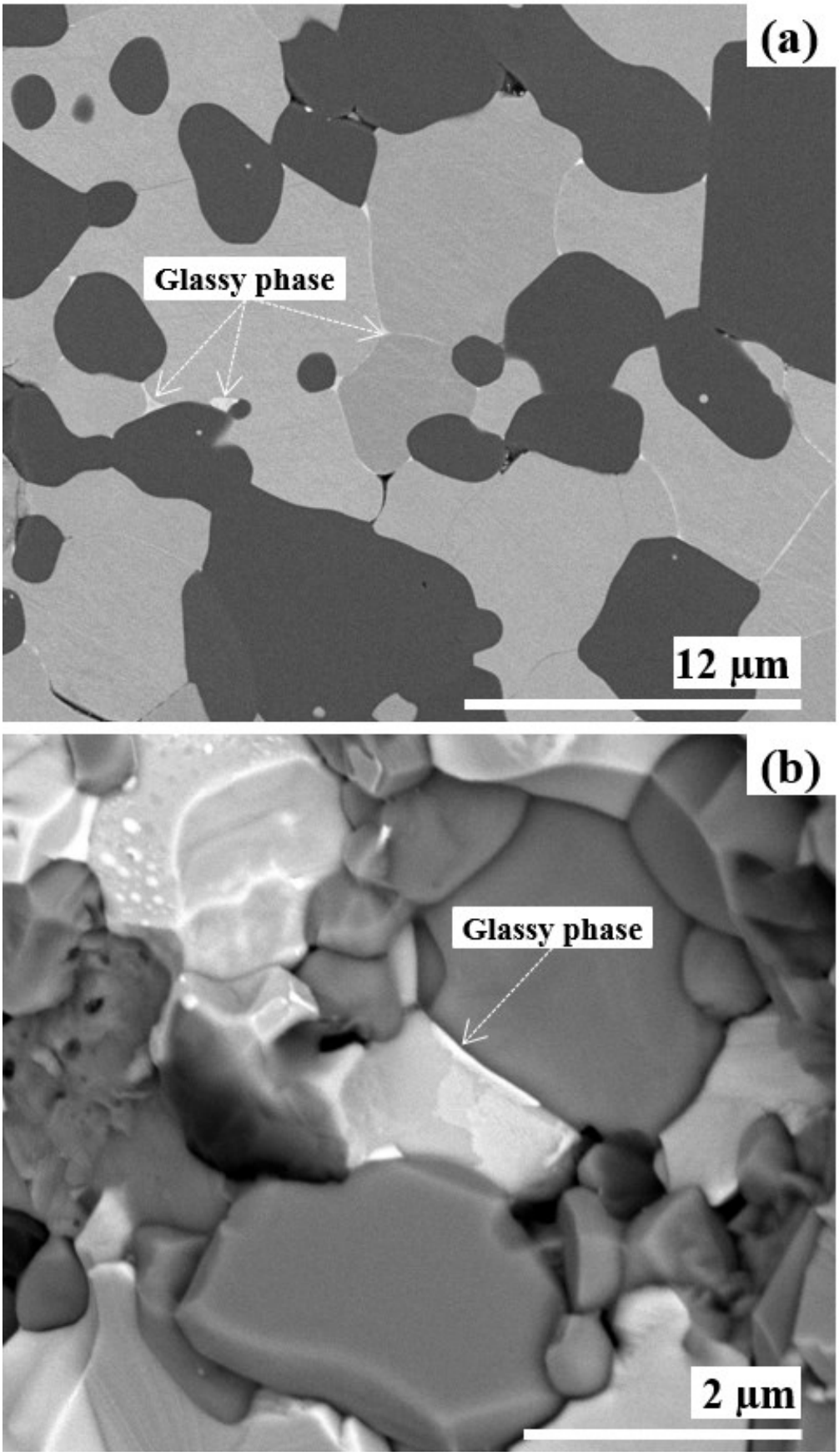

Figure 5.6 The BSE images illustrating the glassy phase at the grain boundaries on (a) the polished surface and (b) the fracture surface

5.1.2 Fracture toughness of TiC-SiC composites

The drawback of refractory carbides is their brittleness. The development of ceramic fracture toughness (K_{IC}) has been the subject of considerable research interest. In this project, it is confirmed that the combination of SiC and TiC can cause the toughening. Remarkably, the indentation K_{IC} of TiC-50%SiC and TiC-30%SiC (7.9 ± 0.4 and 7.9 ± 0.2 MPa. √m. respectively) was considerably higher compared to TiC, SiC, and other previous reports as shown in Table 5.1.

Table 5.1 Fracture toughness (measured by the indentation method) of SPSed SiC-TiC composites reported by Luo *et al.*[21]

SiC (% mole)	TiC (% mole)	Relative density (%)	Fracture toughness (MPa. √m)
93	7	99.4	4.8 ± 0.2
86	14	99.5	5.3 ± 0.4
78	22	99.8	5.8 ± 0.3
69	31	100	6.3 ± 0.4

Note: SiC-TiC composites were synthesised by SPS at 1800 °C with 40 MPa for 10 minutes

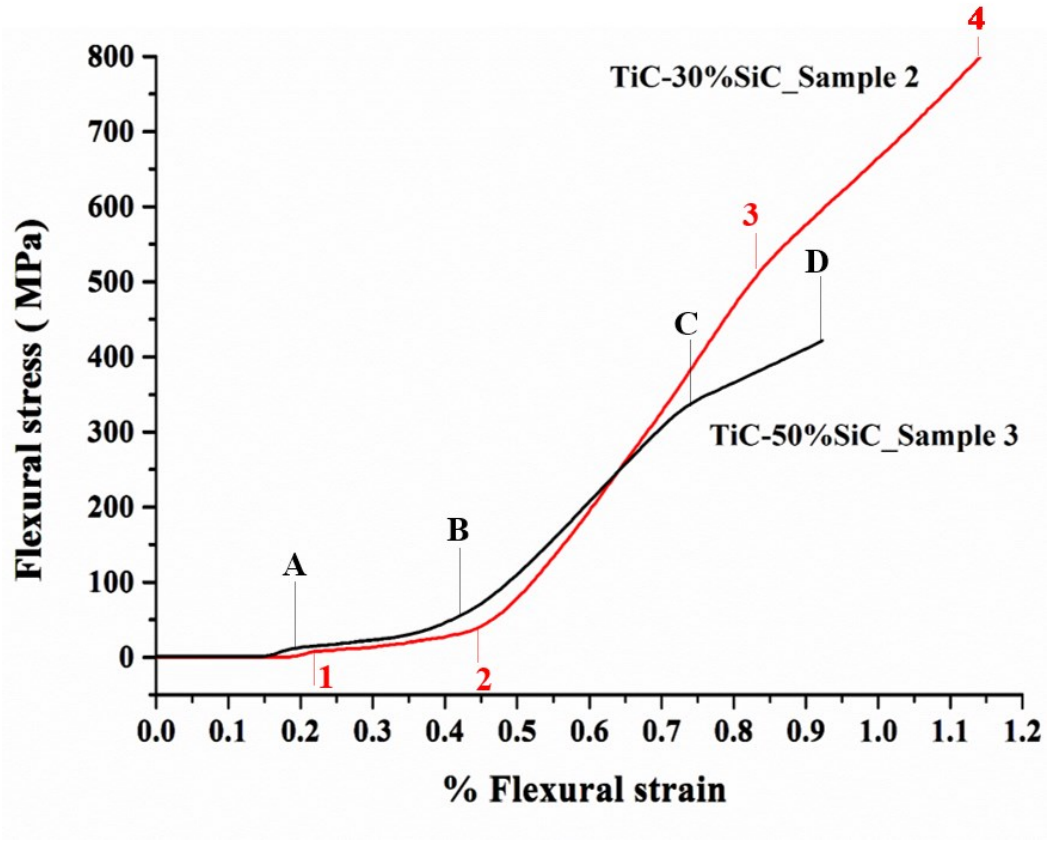

Figure 5.7 Strain-strain curve of TiC-30%SiC sample 2 and TiC-50%SiC sample 3 illustrating the toughening process

As shown in Figure 5.7, the selected stress-strain curves of TiC-50%SiC and TiC-30%SiC exhibited a toughed composite behaviour because the stiffness, 'slope', of the curve changed significantly before failure. Moreover, the flexural stain at the breaking point was larger compared to a typical brittle ceramic. It may be implied that the crack propagation was delayed by some features in the composites. At low stresses, TiC-50%SiC responded linearly with high stiffness till the point A. Then the strain deviated considerably which maybe because of the generation of micro-cracks in TiC matrix. At the stage A→B, the slope of the stress strain curve dramatically drops which could result from the crack propagation originating from the micro-crack. However, the slope of the stress strain curve increases again from point B → C and then breaks at point D which implies that the toughening processes exists which could from the interaction between cracks and crack barriers that result in the crack changing direction.

Likewise, for the TiC-30%SiC composite, the slope of the stress-strain curve changes from the "1" point till the "4" point before breaking. Notably, the flexural stress at fracture of TiC-30%SiC (~ 800 MPa) is significantly higher than that of TiC-50%SiC (~400 MPa). Moreover, considering an area under the stress-strain curve, which particularly relates to the toughness of materials, TiC-30%SiC shows significantly larger than that TiC-50%SiC. However, unexpectedly, no significant difference was found in the K_{IC} of TiC-50%SiC, and TiC-30%SiC measured from the indentation method and precracked bend testing.

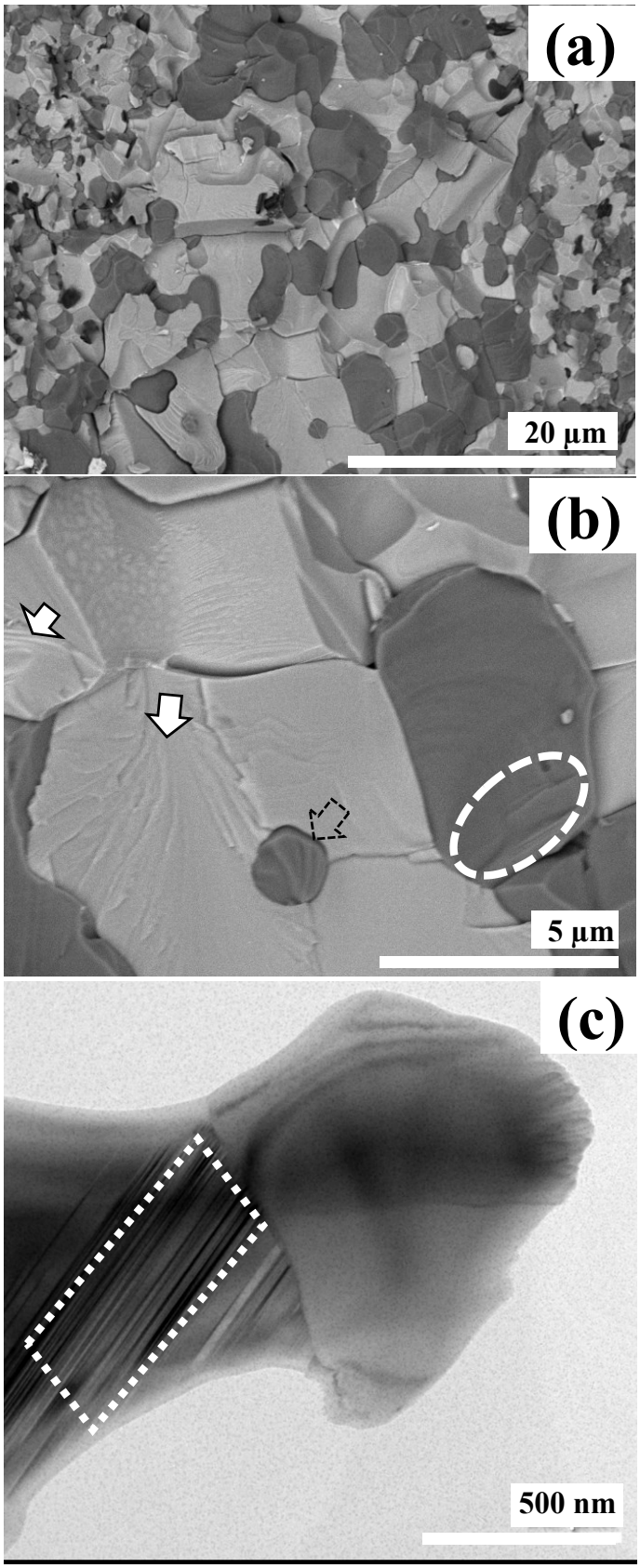

Figure 5.8 BSE SEM micrographs (a and b) and (c) TEM micrographs of TiC-50%SiC

Further SEM analysis of the fracture surface was used to explain the failure processes. In composites, grain size and the interface strength play an importance role in controlling crack direction. The crack will follow the easiest path through the material, which may not necessarily be the shortest path. Understanding the crack propagation is difficult because of the interaction between the different variables. For example, the crack may not follow the weakest interface because of the local residual stresses. Equally, the crack may propagate in a transgranular manner even if the grain boundary is weaker if the path length along the grain boundary is too long. The grain size has a major effect as it controls both the residual stresses and the crack path length [138]. In the current work, the cracks preferred travelling through the larger TiC grains rather than the smaller SiC grains. Also, the transgranular fracture was more dominant in the large TiC/SiC grain zone of TiC-50%SiC than the smaller grain region, (Figure 5.8a). On the other hand, intergranular fracture was observed in the submicron SiC grains and the small TiC grains. Stress fields from second phase interfaces may induce the intergranular mode and allow the crack to easily propagate along the grain boundaries. Cheng *et al.* pointed out that the transition of fracture modes is the main reason for the improved toughness in TiC-SiC composites [148].

Crack deflection is a crucial toughening process in TiC-SiC composites which depends on grain size, grain morphologies and volume fractions of the phases present. Variation in elastic anisotropy (EA) and thermal expansion anisotropy (TEA) of TiC and SiC can cause local stresses around the submicron SiC grains which act as good crack deflectors. Therefore, the degree of tortuosity increases during the crack propagation. Furthermore, the intragranular SiC grains (Figure 5.8b, indicated by the dashed arrow) not only induce the tangential tensile stress resulting in crack propagating toward the grains but also act as crack deflecting grains.

Cracks prefer travelling along the weakest interfaces such as micro-pores, defects, and weak interfaces. Similarly, the β/α interfaces, partial dislocations and/or faulted layers in the SiC composites grains (Figure 5.8c) also induce the crack transition (indicated by the dashed circle, Figure 5.8b). This is in good agreement with Zhan *et al.* in that the degree of $\beta \rightarrow \alpha$ transformation resulting in a significant improvement in fracture toughness due to crack deflection and bridging mechanism [146].

5.1.3 Thermal properties of TiC-SiC composites

Lattice vibration ('phonon', k_p) and conducting electrons (k_e) participate in the heat transfer within TiC and SiC. According to Section 4.2.5, the thermal conductivity (K) of TiC-SiC composites was stable from 100 to 500 °C due to the opposing changes in the K of TiC and SiC with temperature. The K of SiC (a covalent carbide ceramic) dramatically decreases with increasing temperatures because of a significant increase in a phonon scattering (Umklapp scattering) [15, 46]. In contrast, TiC (an interstitial carbide ceramic) has a unique heat transfer in that the K increases with increasing temperatures due to a significant increase in the k_e of TiC [15].

Contrary to expectation, the K of TiC-50%SiC and TiC-30%SiC did not follow the rule of mixtures as shown in Figure 4.19. Although SiC exhibits greater K than TiC, the K slightly decreases as SiC contents increase from 30 to 50%, over temperatures of 50 to 500 °C. Therefore, other factors crucially impact on the K such as microstructures, defects and impurities. Micro-pores may be the main reason for the decreasing K of TiC-50%SiC. The presence of TiC/SiC inclusions (the large grain zone as mentioned in Chapter 4) in TiC-50% SiC leave the micro-pores at their interfaces containing air, which has very low thermal conductivity (0.026 W m^{-1} K^{-1}), decreasing the heat transfer [108]. Moreover, defects also have a potential effect on decreasing K. According to the TEM results (Section 4.2.4), partial dislocations and twin boundaries were found in the α/β SiC grains, which cause more phonon scattering leading to a reduction in the K. The higher the SiC content, the more defects in the sample. Therefore, it is reasonable that TiC-50%SiC exhibited the lower K according to the combination of micro-pores and defect factors.

Thermal stability was investigated by TGA- DTA followed by SEM analyses of the resultant surfaces. TiC-50% SiC and TiC-30% SiC have excellent thermal stability with only a slight mass change in the range of 50 - 1450 °C. Oxide layers formed over the TiC and SiC grains of TiC-30%SiC and TiC-50%SiC. Active silicon oxide layers have been reported that can reduce the strength of materials, whereas passive silicon oxide layers lead to the formation of coherent silica layer over the silicon carbide surface, thereby improving its performances in several applications [15, 46, 149]. Their formation depends upon the nature of the substrate used, atmosphere, and oxygen partial pressure [149]. Banu *et al.* reported the oxidation of mixed TiC-SiC powder [150]. SiC starts being oxidised to passive oxide layers at about 650 °C, whereas TiC is readily oxidised to oxycarbide and then further crystallise to anatase further

crystallisation to anatase and rutile TiO_2 at about 450 °C [151]. This is consistent with the exothermal peaks appeared in our DTA results (Section 4.2.6)

5.4. Discussion of the ZrC-SiC composite characterisations

In this section, the structure-property correlation will be explained based on the evidence found and shown in Section 4.3.

5.1.4 Morphology of ZrC-SiC composites

According to the high melting point and low self-diffusion coefficients, it is difficult to achieve sufficiently dense ZrC without sintering aids. SPS is the most appropriate technique for additive-free densification [16, 96, 98, 152-155]. Zhou *et al.* found that the relative density of ZrC reached 94.4 % by SPSing at 2100 °C [128]. In contrast, for hot pressing (HP), it was only 83% at 2000 °C [156].

In this work, the SPSed ZrC reached 98 ± 0.4 % at 2100 °C without sintering aids. However, no significant differences between the relative density of ZrC-30%SiC and ZrC-50% were found (97 ± 0.2 and 98 ± 0.2%, respectively). In contrast, Pizon *et al.* reported that as SiC contents increased from 10% to 30 %, the relative densities of ZrC-SiC composites were 100 % and 97 % respectively, compared to ZrC (87 %). From this work, an introduction of SiC does not significantly influence their densities, whereas it is the crucial effect on their microstructures. The presence of SiC grains inhibits the grain growth of ZrC grains in ZrC-SiC composites. As SiC contents increased, the ZrC grain sizes got smaller; 2.5 and 3.5 μm for ZrC-50% and ZrC-30% SiC, respectively. Therefore, it may result from an excellent distribution of spark/Joule heat throughout the powder and zirconium oxycarbide (ZrC_xO_y) formation. The oxygen atoms can quickly enter into the ZrC lattice as the interstitial vacancies and rapidly form ZrC_xO_y ($x < 1$ and $y << 1$) at low temperature [80]. In addition, Katrin *et al.* confirmed the formation of ZrC_xO_y during the manufacturing process improves Zr lattice diffusion [127]. Hence, the sintering behaviour of ZrC power improves and promotes a better densification process. Moreover, carbon vacancies in substoichiometric ZrC enhance atomic diffusion during the sintering process [22, 79, 80, 127, 153, 155, 157, 158].

The XRD results confirm that there was a zirconium dioxide (ZrO_2) formation in SPSed ZrC, ZrC-30%SiC and ZrC-50%SiC. ZrC_xO_y can be further reduced to be ZrC, or/and can be oxidised to ZrO_2 [79]. However, in this research, the oxygen contents in starting ZrC powder were not measured before SPSing. Hence, zirconium oxycarbide and zirconium oxide might

have come from the starting ZrC powder. This is more probable than being generated during the sintering process since the graphite mould promotes reducing conditions.

The results of this study will now be compared to the findings of previous work. Zhao *et al.* studied the microstructure of ZrC and ZrC-30%SiC SPSed at 2100 °C and observed intragranular pores in SPSed ZrC, but no evidence of them were found in ZrC-30%SiC, as shown in Figure 5.9a [128]. In contrast to this work, only micro-pores from pull-out grains and intergranular pores were found as shown in Figure 5.9b. Regarding Zhao's report, SiC grains in ZrC-30%SiC were only located along grain boundaries. In contrast, in this work, we found the intragranular SiC (Figure 5.9b) which may be due to the low migration speed of SiC. Therefore, submicron SiC grains were trapped within ZrC grains during the sintering process [22, 79, 80, 88, 127, 128, 153, 155, 158].

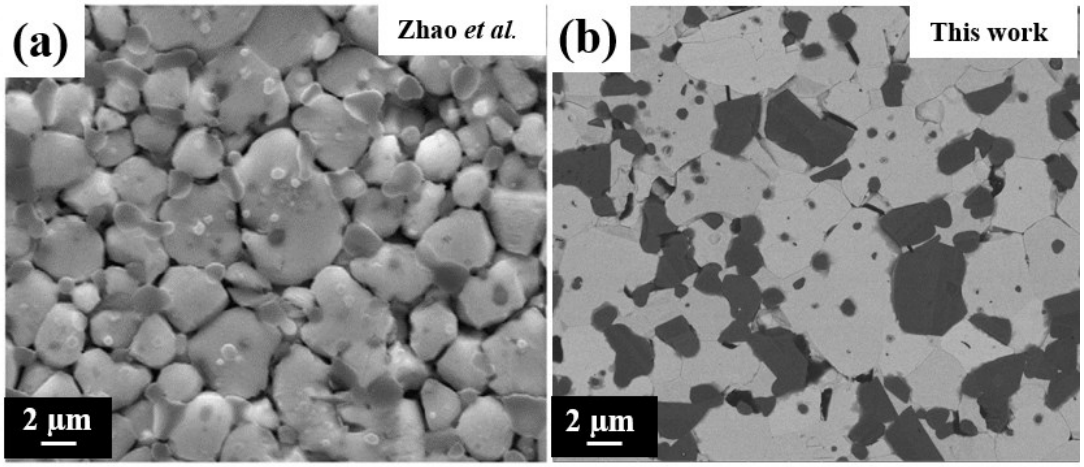

Figure 5.9 Comparing the microstructure of SPSed ZrC-30% SiC reported by (a) Zhao *et al.* [128] and (b) this work

5.1.5 Mechanical properties of ZrC-SiC composites

The ZrC-50% SiC (3.6 ± 0.2 MPa √m) and ZrC -30%SiC (3.2 ± 0.3 MPa √m) in this work showed higher fracture toughness than that of ZrC reference (1.1-2.7 MPa √m [79]). The incorporation of SiC in the ZrC matrix leads to a substantial reduction in ZrC grain sizes, which may result in a decrease in the initial crack size. Intragranular SiC grains can also deflect cracks, therefore crack propagation is retarded and consequently the K_{IC} increases (Figure 5.10) [159]. According to the SEM results in Section 4.3.3 and fracture surface results in Section 4.3.5, due to the variation of SiC and ZrC size, the transition between trans- and intergranular fracture

were observed which may have retarded the crack propagation and therefore resulted in an increase in the K_{IC} of ZrC-SiC composites in this work.

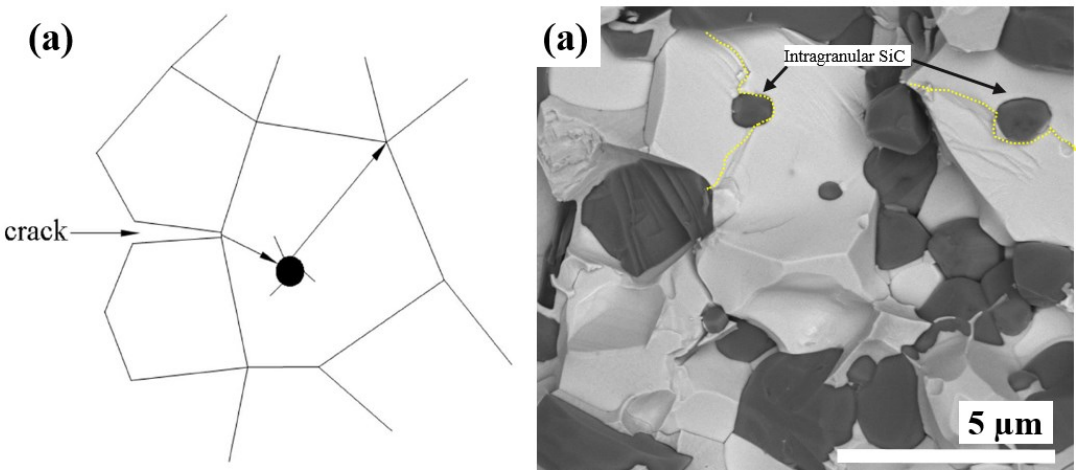

Figure 5.10 (a) Schematic diagram of crack propagation of grains containing submicron intragranular grains [159] comparing with (b) fracture surface SEM images of ZrC-30%SiC in this work

Contrary to expectation, according to Vickers hardness results (Section 4.3.4), there was no significant differences between ZrC-SiC composites and SPSed ZrC. Moreover, it is apparent from their stress-strain curve (Figure 4.49) that ZrC-30%SiC (~ 270 MPa) have much lower flexural strength than ZrC-50%SiC (~ 625 MPa). However, the flexural strength of ZrC-30%SiC was slightly lower than the standard value of stoichiometric ZrC (337 MPa) [128]. It is well known that the bend test of ceramics is quite sensitive to flaws in specimens [48]. Hence, localised flaws created from the specimen preparation might lead to a decline in the flexural strength [48].

5.1.6 Thermal properties of ZrC-SiC composites

Not only mechanical properties improved by the incorporation of SiC, but also thermal properties. In this work, the thermal conductivity of ZrC-50%SiC and ZrC-30%SiC were considerably higher than SPSed ZrC and stable over 500 °C. ZrC is prone to oxidation readily at low temperature [80, 97, 98, 160]. On the other hand, it is well known that SiC has high oxidation resistance and also form passive oxide layer to protect the surface from further oxidation [15, 46]. According to TGA/DTA results in section 4.3.7, small mass changes were observed for ZrC-50%SiC and ZrC-30%SiC in the temperature range of 200 - 1450 °C. From the BSE SEM-EDX of resultant TGA/DTA specimens, there were oxide layers on ZrC and SiC

grains. This evidence implies that after the passive silicon oxide layer was formed, this layer protected the specimen from further oxidation. Therefore, the mass of ZrC-SiC composites was stable in the temperature range of 200-1450 °C.

6. Conclusions

SiC, TiC, ZrC and their composites are promising candidates for Gas-cooled fast reactor (GFR) and Very high-temperature reactor (VHTR). Large properties databases are required for efficient material selection for Gen IV reactors; however, to date the extent of research in this field is not sufficient. This project was undertaken to investigate the physical, thermal and mechanical properties of dense TiC-SiC and ZrC-SiC composites.

For TiC-SiC composites, we succeeded in;

- Fabricating dense TiC-SiC composites (with 30% and 50% mole of SiC) by spark plasma sintering (SPS) without sintering aids at 2100 °C, 50 MPa for 15 minutes.
- Gaining good fracture toughness (7.9 MPa. √m); considerably higher than previous reports and higher than for TiC and SiC.
- Modifying microstructure in that TiC grains of TiC-SiC composites are significant smaller than that pure TiC. Also, SiC grains are less elongated shape than that of pure SiC.
- Understanding their toughening processes of the TiC-SiC composites are the crack deflection and the crack transitions (intergranular ↔ transgranular) from the differences in grain size and arrangement of SiC and TiC.
- Gaining the acceptable and stable thermal conductivity (*K*) over the temperature range of 100-500 °C (the *K* of TiC-30%SiC and TiC-50%SiC were 50 and 70 W/m °C at 50 °C respectively.

On the other hand, ZrC-SiC composites (with 30% and 50% mole of SiC) were prepared by the same procedure as TiC-SiC composites. The fracture toughness of ZrC-30%SiC and ZrC-50%SiC were 3.2 and 3.6 MPa.√m respectively, which is significantly higher than ZrC. Regarding their fracture surface results, intragranular SiC grains in ZrC-SiC plays an essential role in deflecting crack directions. Also, the thermal conductivity of ZrC-30%SiC and ZrC-50%SiC was tuned to be stable at the range of 100-500 °C (30 and 50 W/m. °C at room temperature, respectively).

Although they bear some similarities, the differences between ZrC-SiC and TiC-SiC were pronounced. In this work, the mechanical properties (hardness, flexural stress and fracture toughness) of TiC-30%SiC and TiC-50%SiC were far better than that of ZrC-30%SiC and ZrC-30%SiC. From TGA-DTA results, ZrC-SiC composites were prone to be oxidised at a lower temperature compared to TiC-SiC composites.

7. Future work

Because of limited time, TEM of the ZrC-SiC composites was not undertaken. This could provide insight into the poor fracture toughness of these composites. TEM could also be used to further understand the TiC-SiC composite failure mechanisms. In this work, the stress fields and residual stresses that would generate because of difference in thermal expansion of α-SiC, β-SiC, TiC and ZrC, have not been fully investigated, which is important to develop a full understanding of the fracture mechanisms. High-temperature XRD analysis and Raman microscopy are proposed for this investigation.

At present, few studies have investigated induced irradiation damages on TiC-SiC and ZrC-SiC composites and their interfaces. Therefore, for the future work, the SiC-SiC, TiC-SiC, ZrC-ZrC and ZrC-SiC composites should be irradiated by Kr/He/Xe to determine the relative fluencies required for each carbide phase for amorphisation. Additionally, in situ irradiation along with post-irradiation characterisations by advance TEM, and atom probe tomography would be beneficial information in order to understand amorphisation, gas bubble formation and damage tolerance. Understanding how such materials behave whilst undergoing induced radiation damage is paramount to understanding the applicability of these materials.

TiC-SiC composites are not only promising candidates for nuclear application but also tribological ceramics. It would be interesting to study the wear behaviour of these composites in the continuous or reciprocating conditions along with the corrosion test of TiC-SiC composites in order to efficiently determine wear-resistant applications during the service life.

8. References

1. *Greenhouse gas emissions avoided through use of nuclear energy*. Available from: http://www.world-nuclear.org/nuclear-basics/greenhouse-gas-emissions-avoided.aspx.
2. IEA, *World Energy Outlook 2016*. 2016: IEA.
3. Forum, t.O.N.E.A.f.t.G.I.I., *Technology Roadmap Update for Generation IV Nuclear Energy Systems*. 2014.
4. Locatelli, G., M. Mancini, and N. Todeschini, *Generation IV nuclear reactors: Current status and future prospects.* Energy Policy, 2013. **61**: p. 1503-1520.
5. Zinkle, S.J. and G.S. Was, *Materials challenges in nuclear energy.* Acta Materialia, 2013. **61**(3): p. 735-758.
6. Marques, J.G., *Evolution of nuclear fission reactors: Third generation and beyond.* Energy Conversion and Management, 2010. **51**(9): p. 1774-1780.
7. Francis, J.A., *Nuclear Materials.* Materials Science and Technology, 2018. **34**(5): p. 503-503.
8. Whittle, K., *Nuclear Materials Science*. 2016, IOP Publishing.
9. John, M., *Advanced ceramic materials for next-generation nuclear applications.* IOP Conference Series: Materials Science and Engineering, 2011. **18**(16): p. 162001.
10. Deck, C.P., et al., *Characterization of SiC–SiC composites for accident tolerant fuel cladding.* Journal of Nuclear Materials, 2015. **466**: p. 667-681.
11. Rivai, A. and M. Takahashi, *Design Study of Small Lead-Cooled Fast Reactor Cores Using SiC Cladding and Structure.* Journal of Power and Energy Systems, 2007. **1**(2): p. 134-142.
12. Kim, W.-J., D. Kim, and J.Y. Park, *FABRICATION AND MATERIAL ISSUES FOR THE APPLICATION OF SiC COMPOSITES TO LWR FUEL CLADDING.* Nuclear Engineering and Technology, 2013. **45**(4): p. 565-572.
13. Azevedo, C.R.F., *Selection of fuel cladding material for nuclear fission reactors.* Engineering Failure Analysis, 2011. **18**(8): p. 1943-1962.
14. Ben-Belgacem, M., et al., *Thermo-mechanical analysis of LWR SiC/SiC composite cladding.* Journal of Nuclear Materials, 2014. **447**(1): p. 125-142.
15. Pierson, H.O., *Handbook of Refractory Carbides and Nitrides: Properties, Characteristics, Processing and Applications*. 1996: Elsevier Science.
16. Sciti, D. and M. Nygren, *Spark plasma sintering of ultra refractory compounds.* Journal of Materials Science, 2008. **43**(19): p. 6414-6421.
17. Chen, J., W. Li, and W. Jiang, *Characterization of sintered TiC–SiC composites.* Ceramics International, 2009. **35**(8): p. 3125-3129.
18. Khodaei, M., et al., *Effects of different sintering methods on the properties of SiC-TiC, SiC-TiB2 composites.* International Journal of Refractory Metals and Hard Materials, 2018. **70**: p. 19-31.
19. Cabrero, J., F. Audubert, and R. Pailler, *Fabrication and characterization of sintered TiC–SiC composites.* Journal of the European Ceramic Society, 2011. **31**(3): p. 313-320.
20. Li, Y., et al., *Fabrication and crack propagation behaviour of laminated ZrC–SiC composites.* Materials Science and Engineering: A, 2015. **647**: p. 1-6.
21. Luo, Y., et al., *Fabrication and mechanical evaluation of SiC–TiC nanocomposites by SPS.* Materials Letters, 2004. **58**(1–2): p. 150-153.
22. Zhao, L., et al., *Low temperature sintering of ZrC–SiC composite.* Journal of Alloys and Compounds, 2011. **509**(41): p. 9816-9820.

23. Kelly, J.E., *Generation IV International Forum: A decade of progress through international cooperation.* Progress in Nuclear Energy, 2014. **77**: p. 240-246.
24. Tuček, K., et al., *Generation IV Reactor Safety and Materials Research by the Institute for Energy and Transport at the European Commission's Joint Research Centre.* Nuclear Engineering and Design, 2013. **265**: p. 1181-1193.
25. Abram, T. and S. Ion, *Generation-IV nuclear power: A review of the state of the science.* Energy Policy, 2008. **36**(12): p. 4323-4330.
26. Chadwick, M.B., et al., *ENDF/B-VII.0: Next Generation Evaluated Nuclear Data Library for Nuclear Science and Technology.* Nuclear Data Sheets, 2006. **107**(12): p. 2931-3060.
27. Bloom, E.E., *The challenge of developing structural materials for fusion power systems.* Journal of Nuclear Materials, 1998. **258–263, Part 1**(0): p. 7-17.
28. Hallstadius, L., S. Johnson, and E. Lahoda, *Cladding for high performance fuel.* Progress in Nuclear Energy, 2012. **57**(0): p. 71-76.
29. Weaver, K.D., *Gas cooled fast reactor.* Sociedad Nuclear Mexican, 2005.
30. Hosemann, P., et al., *Materials selection for nuclear applications: Challenges and opportunities.* Scripta Materialia, 2017.
31. Grape, S., et al., *New perspectives on nuclear power—Generation IV nuclear energy systems to strengthen nuclear non-proliferation and support nuclear disarmament.* Energy Policy, 2014. **73**: p. 815-819.
32. Murty, K.L. and I. Charit, *Structural materials for Gen-IV nuclear reactors: Challenges and opportunities.* Journal of Nuclear Materials, 2008. **383**(1): p. 189-195.
33. Karoutas, Z., et al., *The maturing of nuclear fuel: Past to Accident Tolerant Fuel.* Progress in Nuclear Energy.
34. Katoh, Y., et al., *Radiation effects in SiC for nuclear structural applications.* Current Opinion in Solid State and Materials Science, 2012. **16**(3): p. 143-152.
35. Zeman, A., et al., *IAEA coordinated research activities on materials for advanced reactor systems.* Journal of Nuclear Materials, 2013. **442**(1–3, Supplement 1): p. S77-S83.
36. Jiang, D.L., et al., *Studies on the strengthening of silicon carbide-based multiphase ceramics I: The SiC□TiC system.* Materials Science and Engineering: A, 1989. **109**: p. 401-406.
37. Alam, T., et al., *A review on the clad failure studies.* Nuclear Engineering and Design, 2011. **241**(9): p. 3658-3677.
38. Yvon, P. and F. Carré, *Structural materials challenges for advanced reactor systems.* Journal of Nuclear Materials, 2009. **385**(2): p. 217-222.
39. Heinisch, H.L., et al., *Displacement damage in silicon carbide irradiated in fission reactors.* Journal of Nuclear Materials, 2004. **327**(2–3): p. 175-181.
40. Lee, Y. and M.S. Kazimi, *A structural model for multi-layered ceramic cylinders and its application to silicon carbide cladding of light water reactor fuel.* Journal of Nuclear Materials, 2015. **458**(0): p. 87-105.
41. Zinkle, S.J., *Advanced materials for fusion technology.* Fusion Engineering and Design, 2005. **74**(1–4): p. 31-40.
42. Porter, I.E., et al., *Design and fabrication of an advanced TRISO fuel with ZrC coating.* Nuclear Engineering and Design, 2013. **259**: p. 180-186.
43. Vasudevamurthy, G., et al., *Microstructure and mechanical properties of heat-treated and neutron irradiated TRISO-ZrC coatings.* Journal of Nuclear Materials, 2015. **464**: p. 245-255.

44. McEachern, D.W., W. Wu, and F. Venneri, *Performance of PyC, SiC, ZrC coatings in the geologic repository.* Nuclear Engineering and Design, 2012. **251**: p. 102-110.
45. Powers, J.J. and B.D. Wirth, *A review of TRISO fuel performance models.* Journal of Nuclear Materials, 2010. **405**(1): p. 74-82.
46. Snead, L.L., et al., *Handbook of SiC properties for fuel performance modeling.* Journal of Nuclear Materials, 2007. **371**(1-3): p. 329-377.
47. Johan, B.M., *Diffusion of fission products and radiation damage in SiC.* Journal of Physics D: Applied Physics, 2013. **46**(47): p. 473001.
48. Carter, C.B. and M.G. Norton, *Ceramic Materials: Science and Engineering*. Springer ebook collection / Chemistry and Materials Science 2005-2008. 2007: Springer New York.
49. Pickering, M.A., et al., *Chemically vapor deposited silicon carbide (SiC) for optical applications.* Nuclear Inst. and Methods in Physics Research, A, 1990. **291**(1-2): p. 95-100.
50. Product sheet from Rohm and Haas Co.
51. Suzuki, H., T. Iseki, and M. Ito, J. Nucl. Mater., 1973. **48**.
52. Li, Z. and R.C. Bradt, *Thermal expansion of the cubic (3C) polytype of SiC.* Journal of Materials Science, 1986. **21**(12): p. 4366-4368.
53. Pojur, A.F., B. Yates, and B.T. Kelly, *Thermal expansion at elevated temperatures III. A hemispherical laminar composite of pyrolytic graphite, silicon carbide and its constituents between 300 and 800 K.* Journal of Physics D: Applied Physics, 1972. **5**(7): p. 1321-1329.
54. McCullum, D.E., et al., *Summary of Results of the Effects of Environment on Mechanical Behavior of High-Performance Ceramics.* Ceram. Eng. Sci. Proc., 1991. **12**(9-10): p. 1886-1913.
55. Hecht, N.L., D.E. McCullum, and G.A. Graves, *Investigation of Selected Si<inf>3</inf>N<inf>4</inf> and SiC Ceramics.* Proceedings of the Third International Symposium on Ceramic Materials and Components for Engines (Las Vegas, NV, November 27–30, 1988: p. 806-817.
56. G.A. Graves, N.L.H., *Effects of Environment on the Mechanical Behavior of High-Performance Ceramics.* Report No. UDR-TR-94-136, U.S. Department of Energy Contract DE-AC05-84R21400 1995.
57. Tracy, C.A. and G.D. Quinn, *Fracture toughness by the surface crack in flexure (SCF) method.* Ceramic Engineering and Science Proceedings, 1994. **15**(5): p. 837-845.
58. Ghosh, A., et al., *Elevated-Temperature Fracture Resistance of a Sintered α-Silicon Carbide.* Journal of the American Ceramic Society, 1989. **72**(2): p. 242-247.
59. E.H. Kraft and R.H. Smoak, x., *Crack Propagation in Sintered Alpha Silicon Carbide.* Presented at the Fall Meeting of the American Ceramic Society, 1977.
60. Zdaniewski, W.A. and H.P. Kirchner, *Effect of Grain-Boundary Oxidation on Fracture Toughness of SiC.* Journal of the American Ceramic Society, 1987. **70**(8): p. 548-552.
61. Kodama, H. and T. Miyoshi, *Study of Fracture Behavior of Very Fine-Grained Silicon Carbide Ceramics.* Journal of the American Ceramic Society, 1990. **73**(10): p. 3081-3086.
62. Osborne, M.C., et al., *Mechanical- and physical-property changes of neutron-irradiated chemical-vapor-deposited silicon carbide.* Journal of the American Ceramic Society, 1999. **82**(9): p. 2490-2496.

63. Nogami, S., A. Hasegawa, and L.L. Snead, *Indentation fracture toughness of neutron irradiated silicon carbide.* Journal of Nuclear Materials, 2002. **307-311**(2 SUPPL.): p. 1163-1167.
64. Wang, H., R.N. Singh, and J.S. Goela, *Effects of Postdeposition Treatments on the Mechanical Properties of a Chemical-Vapor-Deposited Silicon Carbide.* Journal of the American Ceramic Society, 1995. **78**(9): p. 2437-2442.
65. NIIHARA, K., *Mechanical properties of chemically vapor deposited nonoxide ceramics.* Am. Ceram. Soc. Bull.. **63**: p. 1160.
66. Slavin, M.J. and G.D. Quinn, *Mechanical property evaluation at elevated temperature of sintered β-silicon carbide.* International Journal of High Technology Ceramics, 1986. **2**(1): p. 47-63.
67. Evans, A.G. and E.A. Charles, *Fracture Toughness Determinations by Indentation.* Journal of the American Ceramic Society, 1976. **59**(7-8): p. 371-372.
68. Yavuz, B.O. and R.E. Tressler, *Threshold Stress Intensity for Crack Growth in Silicon Carbide Ceramics.* Journal of the American Ceramic Society, 1993. **76**(4): p. 1017-1024.
69. Kodama, H. and T. Miyoshi, *Study of Fracture Behavior of Very Fine-Grained Silicon Carbide Ceramics.* Journal of the American Ceramic Society, 1990. **73**(10): p. 3081-3086.
70. Jiang, M., et al., *A comparative study of low energy radiation responses of SiC, TiC and ZrC.* Acta Materialia, 2016. **110**(Supplement C): p. 192-199.
71. Katoh, Y., et al., *Current status and critical issues for development of SiC composites for fusion applications.* Journal of Nuclear Materials, 2007. **367**: p. 659-671.
72. Kondo, S., Y. Katoh, and L.L. Snead, *Microstructural defects in SiC neutron irradiated at very high temperatures.* Journal of Nuclear Materials, 2008. **382**(2–3): p. 160-169.
73. Katoh, Y., et al., *Microstructural development in cubic silicon carbide during irradiation at elevated temperatures.* Journal of Nuclear Materials, 2006. **351**(1-3): p. 228-240.
74. Pouchon, M.A., et al., *Irradiation effects in helium implanted silicon carbide measured by X-ray absorption spectrometry.* Journal of Nuclear Materials, 2009. **385**(2): p. 299-303.
75. Gan, J., et al., *Proton irradiation study of GFR candidate ceramics.* Journal of Nuclear Materials, 2009. **389**(2): p. 317-325.
76. Gan, J., et al., *Ion Irradiation study on Microstructure Stability of GFR Ceramics: ZrC, ZrN, TiC, TiN and SiC Irradiated with 1 MeV Kr Ions to 10 and 70 dpa at 800 C.* FY-2005 Summary Report, 2005.
77. Pellegrino, S., et al., *Radiation effects in carbides: TiC and ZrC versus SiC.* Nuclear Instruments and Methods in Physics Research Section B: Beam Interactions with Materials and Atoms, 2014. **327**: p. 103-107.
78. Ishimaru, M., I.-T. Bae, and Y. Hirotsu, *Electron-beam-induced amorphization in SiC.* Physical Review B, 2003. **68**(14): p. 144102.
79. Katoh, Y., et al., *Properties of zirconium carbide for nuclear fuel applications.* Journal of Nuclear Materials, 2013. **441**(1): p. 718-742.
80. Shimada, S. and T. Ishil, *Oxidation Kinetics of Zirconium Carbide at Relatively Low Temperatures.* Journal of the American Ceramic Society, 1990. **73**(10): p. 2804-2808.
81. Snead, L.L., Y. Katoh, and S. Kondo, *Effects of fast neutron irradiation on zirconium carbide.* Journal of Nuclear Materials, 2010. **399**(2): p. 200-207.
82. R.A. Andrievskii, e.a., Neorg. Meter., 1978. **14** p. pp. 680-683.

83. Rahaman, M.N., *Ceramic Processing and Sintering*. Materials Engineering. 2003: Taylor & Francis.
84. Nosek, A., et al., *Thermomechanics of candidate coatings for advanced gas reactor fuels.* Journal of Nuclear Materials, 2007. **371**(1): p. 288-303.
85. Ferraris, M., et al., *Joining of machined SiC/SiC composites for thermonuclear fusion reactors.* Journal of Nuclear Materials, 2008. **375**(3): p. 410-415.
86. Henager Jr, C.H., et al., *Coatings and joining for SiC and SiC-composites for nuclear energy systems.* Journal of Nuclear Materials, 2007. **367–370, Part B**(0): p. 1139-1143.
87. Marcio Florian, L.E.d.C.a.C.A.A.C., *SiCf/SiC Composite: Attainment Methods, Properties and Characterization,.* Advances in Ceramics Costas Sikalidis, IntechOpen, August 9th 2011.
88. Taylor, R.E. and J. Morreale, *Thermal Conductivity of Titanium Carbide, Zirconium Carbide, and Titanium Nitride at High Temperatures.* Journal of the American Ceramic Society, 1964. **47**(2): p. 69-73.
89. Kohyama Akira, a.K.h., *SiC/SiC composite materials for nuclera applications.* Nuclear safety and Simulation, 2013. **4**.
90. `Li, M., et al., *The critical issues of SiC materials for future nuclear systems.* Scripta Materialia, 2017.
91. Katoh, Y., et al., *Current status and recent research achievements in SiC/SiC composites.* Journal of Nuclear Materials, 2014. **455**(1–3): p. 387-397.
92. Radovic, B.M. and M.W. Barsoum, *MAX phases : Bridging.* American Ceramic Society Bulletin, 2013. **92**(3): p. 20-27.
93. Wei, G.C. and P.F. Becher, *Improvements in Mechanical Properties in SiC by the Addition of TiC Particles.* Journal of the American Ceramic Society, 1984. **67**(8): p. 571-574.
94. An, H.-G., Y.-W. Kim, and J.-G. Lee, *Effect of initial α-phase content of SiC on microstructure and mechanical properties of SiC–TiC composites.* Journal of the European Ceramic Society, 2001. **21**(1): p. 93-98.
95. Kim, Y.-W., et al., *Effect of initial particle size on microstructure of liquid-phase sintered α-silicon carbide.* Journal of the European Ceramic Society, 2000. **20**(7): p. 945-949.
96. Sciti, D., S. Guicciardi, and M. Nygren, *Spark plasma sintering and mechanical behaviour of ZrC-based composites.* Scripta Materialia, 2008. **59**(6): p. 638-641.
97. Zhao, L., et al., *Oxidation of ZrC–30vol% SiC composite in air from low to ultrahigh temperature.* Journal of the European Ceramic Society, 2012. **32**(4): p. 947-954.
98. Pizon, D., et al., *Oxidation behavior of spark plasma sintered ZrC–SiC composites obtained from the polymer-derived ceramics route.* Ceramics International, 2014. **40**(3): p. 5025-5031.
99. Barsoum, M. and M.W. Barsoum, *Fundamentals of Ceramics*. Series in Material Science and Engineering. 2002: Taylor & Francis.
100. Hull, D. and T.W. Clyne, *An Introduction to Composite Materials*. 2 ed. Cambridge Solid State Science Series. 1996, Cambridge: Cambridge University Press.
101. Chawla, K.K., *Ceramic Matrix Composites*. 2013: Springer US.
102. Raju, K. and D.-H. Yoon, *Sintering additives for SiC based on the reactivity: A review.* Ceramics International, 2016. **42**(16): p. 17947-17962.
103. Tokita, M., *Chapter 11.2.3 - Spark Plasma Sintering (SPS) Method, Systems, and Applications*, in *Handbook of Advanced Ceramics (Second Edition)*, S. Somiya, Editor. 2013, Academic Press: Oxford. p. 1149-1177.

104. Bradt, R.C., et al., *Fracture Mechanics of Ceramics: Fatigue, Composites, and High-Temperature Behavior*. 2012: Springer US.
105. Fett, T. and D. Munz, *Chapter 9.5 - Fracture Mechanics*, in *Handbook of Advanced Ceramics (Second Edition)*, S. Somiya, Editor. 2013, Academic Press: Oxford. p. 681-715.
106. Freiman, S.W., *Chapter 9.6 - Fracture Mechanics Measurements*, in *Handbook of Advanced Ceramics (Second Edition)*, S. Somiya, Editor. 2013, Academic Press: Oxford. p. 717-731.
107. Suryanarayana, C. and M.G. Norton, *X-Ray Diffraction: A Practical Approach*. 2013: Springer US.
108. Callister, W.D. and D.G. Rethwisch, *Fundamentals of Materials Science and Engineering: An Integrated Approach*. 2012: Wiley.
109. Young, R.A., *The Rietveld Method*. IUCr monographs on crystallography. 1995: Oxford University Press.
110. Hawkes, P.W. and L. Reimer, *Scanning Electron Microscopy: Physics of Image Formation and Microanalysis*. 2013: Springer Berlin Heidelberg.
111. Williams, D.B., *Transmission electron microscopy. Vol.2, Diffraction*, ed. C.B. Carter. 1996.
112. Williams, D.B., *Transmission electron microscopy. Vol.3, Imaging*, ed. C.B. Carter. 1996.
113. Williams, D.B. and C.B. Carter, *Transmission Electron Microscopy: A Textbook for Materials Science*. 1996: Springer.
114. Glauert, A.M., *Practical Methods in Electron Microscopy: Principles and practice of electron microscope operation*. 1974: North-Holland Publishing Company.
115. http://www.tainstruments.com/products/flash-diffusivity/.
116. Bradt, R.C., et al., *Fracture Mechanics of Ceramics: Active Materials, Nanoscale Materials, Composites, Glass, and Fundamentals*. Fracture Mechanics of Ceramics. 2010: Springer US.
117. *Fracture Resistance Testing of Monolithic and Composite Brittle Materials*. 2002.
118. Ceramics, C.A., *Standard Practice for Fractography and Characterization of Fracture Origins in Advanced Ceramics*. 2010.
119. *Standard Test Methods for Determination of Fracture Toughness of Advanced Ceramics at Ambient Temperature.* C28.01 Advanced Ceramics, 2010.
120. Quinn, G.D. and R.C. Bradt, *On the Vickers Indentation Fracture Toughness Test.* Journal of the American Ceramic Society, 2007. **90**(3): p. 673-680.
121. Ćorić, D., M. Majić Renjo, and L. Ćurković, *Vickers indentation fracture toughness of Y-TZP dental ceramics.* International Journal of Refractory Metals and Hard Materials, 2017. **64**: p. 14-19.
122. Strecker, K., S. Ribeiro, and M.-J. Hoffmann, *Fracture toughness measurements of LPS-SiC: a comparison of the indentation technique and the SEVNB method.* Materials Research, 2005. **8**: p. 121-124.
123. Alireza MORADKHANI, H.B., Mehdi TAJDARI,Hamidreza LATIFI,Jukka MARTIKAINEN, *Determination of fracture toughness using the area of micro-crack tracks left in brittle materials by Vickers indentation test.* Journal of Advanced Ceramics, 2013. **2**(1): p. 87-102.
124. Anstis, G.R., et al., *A Critical Evaluation of Indentation Techniques for Measuring Fracture Toughness: I, Direct Crack Measurements.* Journal of the American Ceramic Society, 1981. **64**(9): p. 533-538.

125. Niihara, K., R. Morena, and D. Hasselman, *Evaluation of K Ic of brittle solids by the indentation method with low crack-to-indent ratios.* Journal of Materials Science Letters, 1982. **1**(1): p. 13-16.
126. Chinn, R.E., *Ceramography: Preparation and Analysis of Ceramic Microstructures*. 2002: ASM International.
127. Schönfeld, K., H.-P. Martin, and A. Michaelis, *Pressureless sintering of ZrC with variable stoichiometry.* Journal of Advanced Ceramics, 2017. **6**(2): p. 165-175.
128. Zhao, L., et al., *Pressureless sintering of ZrC-based ceramics by enhancing powder sinterability.* International Journal of Refractory Metals and Hard Materials, 2011. **29**(4): p. 516-521.
129. Wang, L., W. Jiang, and L. Chen, *Rapidly sintering nanosized SiC particle reinforced TiC composites by the spark plasma sintering (SPS) technique.* Journal of Materials Science. **39**(14): p. 4515-4519.
130. Barsoum, M.W. and T. El-Raghy, *The MAX phases: unique new carbide and nitride materials.* American Scientist, 2001.
131. Heuer, A.H., et al., *β→α Transformation in Polycrystalline SiC: I, Microstructural Aspects.* Journal of the American Ceramic Society, 1978. **61**(9-10): p. 406-412.
132. Mitchell, T.E., L.U. Ogbuji, and A.H. Heuer, *β→α Transformation in Polycrystalline Sic: II, Interfacial Energetics.* Journal of the American Ceramic Society, 1978. **61**(9-10): p. 412-413.
133. Ogbuji, L.U., et al., *The β→α Transformation in Polycrystalline SiC: IV, A Comparison of Conventionally Sintered, Hot-Pressed, Reaction-Sintered, and Chemically Vapor-Deposited Samples.* Journal of the American Ceramic Society, 1981. **64**(2): p. 100-105.
134. Ogbuji, L.U., T.E. Mitchell, and A.H. Heuer, *The β→αTransformation in Poly crystalline SiC: III, The Thickening of α Plates.* Journal of the American Ceramic Society, 1981. **64**(2): p. 91-99.
135. Cheng, L., et al., *Densification and mechanical properties of TiC by SPS-effects of holding time, sintering temperature and pressure condition.* Journal of the European Ceramic Society, 2012. **32**(12): p. 3399-3406.
136. Baillet, J., et al., *Influence of grain size and microstructure on oxidation rate and mechanism in sintered titanium carbide under high temperature and low oxygen partial pressure.* Journal of the European Ceramic Society, 2016. **36**(13): p. 3099-3111.
137. Ning, F., et al., *Effects of TiO2 crystal structure on the performance of Li4Ti5O12 anode material.* Journal of Alloys and Compounds, 2012. **513**: p. 524-529.
138. Mecholsky, J. and S. Powell, *Fractography of Ceramic and Metal Failures*. 1984.
139. Lorrette, C., A. Réau, and L. Briottet, *Mechanical properties of nanostructured silicon carbide consolidated by spark plasma sintering.* Journal of the European Ceramic Society, 2013. **33**(1): p. 147-156.
140. Herrmann, M., et al., *Micro-segregations in liquid phase sintered silicon carbide ceramics.* Journal of the European Ceramic Society, 2010. **30**(6): p. 1495-1501.
141. Grasso, S., et al., *Joining of β-SiC by spark plasma sintering.* Journal of the European Ceramic Society, 2014. **34**(7): p. 1681-1686.
142. Awaji, H., S.-M. Choi, and E. Yagi, *Mechanisms of toughening and strengthening in ceramic-based nanocomposites.* Mechanics of Materials, 2002. **34**(7): p. 411-422.
143. Endo, H., M. Ueki, and H. Kubo, *Microstructure and mechanical properties of hot-pressed SiC-TiC composites.* Journal of Materials Science, 1991. **26**(14): p. 3769-3774.

144. Evans, A.G. and R.M. McMeeking, *On the toughening of ceramics by strong reinforcements.* Acta Metallurgica, 1986. **34**(12): p. 2435-2441.
145. Lee, Y.-I. and Y.-W. Kim, *Toughening Mechanisms in SiC–TiC Composites.* Journal of the Ceramic Society of Japan, 2004. **112**(1301): p. 18-21.
146. Zhan, G.-D., et al., *Effect of β-to-α Phase Transformation on the Microstructural Development and Mechanical Properties of Fine-Grained Silicon Carbide Ceramics.* Journal of the American Ceramic Society, 2001. **84**(5): p. 945-950.
147. Bellosi, A., T. Kosmac, and A.P. Tomsia, *Interfacial Science in Ceramic Joining*. Nato Science Partnership Subseries: 3. 2013: Springer Netherlands.
148. Cheng, L., Z. Xie, and G. Liu, *Spark plasma sintering of TiC-based composites toughened by submicron SiC particles.* Ceramics International, 2013. **39**(5): p. 5077-5082.
149. Ervin, G., *Oxidation behavior of silicon carbide.* Journal of the American Ceramic Society, 1958. **41**(9): p. 347-352.
150. Banu, N.D., et al., *Identification of selective oxidation of TiC/SiC composite with X-ray diffraction and Raman spectroscopy.* Chemical Papers, 2016. **70**(11): p. 1503-1511.
151. Nie, X., et al., *Doping of TiO2 Polymorphs for Altered Optical and Photocatalytic Properties.* International Journal of Photoenergy, 2009: p. n/a.
152. Román-Manso, B., et al., *Effects of Current Confinement on the Spark Plasma Sintering of Silicon Carbide Ceramics.* Journal of the American Ceramic Society, 2015. **98**(9): p. 2745-2753.
153. Sun, S.-K., et al., *Reactive spark plasma sintering of ZrC and HfC ceramics with fine microstructures.* Scripta Materialia, 2013. **69**(2): p. 139-142.
154. Hungría, T., J. Galy, and A. Castro, *Spark Plasma Sintering as a Useful Technique to the Nanostructuration of Piezo-Ferroelectric Materials.* Advanced Engineering Materials, 2009. **11**(8): p. 615-631.
155. Wei, X., et al., *Spark Plasma Sintering of Commercial Zirconium Carbide Powders: Densification Behavior and Mechanical Properties.* Materials, 2015. **8**(9): p. 6043-6061.
156. Wang, X.-G., et al., *Densification behavior and properties of hot-pressed ZrC ceramics with Zr and graphite additives.* Journal of the European Ceramic Society, 2011. **31**(6): p. 1103-1111.
157. Kohama, K. and K. Ito, *Direct solid-state diffusion bonding of zirconium carbide using a spark plasma sintering system.* Materials & Design, 2016. **110**: p. 888-894.
158. Nachiappan, C., et al., *Synthesis and Densification of Monolithic Zirconium Carbide by Reactive Hot Pressing.* Journal of the American Ceramic Society, 2010. **93**(5): p. 1341-1346.
159. Zhao, G., et al., *Mechanical properties, strengthening and toughening mechanisms of reactive-hot-pressed TiB2-SiC-Ni ceramic composites*. Vol. 8. 2017. 233-242.
160. Ma, B., W. Han, and E. Guo, *Oxidation behavior of ZrC-based composites in static laboratory air up to 1300°C.* International Journal of Refractory Metals and Hard Materials, 2014. **46**: p. 159-167.